

**STABLE VANADIUM-DOPED MAGNÉLI PHASE TITANIUM OXIDES FOR
THE ELECTROCHEMICAL OXIDATION OF INDUSTRIAL WASTEWATER**

by

Joseph English

B.Sc., The University of Manitoba, 2004

B.A.Sc., The University of British Columbia, 2016

A THESIS SUBMITTED IN PARTIAL FULFILLMENT OF
THE REQUIREMENTS FOR THE DEGREE OF

DOCTOR OF PHILOSOPHY

in

THE FACULTY OF GRADUATE AND POSTDOCTORAL STUDIES

(Chemical & Biological Engineering)

THE UNIVERSITY OF BRITISH COLUMBIA

(Vancouver)

July 2023

© Joseph English, 2023

The following individuals certify that they have read, and recommend to the Faculty of Graduate and Postdoctoral Studies for acceptance, the dissertation entitled:

Stable vanadium-doped Magnéli phase titanium oxides for the electrochemical oxidation of industrial wastewater

submitted by Joseph English in partial fulfilment of the requirements for

the degree of Doctor of Philosophy

in Chemical & Biological Engineering

Examining Committee:

David Wilkinson, Professor, Chemical & Biological Engineering, UBC

Supervisor

Jurgen Stumper, Adjunct Professor, Chemical & Biological Engineering, UBC

Supervisory Committee Member

Anthony Lau, Associate Professor, Chemical & Biological Engineering, UBC

University Examiner

John Madden, Professor, Materials Engineering, UBC

University Examiner

Additional Supervisory Committee Members:

Madjid Mohseni, Professor, Chemical & Biological Engineering, UBC

Supervisory Committee Member

Abstract

The development of effective yet inexpensive technologies for wastewater treatment is critical to the safeguarding of water resources and the delivery of clean water for sanitation and drinking. Electrochemical technologies are of growing relevance in an increasingly decentralized, distributed, and electrified system. High oxidation potential (HOP) materials, so called for their ability to generate efficacious conditions for water treatment, are critical to their development. One such HOP, Magnéli phase titanium oxides (MPTOs), are being utilized to advance this domain; however, issues of its stability constrain the applicability of devices that employ them. Doping influences many physicochemical properties of MPTOs relevant to their use as electrode materials. The rational selection of dopants for MPTOs is explored using Hume-Rothery rules for solid substitutional solutions, selecting transition metals vanadium, chromium, and iron as potentially highly soluble dopants. Their thermal stability is investigated using thermogravimetric analysis (TGA) in air and a model for their thermal oxidation is developed from kinetic data. Electrochemical accelerated life testing (ALT) is conducted with doped MPTO electrodes and their influence on the time to failure is evaluated. These tests establish that vanadium doping provides a significant improvement to the stability of MPTOs in thermally and electrochemically oxidizing conditions. Porous transport layers (PTLs) of vanadium-doped MPTOs are prepared and incorporated into a compact electrolyzer, which is used to treat industrial wastewater. Vanadium-doped MPTO PTLs provide a significant improvement in performance over pristine materials in terms of volumetric energy consumption. Furthermore, the compact electrolyzer design places this approach in the top quartile of this class of electrochemical devices, which is attributed to the reduced interelectrode distance.

Lay Summary

The development of effective yet inexpensive technologies for wastewater treatment is critical to the safeguarding of water resources and the delivery of clean water for sanitation and drinking. Electrochemical technologies are of growing relevance for complementing legacy infrastructure to provide solutions in an increasingly decentralized, distributed, and electrified system. In this work, novel electrode materials were developed and characterized and their efficacy for the treatment of industrial wastewater was evaluated. Specifically, additives called dopants were incorporated into a conventional electrode material called Magnéli phase titanium oxides or MPTOs. The influence of this modification on relevant properties such as electrical conductivity and stability were investigated using analytical techniques. This work demonstrates that this approach improves these characteristics of the electrodes. Furthermore, the use of these electrodes with modern electrochemical cells called zero-gap electrolyzers demonstrates that these electrodes based on doped MPTOs perform significantly better than pristine materials with superior energy efficiency.

Preface

Chapter 3: The Thermal-Oxidation Behaviour of Pristine and Doped Magnéli Phase Titanium Oxides is based on experimental work that Dr. David P. Wilkinson and I conceptualized, planned, collected, analyzed, and wrote. It has been published: J. T. English and D. P. Wilkinson, “The Thermal-Oxidation Behavior of Pristine and Doped Magnéli Phase Titanium Oxides,” *ECS Journal of Solid State Science and Technology*, 10, 034004, 2021. It was also presented at a refereed conference: J. T. English and D. P. Wilkinson, “The Thermal-Oxidation Behavior of Pristine and Doped Magnéli Phase Titanium Oxides,” presented at the ECS 238th Meeting & PRiME 2020, Virtual, Oct. 4–9, 2020.

Chapter 4: The Superior Electrical Conductivity and Anodic Stability of Vanadium-Doped Ti_4O_7 is also based on experimental work that Dr. David P. Wilkinson and I conceptualized, planned, collected, analyzed, and wrote. It has been published: J. T. English and D. P. Wilkinson, “The Superior Electrical Conductivity and Anodic Stability of Vanadium-Doped Ti_4O_7 ,” *Journal of The Electrochemical Society*, 168(10), 103509, 2021. It was also presented at a refereed conference: J. T. English and D. P. Wilkinson, “The Superior Electrical Conductivity and Anodic Stability of Vanadium-Doped Ti_4O_7 ,” presented at the ECS 240th Meeting, Virtual, Oct. 10–14, 2021.

Chapter 5: Vanadium-Doped Ti_4O_7 Porous Transport Layers for Efficient Electrochemical Oxidation of Industrial Wastewater Contaminants also based on experimental work that Dr. David P. Wilkinson and I conceptualized, planned, collected, analyzed, and wrote. It was also presented in part at two refereed conferences: 1) J. T. English and D. P. Wilkinson, “Electrochemistry on the Edge: Advancing High Oxidation Power Materials for Applications at Strongly Oxidizing Potentials” presented at the ECS 241st Meeting, Vancouver, May 29–June 2, 2022. 2) J. T. English and

D. P. Wilkinson, “A Compact Electrolyzer with Vanadium-Doped Ti_4O_7 Porous Transport Layers for Effective Industrial Wastewater Treatment” presented at CCEC 2022, Vancouver, Oct 23–26, 2022. A manuscript has been submitted for publication: J. T. English and D. P. Wilkinson, Vanadium-Doped Ti_4O_7 Porous Transport Layers for Efficient Electrochemical Oxidation of Industrial Wastewater Contaminants, submitted.

All publications and presentations produced during the program are summarized in Appendix B.

Table of Contents

Abstract.....	iii
Lay Summary	iv
Preface.....	v
Table of Contents	vii
List of Tables	xiii
List of Figures.....	xvii
List of Symbols	xxix
List of Abbreviations	xxxiii
Acknowledgements	xxxvi
Dedication	xxxviii
Chapter 1: Introduction	1
1.1 Motivation.....	1
1.2 Background.....	3
1.2.1 Stoichiometry in Aqueous Electrochemical Processes.....	5
1.2.2 Electrochemical Thermodynamics.....	7
1.2.3 Losses in Electrochemical Systems	8
1.2.3.1 Electrode Kinetics	9
1.2.3.2 Transport Phenomena	11
1.2.3.3 Ohmic Drop	15
1.2.4 Overall Cell Potential.....	16
1.2.5 Electrochemical Treatment of Wastewater	18

1.3	Literature Review.....	20
1.3.1	Preparation of MPTOs	23
1.3.2	MTPOs as Electrodes.....	25
1.3.3	Electrochemical Wastewater Treatment with MPTO-Based Electrodes	28
1.4	Research Questions and Objectives	33
Chapter 2: Methodology.....		35
2.1	Material Preparation.....	35
2.1.1	Sol-gel Methods	35
2.1.2	Solid-State Diffusion Methods	38
2.1.3	Thermal Reduction.....	40
2.2	Material Characterization.....	42
2.2.1	Structure.....	42
2.2.1.1	X-ray Diffraction	42
2.2.2	Composition.....	44
2.2.2.1	X-ray Fluorescence	44
2.2.2.2	Energy-Dispersive X-ray Spectroscopy.....	46
2.2.2.3	X-ray Photoelectron Spectroscopy	47
2.2.3	Morphology.....	48
2.2.3.1	Scanning Electron Microscopy	48
2.2.4	Thermogravimetric Analysis	49
2.3	Electrochemical Measurements	51
2.3.1	Cyclic Voltammetry.....	51
2.3.2	Galvanostatic Methods.....	52

2.4	Water Quality Measurements	53
2.4.1	Colorimetry	54
2.4.1.1	Decolorization.....	55
2.4.1.2	Chemical Oxygen Demand Removal.....	55

Chapter 3: The Thermal-Oxidation Behaviour of Pristine and Doped Magnéli Phase

Titanium Oxides.....	57	
3.1	Introduction.....	57
3.2	Experimental.....	59
3.2.1	Preparation of doped titanium oxides	59
3.2.2	Preparation of pristine and doped magnéli phase titanium oxides	60
3.2.3	Scanning electron microscopy and energy-dispersive X-ray spectroscopy.....	60
3.2.4	Gas adsorption analysis.....	61
3.2.5	X-ray fluorescence spectroscopy	61
3.2.6	X-ray photoelectron spectroscopy	61
3.2.7	Powder X-ray diffractometry and structure refinement.....	62
3.2.8	Thermogravimetric analysis.....	62
3.3	Results & Discussion	63
3.3.1	Vanadium, chromium, and iron are suitable dopants	63
3.3.2	Powders are highly-doped Ti_4O_7	65
3.3.3	Vanadium and iron improve thermal stability	70
3.3.4	Thermal oxidation in air is diffusion-controlled.....	74
3.4	Summary.....	79

Chapter 4: The Superior Electrical Conductivity and Anodic Stability of Vanadium-Doped

Ti₄O₇81

4.1	Introduction.....	81
4.2	Experimental.....	84
4.2.1	Materials	84
4.2.2	Electrode preparation	84
4.2.3	Physicochemical characterization.....	85
4.2.3.1	Scanning electron microscopy and energy-dispersive X-ray spectroscopy.....	85
4.2.3.2	X-ray fluorescence spectroscopy	86
4.2.3.3	X-ray photoelectron spectroscopy	86
4.2.3.4	Powder X-ray diffractometry	87
4.2.3.5	4-point probe method.....	87
4.2.4	Electrochemical measurements.....	88
4.3	Results & Discussion	89
4.3.1	Physical characteristics highly-doped Ti ₄ O ₇	89
4.3.2	V- and Fe-doping improve electrical conductivity	94
4.3.3	Electrocatalytic behavior for water splitting reactions unaffected by doping	95
4.3.4	V-doping improves anodic stability.....	99
4.4	Summary.....	104

Chapter 5: Vanadium-Doped Ti₄O₇ Porous Transport Layers for Efficient Electrochemical

Oxidation of Industrial Wastewater Contaminants105

5.1	Introduction.....	105
5.2	Experimental.....	107

5.2.1	Materials	108
5.2.2	Electrode characterization.....	109
5.2.3	Electrochemical measurements.....	111
5.2.4	Evaluation of cell performance.....	112
5.3	Results & Discussion	114
5.3.1	Porous transport layers are monophasic and highly doped, exhibiting electrochemical behavior typical of Ti_4O_7	114
5.3.2	Compact wastewater electrolyzer exhibits mass-transport controlled behavior.....	118
5.3.3	Flow rate, current density, and PTL composition have varying influence on performance	124
5.4	Conclusions.....	127
Chapter 6: Conclusions & Recommendations		129
6.1	Conclusions.....	129
6.2	Recommendations.....	131
Bibliography		134
Appendices.....		164
Appendix A Supplementary Data		165
A.1	Supplementary Data for Chapter 1: Introduction.....	166
A.2	Supplementary Data for Chapter 3:The Thermal-Oxidation Behaviour of Pristine and Doped Magnéli Phase Titanium Oxides	174
A.3	Supplementary Data for Chapter 4:The Superior Electrical Conductivity and Anodic Stability of Vanadium-Doped Ti_4O_7	186

A.4	Supplementary Data for Chapter 5: Vanadium-Doped Ti ₄ O ₇ Porous Transport Layers for Efficient Electrochemical Oxidation of Industrial Wastewater Contaminants .	197
	Appendix B Publications and Presentations	210
B.1	Publications.....	210
B.2	Presentations	210

List of Tables

Table 1.1 Overpotential for the oxygen evolution reaction (η_{OER}), logarithm base 10 of the electrical conductivity (σ) and the relative cost of high oxidation power (HOP) materials lead(IV) oxide (PbO_2), antimony-doped tin(IV) oxide (ATO), boron-doped diamond (BDD) and Magnéli phase titanium oxides (MPTOs).	22
Table 1.2 Methods of preparing doped Magnéli phase titanium oxides.....	25
Table 1.3 Selected physical properties of high oxidation power (HOP) materials. Data for Magnéli phase titanium oxides (MPTOs, <i>i.e.</i> , Ti_4O_7) obtained from [30, 67, 68, 69].....	26
Table 1.4 Selected examples of flow-by reactors with Magnéli phase titanium oxides treating wastewater and their removal efficiency (or conversion, X), current efficiency (ϕ), and electrical energy per order (90%) removal (E_{EO})	31
Table 1.5 Selected examples of flow-through continuous reactors with Magnéli phase titanium oxides treating wastewater and their removal efficiency (or conversion, X), current efficiency (ϕ), and electrical energy per order (90%) removal (E_{EO}).....	32
Table 3.1 Summary of statistical analysis (5 observations at a 5% significance level) of energy-dispersive X-ray (EDX) spectroscopy and X-ray fluorescence (XRF) of dopant in H_2 -reduced TiO_2	67
Table 3.2 Summary of statistical (3 observations at a 5% significance level) analysis of fitted total relative mass change ($\Delta m/m_0$), onset and peak temperatures (T_o and T_p , respectively) for the thermal oxidation ($5\text{ }^\circ\text{C min}^{-1}$) of pristine and doped Ti_4O_7 in air.....	73
Table 3.3 Summary of statistical (5% significance level) analysis of fitted activation energy (E), Arrhenius pre-exponential factor (A), and the coefficient of variance (R^2) for the thermal	

oxidation (1, 2, 5, and 10 °C min ⁻¹) of pristine and doped Ti ₄ O ₇ in air using the integral isoconversional Kissinger–Akahira–Sunose (KAS) method and linear model-fitting with Jander (D3) and Ginstling–Brounshtein (D4) reaction models.....	77
Table 4.1 Summary of statistical analysis (5 observations, 5% significance level) of energy-dispersive X-ray (EDX) spectroscopy and X-ray fluorescence (XRF) of dopant in H ₂ -reduced pristine and nominally 2 at% doped TiO ₂ disks.....	91
Table 4.2 Summary of statistical analysis (5 observations, 5% significance level) of electrical conductivities (σ) of pristine and doped Ti ₄ O ₇ disks.	95
Table 4.3 Summary of statistical analysis (3 observations, 5% significance level) of fitted Tafel parameters of pristine and doped Ti ₄ O ₇ disk electrodes (2,000 RPM) in 0.5 M H ₂ SO ₄ (0.4 pH, 22 °C). Tafel slope, b , and exchange current density, j_0 , the latter normalized for both geometric and electrochemically-active surface areas (subscripts "geo" and "ECSA", respectively).	98
Table 4.4 Summary of statistical analysis (3 observations, 5% significance level) of time-to-failures (TTFs, 100 mA cm _{geo} ⁻²) of pristine and doped Ti ₄ O ₇ disk electrodes in 0.5 M H ₂ SO ₄ (pH 0.4, 22 °C).....	101
Table A.2.1 Summary of elemental analysis of survey spectra from X-ray photoelectron spectroscopy of pristine and dopant-containing H ₂ -reduced TiO ₂	176
Table A.2.2 Summary of peak fitting of high-resolution X-ray photoelectron spectra including their binding energy (BE), full width half maximum (FWHM), Lorentzian-Gaussian (L-G), and results of chi-squared (χ^2) testing of pristine and V-containing H ₂ -reduced TiO ₂	178
Table A.2.3 Summary of peak fitting of high-resolution X-ray photoelectron spectra including their binding energy (BE), full width half maximum (FWHM), Lorentzian-Gaussian (L-G), and results of chi-squared (χ^2) testing of Cr- and Fe-containing H ₂ -reduced TiO ₂	179

Table A.2.4 Summary of the fitted lattice parameters and volume (V) of the unit cell, crystallite size (τ), and strain (ε) of the Ti_4O_7 phase as well as the weighted profile R-factor (R_{wp}) obtained by structure refinement of powder X-ray diffraction data of H_2 -reduced pristine and doped TiO_2	181
Table A.2.5 Summary of the positional parameters of the unit cell of the Ti_4O_7 phase obtained by structure refinement of powder X-ray diffraction data of H_2 -reduced pristine and doped TiO_2 .	182
Table A.2.6 (Continued from Table A.2.5) Summary of the positional parameters of the unit cell of the Ti_4O_7 phase obtained by structure refinement of powder X-ray diffraction data of H_2 -reduced pristine and doped TiO_2	183
Table A.3.1 Summary of peak fitting of high-resolution X-ray photoelectron spectra including their binding energy (BE), full width half maximum (FWHM), Lorentzian-Gaussian (L-G), and results of chi-squared (χ^2) testing of H_2 -reduced pristine sintered TiO_2 disks.	188
Table A.3.2 Summary of peak fitting of high-resolution X-ray photoelectron spectra including their binding energy (BE), full width half maximum (FWHM), Lorentzian-Gaussian (L-G), and results of chi-squared (χ^2) testing of H_2 -reduced vanadium-containing sintered TiO_2 disks.	189
Table A.3.3 Summary of peak fitting of high-resolution X-ray photoelectron spectra including their binding energy (BE), full width half maximum (FWHM), Lorentzian-Gaussian (L-G), and results of chi-squared (χ^2) testing of H_2 -reduced chromium-containing sintered TiO_2 disks.....	190
Table A.3.4 Summary of peak fitting of high-resolution X-ray photoelectron spectra including their binding energy (BE), full width half maximum (FWHM), Lorentzian-Gaussian (L-G), and results of chi-squared (χ^2) testing of H_2 -reduced iron-containing sintered TiO_2 disks.....	191

Table A.3.5 Summary of statistical analysis of reported values of compounds used in the deconvolution of high-resolution X-ray photoelectron spectra including the binding energy (BE), its sample standard deviation (s_{BE}), and number of observations (n). 192

Table A.3.6 Summary of prominent peaks (>15% intensity) of powder X-ray diffractograms of Ti_3O_5 , their (relative) intensity, and assigned Miller indices (h, k, and l) between 20 and $50^\circ 2\theta$.
..... 194

Table A.3.7 Summary of prominent peaks (>15% intensity) of powder X-ray diffractograms of Ti_4O_7 , their (relative) intensity, and assigned Miller indices (h, k, and l) between 20 and $50^\circ 2\theta$.
..... 195

List of Figures

Figure 1.1 Wastewater safely treated having undergone at least secondary (or biological) treatment in Canada between 2007–2015. Labels indicate average costs per m ³ of wastewater treated.....	2
Figure 1.2 Components of an electrochemical cell including two electrodes (anode and cathode), separator, reference electrode (RE) immersed in electrolyte and a potentiostat (PS). Adapted from [16].	4
Figure 1.3 Methods of preparing Magnéli phase titanium oxide (MPTO) materials from various precursors such as titanium metal (Ti ⁰), organotitanium (TiR _n), titanium halides (TiX _m), and titanium(IV) oxide (TiO ₂). Adapted and modified from [43].....	23
Figure 1.4 Electrochemical behaviour of an Ebonex® electrode in 1 M H ₂ SO ₄ (50 mV s ⁻¹ , 298 K). Data obtained from [70].....	26
Figure 1.5 Potential (E_{eq})-pH equilibrium or Pourbaix diagram for titanium in aqueous solutions (see Appendix A.1 for equilibria).....	27
Figure 1.6 a) Flow-by and b) flow-through reactor configurations	29
Figure 2.1 Hydration of tetratitanium isopropoxide (TTIP) forming titanium(IV) hydroxide (Ti(OH) ₄) and isopropanol (<i>i</i> PrOH).....	36
Figure 2.2 Condensation of titanium(IV) hydroxide (Ti(OH) ₄) monomers forming a dimer.	36
Figure 2.3 Polycondensation of dimer and titanium(IV) hydroxide (Ti(OH) ₄) monomers forming eventual TiO ₂ network	36
Figure 2.4 Condensation and polycondensation of titanium(IV) hydroxide (Ti(OH) ₄) and metal(III) hydroxide (M(OH) ₃) monomers eventually forming a M-doped TiO ₂ network	38

Figure 2.5 Solid-state diffusion process showing the distribution of atoms with time after two heterogenous materials are put together at sufficiently elevated temperatures.	39
Figure 2.6 Components of a tube furnace.....	41
Figure 2.7 Visual description of Bragg’s law and related diffraction phenomena	43
Figure 2.8 Bohr model of titanium atom undergoing X-ray fluorescence and related phenomena	45
Figure 2.9 Types of signals generated by electron beam in a scanning electron microscope	49
Figure 2.10 Components of a thermogravimetric analyzer. Adapted from [88]	50
Figure 2.11 A cyclic voltammetry experiment (left) and the construction of a cyclic voltammogram (right).....	52
Figure 3.1 Darken-Gurry map of elements having a coordination number of 6, an oxidation state of III, and a corundum-like crystal structure where "HS" refers to the high-spin complex. The red circle is an ellipse with a width of $\pm 15\%$ the radius of Ti^{III} (0.67 \AA) and a height of ± 0.4 on the Pauling scale of electronegativity. Image reproduced from [65], which permits unrestricted reuse of the work via the Creative Commons Attribution 4.0 License (CC BY, http://creativecommons.org/licenses/by/4.0/).....	64
Figure 3.2 Optical microscope images of pristine and dopant-containing TiO_2 powders before a)–d) and after e)–h) H_2 reduction. Image reproduced from [65], which permits unrestricted reuse of the work via the Creative Commons Attribution 4.0 License (CC BY, http://creativecommons.org/licenses/by/4.0/).....	66
Figure 3.3 Powder X-ray diffraction patterns (1.5406 \AA) of H_2 -reduced pristine and dopant-containing TiO_2 , which are well-indexed with Ti_4O_7 (COD 1008048). An extraneous peak in the Fe-doped, H_2 -reduced TiO_2 pattern at $44.7^\circ 2\theta$ is assigned to the (110) Miller index of crystalline	

alpha Fe (α -Fe, COD 9005836). Image reproduced from [65], which permits unrestricted reuse of the work via the Creative Commons Attribution 4.0 License (CC BY, <http://creativecommons.org/licenses/by/4.0/>). 69

Figure 3.4 (a) Thermograms and (b) differential thermograms ($5\text{ }^\circ\text{C min}^{-1}$) of pristine and doped Ti_4O_7 in air. The data sampling intervals are reduced from 1/12 to $25\text{ }^\circ\text{C}$ for clarity. Image reproduced from [65], which permits unrestricted reuse of the work via the Creative Commons Attribution 4.0 License (CC BY, <http://creativecommons.org/licenses/by/4.0/>). 72

Figure 3.5 (a) & (b) $y(\alpha)$ and (c) & (d) $z(\alpha)$ master plots for the thermal oxidation of (a) & (c) pristine and (b) & (d) V-doped Ti_4O_7 in air. Image reproduced from [65], which permits unrestricted reuse of the work via the Creative Commons Attribution 4.0 License (CC BY, <http://creativecommons.org/licenses/by/4.0/>). 76

Figure 3.6 (a) Linearized differential data ($\ln\{f(d\alpha/dt)[1/f(\alpha)]\}$) for three-dimensional diffusion reaction models (a) & (b) Jander (D_3 , $f(\alpha) = f_{\text{D}_3}(\alpha)$) and (c) & (d) Ginstling–Brounshtein (D_4 , $f(\alpha) = f_{\text{D}_4}(\alpha)$) vs $1,000/T$ for the thermal oxidation of (a) & (c) pristine and (b) & (d) V-doped Ti_4O_7 in air with linear fit (straight line, empty markers indicating outliers). Image reproduced from [65], which permits unrestricted reuse of the work via the Creative Commons Attribution 4.0 License (CC BY, <http://creativecommons.org/licenses/by/4.0/>). 78

Figure 3.7 (a) Relative fixed-conversion lifetimes (t_{α} , 5% conversion) of pristine and doped Ti_4O_7 from kinetic prediction using Jander (D_3) and Ginstling–Brounshtein (D_4) reaction models. Image reproduced from [65], which permits unrestricted reuse of the work via the Creative Commons Attribution 4.0 License (CC BY, <http://creativecommons.org/licenses/by/4.0/>). 80

Figure 4.1 (a) Optical image and (b)–(e) scanning electron micrographs (20 kV) of H₂-reduced pristine and nominally 2 at% doped TiO₂ disks. Image reproduced from [66], which permits unrestricted reuse of the work via the Creative Commons Attribution 4.0 License (CC BY, <http://creativecommons.org/licenses/by/4.0/>). 90

Figure 4.2 X-ray photoelectron spectra of Ar-ion etched (4 keV) H₂-reduced pristine and nominally 2 at% doped TiO₂ disks: (a) survey spectra and high resolution spectra of (b) V 2p and (c) Fe 2p peaks. Image reproduced from [66], which permits unrestricted reuse of the work via the Creative Commons Attribution 4.0 License (CC BY, <http://creativecommons.org/licenses/by/4.0/>). 92

Figure 4.3 Powder X-ray diffraction patterns (1.5406 Å) of ground H₂-reduced pristine and nominally 2 at% doped TiO₂ disks, which are well-indexed with Ti₄O₇ (empty diamonds, COD 1008048) along with a minor adventitious phase attributed to Ti₃O₅ (filled diamonds, COD 4512563) in the V- and Cr-doped samples. Image reproduced from [66], which permits unrestricted reuse of the work via the Creative Commons Attribution 4.0 License (CC BY, <http://creativecommons.org/licenses/by/4.0/>). 93

Figure 4.4 Cyclic voltammograms (50 mV s⁻¹, 5th cycle) of pristine and doped Ti₄O₇ disk electrodes (2,000 RPM) in 0.5 M H₂SO₄ (pH 0.4, 22 °C). Plus signs (+) indicate origins for their respective plots. Image reproduced from [66], which permits unrestricted reuse of the work via the Creative Commons Attribution 4.0 License (CC BY, <http://creativecommons.org/licenses/by/4.0/>). 97

Figure 4.5 Selected Tafel plots of pristine and doped Ti₄O₇ disk electrodes (2,000 RPM) in 0.5 M H₂SO₄ (pH 0.4, 22 °C) for the oxygen evolution reaction. Image reproduced from [66], which

permits unrestricted reuse of the work via the Creative Commons Attribution 4.0 License (CC BY, <http://creativecommons.org/licenses/by/4.0/>). 99

Figure 4.6 Selected chronopotentiograms (100 mA cm^{geo-2}) of pristine and doped Ti₄O₇ disk electrodes (2,000 RPM) in 0.5 M H₂SO₄ (pH 0.4, 22 °C).Image reproduced from [66], which permits unrestricted reuse of the work via the Creative Commons Attribution 4.0 License (CC BY, <http://creativecommons.org/licenses/by/4.0/>). 100

Figure 4.7 Nyquist plots (100 ± 1 mA cm^{geo-2}) of pristine and doped Ti₄O₇ disk electrodes (2,000 RPM) in 0.5 M H₂SO₄ (pH 0.4, 22 ° C) at the beginning (BOL, full circles, ·) and near the end of life (EOL, open circles, ○) during accelerated life testing. Image reproduced from [66], which permits unrestricted reuse of the work via the Creative Commons Attribution 4.0 License (CC BY, <http://creativecommons.org/licenses/by/4.0/>). 103

Figure 5.1 (a) Schematic of preparation of a) porous transport layers (PTLs), b) composition and assembly of compact wastewater electrolyzer, and c) its process flow diagram operating in a recirculating batch mode. 109

Figure 5.2 X-ray (1.5406 Å) diffraction patterns of H₂-reduced pristine and nominally 1, 2, and 5 at% doped TiO₂ sintered plates along with idealized patterns for Ti₄O₇ (COD 1008048) and Ti₅O₉ (COD 1539580). 115

Figure 5.3 a–d) Electron micrographs (20 kV), e–g) elemental mapping of titanium (blue) and vanadium (red), and h) V/(Ti+V) determined by energy dispersive X-ray spectroscopy and X-ray fluorescence (EDX and XRF, respectively) of (Ti_{1-x}V_x)₄O₇ (0 ≤ x ≤ 0.05) porous transport layers. Error bars indicate 95% confidence intervals (5 observations). 116

Figure 5.4 Cyclic voltammograms (100 mV s^{-1} , tenth cycle) of $(\text{Ti}_{1-x}\text{V}_x)_4\text{O}_7$ ($0 \leq x \leq 0.05$) porous transport layers in $1,500 \text{ mg}_{\text{NaCl}} \text{ L}^{-1}$ (22°C , pH 5.3). Plus signs (+) indicate origins of their respective plots..... 118

Figure 5.5 Current-voltage behavior of the compact wastewater electrolyzer with $(\text{Ti}_{1-x}\text{V}_x)_4\text{O}_7$ ($0 \leq x \leq 0.05$) porous transport layers in $1,500 \text{ mg}_{\text{NaCl}} \text{ L}^{-1}$ (22°C , pH 5.3). Error bars indicate 95% confidence intervals (5 observations). 119

Figure 5.6 a) Conversion (X), b) linearized conversion data ($-\ln(1 - X)$), c) current efficiency (ϕ), d) specific and e) volumetric energy consumption (E_{SP} & E_{EO} , respectively) for the decolorization and chemical oxygen demand (COD) removal (empty and filled symbols, respectively) of $100 \text{ ppm}_{\text{MO}}$ in $1,500 \text{ g}_{\text{NaCl}}$ (200 mL min^{-1} , 21°C , pH 4.0) with a $(\text{Ti}_{0.98}\text{V}_{0.02})_4\text{O}_7$ porous transport layer in a compact electrolyzer operated galvanostatically (10 mA cm^{-2} , 200 mL min^{-1}). Dotted and dash-dotted lines indicate either lines of best fit (a & b) or model predictions (c–e, Eqs. 5.10,) for decolorization and COD removal, respectively. 121

Figure 5.7 a)–c) Mass transfer coefficients (k_m) and d)–f) volumetric energy consumption (E_{EO}) for decolorization and COD removal (empty and filled markers, respectively) of $100 \text{ ppm}_{\text{MO}}$ in $1,500 \text{ mg}_{\text{NaCl}}$. Unless otherwise stated, the flow rate, current density, and x (in $(\text{Ti}_{1-x}\text{V}_x)_4\text{O}_7$) are 200 mL min^{-1} , 10 mA cm^{-2} , and 0.02, respectively. Error bars indicate 95% confidence intervals derived from parameter fitting of linear-regressed data to analytical models. 125

Figure A.2.1 Scanning electron micrographs (20 kV) of pristine and dopant-containing H_2 -reduced TiO_2 at 200 (a, c, e, & g) and 3,200 (b, d, f, & h) magnification. Image reproduced from [65], which permits unrestricted reuse of the work via the Creative Commons Attribution 4.0 License (CC BY, <http://creativecommons.org/licenses/by/4.0/>). 175

Figure A.2.2 Survey X-ray photoelectron spectra of pristine (blue line) and V-, Cr-, and Fe-doped (magenta, green, & red lines, respectively) H₂-reduced TiO₂. Image reproduced from [65], which permits unrestricted reuse of the work via the Creative Commons Attribution 4.0 License (CC BY, <http://creativecommons.org/licenses/by/4.0/>)..... 176

Figure A.2.3 High resolution X-ray photoelectron spectra (black dots) of (a, c, e, & g) Ti 2p and (b, d, f, & h) O 1s of (a & b) pristine and (c–h) dopant-containing H₂-reduced TiO₂ along with a Taylor baseline (green line), constituent peaks (blue, magenta, & black lines), and sum of baseline and constituent peaks (red line) Image reproduced from [65], which permits unrestricted reuse of the work via the Creative Commons Attribution 4.0 License (CC BY, <http://creativecommons.org/licenses/by/4.0/>)..... 177

Figure A.2.4 Structure refinement data (Y_{calc} , black line) of powder X-ray diffraction data (Y_{obs} , red dots), their difference ($Y_{\text{obs}} - Y_{\text{calc}}$, blue line), and the Bragg positions of Ti₄O₇ (green vertical lines) and alpha iron (α -Fe, magenta vertical lines) for (a) pristine and (b–d) dopant-containing H₂-reduced TiO₂. Image reproduced from [65], which permits unrestricted reuse of the work via the Creative Commons Attribution 4.0 License (CC BY, <http://creativecommons.org/licenses/by/4.0/>)..... 180

Figure A.2.5 (a & b) $y(\alpha)$ and (c & d) $z(\alpha)$ master plots for the thermal oxidation of (a & c) Cr- and (b & d) Fe-doped Ti₄O₇ in air. Image reproduced from [65], which permits unrestricted reuse of the work via the Creative Commons Attribution 4.0 License (CC BY, <http://creativecommons.org/licenses/by/4.0/>)..... 184

Figure A.2.6 Linearized differential data ($\ln\{f(d\alpha/dt)[1/f(\alpha)]\}$) for three-dimensional diffusion reaction models (a & b) Jander ($D_3, f(\alpha) = f_{D3}(\alpha)$) and (c & d) Ginstling-Brounshtein ($D_4, f(\alpha) = f_{D4}(\alpha)$) versus $1,000/T$ for the thermal oxidation of (a & c) Cr- and (b & d) Fe-doped Ti₄O₇ in air

with linear fit (straight line, empty markers indicating outliers). Image reproduced from [65], which permits unrestricted reuse of the work via the Creative Commons Attribution 4.0 License (CC BY, <http://creativecommons.org/licenses/by/4.0/>)..... 185

Figure A.3.1 High-resolution X-ray photoelectron spectra (20 kV) of (a, c, e, & g) Ti 2p and O 1s (b, d, f, & h) peaks of Ar-ion etched (4 keV) H₂-reduced (a & b) pristine and (c–h) dopant-containing sintered TiO₂ disks and their deconvolution including Taylor baseline (green lines), constituent peaks (blue, magenta, and black lines) and sum of baseline and constituent peaks (red lines). Image reproduced from [66], which permits unrestricted reuse of the work via the Creative Commons Attribution 4.0 License (CC BY, <http://creativecommons.org/licenses/by/4.0/>). 187

Figure A.3.2 Valence band spectra of H₂-reduced pristine and dopant-containing sintered TiO₂ disks obtained by X-ray photoelectron spectroscopy (20 kV). Plus signs (+) indicate the origin for their respective spectra. Image reproduced from [66], which permits unrestricted reuse of the work via the Creative Commons Attribution 4.0 License (CC BY, <http://creativecommons.org/licenses/by/4.0/>). 193

Figure A.3.3 Bode plots ($100 \pm 1 \text{ mA cm}^{-2}_{\text{geo}}$) of (a) pristine and (b & c) doped Ti₄O₇ disk electrodes (2,000 RPM) in 0.5 M H₂SO₄ (pH 0.4, 22 °C) at the beginning (BOL, full circles) and near the end of life (EOL, open circles) during accelerated life testing. Image reproduced from [66], which permits unrestricted reuse of the work via the Creative Commons Attribution 4.0 License (CC BY, <http://creativecommons.org/licenses/by/4.0/>). 196

Figure A.3.4 Voigt-type electrical circuit as possible equivalent electrochemical circuit. Elements labelled with C and R refer to capacitors and resistors, respectively. R1 refers to the solution resistance, C2 & R2 and C3 & R3 refer to individual Voigt elements, accounting for

double layer and film capacitances and charge transfer and film resistances. Image reproduced from [66], which permits unrestricted reuse of the work via the Creative Commons Attribution 4.0 License (CC BY, <http://creativecommons.org/licenses/by/4.0/>). 196

Figure A.4.1 UV-Visible absorbance spectra of methyl orange (100 ppm in 1,500 mg_{NaCl} L⁻¹). 198

Figure A.4.2 Cyclic voltammograms (100 mV s⁻¹, tenth cycle) of Sigracet 29 BC gas diffusion layer in 1,500 mg_{NaCl} L⁻¹ (22 °C, pH 5.3)..... 199

Figure A.4.3 Conversion (X , a), linearized conversion data ($-\ln(1 - X)$, b), current efficiency (ϕ , c), specific and volumetric energy consumption (E_{SP} & E_{EO} , respectively, d & e) for the decolorization and chemical oxygen demand (COD) removal (empty and filled symbols, respectively) of 100 ppm_{MO} in 1,500 g_{NaCl} (150 mL min⁻¹, 21 °C, 4.0 pH) with a (Ti_{0.98}V_{0.02})₄O₇ porous transport layer in a compact electrolyzer operated galvanostatically (10 mA cm⁻²). Dotted and dash-dotted lines indicate either lines of best fit (a & b) or model predictions (c–e, Eqs. 5.10, 5.11, & 5.6) for decolorization and COD removal, respectively. 200

Figure A.4.4 Conversion (X , a), linearized conversion data ($-\ln(1 - X)$, b), current efficiency (ϕ , c), specific and volumetric energy consumption (E_{SP} & E_{EO} , respectively, d & e) for the decolorization and chemical oxygen demand (COD) removal (empty and filled symbols, respectively) of 100 ppm_{MO} in 1,500 g_{NaCl} (250 mL min⁻¹, 21 °C, 4.0 pH) with a (Ti_{0.98}V_{0.02})₄O₇ porous transport layer in a compact electrolyzer operated galvanostatically (10 mA cm⁻²). Dotted and dash-dotted lines indicate either lines of best fit (a & b) or model predictions (c–e, Eqs. 5.10, 5.11, & 5.6) for decolorization and COD removal, respectively. 201

Figure A.4.5 Conversion (X , a), linearized conversion data ($-\ln(1 - X)$, b), current efficiency (ϕ , c), specific and volumetric energy consumption (E_{SP} & E_{EO} , respectively, d & e) for the

decolorization and chemical oxygen demand (COD) removal (empty and filled symbols, respectively) of 100 ppm_{MO} in 1,500 g_{NaCl} (200 mL min⁻¹, 21 °C, 4.0 pH) with a (Ti_{0.98}V_{0.02})₄O₇ porous transport layer in a compact electrolyzer operated galvanostatically (2.5 mA cm⁻²).

Dotted and dash-dotted lines indicate either lines of best fit (a & b) or model predictions (c–e, Eqs. 5.10, 5.11, & 5.6) for decolorization and COD removal, respectively. 202

Figure A.4.6 Conversion (X , a), linearized conversion data ($-\ln(1 - X)$, b), current efficiency (ϕ , c), specific and volumetric energy consumption (E_{SP} & E_{EO} , respectively, d & e) for the

decolorization and chemical oxygen demand (COD) removal (empty and filled symbols, respectively) of 100 ppm_{MO} in 1,500 g_{NaCl} (200 mL min⁻¹, 21 °C, 4.0 pH) with a (Ti_{0.98}V_{0.02})₄O₇ porous transport layer in a compact electrolyzer operated galvanostatically (5 mA cm⁻²).

Dotted and dash-dotted lines indicate either lines of best fit (a & b) or model predictions (c–e, Eqs. 5.10, 5.11, & 5.6) for decolorization and COD removal, respectively. 203

Figure A.4.7 Conversion (X , a), linearized conversion data ($-\ln(1 - X)$, b), current efficiency (ϕ , c), specific and volumetric energy consumption (E_{SP} & E_{EO} , respectively, d & e) for the

decolorization and chemical oxygen demand (COD) removal (empty and filled symbols, respectively) of 100 ppm_{MO} in 1,500 g_{NaCl} (200 mL min⁻¹, 21 °C, 4.0 pH) with a (Ti_{0.98}V_{0.02})₄O₇ porous transport layer in a compact electrolyzer operated galvanostatically (7.5 mA cm⁻²).

Dotted and dash-dotted lines indicate either lines of best fit (a & b) or model predictions (c–e, Eqs. 5.10, 5.11, & 5.6) for decolorization and COD removal, respectively. 204

Figure A.4.8 Conversion (X , a), linearized conversion data ($-\ln(1 - X)$, b), current efficiency (ϕ , c), specific and volumetric energy consumption (E_{SP} & E_{EO} , respectively, d & e) for the

decolorization and chemical oxygen demand (COD) removal (empty and filled symbols, respectively) of 100 ppm_{MO} in 1,500 g_{NaCl} (200 mL min⁻¹, 21 °C, 4.0 pH) with a (Ti_{0.98}V_{0.02})₄O₇

porous transport layer in a compact electrolyzer operated galvanostatically (12.5 mA cm^{-2}).

Dotted and dash-dotted lines indicate either lines of best fit (a & b) or model predictions (c–e, Eqs. 5.10, 5.11, & 5.6) for decolorization and COD removal, respectively. 205

Figure A.4.9 Conversion (X , a), linearized conversion data ($-\ln(1 - X)$, b), current efficiency (ϕ , c), specific and volumetric energy consumption (E_{SP} & E_{EO} , respectively, d & e) for the decolorization and chemical oxygen demand (COD) removal (empty and filled symbols, respectively) of 100 ppm_{MO} in $1,500 \text{ g}_{NaCl}$ (200 mL min^{-1} , $21 \text{ }^\circ\text{C}$, 4.0 pH) with a $(Ti_{0.98}V_{0.02})_4O_7$ porous transport layer in a compact electrolyzer operated galvanostatically (15 mA cm^{-2}). Dotted and dash-dotted lines indicate either lines of best fit (a & b) or model predictions (c–e, Eqs. 5.10, 5.11, & 5.6) for decolorization and COD removal, respectively. 206

Figure A.4.10 Conversion (X , a), linearized conversion data ($-\ln(1 - X)$, b), current efficiency (ϕ , c), specific and volumetric energy consumption (E_{SP} & E_{EO} , respectively, d & e) for the decolorization and chemical oxygen demand (COD) removal (empty and filled symbols, respectively) of 100 ppm_{MO} in $1,500 \text{ g}_{NaCl}$ (200 mL min^{-1} , $21 \text{ }^\circ\text{C}$, 4.0 pH) with a Ti_4O_7 porous transport layer in a compact electrolyzer operated galvanostatically (10 mA cm^{-2}). Dotted and dash-dotted lines indicate either lines of best fit (a & b) or model predictions (c–e, Eqs. 5.10, 5.11, & 5.6) for decolorization and COD removal, respectively. 207

Figure A.4.11 Conversion (X , a), linearized conversion data ($-\ln(1 - X)$, b), current efficiency (ϕ , c), specific and volumetric energy consumption (E_{SP} & E_{EO} , respectively, d & e) for the decolorization and chemical oxygen demand (COD) removal (empty and filled symbols, respectively) of 100 ppm_{MO} in $1,500 \text{ g}_{NaCl}$ (200 mL min^{-1} , $21 \text{ }^\circ\text{C}$, 4.0 pH) with a $(Ti_{0.99}V_{0.01})_4O_7$ porous transport layer in a compact electrolyzer operated galvanostatically (10 mA cm^{-2}). Dotted

and dash-dotted lines indicate either lines of best fit (a & b) or model predictions (c–e, Eqs. 5.10, 5.11, & 5.6) for decolorization and COD removal, respectively. 208

Figure A.4.12 Conversion (X , a), linearized conversion data ($-\ln(1 - X)$, b), current efficiency (ϕ , c), specific and volumetric energy consumption (E_{SP} & E_{EO} , respectively, d & e) for the decolorization and chemical oxygen demand (COD) removal (empty and filled symbols, respectively) of 100 ppm_{MO} in 1,500 g_{NaCl} (200 mL min⁻¹, 21 °C, 4.0 pH) with a (Ti_{0.95}V_{0.05})₄O₇ porous transport layer in a compact electrolyzer operated galvanostatically (10 mA cm⁻²). Dotted and dash-dotted lines indicate either lines of best fit (a & b) or model predictions (c–e, Eqs. 5.10, 5.11, & 5.6) for decolorization and COD removal, respectively. 209

List of Symbols

LATIN

Symbol	Description	Units
<i>a</i>	Coefficient (in dimensional analysis)	unitless
	Length (of unit cell)	Å
	Conversion (in thermal analysis)	%
	Tafel intercept	mV, V
<i>A</i>	Area	cm ² , m ²
	Tafel slope	mV dec ⁻¹
	Absorbance	unitless
	Arrhenius Pre-exponential Factor	varies
<i>b</i>	coefficient (in dimensional analysis)	unitless
	Length (of unit cell)	Å
	Tafel slope	mV dec ⁻¹
<i>c</i>	concentration	M, mol cm ⁻³
	coefficient (in dimensional analysis)	unitless
	speed of light	m s ⁻¹
	Length of unit cell	Å
<i>d</i>	Lattice spacing	Å, nm
<i>D</i>	Diffusion coefficient	cm ² s ⁻¹ , m ² s ⁻¹
<i>D</i> ₀	Diffusion coefficient at infinite temperature	cm ² s ⁻¹ , m ² s ⁻¹

E	Electrode potential	V
	Energy	J, kJ, eV
E^0	Standard potential	V
E_a	Energy of activation	kJ mol^{-1}
E_{eq}	Equilibrium potential	V
E_{EO}	Electrical Energy Per Order	$\text{kWh m}^{-3} \text{ order}^{-1}$
E_{SP}	Specific Energy Consumption	kWh kg^{-1}
f	Dilution factor	unitless
F	Faraday's constant	C mol_e^{-1} , Ah mol_e^{-1}
$\Delta_f G^0$	Standard Gibbs free energy of formation	kJ mol^{-1}
$\Delta_r G^0$	Standard Gibbs free energy of (half) reaction	kJ mol^{-1}
h	Planck's constant	J s, eV s
I	Current	A, mA
I_0	Exchange current	A, mA
j	Current density	mA cm^{-2}
J	Flux	$\text{mol cm}^{-2} \text{ s}^{-1}$
k_m	Mass transfer coefficient	m s^{-1}
ℓ	Characteristic length (in dimensional analysis)	mm, cm, m
	Path length (in Beer's law)	cm
m	Mass	g, mg
M	Conversion factor	$\text{g}_{\text{COD}} \text{ mol}_e^{-1}$
n	Stoichiometry of electrons in half reaction	mol_e^-

	Diffraction order (in Bragg's law)	
Q	Reaction quotient	none
Q_v	Volumetric charge	mAh L ⁻¹ , Ah L ⁻¹
R	Gas constant	J K ⁻¹ mol ⁻¹
R_{wp}	Weighted profile R-factor	unitless
Re	Reynolds number	unitless
Sc	Schmidt number	unitless
Sh	Sherwood number	unitless
T	Temperature	K, °C
	Transmittance	%
T_o	Onset temperature	K, °C
T_p	Peak temperature	K, °C
u	Velocity component in x-direction	cm s ⁻¹ , m s ⁻¹
U_{cell}	Cell potential	V
\dot{V}	Volumetric flow rate	mL min ⁻¹
z	Charge (or valence)	unitless

GREEK

Symbol	Description	Units
α	Charge transfer coefficient	unitless
	Angle (of unit cell)	°, radians
β	Angle (of unit cell)	°, radians
	Temperature ramp rate	°C min ⁻¹
γ	Angle (of unit cell)	°, radians
δ	Diffusion layer thickness	μm
ε	Molar absorptivity	M ⁻¹ cm ⁻¹
	Crystallite strain	%, ppm
η	Overpotential (or overvoltage)	V, mV
θ	Incident angle (of radiation)	°, radians
κ	(Ionic) conductivity	μS cm ⁻¹
λ	Wavelength	nm
ν	Kinematic viscosity	m ² s ⁻¹ , cm ² s ⁻¹
σ	(Electrical) conductivity	S cm ⁻¹
τ	Crystallite size	Å
ϕ	Current efficiency	%
Φ	Electric field	V/m
	Work function of the surface (in XPS)	J, eV

List of Abbreviations

Abbreviation	Meaning
ACS	Active Chlorine Species
ALT	Accelerated Life Testing
ATO	Antimony-doped Tin(IV) Oxide
BDD	Boron-Doped Diamond
BET	Brunauer–Emmett–Teller
BOL	Beginning of Life
BSE	Backscattered Electrons
CIF	Crystallographic Information File
CN	Coordination Number
COD	Chemical Oxygen Demand
	Crystallography Open Database
CP	Chronopotentiogram
CS	Crystalline Shear
CV	Cyclic Voltammetry
D3	Jander Reaction Model
D4	Ginstling–Brounshtein Reaction Model
DTG	Differential Thermogram
EAOP	Electrochemical Advanced Oxidation Process
ECSA	Electrochemically-Active Surface Area

EDLC	Electrolytic Double-Layer Capacitor
EDX	Energy-Dispersive X-ray
EIS	Electrochemical Impedance Spectroscopy
EO	Electrochemical Oxidation
EOL	End of Life
EtOH	Ethanol
FC	Fuel Cell
GDL	Gas Diffusion Layer
HER	Hydrogen Evolution Reaction
HOP	High Oxidation Power
KAS	Kissinger–Akahira–Sunose
KHP	Potassium Hydrogen Phthalate
MEA	Membrane–Electrode Assembly
MO	Methyl Orange
mt	Mass Transfer (or Diffusion) Losses
MPTO	Magnéli Phase Titanium Oxide
NHE	Normal Hydrogen Electrode
OER	Oxygen Evolution Reaction
OS	Oxidation State
OV	Oxygen Vacancy
PEM	Proton-Exchange Membrane
PEMWE	Proton-Exchange Membrane Water Electrolyzer

PS	Potentiostat
PTL	Porous Transport Layer
PXRD	Powder X-ray Diffraction
4-POBN	α -(4-Pyridyl <i>N</i> -oxide)- <i>N</i> - <i>tert</i> -butylnitrone
RDE	Rotating Disk Electrode
REM	Reactive Electrochemical Membrane
SDG	Sustainable Development Goal
SE	Secondary Electrons
SEM	Scanning Electron Microscopy
SHE	Standard Hydrogen Electrode
TG	Thermogram
TGA	Thermogravimetric Analysis
TOC	Total Organic Carbon
TTF	Time-to-Failure
TTIP	Titanium Tetraisopropoxide
UPW	Ultrapure Water
WE	Water Electrolyzer
WWE	Wastewater Electrolyzer
XPS	X-ray Photoelectron Spectroscopy
XRD	X-ray Diffraction
XRF	X-ray Fluorescence

Acknowledgements

Firstly, I would like to give heartfelt thanks to my supervisor, Dr. David P. Wilkinson, for his support and guidance during my time in the program. It has been my privilege and pleasure to learn under his tutelage. Dr. Wilkinson has never made me want for anything, having cultivated an inspiring and supportive environment for doing research.

I would also like to acknowledge other members of my supervisory committee: Drs. Madjid Mohseni and Jürgen Stumper. It was a pleasure to be both a student and TA in a course taught by Dr. Mohseni: CHBE 377 – Water Pollution Control. I am also very fortunate to call Dr. Stumper my mentor through the NSERC CREATE NanoMat program.

I am very grateful for the financial support I have received during my doctoral studies: NSERC CREATE NanoMat, NSERC CGS-M, Killam Doctoral Scholarship, UBC 4-Year Fellowship, John Tiedje Fellowship in GHG Mitigation, and a JSPS Summer Program Fellowship.

I would like to express gratitude towards all members of the Wilkinson Laboratory, past and present, for their comradery and insights. In particular, I thank Drs. Arman Bonakdarpour, Baizeng Fang, Ivan Stoševski, and Macarena Cataldo-Hernández for being generous with their time and expertise. I would also like to recognize the excellent work of 2 summer students: Samuel J. Lee and Z. Amelia Dai. It was a pleasure to supervise you for our brief time together.

I thank my office mates, Matthias Kroschel, Alec Jameson, and Andrew Hakim, for their patience and friendship during our time in the program. I could not think of a more excellent people to have shared an office together.

I would also like to thank Dr. Kazuhiro Takanabe of the University of Tokyo as well as members of his group—in particular Drs. Fuminao Kishimoto and Keisuke Obata—for hosting me the summer of 2022. Thank you for the welcome and inspiring time in your lab.

Finally, to my family: my wife, Naoko, and our two children, Stanford and Cameron. And to my parents, Mary Lynn and Brian. Thank you for your unwavering support and sacrifice over the years. Thank you for believing in me.

To my wife
And children
With thanks

Chapter 1: Introduction

1.1 Motivation

Everyone in Canada should have access to clean water for drinking and sanitation. In September 2015, the United Nations adopted the *2030 Agenda for Sustainable Development*, a global call to action addressing a broad range of urgent social, economic, and environmental issues. Founded upon 17 Sustainable Development Goals (SDGs), it envisions an end to poverty, the protection of the environment, and an equal enjoyment of peace and prosperity. *SDG 6: Clean Water and Sanitation* commits Canada to guaranteeing the availability and sustainable management of clean water and sanitation.

Challenges for the treatment and disposal of industrial wastewater in Canada, however, put SDG 6 at risk. Per its target 6.3, Canada will, “by 2030, improve water quality by... halving the proportion of untreated wastewater”. Yet, since 2015, Canadian industry has decreased the proportion of wastewater safely treated (Figure 1.1) as defined as having undergone a secondary (or biological) level of treatment or greater [1].¹ Generally, this fraction decreases with increasing costs per unit [2], demonstrating the role for effective yet inexpensive technologies in helping Canada achieve its sustainability targets.

¹ Methods for wastewater treatment are classified into 3 levels: primary (1°), secondary (2°), and tertiary (3°) [185]. Primary methods remove solid matter by physical separation such as sedimentation. Secondary methods utilize biological systems to metabolize organic matter. Tertiary methods involve physicochemical techniques to treat contaminants inadequately addressed by or potentially harmful to primary and secondary treatment systems.

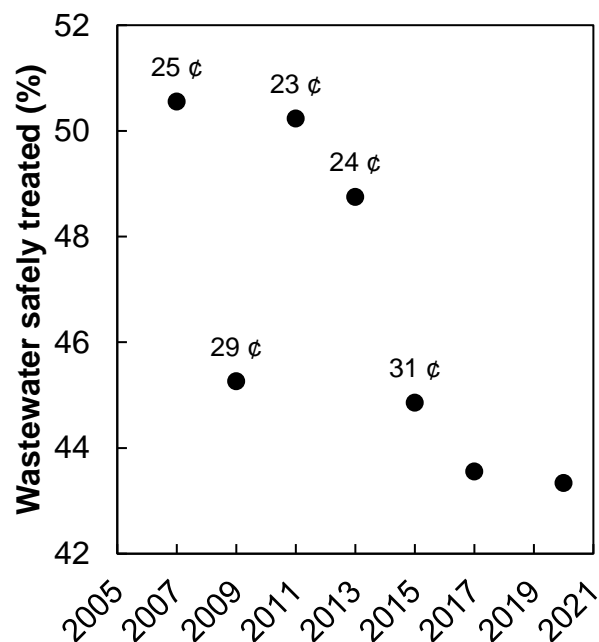


Figure 1.1 Wastewater safely treated having undergone at least secondary (or biological) treatment in Canada between 2007–2015. Labels indicate average present-day costs per m³ of wastewater treated.

Developing effective yet inexpensive tertiary (or advanced) technologies for the treatment of industrial wastewater will therefore help Canada to achieve SDG 6. The advancement of effective devices for the electrochemical approaches are of growing importance given their suitability for emerging decentralized and distributed treatment paradigms [3]. Electrochemical technologies operate at ambient conditions generating chemical oxidants in situ [4, 5, 6], obviating any need for the transportation, storage, and handling of hazardous chemicals. Electrochemical cells are modular in construction, simplifying the scale-up of treatment facilities [5, 6, 7]. Furthermore, electrochemical devices facilitate automated and remote operation [4, 5], utilizing clean, renewable, and increasingly inexpensive sources of energy such as wind and solar [8].

In a Canadian context, electrochemical technologies may already be sufficiently cost-competitive due to the low prices for electricity. Electrochemical advanced oxidation processes (EAOPs) are reported to reduce the level of pollutant by an order of magnitude for less than 1 kWh m^{-3} [9]. Considering that the average price of electricity for large users in Canada was 7.4 ¢ kWh^{-1} during 2007–2015 [10], this translates into a removal of more than 99.5% of pollutant at less than 19 ¢ m^{-3} . Nevertheless, the selection of effective electrode materials is critical to the viability of electrochemical technologies for industrial wastewater treatment. High oxidation power (HOP) materials, so called for their ability to access strongly oxidizing electrochemical potentials due to their poor electrocatalytic characteristics for the electrochemical water splitting reactions [7], reduce the permissiveness of these parasitic reaction in systems such as EAOPs electrochemically treating industrial wastewater. Magnéli phase titanium oxides (MPTOs), one such HOP material [11], are of broad interest for the advancement of electrochemical technologies as low-cost electrodes with wide solvent windows [6, 12], *i.e.*, accessing electrode potentials outside the range of a thermodynamic stability of a solvent, but also for clean energy as dimensionally-stable electrocatalyst supports and as an electrically-conductive filler in electrodes [13, 14, 15].

1.2 Background

Electrochemical processes are, as the name implies, chemical transformations coupled with electrical phenomena. They are both ubiquitous and important, ranging from batteries powering our portable electronic devices to water electrolyzers (WEs) for hydrogen production and will be foundational for a carbon-neutral future.

All electrochemical devices are comprised of the following (Figure 1.2):

1. 2 electrodes, termed the cathode and anode, at which electron transfer to and from the electrolyte occurs, respectively;
2. Electrolyte, which both receives and provides electrons at the respective electrode–electrolyte interfaces as well as conducts an ionic current between the electrodes; and
3. An external electric circuit connecting the electrodes via a power supply or an electrical load, which are referred to as electrolytic and voltaic or galvanic cells, respectively.

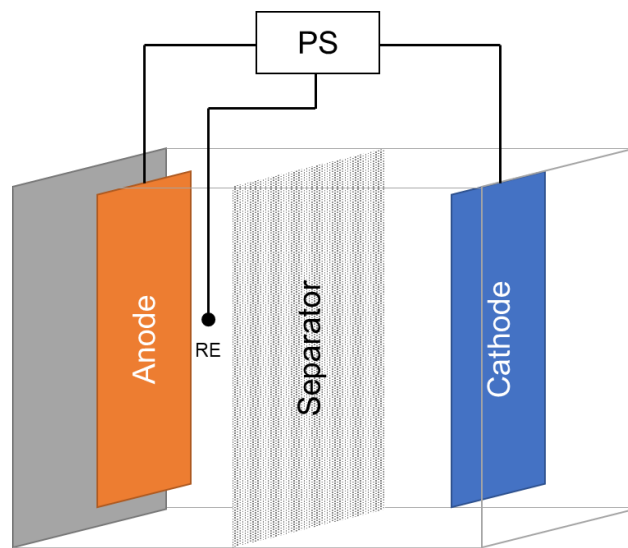


Figure 1.2 Components of an electrochemical cell including two electrodes (anode and cathode), separator, reference electrode (RE) immersed in electrolyte and a potentiostat (PS). Adapted from [16].

Such a setup, irrespective of whether a load or a power supply is included in the external circuitry, is called an electrochemical *cell*. There can be additional components of an electrochemical cell, such as:

- A barrier—such as a salt bridge, a separator, or a membrane—between the cathodic and anodic electrolyte chambers mitigating any undesired transport of chemical species from one compartment to another; and
- Auxiliary electrodes such as a *reference electrode*, which assist in the precise measurement and therefore control of the voltage being applied at an electrode of interest, one of either the cathode or anode and called the *working electrode*. Electrochemical cells employing a reference electrode are referred to as using a “3-electrode setup”.

1.2.1 Stoichiometry in Aqueous Electrochemical Processes

When a sufficiently large current (or voltage) is applied by the power supply to a WE and under the appropriate conditions, the evolution of gas bubbles can be observed on the surfaces of both electrodes. In acidic electrolyte, the following two so-called half reactions occur:



with the hydrogen evolution reaction (HER, Eq. 1.1)—the reaction of interest—occurring at the cathode and the oxygen evolution reaction (OER, Eq. 1.2)—completing the circuit—at the anode. Combining the two reactions gives the overall water splitting reaction (Eq. 1.3):



Based on the stoichiometry of the overall reaction, the rate of evolution of the gases H₂ and O₂ is 2:1. And based on the half reactions, 4 moles of electrons must pass through the external circuit for every 2 moles of H₂ and 1 mole of O₂. This flow of electrons can be measured in the external circuitry as an electric current (I , Eq. 1.4), the magnitude of which is proportional to the stoichiometry of the electrons in the reaction (n), Faraday's constant (F) relating charge and moles of electrons, and the flux (J) of electroactive species to the electrode-electrolyte interface:

$$I = -nFJ \quad 1.4$$

Note that an equivalent current must also pass through the electrolyte in order to complete the electric circuit. This current carried by charged ionic species such as protons in the case of an acid electrolyte as opposed to electrons in the case of the external circuit.

It is also noted that the previous discussion assumed that all the electrons participated in the desired electrochemical reaction. As these are complex systems, it is possible that a fraction of the current went towards undesired processes such as electrode corrosion, passivation, fouling, and side reactions. With such phenomena, it is useful to describe the extent to which electrons are used for their desired purpose by the parameter current efficiency (ϕ , Eq. 1.5):

$$\phi := \frac{I_{\text{reaction}}}{I} \quad 1.5$$

where I_{reaction} is the current contributing towards the desired electrochemical process.

1.2.2 Electrochemical Thermodynamics

The central thermodynamic concept in electrochemical systems is that of electrode potential (E). This parameter, broadly speaking, is a measure of the energy of electrons at some thermodynamic, or equilibrium (subscript “eq”, Eq. 1.6) state:

$$\Delta_r G = -nFE_{eq} \quad 1.6$$

where $\Delta_r G$ is the change in Gibbs free energy for a given chemical equilibrium. There are two conventions to note:

1. Equilibria are generally written as reductions to be in accord with the sign convention used in the above equation. If an oxidation is written, the opposite sign (for the right-hand side) must therefore be used.
2. Electrode potentials are described with reference to some reference electrode potential. For practical purposes, this may be with reference to the equilibrium electrode potential present in the reference electrode employed in the cell. However, it is more common for electrode potentials to be described with reference to the standard hydrogen electrode (SHE), which is therefore 0.0000 V (vs. SHE) by definition. This is because all chemical species in equilibrium in the SHE are in their standard state, meaning that their Gibbs free energies of formation are also zero. The electrode potential of the SHE must therefore also be zero.

Electrode potentials determined for standard conditions such as the SHE are referred to as standard (superscript “0”) electrode potentials (E^0). Standard electrode potentials are determined easily consulting values for standard Gibbs free energies of formations ($\Delta_f G^0$), which can be found in thermodynamic tables, of the species involved in the chemical equilibrium of interest. For example, such an analysis would yield electrode potentials for the cathode (Eq. 1.1) and anode (Eq. 1.2) of a WE in standard acid electrolyte (pH 0) of 0.0000 and 1.229 V (vs. SHE), respectively.

For nonstandard conditions, equilibrium electrode potentials can be determined using the Nernst equation:

$$E_{eq} = E^0 - \frac{RT}{nF} \ln Q \quad 1.7$$

where R , T , and Q are the gas constant, temperature, and reaction quotient, respectively. For example, while the HER has a standard potential of 0.0000 V (vs. SHE), in basic electrolyte (pH 13–14) such as that found in alkaline water electrolysis, its equilibrium potential in an atmosphere of H_2 (1 atm) would range between $-(0.767-0.828)$ V (vs. SHE).

1.2.3 Losses in Electrochemical Systems

By definition, equilibrium potentials are only observed in open circuit, *i.e.*, no net current, conditions. In practice, however, electrode potentials stray from equilibrium potentials as a current begins to flow through the circuit. The magnitude by which the electrode potential exceeds the equilibrium potential is called the overpotential (η) or overvoltage:

$$\eta = E - E_{eq} \quad 1.8$$

This deviation from equilibrium, called polarization, is due to losses, or inefficiencies, at the electrode.

1.2.3.1 Electrode Kinetics

One inefficiency inherent in electrochemical systems is due to electrode kinetics and termed charge transfer or activation losses (subscript “ct”). An empirical relationship between this overpotential and the current was first described by Tafel over a century ago [17]:

$$|\eta_{ct}| = b \log_{10}|I| - a \quad 1.9$$

where a and b are the Tafel intercept and slope, respectively. A good electrocatalyst for some electrochemical reaction being described by these Tafel parameters would have values of the slope and intercept such that the overpotential remains as small as possible during polarization. Conversely, a poor electrocatalyst would have relatively large overpotentials, suggesting a considerable increase in an electrode potential for a marginal increment in electric current.

Electrode kinetic theory based on first principles was developed by Erdey-Grúz and Volmer [18], called Erdey-Grúz–Volmer kinetics (though sometimes attributed to Butler and referred to as Butler–Volmer kinetics):

$$I = I_0 \left\{ \exp \left[\frac{(1 - \alpha)nF}{RT} \eta_{ct} \right] - \exp \left(- \frac{\alpha nF}{RT} \eta_{ct} \right) \right\} \quad 1.10$$

where α is the charge transfer coefficient, which provides a measure of the relative energetic ease for the forward and reverse reactions involved in the electrochemical equilibrium, and I_0 is the exchange current density, which provides a measure of the rates of forward and reverse reactions at dynamic equilibrium. While the charge transfer coefficient remains inherent to the catalyst material, the exchange current density can vary considerably for given thermodynamic conditions such as activity and temperature. Exchange current density also depends on the geometry of the electrode, with increasing electrode area and roughness or catalyst loading improving this parameter. An Erdey-Grúz–Volmer analysis of electrocatalysts therefore depends on these two parameters, the charge transfer coefficient and exchange current density. Catalyst behaviour generally improves with increasing exchange current density whereas the charge transfer coefficient is mixed.

Applying their theory to Tafel's empiricism and assuming a symmetric system, i.e., $\alpha = 1 - \alpha = 0.5$, it can be seen that when the overpotential is sufficiently large, Tafel's parameters become:

$$b = \frac{\ln(10) RT}{\alpha nF} \quad 1.11$$

$$a = b \log_{10}(I_0) \quad 1.12$$

1.2.3.2 Transport Phenomena

Another inefficiency in electrochemical systems is losses due to transport phenomena termed mass transfer (or diffusion) losses (subscript “mt”). As a current is drawn in the vicinity of the electrode-electrolyte interface, electroactive species—those receiving or providing electrons—undergo chemical transformation. As a result, their local concentrations change and redistribute, influenced by dynamic processes collectively referred to as transport phenomena:

1. Diffusion: the motion of chemical species in response to the concentration gradient (dc/dx). This phenomenon is governed by Fick’s first law of diffusion:

$$J = -D \frac{dc}{dx} \quad 1.13$$

where J and D are the flux and diffusion coefficient (or diffusivity), respectively.

2. Convection: the motion of chemical species due to the motion of a fluid. The motion of a fluid is generally brought about by differences in pressure, with the fluid travelling from regions of high pressure to low. The difference in pressure can be caused by natural phenomena such as the heat transfer at a surface of a fluid, causing a change in density of the fluid near that surface. A difference in pressure can also be intentional such as by the use of pumps. Nevertheless, the convective flux due to motion of a fluid is described as follows:

$$J = uc \quad 1.14$$

where u is the velocity of the fluid in the x plane.

3. Migration: the motion of a charged chemical species in response to an electric field ($d\Phi/dx$).

$$J = -\frac{zF}{RT}Dc \frac{d\Phi}{dx} \quad 1.15$$

where z is the charge.

Combining these 3 phenomena yields the general flux equation:

$$J = -D \frac{dc}{dx} - \frac{zF}{RT}Dc \frac{d\Phi}{dx} + uc \quad 1.16$$

Generally, all three phenomena are present to varying extents at varying length scales in electrochemical systems. At a macroscopic level, the extent of one mode of mass transport relative to the others can be made considerably more or less prominent by design or operation. For example, the extent of diffusive flux relative to convective is influenced by whether the electrolyte is quiescent or agitated such as by either stirring or imposed flow. Migration is typically rendered less important by the addition of supporting electrolyte: charged species such as salts that do not participate in the electrochemical process other than to carry the ionic current in the electrolyte, lessening the electric field.

At a systems level, the relative importance of these and other transport phenomena with reference one another is expressed by dimensionless numbers:

1. Reynolds (Re): the ratio of inertial and viscous forces:

$$\text{Re} = \frac{\ell u}{\nu} \quad 1.17$$

2. Schmidt (Sc): the ratio of momentum (kinematic viscosity) and mass diffusivity:

$$\text{Sc} = \frac{\nu}{D} \quad 1.18$$

3. Sherwood (Sh): ratio mass transfer by convection and diffusion

$$\text{Sh} = \frac{k_m \ell}{D} \quad 1.19$$

where ℓ , ν , u , D , and k_m are the characteristic length, the kinematic viscosity, velocity, diffusion coefficient, and mass transfer (by convection) coefficient, respectively.

In electrochemical devices, there is often observed an empirical relationship between these 3 dimensionless numbers [19]:

$$\text{Sh} = a\text{Re}^b\text{Sc}^c \quad 1.20$$

where a , b , and c are coefficients determined by experimentation and usually defined by the geometry of the electrochemical cell.

Regardless of dominant mode of mass transport at a macroscopic level, it is recognized that diffusion plays an important role at the microscopic level. For example, while the bulk of the electrolyte may be agitated by stirring or flow, there is a finite yet minute layer of fluid near the electrode-electrolyte interface that is relatively calm and referred to as the stagnant layer. As transport by migration is minimized by the presence of supporting electrolyte, diffusion is the dominant mode of mass transport in this domain up until its boundary, the distance from the electrode-electrolyte interface being the boundary layer thickness (δ). Assuming a linear concentration profile over this domain, it can be determined that the flux of electroactive species at the surface of the electrode ($x = 0$) is:

$$J|_{x=0} = -\mathcal{D} \frac{(c^* - c|_{x=0})}{\delta} \quad 1.21$$

where c^* is the bulk concentration (superscript “**”) of electroactive species, noting that x is a vector normal to the surface of the electrode. For systems under mass transfer control, the concentration at the surface is miniscule relative to the bulk concentration and following approximation can be made:

$$J|_{x=0} \approx -k_m c^* \quad 1.22$$

where the mass transfer coefficient (k_m) is defined as follows:

$$k_m = \frac{D}{\delta} \quad 1.23$$

This substitution is made for practical purposes as the diffusion coefficient and diffusion layer thickness can be more challenging to determine relative to the composite parameter.

With relationship in hand, it is relatively straight-forward to derive an expression for the limiting current (subscript “L”), the current attributed to an electroactive species under mass transfer control:

$$I_L = nFAk_m c^* \quad 1.24$$

Accordingly, an expression can be derived for determining the loss or overpotential due to diffusion (η_{mt}) by invoking Erdey-Grúz–Volmer kinetics:

$$|\eta_{mt}| \propto -\frac{RT}{nF} \ln \left(1 - \frac{\phi I}{I_L} \right) \quad 1.25$$

1.2.3.3 Ohmic Drop

Excluding the circuit resistances, the ohmic drop (subscript “ Ω ”) is the drop in an electrochemical cell arises from the difficulty for charge to travel via ions in the electrolyte. The resistance to this ionic current is attributed to a variety of factors such as the concentration of charged species and their diffusivity in the electrolyte solvent. The ease by which charge can travel in a solvent is represented by its conductivity (κ). This parameter is improved by increasing the electrolyte, *i.e.*, salt, concentration, choosing salts with greater diffusivity, as well as reducing solution viscosity as predicted by models such as Debye–Hückle–Onsager theory [20, 21, 22].

In addition to conductivity, the ohmic drop also depends on the operation and geometry of the electrochemical cell:

$$\eta_{\Omega} = I \frac{\ell}{\kappa A} \quad 1.26$$

where ℓ is the inter-electrode distance and A is the cross-sectional area. Operationally, the greater the current, the greater the ohmic drop analogous to Ohm’s law. From a design perspective, inter-electrode distance should be kept to a minimum and areas should be as large as possible in electrolyte systems with low conductivity.

1.2.4 Overall Cell Potential

The potential of an electrochemical cell (U_{cell}) is simply the difference of the electrode potentials, which at best can be the equilibrium potential ($U_{cell,eq}$), but in drawing a current incurs losses due to the different overpotentials:

$$U_{cell} = U_{cell,eq} - \sum |\eta_i| \quad 1.27$$

where, by convention, the equilibrium cell potential is the difference between the cathode and anode equilibrium cell potentials ($E_{c,eq}$ and $E_{a,eq}$, respectively):

$$U_{cell,eq} := E_{c,eq} - E_{a,eq} \quad 1.28$$

By this convention, an electrolytic cell such as a WE will have a negative cell potential. Losses to such electrochemical systems make the cell potential more negative, meaning that more power (P) is needed to obtain a desired current:

$$P = U_{cell}I \quad 1.29$$

A galvanic or voltaic cell such as a fuel cell (FC) will have a positive cell potential. Losses to such systems make the cell potential less positive, meaning that less power is obtained from such systems. Electrical work ($W_{electrical}$), which is the integral of power with time, either supplied or obtained, are affected accordingly:

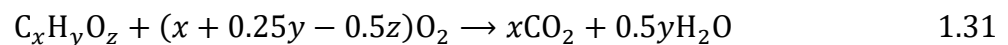
$$W_{\text{electrical}} = \int_0^t P d\tau \quad 1.30$$

It is therefore imperative to minimize these losses through selecting suitable electrode materials, improving mass transport, and reducing ohmic losses.

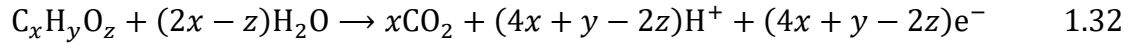
1.2.5 Electrochemical Treatment of Wastewater

Broadly speaking, there are many modes by which an electrochemical cell can treat wastewater [6]. These can be direct or indirect methods, depending on whether the wastewater pollutant is the electroactive species. They include anodic, cathodic, and coupled methods meaning that the current at only one or both electrodes contribute to the transformation of wastewater contaminants. They can also be faradaic and non-faradaic processes, meaning that electrons may or may not, respectively, transfer across the electrode–electrolyte interface.

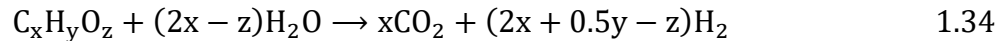
Concerning organic wastewater contaminants, in parallel to conventional secondary or biological treatment, the goal of electrochemical wastewater treatment is to reduce the oxygen demand in the water. Oxygen demand refers to the amount of oxygen an ecosystem would require metabolizing the organic material in the wastewater. At a macroscopic level, metabolism is analogous to combustion (Eq. 1.31):



where $C_xH_yO_z$ is the generic formula for an organic substance. An electrochemical cell mimicking a biological metabolic process in acid electrolyte would have the following half-reactions (Eqs. 1.32 & 1.33):



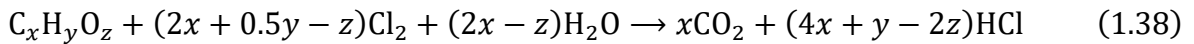
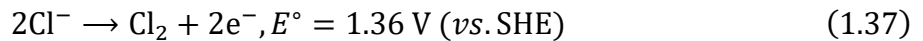
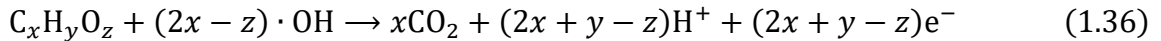
the latter referred to as the oxygen reduction reaction (ORR, Eq. 1.33) and whose net reaction would be combustion (Eq. 1.31). This process is thermodynamically spontaneous under appropriate conditions, which is exploited to provide electrical work such as with direct methanol (CH_3OH) and direct formic acid ($HCOOH$) FCs [23, 24]. However, in contrast to these FCs wherein the organic content is high, wastewater systems are relatively dilute. As a result, mass transfer limitations are considerable enough making FC operation impractical. It is therefore more practical to operate electrochemical cells treating wastewater as electrolyzers with the cathode reaction typically being the HER (Eq. 1.1) giving the following overall reaction:



Electrochemical reactions in wastewater electrolyzers (WWEs) are generally non-spontaneous, requiring an external power supply to oxidize organics as well as to produce H_2 . Their cell potentials are usually well in excess of what is observed for WEs for H_2 production due to the aforementioned mass transport limitations as well as electrode materials whose catalytic behaviour

for oxidation of organics is generally poor. This latter consideration is due in part to an effort towards reducing parasitic currents due to the OER, whose greater prevalence reduces the current and therefore energy efficiency of WWEs.

The complete oxidation of an organic species into inorganic carbon dioxide (CO₂) can be accomplished by direct electron transfer between the organic species and the electrode at the electrode surface or mediated by an electrochemically-generated intermediate species [4]. Examples of electrochemically-generated chemical intermediate species are hydroxyl radicals ($\cdot\text{OH}$, Eqs. 1.35 & 1.36) and active chlorine species (ACS) such as molecular chlorine (Cl₂, Eqs. 1.37 & 1.38), the latter forming when appropriate precursors such as chloride (Cl⁻) are present in the wastewater matrix.



1.3 Literature Review

Given their ability to access strongly oxidizing electrode potentials in aqueous media [7], HOP materials are important for the development of effective electrochemical technologies for clean water and energy. Prominent HOP materials include lead(IV) oxide (PbO₂), antimony-doped

tin(IV) oxide (ATO), boron-doped diamond (BDD), and MPTOs. These materials share poor electrocatalytic behaviour for the electrochemical oxidation of water forming oxygen, referred to as the oxygen evolution reaction (OER, Eq. 1.39).



This behaviour measured by their overpotential (η) for the OER is typically greater than 0.5 V (Table 1.1) [7, 11]. Comparatively, electrocatalysts exhibiting “good” electrocatalytic behaviour for the OER such as ruthenium(IV) oxide, iridium(IV) oxide, and platinum(IV) oxide are 0.16, 0.23, and 0.25 V, respectively [25, 26]. Poor electrocatalytic behaviour for the OER and serviceable electrical conductivity (σ , Table 1.1) [27, 28, 29, 30] have led to the growing interest in the use of HOP materials in fuel cells (FCs) and electrolyzers as dimensionally-stable supports for electrocatalysts; aqueous secondary batteries as electrically-conductive additives in positive plates; and electrochemical sensors, electrolytic double-layer capacitors (EDLCs), and electrochemical devices for electrochemical water purification and wastewater treatment as efficient and selective electrodes [4, 5, 13, 14, 15, 31, 32, 33].

HOP	η_{OER} (V)	$\log_{10}(\sigma/(\text{S cm}^{-1}))$	Relative cost
PbO ₂	0.5	3–4	Low
ATO	0.7	2–3	Medium
BDD	1.0	1–2	High
MPTOs (<i>e.g.</i> , Ti ₄ O ₇)	1.0	2–3	Medium

Table 1.1 Overpotential for the oxygen evolution reaction (η_{OER}), logarithm base 10 of the electrical conductivity (σ) and the relative cost of high oxidation power (HOP) materials lead(IV) oxide (PbO₂), antimony-doped tin(IV) oxide (ATO), boron-doped diamond (BDD) and Magnéli phase titanium oxides (MPTOs).

MPTOs are promising HOP materials available at relatively modest cost and exhibiting characteristics superior to other materials in their class (Table 1.1). The best-in-class material is BDD is used for the treatment of water and wastewater [33, 34, 35, 36]. BDD exhibits poor electrocatalytic behavior for the electrochemical water splitting reactions, permitting the production of hydroxyl radicals [37], which promote the selective and complete mineralization of organic pollutants [38, 39]. However, BDD can be cost prohibitive due to planar electrode geometries, exceeding 5,000 USD m⁻² [6] and motivating the development of inexpensive alternatives. While issues of lead and antimony toxicity have limited the use of PbO₂ and ATO, the latter also exhibiting poor stability [40], MPTOs are emerging as a viable alternative to BDD. MPTOs are nontoxic [41], excellent electrical conductors whose single-crystal conductivity approaching 2,000 S cm⁻¹ [30], dimensionally stable in aggressive media such as nitric and hydrofluoric acid [42], and orders-of-magnitude less expensive at <0.5 USD m⁻² [6].

1.3.1 Preparation of MPTOs

Methods for obtaining MPTOs vary considerably in both the starting materials and the conditions of their preparation (Figure 1.3) [15, 43]. Magnéli and co-workers first used metallothermic reduction [44], so called for the reduction of TiO_2 with titanium metal. Pathways to MPTO electrodes by reduction of TiO_2 are commonly encountered in the literature, especially with hydrogen—though carbon and ammonia are also used—requiring relatively mild temperatures of 600–1,000 °C. Such methods are routinely used to prepare condensed and porous monophasic monoliths as well as high surface area powders. Other less frequently encountered methods such as solvothermal and sol-gel methods are promising given their reported ability to produce nano-materials [45, 46, 47, 48] though they often contain mixed phases.

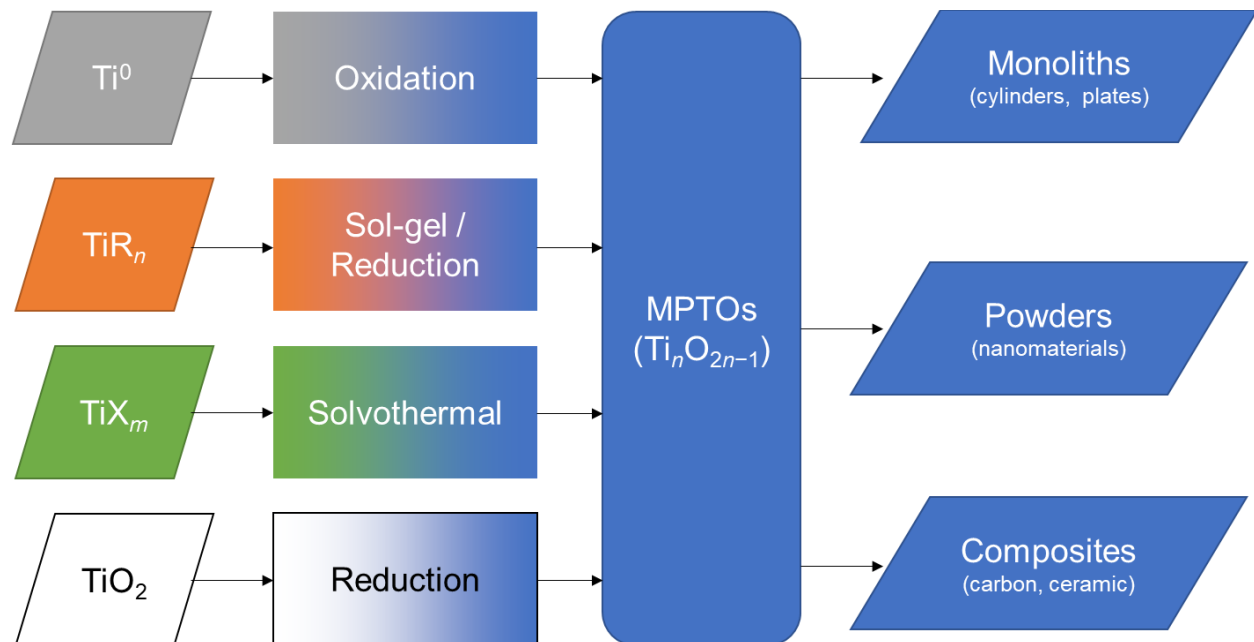


Figure 1.3 Methods of preparing Magnéli phase titanium oxide (MPTO) materials from various precursors such as titanium metal (Ti^0), organotitanium (TiR_n), titanium halides (TiX_m), and titanium(IV) oxide (TiO_2). Adapted and modified from [43].

The addition of dopants into otherwise pristine MPTOs is a method of growing activity, demonstrating influence over its tribological [49, 50], electrical [51, 52, 53], photocatalytic [54, 55], thermoelectric [56, 57, 58], electrocatalytic [52, 53, 59], and thermal-oxidation [60] behavior. Period 2 reactive non-metals and Period 4 and 5 transition metals are claimed to dope MPTOs by various methods (Table 1.2). However, doped MPTOs are poorly understood: evidence for their formation can be weak [54, 55], and suggests mixed phases [51], or is unclear in the absence of characterizing data, and their behavior compared to the pristine material are often not evaluated [52]. For example, samples described as doped MPTOs could alternatively be catalyst-decorated MPTOs or MPTO-supported catalyst materials. Lastly, materials claiming moderate-to-low doping could alternatively be causal or bulk mixtures particularly with preparations involving conventional methods.

Type	Dopant	Method	Reference
Non-metal	Carbon	Solvothermal	[54]
	Nitrogen	Solvothermal	[55]
	Nitrogen	Sol-gel	[52]
Transition metal	Vanadium	Metallothermic reduction	[49, 51]
	Iron	Metallothermic reduction	[51]
	Copper	Metallothermic reduction	[50]
	Gallium	Solid-state diffusion	[59]
	Yttrium	Solid-state diffusion	[59]
	Zirconium	Metallothermic reduction	[56]

	Niobium	Metallothermic reduction	[51]
	Niobium	Solid-state diffusion	[57, 58]
	Molybdenum	Not reported	[60]
	Cerium	Not reported	[61]
	Tantalum	Not reported	[60]

Table 1.2 Methods of preparing doped Magnéli phase titanium oxides.

1.3.2 MTPOs as Electrodes

The viability of the most electrically-conductive members of the MPTOs, Ti_4O_7 and Ti_5O_9 , has been investigated since the 1980s [11], being commercially traded for a period of time as Ebonex® [62]. MPTOs exhibit many desirable properties for electrodes [63] (Table 1.3). Specifically, they have high electrical conductivity [30], suitable electrocatalytic characteristics [11] (Figure 1.4), good chemical and physical stability [42], easily fabricated [15, 43], easily repaired [64], long-lasting [61, 65, 66], low cost [6], non-polluting [41] and non-contaminating, and safe.

HOP	Density (g cm ⁻³)	Linear expansion (10 ⁻⁶ K ⁻¹)	Melting point (°C)	Thermal conductivity (W cm ⁻¹ K ⁻¹)	Electrical resistivity (×10 ⁻⁶ Ω cm)
PbO ₂	9.4	7.0	290	2.8	100
ATO	6.8	5.8	1,630	0.8	4,500
BDD	3.5	0.8	4,000	10	50,000
MPTO	4.3	8.4	1,670	0.03	500

Table 1.3 Selected physical properties of high oxidation power (HOP) materials. Data for Magnéli phase titanium oxides (MPTOs, *i.e.*, Ti₄O₇) obtained from [30, 67, 68, 69].

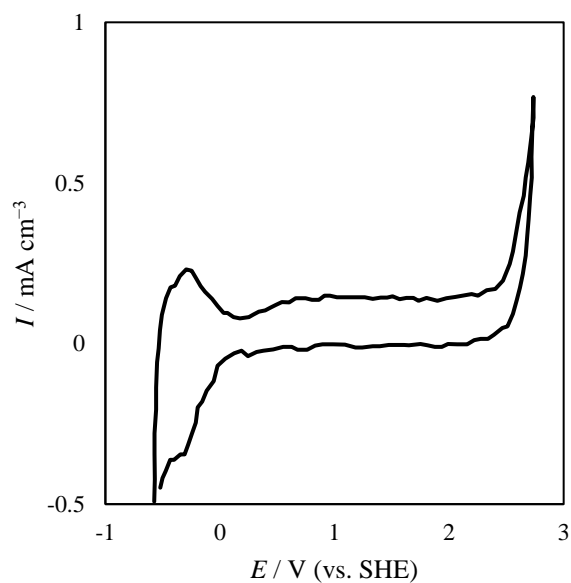


Figure 1.4 Electrochemical behaviour of an Ebonex® electrode in 1 M H₂SO₄ (50 mV s⁻¹, 298 K). Data obtained from [70].

While many aqueous electrochemical applications requiring access to strongly oxidizing potentials are enabled by the characteristics of MPTOs, improving its anodic stability remains an important challenge to be addressed. Passivation is observed in several applications including during the heavy overcharge or reversal of positive plates containing MPTOs as an electrically-conductive filler in lead acid batteries [71], in the electrolysis mode in regenerative fuel cells using MPTO-supported electrocatalysts [16], and in the electrochemical oxidation of organic industrial wastewater pollutants with MPTO anodes [72]. Passivation of MPTOs such as Ti_4O_7 forms the thermodynamically-favored titanium(IV) oxide (TiO_2 , Figure 1.5, A.1 Supplementary Data for Chapter 1: Introduction) (Eq. 1.40, $E^0 = -0.54 \text{ V vs. SHE}$). Cathodic reactivation partially restores its properties [64], but this regeneration process would increase the cost of use.

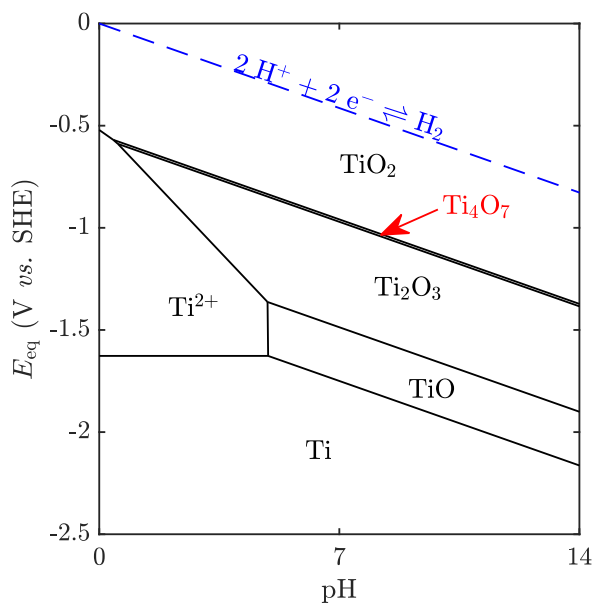
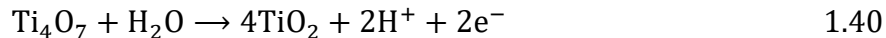


Figure 1.5 Potential (E_{eq})-pH equilibrium or Pourbaix diagram for titanium in aqueous solutions (see Appendix A.1 for equilibria)



1.3.3 Electrochemical Wastewater Treatment with MPTO-Based Electrodes

Perhaps the earliest reported use of MPTOs for water treatment applications is that of Chen, Berterton, & Arnold [16]. The researchers used sheets of Ebonex®, a tradename under which Ti_4O_7 – Ti_5O_9 materials were sold, electrolyzing synthetic wastewater containing trichloroethylene in a 2-chamber and a 3-electrode glass reactor. They observed rapid and nearly complete oxidation of the organic to CO and CO_2 with first-order degradation kinetics at higher anode polarization that was independent of concentration. Hydroxy radicals ($\cdot\text{OH}$), strong and indiscriminate chemical oxidants capable of oxidizing chemical species at appreciable rates, were detected using electron spin resonance with the spin trap α -(4-pyridyl *N*-oxide)-*N*-*tert*-butylnitron (4-POBN). Degradation kinetics are pH-independent, however, suggesting that mass transport of the model pollutant to the anode may be rate-determining and not the formation of hydroxyl radicals. Furthermore, mass transport is inefficient with a maximum mass transfer coefficient of $24.3 \mu\text{m s}^{-1}$ and resulting in poor current efficiencies of <33%.

This early example of MPTO use for water treatment used a batch reactor setup. In an effort to improve mass transport as well as achieve continuous operation, practical designs that rely on flow-by and flow-through configurations can be used (Figure 1.6) [43]. In a flow-by setup, wastewater flows through the reactor whose reactive compartments are lined at least on one side with a monolithic MPTO electrode, parallel to the flow. As the wastewater flows through the reactor, organic matter encounters oxidizing species at the surface of the electrode where they are

transformed. As the electrodes form the boundary of the reactive compartment, they are impermeable to electrolyte flow and thus their interiors do not participate in treating the wastewater.

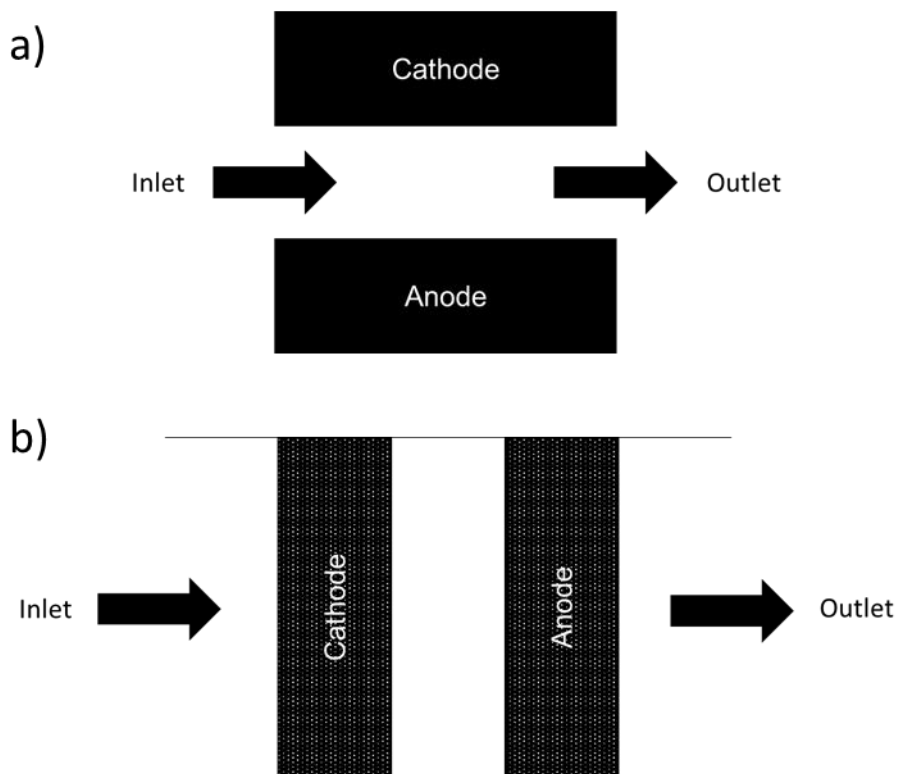


Figure 1.6 a) Flow-by and b) flow-through reactor configurations

To improve utilization of electrode materials as well as improve mass transport, a flow-through setup can be used. In such a configuration, the electrodes are oriented perpendicular to flow. The electrodes are now porous, permitting the flow of electrolyte through them, increasing the surface area over which oxidation of organics or chemical oxidant precursors can occur. The downside of this approach relative to flow-by operation is the increased costs for pumping due to greater pumping head required to pass wastewater through the reactor.

Regardless of the reactor orientation, whether batch or continuous, flow-by or flow-through, MPTOs are shown to effectively treat a wide range of organic industrial wastewater pollutants (Table 1.4 and Table 1.5). Early work demonstrated modest performance as measured by removal efficiency (or conversion, X) and current efficiency (ϕ) [16, 72, 73]. Recently, however, the advent of high-surface area electrodes such as nanotube arrays (NTAs) [74] and reactive electrochemical membranes (REMs) [75, 76, 77, 78, 79, 80] may be considered to be the current state of the art, the latter achieving 5 log removal of recalcitrant perfluoroalkyl substances at a low energetic expenditure of 5.1–6.7 kWh m⁻³ [81]. Still, these technologies must operate at relatively low current densities as a strategy to minimize parasitic reactions and electrode passivation.

Pollutant	Electrolyte	Time (min.)	j (mA cm ⁻²)	ϕ (%)	X (%)	E_{EO} (kWh m ⁻³ order ⁻¹)	Reference
COD (183 ppm)	Real WW	180	20	5	66.5	67	[82]
PFOA ^a (0.1 mM)	Na ₂ SO ₄ (40 mM)	90	10		97.1		[83]
L-PFOS ^b (10 μ M)	Na ₂ SO ₄ (0.1 M)	20	15	10 ^c	75 ^d	3.6	[84]
Methyl orange (150 ppm)	NaCl (10 mM)	300	10	10	91.7 ^d		[85]
Tetracycline (10–50 ppm)	Na ₂ SO ₄ (30 mM)	40	15		95.8		[86]
Phenol (100 ppm)	Na ₂ SO ₄ (0.1 M)	180	2.5		95.3 ^d		[74]

^a PFOA: Perfluorooctanoic acid, ^b PFOS: Perfluorooctanesulfonic acid; ^c TOC basis; ^d COD basis.

Table 1.4 Selected examples of flow-by reactors with Magnéli phase titanium oxides treating wastewater and their removal efficiency (or conversion, X), current efficiency (ϕ), and electrical energy per order (90%) removal (E_{EO})

Pollutant	Electrolyte	Time (min.)	Flux (LMH)	j (mA cm ⁻²)	ϕ (%)	X (%)	E_{EO} (kWh m ⁻³ order ⁻¹)	Reference
TOC (7 ppm)	Real WW		1,340	7.4		>70	0.74	[87]
PFOA ^a (0.5 mM)	Na ₂ SO ₄ (0.25 M)	150		5		>99.9	14.2	[79]
PFOS ^b (0.1 mM)	Na ₂ SO ₄ (0.25 M)	180		5		93.1	36.9	[79]
SMX ^c (0.1 nM)	K ₂ HPO ₄ (0.1 M)		300	2.54		95.7	0.27	[88]
PFOS ^b (2 μM)	Na ₂ SO ₄ (0.1 M)	120		4		98.3		[89]
Benzotriazole (10 ppm)	Na ₂ SO ₄ (0.1 M)		462	20	30	98.1	22	[90]

^a PFOA: Perfluorooctanoic acid, ^b PFOS: Perfluorooctanesulfonic acid; ^c SMX: sulfamethoxazole

Table 1.5 Selected examples of flow-through continuous reactors with Magnéli phase titanium oxides treating wastewater and their removal efficiency (or conversion, X), current efficiency (ϕ), and electrical energy per order (90%) removal (E_{EO})

1.4 Research Questions and Objectives

The aim of this study is to improve the performance of MPTO-based electrodes for the electrochemical treatment of industrial wastewater. The effectiveness of MPTO-based electrodes is based, in part, on their stability as the passivation of MPTOs in conditions relevant to electrochemical applications [71, 91, 72] is an important issue. The efficiency of WWEs is derived, in part, from the design of electrodes. As wastewater pollutants are dilute, enhancing mass transport phenomena is vital to improving the performance of such electrochemical wastewater treatment technologies. In support of this aim, the following research questions have been developed:

1. What dopants can MPTOs accommodate up to a high doping level?
2. How does doping influence the stability of MPTOs in oxidizing environments?
3. How does doping influence the other properties relevant to the use of MPTOs in electrodes? Specifically, their:
 - a. Electrical conductivity and
 - b. Electrochemical behaviour including electrocatalytic properties with respect to parasitic reactions such as the OER
4. How does the performance for the electrochemical treatment of organic industrial wastewater pollutants of doped MPTO electrodes compare with pristine MPTO electrodes in a specified electrochemical device?

The first part of this research was to explore the rational selection of dopants and investigate their influence on the stability of MPTOs. In support of this aim, methods for preparing doped MPTOs were developed as such materials are not commercially available. The quality of materials prepared in-house were characterized by methods encountered in the literature with comparison to

data libraries of previously described materials. With materials of assured composition and quality in hand, the thermal and electrochemical oxidation of said materials were investigated by use of thermogravimetric analysis (TGA) and electrochemical accelerated life testing (ALT), respectively. Not only is a measure of the stability of these materials obtained using these methods, but some insight into why some materials may be more stable than others.

Once suitable dopants were identified, the effectiveness of doped MPTOs for the treatment of industrial wastewater were investigated. High-surface area electrodes called porous transport layers (PTLs) and appropriate for use in a compact electrolyzer were prepared. A PTL, like a REM, is porous, permitting electrolyte to flow through it. However, these PTLs can be used in a zero-gap commercial electrolyzer cell similar in design to a WE for hydrogen production, improving mass transport as well as minimizing ohmic losses. Such cells with doped-MPTO PTLs were characterized and their performance for the treatment of industrial wastewater was investigated with reference to pristine MPTO. An analytical model was developed, predicting performance with respect to key operating parameters.

Chapter 2: Methodology

2.1 Material Preparation

2.1.1 Sol-gel Methods

In Chapter 3: The Thermal-Oxidation Behaviour of Pristine and Doped Magnéli Phase Titanium Oxides and Chapter 4: The Superior Electrical Conductivity and Anodic Stability of Vanadium-Doped Ti_4O_7 , the dopant-containing MPTOs used in hydrogen reduction of TiO_2 (*vide infra*) are prepared by sol-gel methods.

Sol-gel methods involve forming a *sol*, a solution of colloidal nanoparticles, followed by a *gel*, a condensed and interconnected polymer networks [92]. One such method of bringing a sol to a gel used for this study is the hydrolysis and polycondensation of alkoxide precursors followed by aging and drying under ambient conditions. The steps involved in this approach are:

1. Mixing: A sol is formed by the dissolution in an appropriate solvent of an alkoxide precursor (*e.g.*, titanium tetraisopropoxide, TTIP) followed by its hydrolysis (Figure 2.1) and condensation (Figure 2.2), forming a network by condensation (*e.g.*, Figure 2.3).

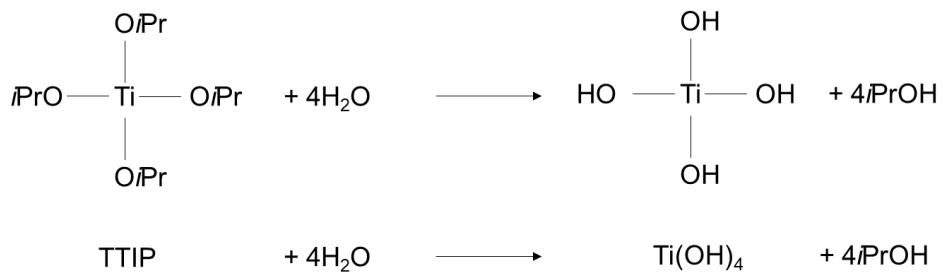


Figure 2.1 Hydration of tetratitanium isopropoxide (TTIP) forming titanium(IV) hydroxide (Ti(OH)₄) and isopropanol (iPrOH).

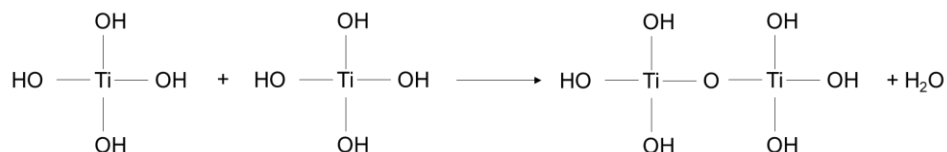


Figure 2.2 Condensation of titanium(IV) hydroxide (Ti(OH)₄) monomers forming a dimer.

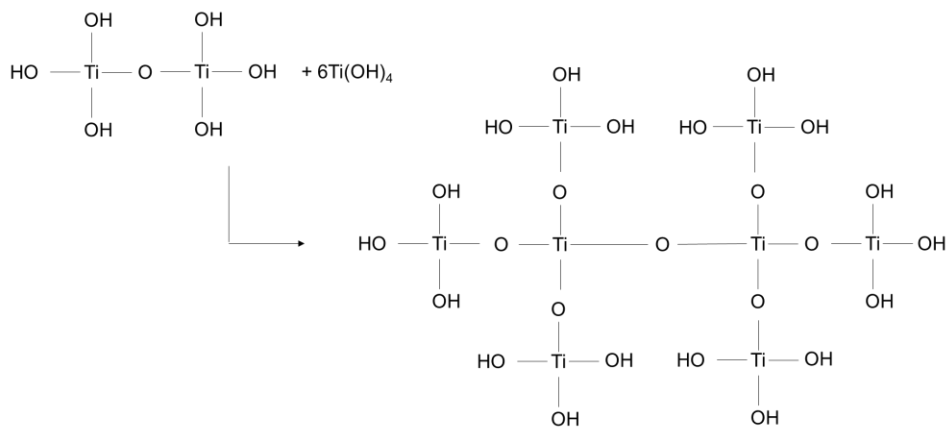


Figure 2.3 Polycondensation of dimer and titanium(IV) hydroxide (Ti(OH)₄) monomers forming eventual TiO₂ network

2. Gelation: After mixing, colloidal particles in the gel will encounter one another and cross-link, forming an extended network. This causes the viscosity of the sol to increase and solid material to precipitate from solution.
3. Drying: After gelation, solvent is removed by decanting and drying under vacuum or near the boiling point of the solvent to form a xerogel. At this point, the interconnected network of atoms is sufficiently irregular such that the material appears crystallographically amorphous.
4. Calcination: Once a xerogel is made, it is heated at temperatures below the melting point of the ceramic. This stabilizes the material by condensing hydroxyl groups ($-OH$), causing further interlinkages to form. The atoms arrange into more regular and repeating structures, increasing the crystallinity of the material.
5. Densification: After calcination, the material can be optionally heated to a temperature near the melting point of the ceramic. This causes particles to sinter and fuse together, causing the density to increase by reducing the overall porosity.

Sol-gel synthesis is a bottom-up method of preparation, permitting the incorporation of heterogeneous materials at the atomic level. For example, heteroatoms can be taken up by the sol-gel network during the mixing step by their incorporation into the network by condensation reactions (Figure 2.4). The incorporation of the heteroatom strains the crystal structure due to differences in atomic radii as well as introduces defects such as voids. This results in opto-electronic properties of the doped materials that are distinct from the pristine materials such as for band gap and electrical conductivity—the former sometimes yielding materials with striking colors.

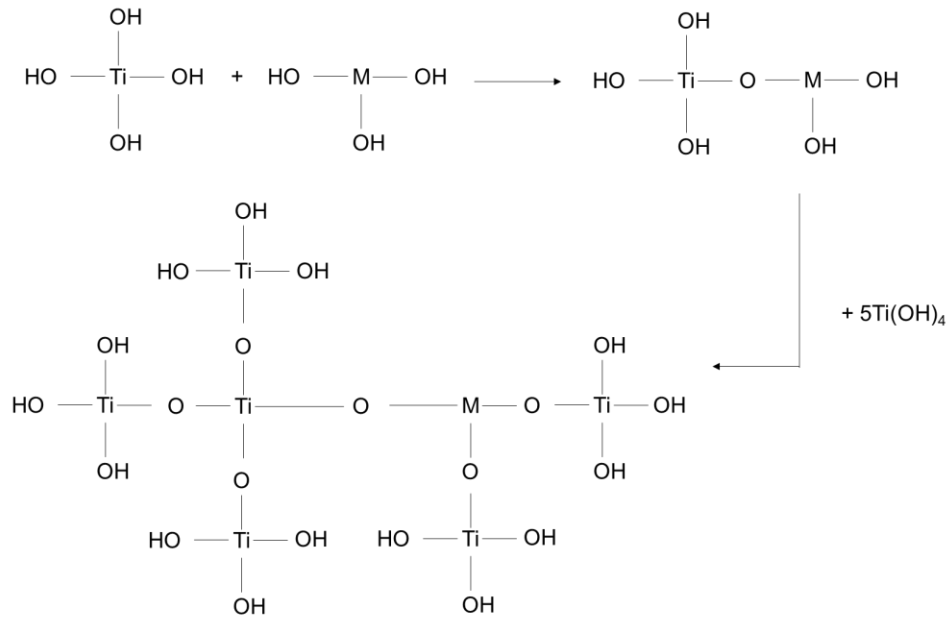


Figure 2.4 Condensation and polycondensation of titanium(IV) hydroxide (Ti(OH)₄) and metal(III) hydroxide (M(OH)₃) monomers eventually forming a M-doped TiO₂ network

2.1.2 Solid-State Diffusion Methods

In Chapter 5: Vanadium-Doped Ti₄O₇ Porous Transport Layers for Efficient Electrochemical Oxidation of Industrial Wastewater Contaminants, solid-state diffusion methods are used to prepare porous transport layers (PTLs) of vanadium-doped Ti₄O₇. A solid-state diffusion method is a process by which a heterogeneous mixture is made more homogeneous by the interdiffusion of the species.

As discussed in 1.2.3.2 Transport Phenomena, species will diffuse against some concentration gradient (Figure 2.5). Per Eq. 1.13, the rate by which this process occurs is not only dependent on the magnitude of the concentration gradient, but also on the diffusion coefficient. In

solid state materials, this process is slow relative to liquid media due to small diffusion coefficients. The diffusion coefficient has an Arrhenius-type relationship (Eq. 2.1):

$$D = D_0 \exp(-E_a/RT) \quad 2.1$$

where D_0 and E_a are the maximum diffusion at infinite temperature and the activation energy for the diffusion process, respectively. Thus, the rate of the diffusion process in a solid-state material can be sped up by increasing the temperature of the solid.

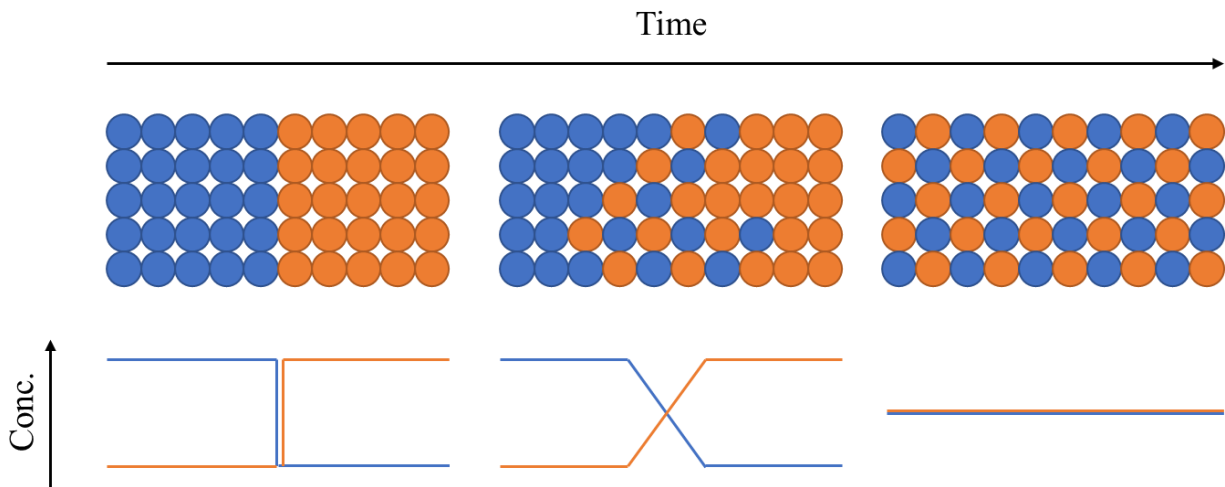


Figure 2.5 Solid-state diffusion process showing the distribution of atoms with time after two heterogeneous materials are put together at sufficiently elevated temperatures.

At elevated temperatures, heteroatoms diffuse into the pristine material, substituting positions with host atoms or occupying interstitial sites resulting in doped materials. However, unlike sol-gel methods whose bottom-up approach involves an atom-by-atom construction, solid-state diffusion methods start with considerably larger materials such as nano- and microscale powders.

Furthermore, the elevated temperatures required to accelerate diffusion also result in the growth of larger particles via sintering and Ostwald ripening processes. It is therefore not particularly well-suited for preparing doped nanomaterials.

2.1.3 Thermal Reduction

In Chapter 3: The Thermal-Oxidation Behaviour of Pristine and Doped Magnéli Phase Titanium Oxides, Chapter 4: The Superior Electrical Conductivity and Anodic Stability of Vanadium-Doped Ti_4O_7 , and Chapter 5: Vanadium-Doped Ti_4O_7 Porous Transport Layers for Efficient Electrochemical Oxidation of Industrial Wastewater Contaminants, thermal reduction in a hydrogen atmosphere is used to prepare all MPTOs.

In a reducing environment such as hydrogen, but also, for example, carbon monoxide or ammonia, an oxide such as TiO_2 can be reduced to form a lower oxide, so called for the metal now possessing a lower oxidation state. For example, TiO_2 (oxidation state +4) in H_2 at a sufficiently high temperature will spontaneously reduce to form an MPTO such as Ti_4O_7 (oxidation state +3.5).



In the process, H_2O is produced as oxygen from the reducing oxide is “captured” by the H_2 in the surrounding environment.

Thermal reduction in a controlled atmosphere is typically conducted in a tube furnace (Figure 2.6). Such an apparatus is typically made of an inert tube such as quartz or alumina. At each

end of the tube are vestibules, which connect the tube to appropriate plumbing shuttling reactant gases from their sources through the tube and to exhaust. Surrounding the tube is a heating element, typically a resistive heating element, which heats up when an electric current passes through it. The temperature of the heating element is controlled by a thermocouple. While manual control is possible, elaborate temperature programs can be developed using a temperature control unit.

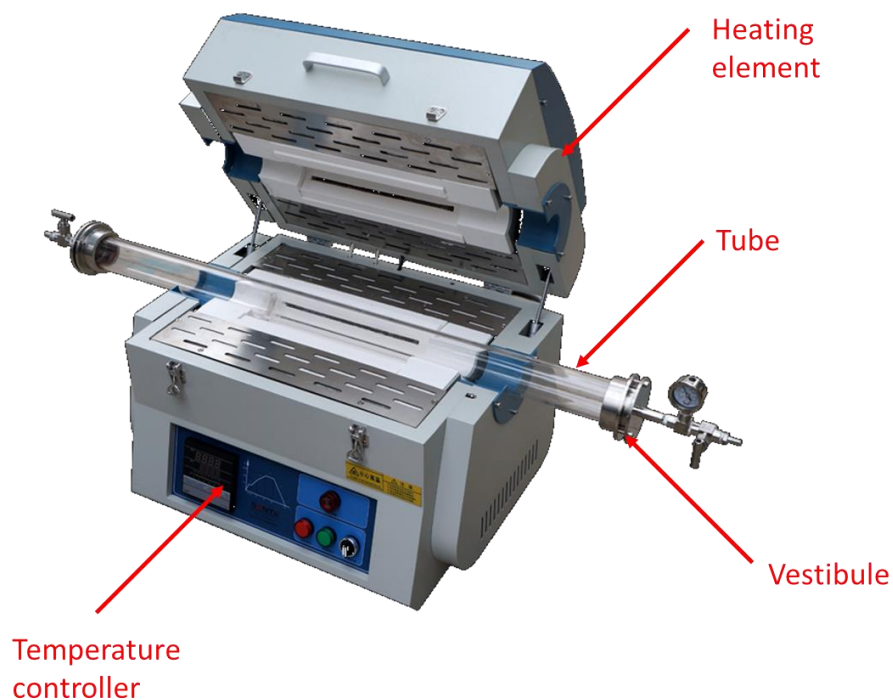


Figure 2.6 Components of a tube furnace

The sample to be reduced is conveyed into the tube furnace by a crucible, usually made of the same material as the tube, and placed in the middle of the tube furnace. This is to ensure that the temperature experienced by the sample is approximately the same as that measured by the thermocouple, which is also usually located near the middle. The region in the middle of the tube

furnace is called the heating zone. As locations in the furnace approach the vestibules, the temperature can drop considerably relative to the heating zone due to cooling from the environment.

It is noted, however, that TiO_2 , MPTOs, and other oxides in a sufficiently reducing environment will continue to reduce to lower and lower oxides, eventually forming the metal and possibly its hydrides. It is therefore imperative to interrupt the reduction so that the sample is not over-reduced. This is typically done by timing the temperature program such that heating stops at a time when a sufficient level of reduction is achieved.

2.2 Material Characterization

2.2.1 Structure

2.2.1.1 X-ray Diffraction

In Chapter 3: The Thermal-Oxidation Behaviour of Pristine and Doped Magnéli Phase Titanium Oxides, Chapter 4: The Superior Electrical Conductivity and Anodic Stability of Vanadium-Doped Ti_4O_7 , and Chapter 5: Vanadium-Doped Ti_4O_7 Porous Transport Layers for Efficient Electrochemical Oxidation of Industrial Wastewater Contaminants, X-ray diffraction (XRD) is used to investigate the crystalline structure of prepared materials.

XRD is an instrumental technique used to obtain information about the structure of crystalline material. This is accomplished by illuminating a crystalline sample with X-rays and ana-

lyzing the diffraction pattern, so called as X-rays diffract as they pass through the crystalline lattice. That is, X-rays from a coherent source interact with one another in either a constructive or destructive manner, generating a pattern of varying intensity as a function of the angle of incident light (θ). The premise of this diffraction pattern is based on Bragg's law (Eq. 2.3, Figure 2.7), which relates the wavelength of the incident light (λ) to the critical angle at which constructive interference occurs in an ordered material with regular spacing of thickness (d) and where n is the diffraction order, taking integral values [93]:

$$n\lambda = 2d \sin \theta \quad 2.3$$

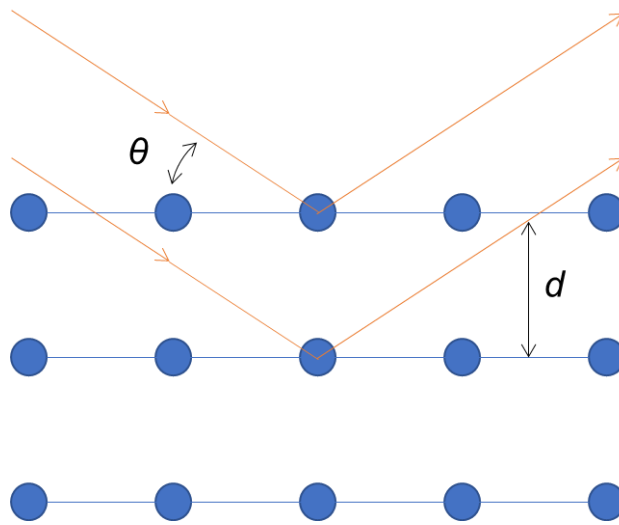


Figure 2.7 Visual description of Bragg's law and related diffraction phenomena

The diffraction pattern is therefore characteristic of the crystalline material, being used to identify crystalline phases present in a given material. Further information can be obtained about the position of atoms in a repeating unit of the lattice, called a unit cell, such as its size and shape

as well as the atoms within it. X-rays are used given the similarity in wavelength and the spacing of atoms in crystalline materials being on the order of angstroms. X-ray diffraction patterns can be 1- or 2-dimensional, 1D being favored for powder analysis and 2D being appropriate for small, single crystal samples. Rietveld refinement can be applied to powder X-ray diffraction patterns to obtain a multitude of information about the unit cell [94].

2.2.2 Composition

2.2.2.1 X-ray Fluorescence

In Chapter 3: The Thermal-Oxidation Behaviour of Pristine and Doped Magnéli Phase Titanium Oxides, Chapter 4: The Superior Electrical Conductivity and Anodic Stability of Vanadium-Doped Ti_4O_7 , and Chapter 5: Vanadium-Doped Ti_4O_7 Porous Transport Layers for Efficient Electrochemical Oxidation of Industrial Wastewater Contaminants, X-ray fluorescence (XRF) is used to investigate the composition of pristine and doped MPTOs.

XRF is an analytical technique to determine the elemental composition of a material. In a typical measurement, a sample is irradiated with X-rays, which cause core electrons of atoms to be ejected (Figure 2.8). This in turn allows electrons in higher energy levels to relax and occupy the vacant spot, releasing X-rays characteristic of the energy released (E) by the transition, the wavelength (λ) of this fluorescent radiation being related by Plank's law:

$$\lambda = hc/E \quad 2.4$$

where h is the Planck constant, c is the speed of light. The incident X-ray energy must be greater than that of the electron being ejected. The intensity of the fluorescent radiation is a function of both the concentration and the element itself, causing detection limits to vary among the elements. Fluorescent radiation can be collected either by energy-dispersive or wavelength-dispersive detectors. XRF may therefore not provide an ultimate analysis of a specimen as some lighter elements may have concentrations lower than the instrumental detection limit. Software packaged with most modern instrumentation will analyze X-ray fluorescence spectra, apply the appropriate factors, and report the relative composition of the elements.

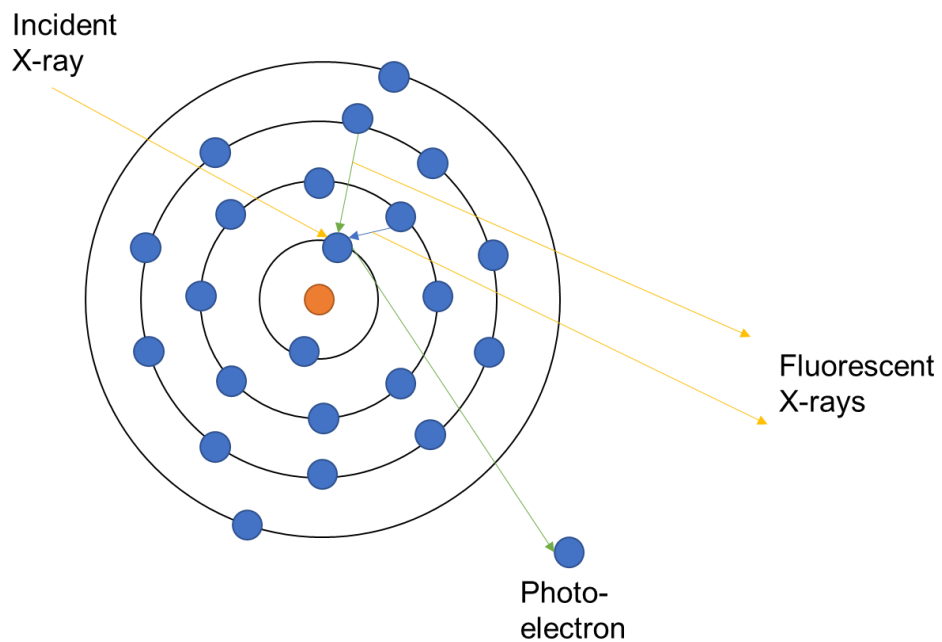


Figure 2.8 Bohr model of titanium atom undergoing X-ray fluorescence and related phenomena

2.2.2.2 Energy-Dispersive X-ray Spectroscopy

In Chapter 3: The Thermal-Oxidation Behaviour of Pristine and Doped Magnéli Phase Titanium Oxides, Chapter 4: The Superior Electrical Conductivity and Anodic Stability of Vanadium-Doped Ti_4O_7 , and Chapter 5: Vanadium-Doped Ti_4O_7 Porous Transport Layers for Efficient Electrochemical Oxidation of Industrial Wastewater Contaminants, energy-dispersive X-ray (EDX) spectroscopy, is used to determine the elemental composition and mapping of pristine and doped MPTOs.

EDX spectroscopy, like XRF, is another instrumental method for determining the elemental composition of a material. Like XRF, electrons from outer levels relax to fill vacancies in inner levels, releasing fluorescent radiation characteristic of the element via Planck's law (Eq. 2.4). Unlike XRF, however, electrons are ejected from core electron levels by collisions with other electrons, the source being an electron beam such as those used in scanning electron microscopy (SEM, *vide infra*). The fluorescent radiation is typically collected by an energy dispersive detector.

As this method is typically used in conjunction with SEM, an elemental map at the microscopic scale be developed using this method. In such an approach, a plot of the intensity of fluorescent radiation at some wavelength characteristic of an element of interest is superimposed onto and electron micrograph. This approach in concert with SEM can provide information about the distribution of elements at the microscopic level, giving insight into its relationship with any morphological features.

2.2.2.3 X-ray Photoelectron Spectroscopy

In Chapter 4: The Superior Electrical Conductivity and Anodic Stability of Vanadium-Doped Ti_4O_7 , X-ray photoelectron spectroscopy (XPS) is used to investigate the surface composition and oxidation state of pristine and doped MPTOs.

XPS is an analytical technique like XRF and EDX spectroscopy used to determine the elemental composition of a material. Like XRF, a sample is irradiated with X-rays, but unlike XRF, the ejected electrons are collected and not X-ray fluorescent radiation. This photoelectric effect first theorized by Einstein [95] and subsequently developed for the technique equates the kinetic energy of the photoelectron (subscript “k”) to the wavelength of the incident X-ray radiation (λ) minus the work function of the surface (Φ) and the binding energy (subscript “B”), the minimum energy required to remove an electron from an atom (Eq. 2.5):

$$E_k = \frac{h\lambda}{c} - \Phi - E_B \quad 2.5$$

The work function is typically an instrumental parameter and is easily measured with reference to photoelectrons originating from a ubiquitous yet adventitious material such as carbon.

Unlike XRF and EDX spectroscopy, the resolution of determination of the binding energy is sufficient that photoelectrons originating from atoms of the same element, but different oxidation states can be observed. However, unlike XRF and EDX, the mean free path of an electron in

solids is considerably shorter limiting XPS analysis to the surfaces of samples. An additional consideration for XPS is that measurements are typically carried out in vacuum to facilitate the unobstructed travel of photoelectrons from the sample to the detector. Nevertheless, analysis of the interior of a sample can be done by etching with an ion beam such as argon.

2.2.3 Morphology

2.2.3.1 Scanning Electron Microscopy

In Chapter 3: The Thermal-Oxidation Behaviour of Pristine and Doped Magnéli Phase Titanium Oxides, Chapter 4: The Superior Electrical Conductivity and Anodic Stability of Vanadium-Doped Ti_4O_7 , and Chapter 5: Vanadium-Doped Ti_4O_7 Porous Transport Layers for Efficient Electrochemical Oxidation of Industrial Wastewater Contaminants, scanning electron microscopy (SEM) is used to investigate the morphology of pristine and doped MPTOs.

SEM is a type of microscopy using a beam of high energy electrons scanned across the surface of a sample. When electrons impact the surface, electrons and radiation is released from the sample (Figure 2.9) providing both topographic and compositional information. For example, backscattered electrons (BSEs) are electrons reflected from the surface due to elastic scattering. Secondary electrons (SEs) originate from atoms in the sample being released by inelastic scattering by incident electrons. X-rays can also be released in a fashion described by EDX spectroscopy (vide supra). These signals are collected by a variety of detectors, if present in the instrument, and

used to generate morphological and compositional data. Images obtained by SEM are of considerably greater resolution than conventional light microscopy, being able to display features in the micro- and nanometer scale.

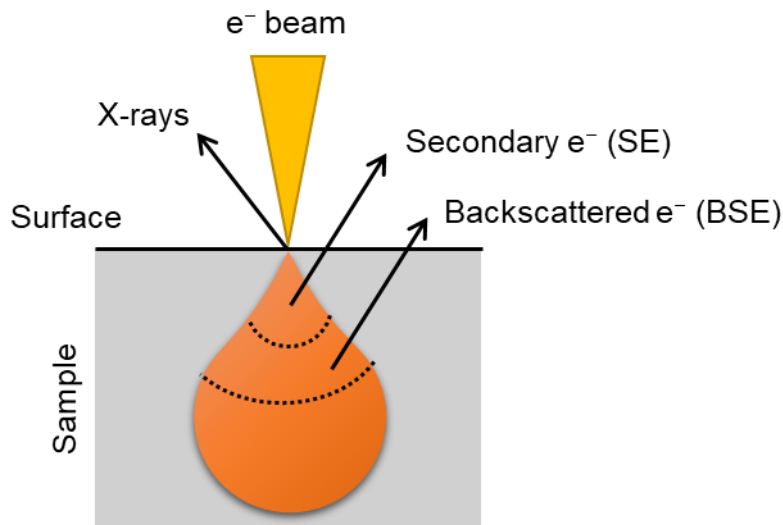


Figure 2.9 Types of signals generated by electron beam in a scanning electron microscope

2.2.4 Thermogravimetric Analysis

In Chapter 3: The Thermal-Oxidation Behaviour of Pristine and Doped Magnéli Phase Titanium Oxides, thermogravimetric analysis (TGA) is used to investigate the thermal oxidation behaviour of pristine and doped Ti_4O_7 .

TGA is an instrumental technique used to observe changes in mass due to decomposition or oxidation upon heating a sample in a prescribed environment. In a typical measurement, a small amount of sample is placed in an inert crucible such as alumina and placed upon a holder suspended in a furnace (Figure 2.10). Similar to the operation of a tube furnace as described in thermal

reduction (vide supra), the furnace of a TGA is purged with some gas of known composition. The temperature of the furnace is then raised per some temperature program using a thermocouple and temperature controller. The weight of the sample is continuously monitored as the temperature program is executed. The data is typically reported as a thermogram, *i.e.*, the mass of the sample as a function of temperature.

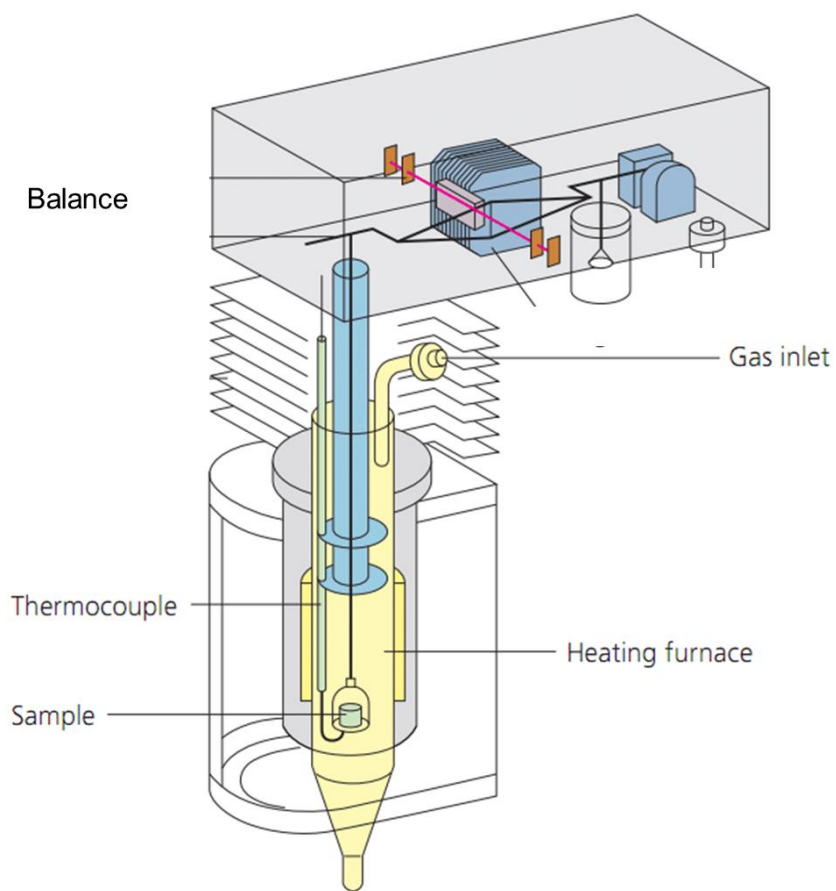


Figure 2.10 Components of a thermogravimetric analyzer. Adapted from [96]

TGA can provide a variety of information about the sample. For example, the extent to which the mass of a sample changes can provide information about its composition. The temperature at which its mass changes, called the onset temperature (T_o), provides information about its thermal stability with higher onset temperatures indicating greater thermal stability. The rate at which the mass changes can provide information about the mechanism by which the sample is undergoing some chemical change such as oxidation or decomposition.

2.3 Electrochemical Measurements

2.3.1 Cyclic Voltammetry

In Chapter 4: The Superior Electrical Conductivity and Anodic Stability of Vanadium-Doped Ti_4O_7 and Chapter 5: Vanadium-Doped Ti_4O_7 Porous Transport Layers for Efficient Electrochemical Oxidation of Industrial Wastewater Contaminants, cyclic voltammetry (CV) is used to investigate the electrochemical behaviour of pristine and doped MPTO electrodes.

CV is an electroanalytical method used to observe the electrochemical behaviour of electrode materials in some defined media [97]. As described in 1.2 Background, in a typical measurement, an electrode containing a material of interest is placed in a solution, typically containing supporting electrolyte to improve its ionic conductivity and aid measurement. Using an instrument called a potentiostat (PS), the potential is swept at some constant rate from a starting potential to some peak or limiting potential and back to the starting potential (Figure 2.11). As the potential is swept, the current passing to or from the electrode of interest is measured. The measurement then

continues between these two peak potentials (or limiting potentials) for a number of cycles. The current-potential data referred to as a cyclic voltammogram is typically reported.

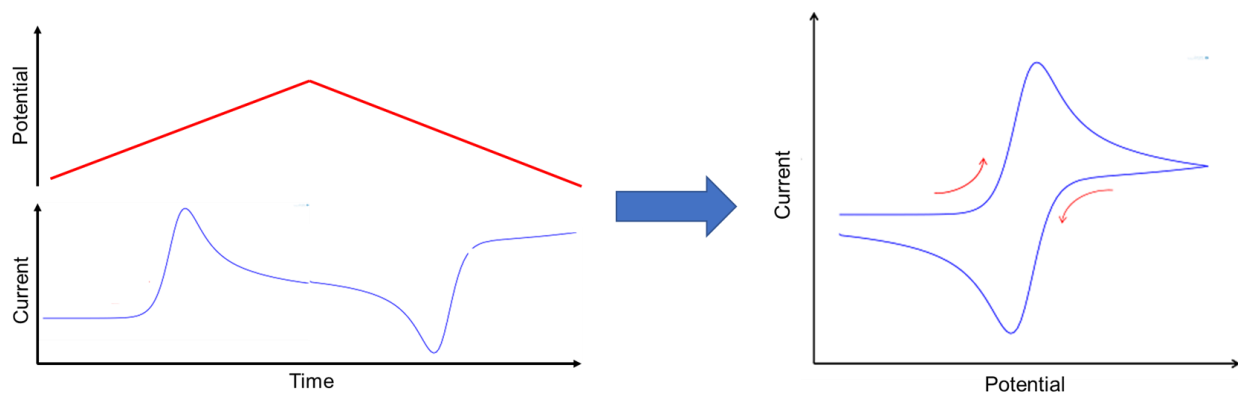


Figure 2.11 A cyclic voltammetry experiment (left) and the construction of a cyclic voltammogram (right).

CV data can provide a variety of information about the material of interest. A cyclic voltammogram plots the electrochemical behavior of a material as measured by current as a function of the electrode potential. This data can be used to determine the stoichiometry of the electrons involved in a redox process, the standard potential of said process, as well as the rate of the reaction.

2.3.2 Galvanostatic Methods

In Chapter 4: The Superior Electrical Conductivity and Anodic Stability of Vanadium-Doped Ti_4O_7 , galvanostatic methods are used to investigate the Tafel behavior for the oxygen evolution reaction (OER) and the time-to-failure (TTF) via electrochemical accelerated life testing (ALT) of pristine and doped MPTO electrodes. In Chapter 5: Vanadium-Doped Ti_4O_7 Porous Transport Layers for Efficient Electrochemical Oxidation of Industrial Wastewater Contaminants, galvanostatic

methods are used to understand the current-voltage behaviour as well as electrolyze wastewater with the assembled WWE containing pristine and doped MPTO PTLs.

Galvanostatic methods are electrochemical measurements involving a static or fixed current and monitoring the potential of an electrode or electrochemical cell. Like CV, a potentiostat is used, but to control the current instead of the potential. A variety of information related to kinetic and transport phenomena can be obtained using this method. For example, a Tafel plot can be constructed by measuring the potential of an electrode for a period of time at a series of fixed currents. A current-voltage plot of an electrochemical cell is constructed in a similar manner. This approach to constructing a Tafel plot or a current-voltage plot over potentiodynamic methods such as CV or linear sweep voltammetry has the advantage of eliminating currents from the charging of the electric double layer, which may inflate kinetic contributions. Electrochemical accelerated life testing (ALT) can also be a galvanostatic method. For such a test, an aggressive or large current is passed at an electrode surface and its potential with time is monitored. As the electrode fails due to, for example, corrosion or passivation, a greater and greater magnitude of electrode potential is needed in order for the same current to pass. At a sufficient level of failure, the potential exceeds some limiting potential, either set experimentally or by the instrument, at a time referred to as the time-to-failure (TTF).

2.4 Water Quality Measurements

2.4.1 Colorimetry

Chapter 5: Vanadium-Doped Ti_4O_7 Porous Transport Layers for Efficient Electrochemical Oxidation of Industrial Wastewater Contaminants, colorimetry is used to determine the extent of decolorization and chemical oxygen demand removal (COD).

Colorimetry is an instrumental technique used to measure the intensity of a color of a substance or a solution. This is accomplished by use of a colorimeter or a spectrophotometer, the difference between the two being that a colorimeter measures a single wavelength or color whereas a spectrophotometer can measure multiple wavelengths. The intensity of the color is with reference to some standard, usually solutions of known concentration of the colored species including a control called a blank. In a typical measurement, the sample is illuminated with light and the light passing through the sample is measured. The degree to which the light passing through the sample is attenuated is proportional to the amount of colored species present within it. This relationship is called the Beer–Lambert law (Eq. 2.6):

$$A = \varepsilon \ell c \quad 2.6$$

where ε is the molar absorptivity, ℓ is the path length, and c is the concentration. A is the absorbance, which is a measure of the extent to which light passes through the sample referred to as transmittance (T , Eq. 2.7)

$$A = -\log_{10} T \quad 2.7$$

2.4.1.1 Decolorization

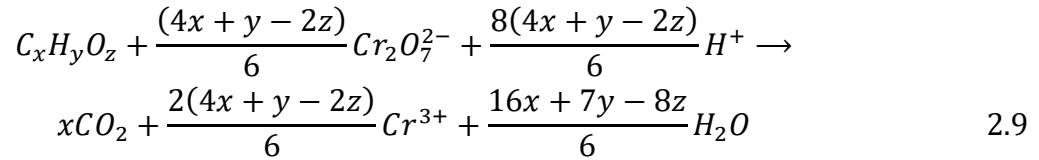
One important aesthetic parameter for water is its clarity. Clarity is a measure of how clear or transparent an aqueous solution is. Wastewater can contain species which reduce the clarity of the water by either scattering or absorbing light. Scattering is caused by suspended particles and the water. Light absorbance is due to electromagnetic radiation interacting with molecular electronic transitions. Unlike scattering, which can occur over a broad range of wavelengths, absorption occurs over a relatively narrower range of wavelengths and may be characteristic of the absorbing species. Decolorization (X_A , Eq. 2.8) is simply the extent to which the initial absorbance (subscript “0”) of a solution at some specific wavelength has been reduced:

$$X_A = 1 - \frac{A}{A_0} \quad 2.8$$

2.4.1.2 Chemical Oxygen Demand Removal

Another important consideration for wastewater which is to be ultimately released into the environment is its organic matter content. Microorganisms in the receiving environment degrade organic matter contained in wastewater, consuming oxygen in the process. If the organic load is too great, the local environment can be starved of oxygen by the microbial action.

One measure of the amount of organic matter is chemical oxygen demand (COD). COD is the amount of oxygen required to chemically oxidize the organic content using an oxidant such as dichromate ($\text{Cr}_2\text{O}_7^{2-}$) at high temperature in the presence of a strong acid catalyst (Eq. 2.9):



The amount of dichromate consumed in the process is stoichiometrically related to the amount of oxygen that would have been required to oxidize the organic material (*viz.* Eq. 1.31). The amount of dichromate is determined colorimetrically as it absorbs strongly at 350 nm relative to chromium(III) ions. Using the Beer–Lambert law (Eq. 2.6) and stoichiometry, the amount of oxygen that would be required to oxidize the organic matter can be calculated. However, it is also common and easier in practice to use a standard solution of known COD to calibrate such a method.

Chapter 3: The Thermal-Oxidation Behaviour of Pristine and Doped Magnéli Phase Titanium Oxides

3.1 Introduction

MPTOs [98, 44] are of growing importance to both solid state and electrochemical technologies. In TiO₂-based memristors, [99] conversion between electrically insulating TiO₂ and conductive Ti_nO_{2n-1} ($n = 4, 5$) provides a mechanistic basis for its resistive switching [100, 101, 102, 103, 104]. Ti₄O₇ and Ti₅O₉ are also promising alternatives to carbon-based materials in aqueous electrochemical systems [13, 14, 15, 6], having electrical conductivities comparable to graphite [30], chemical inertness in aggressive etchants [13, 42], and high overpotentials for the oxygen evolution reaction in water [11]. However, passivation forming TiO₂ occurs in sufficiently oxidizing conditions found in lead-acid batteries [71], regenerative fuel cells [91], and devices electrochemically incinerating aqueous pollutants [72]. Therefore, developing an understanding of the mechanisms for these reactions as well as strategies modulating the conditions for such transformations may lead to more effective MPTO-based materials.

Doping is an emerging method for tailoring MPTOs to better suit their application [14]. The inclusion of various dopants is demonstrated to be capable of modifying tribological [49, 50], electrical [51, 52, 53], photocatalytic [55, 54], thermoelectric [58, 57, 56], and electrocatalytic [52, 53, 59, 60] properties. However, the rationale for selecting dopants is generally sparse apart from a size criterion, which Gardos invokes in selecting Cu [50]. An expansion of this guidance is the Hume-Rothery rules for substitutional solid solutions [105], a set of attributes common to highly

soluble solutes employed in the alloying of metals. This set of 4 empirical qualities exhibited by solutes generally in excess of 5 at% are as follows: 1) the difference in the electronegativities ($\Delta\chi$) should be small, 2) the co-ordination number (CN) should be the same, 3) the atomic radii should not differ by more than $\pm 15\%$, and 4) the crystal structures should be similar. Darken-Gurry maps [106] are visual aids that can be used to identify potentially highly soluble dopants identified by the application of the Hume-Rothery rules. Darken and Gurry also relax rule 1 suggesting a threshold for $\Delta\chi$ of ± 0.4 on the Pauling scale. Finally, prioritizing high solubility minimizes the likelihood of forming causal mixtures, which are challenging to identify at lower additive concentrations. Using this approach, the list of candidate dopants can be refined for the evaluation of their influence on changes between $\text{Ti}_n\text{O}_{2n-1}$ and TiO_2 .

Thermogravimetric analysis (TGA) can reveal insights into such transformations. Hayfield conducted a preliminary investigation of the thermal stability of pristine and doped Ebonex® electrodes, a tradename for MPTO-based products ($n = 4, 5$), by observing their thermal-oxidation behavior in air [60]. Like its passivation in aqueous electrochemical systems, the thermal oxidation of MPTO in air forms the electrically-insulating TiO_2 . The influence of the dopants investigated on the stability appears mixed as measured by the onset temperature (T_o): the temperature at which the mass of the material deviates noticeably from the baseline. However, the composition of these materials is unclear in the absence of both thermogravimetric data at higher temperatures and phase analysis data. Furthermore, a reaction model governing the solid-state kinetics of MPTO oxidation in air has yet to be forwarded.

To elucidate a mechanism for the thermal oxidation of MPTO in air and to investigate the influence of dopants on its oxidation forming TiO_2 , we prepared pristine and doped Ti_4O_7 powders and evaluated them using TGA. Dopants were identified using the Hume-Rothery rules for substitutional solid solutions. Ti_4O_7 powders were obtained by high-temperature H_2 reduction of TiO_2 and characterized by scanning electron microscopy (SEM), gas adsorption analysis, X-ray fluorescence (XRF), energy-dispersive X-ray (EDX) spectroscopy, X-ray photoelectron spectroscopy (XPS), and powder X-ray diffraction (PXRD). Finally, empirical and computational data from TGA were used to evaluate onset temperatures and reaction models for thermal oxidation in air, respectively.

3.2 Experimental

3.2.1 Preparation of doped titanium oxides

The following chemicals were used as received: $\text{CrCl}_3 \cdot 6\text{H}_2\text{O}$ (purum p.a., 98%, Sigma Aldrich), ethanol (EtOH, pure un-denatured, 100%, University of British Columbia Department of Chemistry), FeCl_3 (ACS, 98%, anhydrous, Fisher Scientific), titanium tetraisopropoxide (TTIP, 97%, Sigma-Aldrich), and VCl_3 (97%, Sigma-Aldrich). Ultrapure H_2O (UPW, 18.2 $\text{M}\Omega$ cm) was generated as needed using a laboratory water system (Milli-Q Integral 5, EMD Millipore). Appropriate amounts of $\text{CrCl}_3 \cdot 6\text{H}_2\text{O}$, FeCl_3 , and VCl_3 were dissolved in UPW to obtain 2 M solutions. In a typical preparation theoretically yielding 3.42 g of TiO_2 , either 2.32 ml of UPW or 1.90 ml of UPW and 0.42 ml of 2 M transition metal halide solution were added dropwise to 250 ml of vigorously stirred EtOH. 12.7 ml of TTIP was added dropwise to the previously described solution afterwards stirring for an additional 5 min. The molar ratio of the constituents of the sol was

100:3:1:0.02 EtOH:UPW:TTIP:MC_l where M are either V, Cr, or Fe. The sol was aged overnight, and then the gel was dried on a hot plate at 80 °C. The xerogel was mechanically ground with an agate mortar and pestle, and then calcined at 800 °C in air for 4 h.

3.2.2 Preparation of pristine and doped magnéli phase titanium oxides

Ar (Ultra High Purity 5.0, 99.999%) and H₂ (Ultra High Purity 5.0, 99.999%, Praxair) were used as received. In a typical preparation yielding 0.5 g of H₂-reduced TiO₂, 0.5 g of either pristine or dopant-containing TiO₂ (*vide supra*) was placed in an alumina combustion boat, which was then placed in a tube furnace (Thermolyne F21125, Thermo Scientific) with an 18 inch (45.7 cm) long alumina process tube with a 2 inch (5.1 cm) diameter. Upon purging with Ar, H₂ was introduced into the process tube at a flow rate of 25 ml min⁻¹. The process tube was heated from ambient temperature to 1,050 °C at a heating rate of 5 °C min⁻¹ with a dwell time of 3 h.

3.2.3 Scanning electron microscopy and energy-dispersive X-ray spectroscopy

Surface morphology and elemental analysis were obtained using a field emission gun scanning electron microscope (FEI Quanta 650, Thermo Scientific) with an EDX detector accessory (XFLASH 6130, Bruker). All images and EDX spectra were obtained using an accelerating voltage of 20 kV and a working distance of 10 mm. Elemental analysis of EDX spectra was performed using microanalysis software (ESPIRIT, Bruker, ver. 2.1.2).

3.2.4 Gas adsorption analysis

Surface area using the Brunauer–Emmett–Teller (BET) method [107] were evaluated from N₂ gas adsorption-desorption isotherm data at –196 °C with a surface area analyzer (ASAP 2020, Micrometrics). Samples were degassed at 300 °C for 4 h under vacuum removing moisture prior to analysis.

3.2.5 X-ray fluorescence spectroscopy

The atomic concentration of dopant (M) relative to Ti, $M/(M+Ti)$, was determined in pristine and doped H₂-reduced TiO₂ from XRF spectra obtained using an energy dispersive X-ray fluorimeter (Fischerscope XDV-SDD, Fischer Technology) equipped with a Rh X-ray source and a Si drift detector. In a typical measurement, a powder sample was illuminated for 10 s with radiation from the X-ray source excited at 10 kV passing through a 1,000 μm Al filter. $M/(M+Ti)$ was computed from the relative weight concentrations reported by the instrument software (WinFTM XDV-SDD, ver. 6.35–5-PDM, Fischer Technology).

3.2.6 X-ray photoelectron spectroscopy

Surface analyses including elemental composition and chemical state were performed by XPS with a X-ray photoelectron spectrometer (Axis Ultra DLD, Kratos Analytical) using a monochromatic Al X-ray source and a hemispherical analyzer. Step size, dwell time, and sweeps were 1 eV, 0.8 s, and 2 for survey spectra and 0.1 eV, 0.3 s, and 2 for high resolution spectra, respectively. XPSPEAK (Raymund W. M. Kwok, Chinese University of Hong Kong, ver. 4.1) was used to

process constituent peaks within high-resolution data using Shirley backgrounds. Peak assignments were made upon comparison to published data compiled in the NIST X-ray Photoelectron Spectroscopy Database (ver. 4.1) [108].

3.2.7 Powder X-ray diffractometry and structure refinement

Phase identification and structure refinement was conducted with PXRD data obtained using a Bragg-Brentano θ - θ geometry X-ray diffractometer (Phaser D2, Bruker) with a Cu X-ray source (1.5406 Å) and a Si strip detector (LYNXEYE, Bruker). In a typical measurement, a powder sample was illuminated with radiation from the X-ray source excited at 30 kV with 10 mA passing through a 1.0 mm primary slit module, 2.5° stoller module, and a 0.5 mm Ni filter using a step size of 0.02° and an integration time of 1 s. Phase identification was carried out using the instrument software (DIFFRAC.EVA, Bruker) with reference to the Crystallography Open Database (COD) [109] later generating patterns using VESTA crystallography software [110] (ver. 3.4.7) and relevant Crystallographic Information Files (CIFs). Structure refinement was conducted using GSAS-II crystallography software (ver. 4376, Argonne National Laboratory) [111] using relevant CIFs as the initial structure solution. Uncertainty is reported parenthetically as the computed estimated standard deviation.

3.2.8 Thermogravimetric analysis

The thermal stability and solid-state kinetics of thermal oxidation in air was assessed with data obtained with a thermogravimetric analyzer (TGA-50, Shimadzu) using a data processor (TA-60WS, Shimadzu) and instrument software (ver. 2.21, Shimadzu). In a typical measurement, 5 mg of powder is transferred to an alumina crucible, which was then placed in the heating furnace of

the thermogravimetric analyzer with a flow of 50 ml min⁻¹ of air (Extra Dry 0.0, Praxair) and the temperature program is then started. The data is corrected for instrument drift by subtracting the fitted linear baseline of the thermograms (TGs).

3.3 Results & Discussion

3.3.1 Vanadium, chromium, and iron are suitable dopants

Candidate dopants were identified applying the Hume-Rothery rules for substitutional solid solutions to available databases. A database of effective ionic radii of the elements [112] was restricted to CN 6 and oxidation state (OS) III and IV, the CN and OSs of Ti in Ti_nO_{2n-1}. Considered were elements whose radii are within ±15% of 0.67 and 0.605 Å, the radii of Ti^{III} and Ti^{IV}, for OS III and IV species, respectively. Further refined were elements whose electronegativities are within 1.54 ± 0.4 on the Pauling scale, the electronegativity of Ti [113]. Finally, only elements whose oxides adopt either the rutile-like or corundum-like crystal structures were reviewed noting that Ti can adopt either the rutile or a corundum-like crystal structure in MPTO [67].

An analysis of the dataset (Figure 3.1) identifies 3 potentially highly-soluble dopants: V^{III}, Cr^{III}, and Fe^{III} high-spin complex. Halide salts of V^{III}, Cr^{III}, and Fe^{III} are both commercially available and sufficiently soluble and stable in water. Ga^{III} and Mn^{IV} also meet all 4 criteria. Efforts to prepare heavily Ga-doped materials were first thought to be successful; [114] however, XRF analysis of the samples after H₂ reduction now suggest the unexpected and complete removal of Ga at this step perhaps as a hydride. The dissolution of Mn^{IV} halide and the reaction of MnO₂ with a hydrogen halide form Mn^{II} species along with halogen gas. Therefore, the preparation of Mn-doped MTPO

via H_2 reduction of TiO_2 are infeasible notwithstanding other preparations such as metallothermic reduction. Rule 2 is observed for other reported dopants of MPTO: C [52], N [55, 54], Cu [50], Y [59], Zr [56], Nb [57, 58, 51], Mo [60], Ta [60], and Ce [53]. However, they violate rules 1 (C, N, and Mo) and 3 (C^{IV} , N^{III} , and Cu^{III} low-spin complex, Y^{III} , Zr^{IV} , Ce^{III} , and Ce^{IV}), or there is insufficient data to evaluate rule 4 (all but Zr^{IV}). As a result, only V, Cr, and Fe were investigated as dopants for MPTOs for subsequent study.

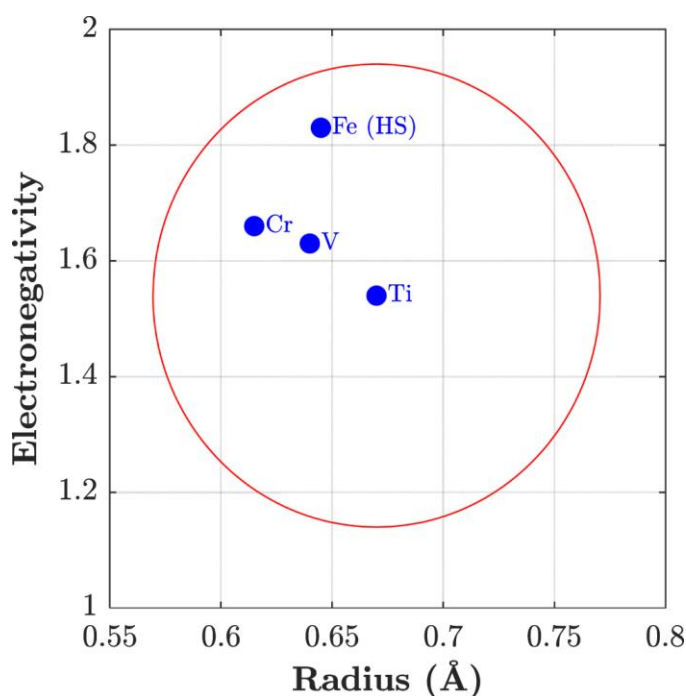


Figure 3.1 Darken-Gurry map of elements having a coordination number of 6, an oxidation state of III, and a corundum-like crystal structure where "HS" refers to the high-spin complex. The red circle is an ellipse with a width of $\pm 15\%$ the radius of Ti^{III} (0.67 \AA) and a height of ± 0.4 on the Pauling scale of electronegativity. Image reproduced from [65], which permits unrestricted reuse of the work via the Creative Commons Attribution 4.0 License (CC BY, <http://creativecommons.org/licenses/by/4.0/>).

3.3.2 Powders are highly-doped Ti₄O₇

The appearance of the powders suggest that the materials are doped and that their morphology is comparable. Optical images of the powders before and after H₂ reduction (Figure 3.2) suggest that both the dopants have been successfully incorporated into TiO₂ as evidenced by the change in color from white in the pristine sample to purplish brown, greenish gray, to reddish orange in the V-, Cr-, and Fe-containing samples, respectively. Upon H₂ reduction, all TiO₂ powders become dark blue, consistent with the preparation of MPTO. Scanning electron micrographs of the H₂-reduced powders (Figure A.2.1) are representative of manually ground materials with a few particles as large as ~100 μm in diameter. Closer examination of the surface of the larger particles suggests that they are porous, composed of a network of fused particles having diameters on the order of micrometers. This feature is consistent with the sintering expected using high temperatures for the stabilization and reduction of TiO₂. It is noted that the surface of the powders of doped materials take on a relatively smoother appearance, suggesting that the fused particles are generally smaller, perhaps due to the peptizing nature of the metal halides in the sol. BET analysis of the N₂ gas adsorption isotherms of H₂-reduced materials gives BET surface areas: 36.4 ± 0.5, 60.8 ± 1.4, 92.9 ± 1.0, and 69.0 ± 2.4 m² g⁻¹ for the pristine, V-doped, Cr-doped, and Fe-doped samples, respectively.

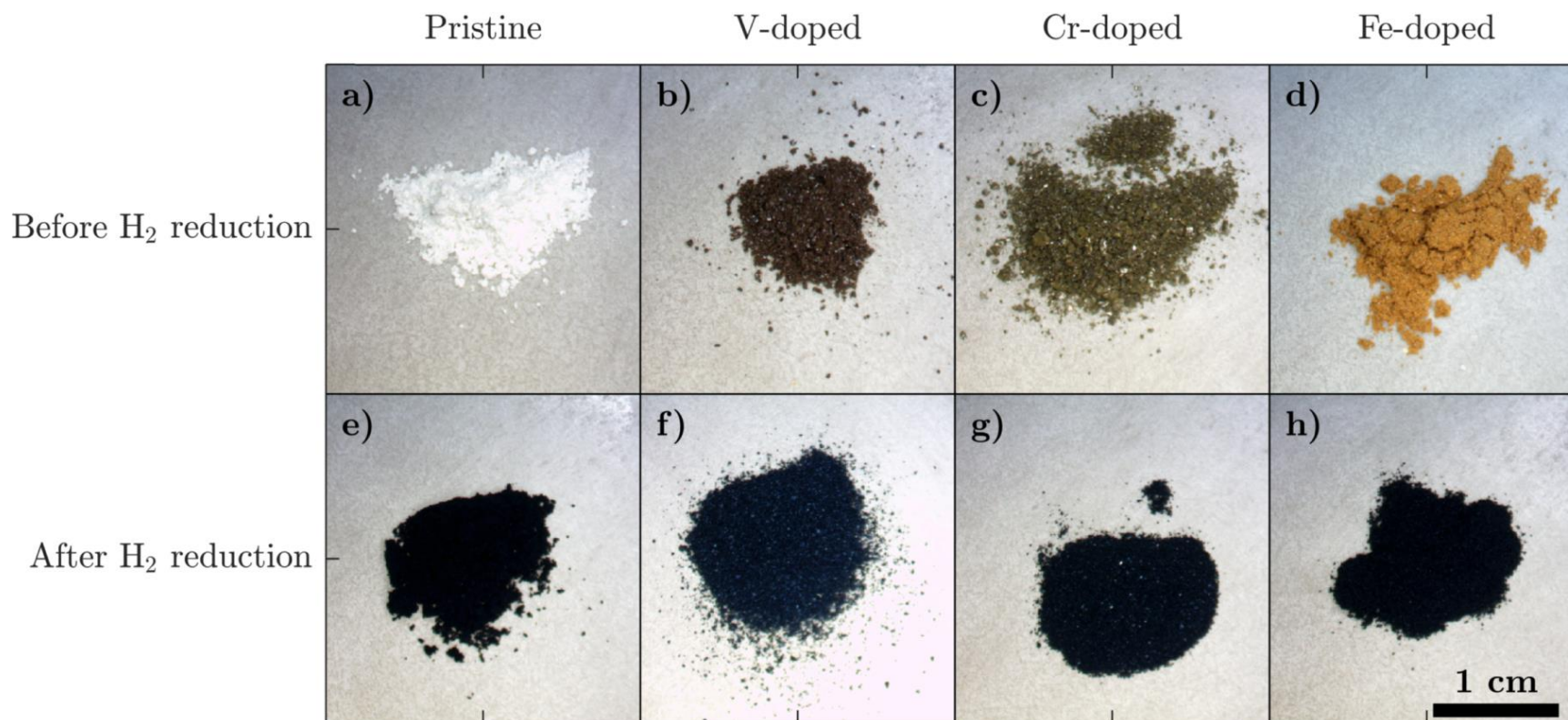


Figure 3.2 Optical microscope images of pristine and dopant-containing TiO₂ powders before a)–d) and after e)–h) H₂ reduction. Image reproduced from [65], which permits unrestricted reuse of the work via the Creative Commons Attribution 4.0 License (CC BY, <http://creativecommons.org/licenses/by/4.0/>).

Statistical analysis of the data obtained by EDX spectroscopy and XRF analysis of the H₂-reduced TiO₂ samples (Table 3.1) suggests that the dopants are present at approximately 2 at%. EDX spectroscopy results are equivalent or marginally lower than expected values whereas XRF results are marginally greater. This disparity is attributed to systematic errors in the preparation and storage of the transition metal halide solutions, the quality of the TTIP reagent, and its volatilization during the aging step of the sol-gel process. XPS of the doped materials (Figure A.2.2, Table A.2.1) was unable to identify doping elements in detectable concentrations on the surface of these particles though there is considerable adventitious Si, likely due to abrasion of the agate mortar and pestle. Analyses of high-resolution XPS spectra (Figure A.2.3, Table A.2.2, & Table A.2.3) suggest the presence of both Ti^{III} and Ti^{IV} as indicated by assignments of constituents of the Ti 2p peaks to Ti₂O₃ and TiO₂, respectively. However, TiO₂ is the dominant feature of this peak based on area and therefore the surface is likely passivated. In addition to TiO₂, metal hydroxides (M(OH)_x) and SiO₂ may also be present at the surface based on assignments of constituents of the O 1s peak.

	Dopant (at%)	
	EDX	XRF
V-doped	2.0 ± 0.9	2.7 ± 0.4
Cr-doped	1.4 ± 0.7	2.8 ± 0.2
Fe-doped	1.0 ± 0.4	2.6 ± 0.4

Table 3.1 Summary of statistical analysis (5 observations at a 5% significance level) of energy-dispersive X-ray (EDX) spectroscopy and X-ray fluorescence (XRF) of dopant in H₂-reduced TiO₂.

Via H₂-reduction of pristine and dopant-containing TiO₂, our objective was to obtain monophasic Ti₄O₇ (Eq. 3.1), the Magnéli phase titanium oxide with the greatest electrical conductivity [30]. Phase identification analysis of the patterns obtained by PXRD (Figure 3.3) provides evidence to suggest that this objective was achieved. Specifically, a pattern typical of Ti₄O₇ can be seen with intense peaks at 20.8° and 31.8° 2θ. The absence of a prominent broad peak in the baseline indicative of amorphous phases suggests that the materials must therefore be highly crystalline. The absence of peaks at 23.8° and 22.0° 2θ indicative of Ti₃O₅ and Ti₅O₇, respectively [44, 60], is also noted, suggesting the absence of adventitious Magnéli phases other than Ti₄O₇. The patterns were poorly indexed with an earlier reported structure of Ti₄O₇ [67], which was later revised [115] and nearly identical to the structure of 0.25% V-doped Ti₄O₇ (COD 1008048) [116], which was used for comparison. The absence of additional phases in the dopant-containing materials suggests that the dopant must therefore be uniformly distributed within the Ti₄O₇ phase.



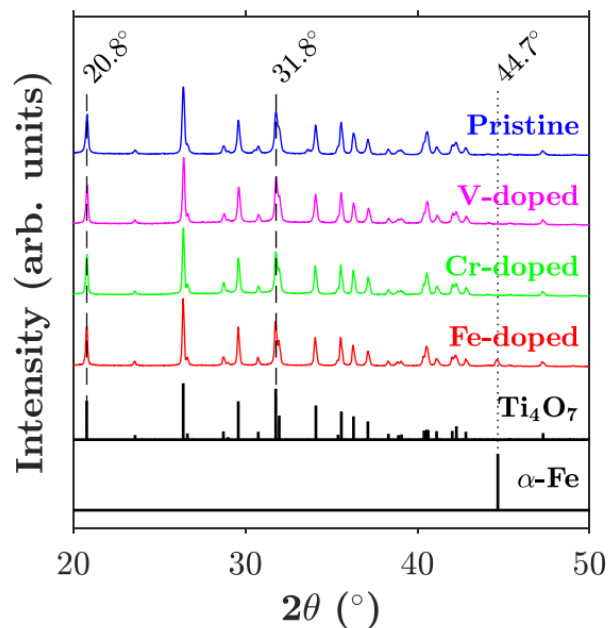


Figure 3.3 Powder X-ray diffraction patterns (1.5406 Å) of H₂-reduced pristine and dopant-containing TiO₂, which are well-indexed with Ti₄O₇ (COD 1008048). An extraneous peak in the Fe-doped, H₂-reduced TiO₂ pattern at 44.7° 2θ is assigned to the (110) Miller index of crystalline alpha Fe (α-Fe, COD 9005836). Image reproduced from [65], which permits unrestricted reuse of the work via the Creative Commons Attribution 4.0 License (CC BY, <http://creativecommons.org/licenses/by/4.0/>).

An extraneous peak in the pattern for the Fe-doped sample is also noted. Phase identification analysis restricting the search to compounds containing O, Ti, and Fe suggests alpha Fe (α-Fe) to be the likely candidate, whose pattern (COD 9005836) [117] was well-indexed. Analysis of thermodynamic values [118] of the H₂ reduction of Fe₂O₃, assuming the oxidation state of Fe^{III} remains the same throughout the sol-gel synthesis, forming α-Fe and H₂O (Eq. 3.2) at 1,050 °C suggests that the process is likely spontaneous, evaluating its standard reaction Gibbs energy to be -41.5 kJ mol⁻¹. Assuming the activities of all reagents to be approximately unity except

H₂O, which is negligible, one can conclude that the formation of α -Fe is at least thermodynamically possible in 1 atm of H₂.



Structure refinement was conducted to obtain lattice parameters of the unit cell as well as the size (τ) and strain (ϵ) of the crystallites (Figure A.2.4, Table A.2.4, Table A.2.5, & Table A.2.6). There is good agreement in the lattice parameters of the unit cells of pristine Ti₄O₇ as compared to the reference CIF (COD 1008048) [116]. One can account for the marginal differences in lattice parameters β and γ to random errors in the structure refinement expressed by the weighted profile R-factor (R_{wp}). There is also good agreement between the pristine and doped Ti₄O₇ samples with marginal differences in lattice parameter γ for all doped samples. Structure refinement of the Fe-doped sample accounting for two phases, Ti₄O₇ and α -Fe, gives a weight fraction for α -Fe of 0.9(2)%. The size and the strain of the crystallites in the pristine samples were evaluated to be 86(5) nm and 0.03(4)%, respectively. By comparison, the crystallites in the doped samples are 1.4(2)–2.0(2) times as large with strain ranging 0.06(5)–0.20(3)% larger. An interpretation of these results is that the variation in the size of the crystallites is due to systematic errors such as differing times for the aging and drying steps of the sol-gel method whereas an increase in the strain of the crystallites is generally concomitant with the presence of dopant.

3.3.3 Vanadium and iron improve thermal stability

TGA of pristine and V-, Cr-, and Fe-doped Ti₄O₇ (Figure 3.4a) provides a measure of their quality. Assuming the product of thermal oxidation of Ti_{*n*}O_{2*n*-1} to be TiO₂ (Eq. 3.3) and conducting a mass

balance, one can obtain information about the oxidation state of Ti from the total relative mass change ($\Delta m/m_0$). Given PXRD evidence suggesting the samples to be predominantly Ti_4O_7 (*vide supra*), a total relative mass change of 5.2722(2)% is expected from stoichiometry [55].



Empirical values are obtained by fitting the TGs to the logistic function to obtain the total relative mass change, the extrapolated onset temperature, and the peak temperature (T_p), the temperature at which the rate of change in the mass is at a maximum. For the exception of Fe-doped Ti_4O_7 , it can be observed that the values of total relative mass change for all pristine and doped samples agree with one another within the limits of uncertainty (Table 3.2). However, they are marginally smaller than the theoretical value. It is inferred from the disagreement between the empirical value of the pristine sample and theoretical value of the total relative mass change that the linear baseline correction of the TGs has introduced a bias towards underestimating total relative mass change. Furthermore, one can attribute the disparity between the empirical and theoretical values for the total relative mass change of Fe-doped Ti_4O_7 to the α -Fe phase as evidenced by phase identification and structure refinement of the PXRD data (*vide supra*).

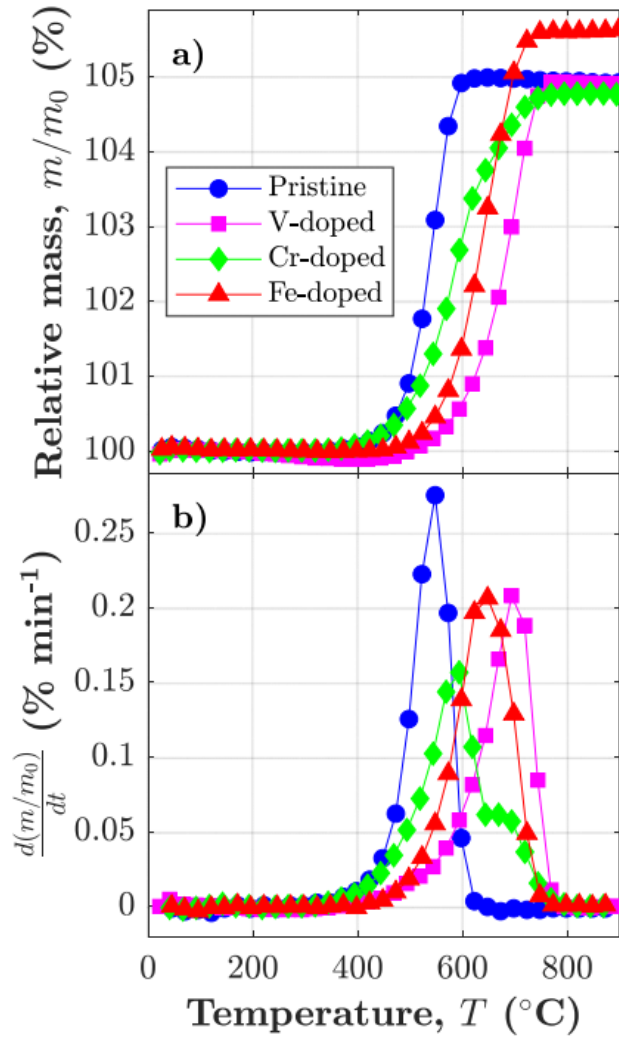


Figure 3.4 (a) Thermograms and (b) differential thermograms ($5^{\circ}\text{C min}^{-1}$) of pristine and doped Ti_4O_7 in air. The data sampling intervals are reduced from 1/12 to 25°C for clarity. Image reproduced from [65], which permits unrestricted reuse of the work via the Creative Commons Attribution 4.0 License (CC BY, <http://creativecommons.org/licenses/by/4.0/>).

	$\Delta m/m_0$ (%)	T_o (°C)	T_p (°C)
Pristine	4.91 ± 0.30	491.1 ± 5.5	543.1 ± 1.6
V-doped	5.08 ± 0.06	608.9 ± 5.0	675.6 ± 3.2
Cr-doped	4.91 ± 0.24	495.3 ± 4.7	586.1 ± 4.9
Fe-doped	5.80 ± 0.29	570.5 ± 3.0	636.9 ± 1.3

Table 3.2 Summary of statistical (3 observations at a 5% significance level) analysis of fitted total relative mass change ($\Delta m/m_0$), onset and peak temperatures (T_o and T_p , respectively) for the thermal oxidation ($5\text{ }^\circ\text{C min}^{-1}$) of pristine and doped Ti_4O_7 in air.

Generally, the thermal stability as measured by the onset temperature either stays the same or increases with doping with the following trend: $\text{V} > \text{Fe} > \approx \text{Cr} \approx \text{Ti}$ (Table 3.2). A similar trend is observed in the peak temperature ($\text{V} > \text{Fe} > \text{Cr} > \text{Ti}$) noting that the peak temperature is not a typical measure of thermal stability. The difference between onset and peak temperatures does provide a measure of the sensitivity to temperature (T) with sensitivity increasing as the difference decreases. This sensitivity becomes more pronounced when plotting the differential TGs (DTGs, Figure 3.4b) wherein sharper and more intense peaks suggest a greater sensitivity to temperature for a fixed temperature ramp rate. The following trend in temperature sensitivity is proposed: $\text{Cr} < \text{V} < \text{Fe} \approx \text{Ti}$. From the shapes of the DTGs one infers that the kinetics of the thermal oxidation of pristine, V-doped, and Fe-doped Ti_4O_7 is governed by a single step whereas peak shoulders in the DTGs of Cr-doped Ti_4O_7 might suggest either a multi-step or parallel chemical reactions. These additional features as well as the asymmetry of the DTG peaks illustrate a limitation of fitting the TG data with a logistic function, which gives a symmetric peak devoid of additional features such as shoulders.

3.3.4 Thermal oxidation in air is diffusion-controlled

Following the guidance of the International Confederation for Thermal Analysis and Calorimetry [119], the development of a reaction model from the thermogravimetric data has been based upon the general rate expression in terms of conversion (α) and the evaluation of its kinetic triplet: (1) an Arrhenius pre-exponential factor (A), (2) an activation energy (E), and (3) a reaction model ($f(\alpha)$). During a thermogravimetric measurement with a constant temperature ramp rate (β), using the integral isoconversional Kissinger–Akahira–Sunose (KAS) method [120, 121], at a fixed conversion (denoted by subscript α), the slope of a plot of $\ln(\beta/T_\alpha)$ for varying values of $1/T_\alpha$ is proportional to E_α . In this fashion, from TGs generated with varying temperature ramp rate, we obtained model-free values of E_α . The span of fitted values for E_α for both pristine and doped materials are observed to be well within 20%–30% the mean, the threshold for significance [119]. Therefore, one can infer that the thermal oxidation of Ti_4O_7 is governed by a single step over for nearly all values of conversion.

The choice of reaction model for the solid-state kinetics of thermal oxidation of Ti_4O_7 was informed using $y(\alpha)$ and $z(\alpha)$ master plots. The shape of the $y(\alpha)$ and $z(\alpha)$ master plots assist in the identification of the reaction model. The Senum and Yang approximation was used to evaluate the integral of the Arrhenius function [122]. The shape of the $y(\alpha)$ master plot of pristine Ti_4O_7 is typical of diffusion reaction models (Figure 3.5a) [119]. Similar shapes are observed in the $y(\alpha)$ master plots of doped Ti_4O_7 (Figure 3.5b, Figure A.2.5a & b) suggesting that a diffusion reaction model could describe their thermal oxidation as well. As the samples were fine powders, it was reasoned that a three-dimensional diffusion reaction model was most physically sensible. Two

such models frequently encountered in literature are the D3 or Jander model [123] and the D4 or Ginstling–Brounshtein model [124]. The difference between the D3 and D4 models is their mathematical development: D3 approximates three-dimensional diffusion with one-dimensional invoking the parabolic law, whereas D4 employs the solution to Fick’s first law for radial diffusion in a sphere [125]. However, uncertainty in the location of the peak of the $z(\alpha)$ curves suggests that both models could be appropriate (Figure 3.5c & d, Figure A.2.5c & d). It is noted that in the $z(\alpha)$ master plot of Cr-doped Ti_4O_7 (Figure A.2.5c) is a discontinuity in the curve suggesting that their mechanism for thermal oxidation could be multi-step. These features in the $z(\alpha)$ master plots are approximately coincident to the peak shoulders in the DTGs (*vide supra*).

Linearized differential data ($\ln\{f(d\alpha/dt)[1/f(\alpha)]\}$) was generated for the purpose of linear model-fitting defining $f(\alpha)$ as either the D3 (f_{D3}) or D4 (f_{D4}) reaction model. Both models provide good fits with values for R^2 greater than 0.95 (Table 3.3). The D3 model (Figure 3.6a) generally fits the data for the pristine Ti_4O_7 better than the D4 model (Figure 3.6c) as well as the doped materials (Figure 3.6b & d, & Figure A.2.6a–d) as determined by the relative values of R^2 except for V-doped Ti_4O_7 . One observes considerably more outliers for the Cr-doped Ti_4O_7 sample occurring at values of conversion near unity. These outliers appear to be coincident with shoulder peaks in the DTGs and discontinuities in the $z(\alpha)$ master plots (*vide supra*). Linear model-fitting produces values of activation energy that are generally greater than model-free ones, with the D4 model being the closer of the two models except for Cr-doped Ti_4O_7 . The fitted values of the Arrhenius pre-exponential factor for the pristine Ti_4O_7 are larger than those for the doped Ti_4O_7 with values obtained by D3 model fitting to be the greater of the two models.

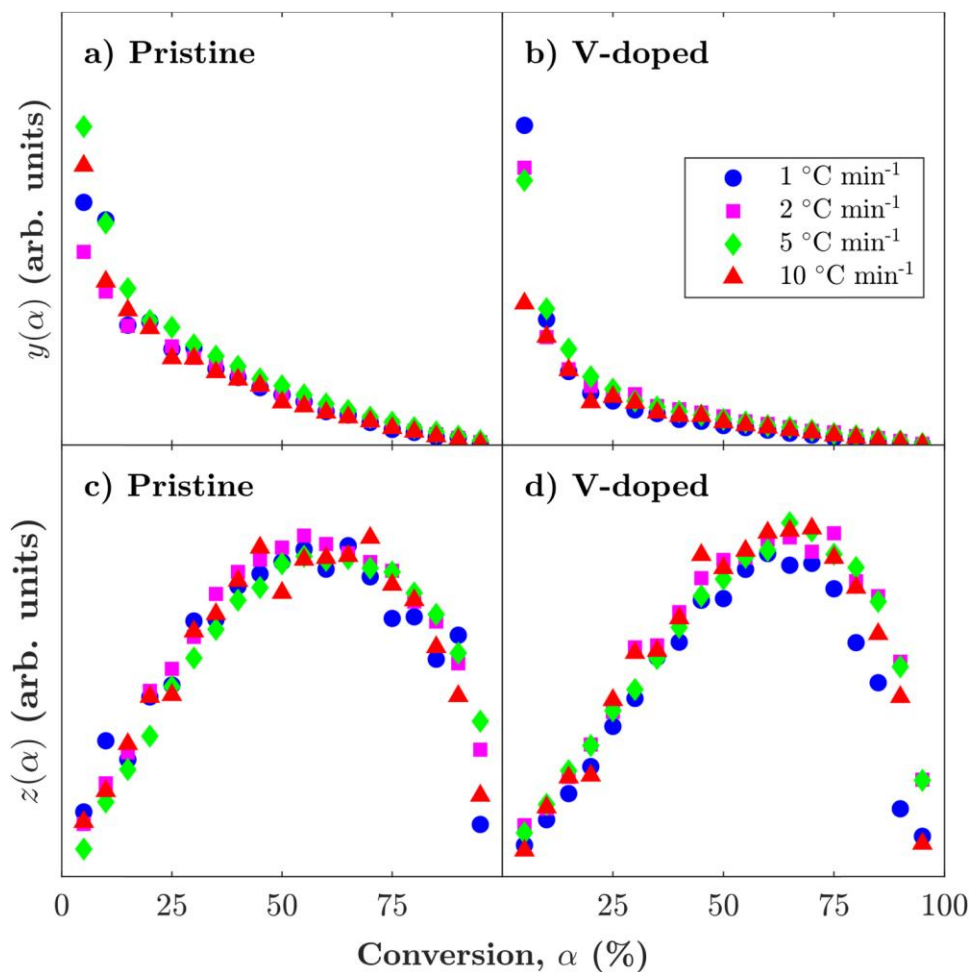


Figure 3.5 (a) & (b) $y(\alpha)$ and (c) & (d) $z(\alpha)$ master plots for the thermal oxidation of (a) & (c) pristine and (b) & (d) V-doped Ti_4O_7 in air. Image reproduced from [65], which permits unrestricted reuse of the work via the Creative Commons Attribution 4.0 License (CC BY, <http://creativecommons.org/licenses/by/4.0/>).

	E (kJ mol⁻¹)			log₁₀(A/min⁻¹)		R²	
	KAS	D3	D4	D3	D4	D3	D4
Pristine	221.6 ± 1.4	262.2 ± 1.1	236.2 ± 1.2	14.9 ± 0.6	13.1 ± 0.6	0.9805	0.9712
V-doped	219.6 ± 4.1	245.1 ± 0.8	230.3 ± 0.7	11.3 ± 0.4	10.3 ± 0.3	0.9861	0.9897
Cr-doped	210.5 ± 3.8	181.3 ± 0.9	171.1 ± 1.0	8.7 ± 0.5	8.0 ± 0.5	0.9794	0.9698
Fe-doped	204.1 ± 4.7	227.0 ± 0.7	203.2 ± 1.2	10.8 ± 0.4	9.3 ± 0.6	0.9876	0.9591

Table 3.3 Summary of statistical (5% significance level) analysis of fitted activation energy (*E*), Arrhenius pre-exponential factor (*A*), and the coefficient of variance (*R*²) for the thermal oxidation (1, 2, 5, and 10 °C min⁻¹) of pristine and doped Ti₄O₇ in air using the integral isoconversional Kissinger–Akahira–Sunose (KAS) method and linear model-fitting with Jander (D3) and Ginstling–Brounshtein (D4) reaction models.

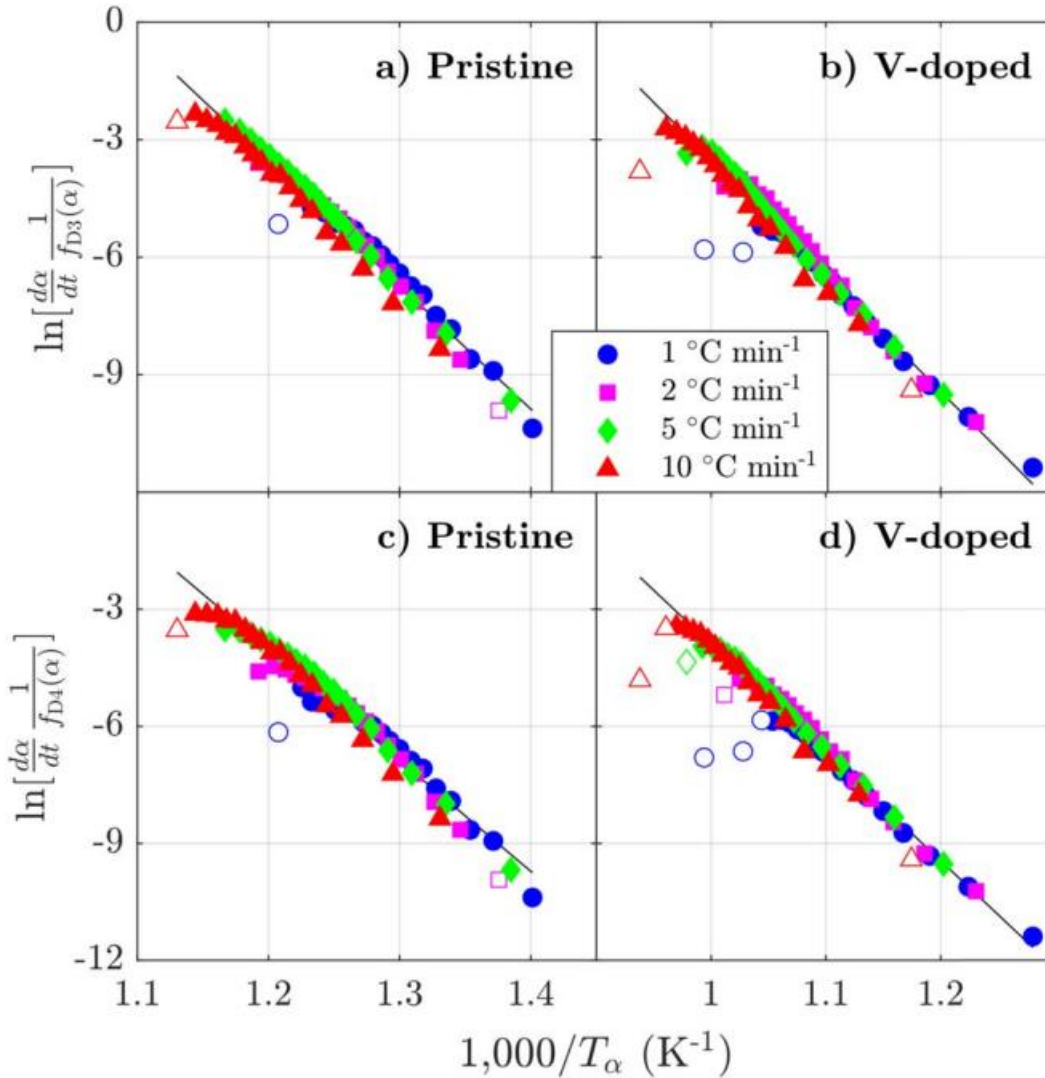


Figure 3.6 (a) Linearized differential data ($\ln\{f(d\alpha/dt)[1/f(\alpha)]\}$) for three-dimensional diffusion reaction models (a) & (b) Jander (D3, $f(\alpha) = f_{D3}(\alpha)$) and (c) & (d) Ginstling–Brounshtein (D4, $f(\alpha) = f_{D4}(\alpha)$) vs $1,000/T$ for the thermal oxidation of (a) & (c) pristine and (b) & (d) V-doped Ti_4O_7 in air with linear fit (straight line, empty markers indicating outliers). Image reproduced from [65], which permits unrestricted reuse of the work via the Creative Commons Attribution 4.0 License (CC BY, <http://creativecommons.org/licenses/by/4.0/>).

From kinetic computation, we observe that (1) a three-dimensional diffusion reaction model, either D3 or D4, satisfactorily describes the solid-state kinetics of thermal oxidation of

pristine and doped Ti_4O_7 in air, and (2) doping reduces both the Arrhenius pre-exponential factor and the activation energy. Therefore, thermal oxidation of Ti_4O_7 to TiO_2 is a diffusion-controlled process forming a superficial layer of TiO_2 . Doping has a mixed effect on the kinetics of oxidation with a lower Arrhenius pre-exponential factor making it sluggish and a lower activation energy having the opposite effect. At ambient conditions, pristine Ti_4O_7 is kinetically stable having a fixed-conversion lifetime (t_α) of $10^{27.5 \pm 1.0}$ and $10^{24.8 \pm 1.1}$ min at a conversion of 5% obtained by kinetic prediction using the D3 and D4 models, respectively (Figure 3.7). The doped Ti_4O_7 are also stable; however, the relative t_α of Cr-doped Ti_4O_7 is predicted to be significantly shorter using both models.

3.4 Summary

Magnéli phase titanium oxides are potentially important materials for both solid-state and electrochemical technologies, and an ability to customize their relevant physicochemical properties must be developed as their prominence grows. As this work demonstrates, doping effectively modifies the oxidation stability of Ti_4O_7 , with V-doping and Fe-doping markedly improving thermal stability in air. The suitability of the diffusion reaction models for the solid-state kinetics of thermal oxidation suggests that dopants hindering diffusion will improve the oxidation stability of Ti_4O_7 . This understanding of the influence of doping on the oxidation kinetics was developed and used to estimate material lifetimes at ambient conditions, with Cr-doping shortening it significantly. While the influence of doping at 2 at% was investigated, this composition has not been optimized.

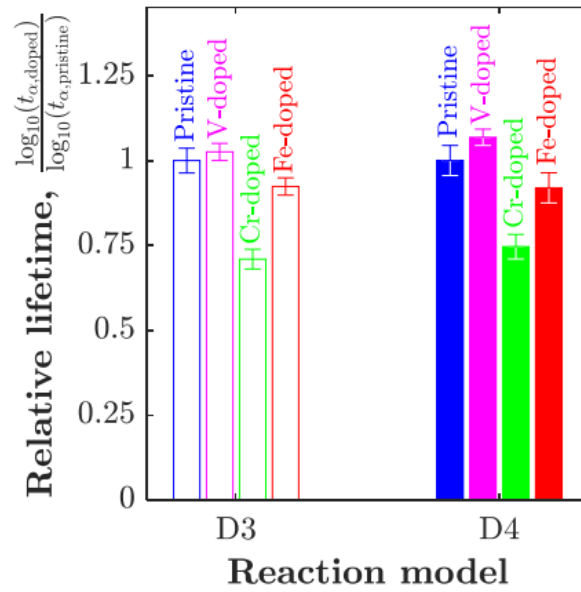
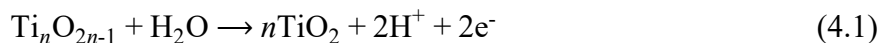


Figure 3.7 (a) Relative fixed-conversion lifetimes (t_{α} , 5% conversion) of pristine and doped Ti_4O_7 from kinetic prediction using Jander (D3) and Ginstling–Brounshtein (D4) reaction models. Image reproduced from [65], which permits unrestricted reuse of the work via the Creative Commons Attribution 4.0 License (CC BY, <http://creativecommons.org/licenses/by/4.0/>).

Chapter 4: The Superior Electrical Conductivity and Anodic Stability of Vanadium-Doped Ti₄O₇

4.1 Introduction

This chapter departs from the thermal oxidation behaviour discussed in Chapter 3, focusing on the electrochemical behaviour relevant to its anodic stability. Ti₄O₇ and Ti₅O₉, the most electrically-conductive members of the Magnéli phase titanium oxides (MPTOs, Ti_nO_{2n-1}, 4 ≤ n ≤ 10) [126, 30], are promising alternatives to carbon-based materials in aqueous electrochemical technologies [13, 14, 15, 6], showing excellent electrical conductivity [30], good chemical inertness [42], and a high overpotential for the oxygen evolution reaction (OER) [11]. While kinetically stable at standard temperature and pressure [65], passivation forming the thermodynamically-favored TiO₂ occurs under sufficiently oxidizing conditions (Eq. 4.1, $E^\circ = -0.545$ V vs SHE for $n = 4$) [70]. This passivation is of concern to the operation of batteries [71] fuel cells, [91] and the electrochemical treatment of wastewater [72]. Strategies to stabilize of these materials against electrochemical oxidation are therefore needed in order to improve the resilience of technologies employing MPTO-based materials.



Magnéli phase titanium oxides including Ebonex®, a trade name for electrodes based on such materials, have been incorporated into fuel cells (FCs) and water electrolyzers (WEs) for H₂

production to great effect. H₂/O₂ proton-exchange membrane (PEM) FCs with membrane electrode assemblies using Ti₄O₇-supported Pt and Nafion ionomer as both anode and cathode catalyst layers exhibit superior anodic stability as compared to Vulcan XC-72 [127, 128, 129, 130, 131]. IrO₂ catalyst loaded MPTO with Nafion ionomer forming the anode catalyst layer of a MEA were used in a PEMWEs, showing improved electrocatalytic activity relative to commercial materials [132] and catalyst-coated membranes [133]. However, 7 hours of anodic conditioning at 1.6 V (vs. SHE) of electrodes of Ebonex®-supported Pt₄Ru₄Ir₁, a bifunctional electrocatalyst, results in the irreversible passivation with Ti^{II} forming Ti^{IV} [91].

Properties relevant to the application of Ti_nO_{2n-1} as electrode materials can be modified by doping, including electrical [134, 51, 53, 52], tribological [50, 49], electrocatalytic [53, 52, 60, 59, 61], thermal oxidative [65, 60], photocatalytic [54, 55], and thermoelectric properties [57, 58, 56]. This approach is broadly used to modify the properties of other titanium oxides. For example, Ta, Nb, and In doping of TiO₂ is shown to improve the cyclability and discharge capacity of Na-ion battery anodes by expanding the diffusion path and improving the electronic conductivity [135, 136, 137]. Doping Ti₃O₅ with Mo, Si, and N yields carbon-free fuel cell electrocatalyst supports with stability and durability [138, 139, 140]. Recently, it has been demonstrated that doping Ti₄O₇ with transition metal atoms V, Cr, and Fe increases its stability toward thermal oxidation in air as expressed by the onset temperature obtained by thermogravimetric analysis discussed in Chapter 3 [65]. The kinetics of the thermal oxidation of Ti₄O₇ in air forming TiO₂, being a diffusion-controlled process, is hindered by doping, improving its resistance to oxidation. Doping Ti₄O₇ with the rare-earth metal Ce may also improve the service lives of electrodes as determined by electrochemical accelerated life testing (ALT) [61]. Therefore, any improvement of the anodic stability

of $Ti_n O_{2n-1}$ due to V-, Cr-, and Fe-doping must be investigated in an effort to address the aforementioned issues of passivation.

ALT provides a rapid measure of the stability of electrodes such as those for the OER [141, 142, 143, 144, 145, 146]. In a typical measurement, an electrode is subjected to demanding conditions, including harsh electrolyte, strongly oxidizing or reducing electrode potentials, high current densities, and extreme temperatures—accelerating its time-to-failure (TTF). For mixed-metal oxide coated titanium electrodes used for the OER and the chlorine evolution reaction, TTFs at two different conditions indicated by subscripts 1 and 2 where only the current density (j) varies is related by a power law expression (Eq. 4.2, $1.4 \leq t \leq 2.0$) [141, 142, 147]. In this fashion, increasing the current density used during an electrochemical ALT changes the TTF by orders of magnitude.

$$TTF_1/TTF_2 = (j_1/j_2)^{-t} \quad (4.2)$$

To investigate the influence of doping on the anodic stability of $Ti_n O_{2n-1}$, we prepared disks of pristine and doped Ti_4O_7 and subjected them to electrochemical ALT. Ti_4O_7 disks were obtained by a high-temperature H_2 reduction of sintered TiO_2 disks and characterized by scanning electron microscopy (SEM), energy-dispersive X-ray (EDX) spectroscopy, X-ray fluorescence (XRF), X-ray photoelectron spectroscopy (XPS), powder X-ray diffractometry (PXRD), 4-point probe method, cyclic voltammetry (CV), Tafel plot analysis, and electrochemical impedance spectroscopy (EIS).

4.2 Experimental

4.2.1 Materials

The following chemicals were used as received: $\text{CrCl}_3 \cdot 6\text{H}_2\text{O}$ (purum p.a., 98%, Sigma Aldrich), ethanol (EtOH, pure un-denatured, 100%, University of British Columbia Department of Chemistry), FeCl_3 (ACS, 98%, anhydrous, Fisher Chemical), H_2SO_4 (Certified ACS Plus, 95%–98%, Fisher Chemical), K_2SO_4 (Certified ACS, 99.2%, Fisher Chemical), titanium tetraisopropoxide (TTIP, 97%, Sigma-Aldrich), and VCl_3 (97%, Sigma-Aldrich). Ultrapure water (18.2 $\text{M}\Omega$ cm) was generated as needed using a laboratory water system (Milli-Q Integral 5, EMD Millipore). Appropriate amounts of $\text{CrCl}_3 \cdot 6\text{H}_2\text{O}$, FeCl_3 , and VCl_3 were dissolved in H_2O to obtain 2 M solutions. Pristine and nominally 2 at% doped TiO_2 were prepared by a previously described sol-gel method [65]. Aqueous solutions of 0.5 M H_2SO_4 and saturated K_2SO_4 were prepared by diluting appropriate amounts of H_2SO_4 and K_2SO_4 in H_2O , respectively.

4.2.2 Electrode preparation

Ar (Ultra High Purity 5.0, 99.999%) and H_2 (Ultra High Purity 5.0, 99.999%, Praxair), heavy mineral oil (0.83 g ml^{-1} , FCC/USP, Fisher Scientific), and paraffin wax (mp 58–62 °C, ASTM D 87, Sigma-Aldrich) were used as received. In a typical preparation yielding 5 mm diameter disks, 8 ml of heavy mineral oil as binder was mixed into 0.25 g of pristine or nominally 2 at% doped TiO_2 prepared by sol gel using titanium tetraisopropoxide and appropriate metal chloride in ethanol [65]. The mixture was then compressed in a 5 mm pellet die (GS03060, Specac) with a 2.00-ton load (910 MPa) using a desktop dry pressing machine (YLJ-24TS, MTI Corporation). The compressed disk was then heated in air in a muffle furnace (Type 48 000, Barnstead Thermolyne)

to 1,200 °C for 1 hour to remove the binder and sinter the powder. Sintered disks then reduced in H₂ at high temperature following a previously-described method [65]. Reduced disks were fitted into a rotating disk electrode (RDE) tip with an interchangeable disk option (ACE4THQ050, Pine Research Instrumentation) and fixed in place with epoxy (Gorilla Epoxy, Gorilla Glue). Fixed disk electrodes were then sealed with molten paraffin wax at 80 °C. Sealed disk electrodes were then polished sequentially with 600 grit sandpaper (CarbiMet, Buehler), 0.3 micron alumina suspension (90-187510, Allied High Tech Products) on nylon cloth (Nylon, Buehler), then 0.05 micron alumina suspension (90-187505, Allied High Tech Products) on rayon cloth (MicroCloth, Buehler). Polished electrodes were inserted into a body (ACE4TB, Pine Research Instrumentation), attached to a shaft (AFE3M, Pine Research Instrumentation) with silver two-part conductive adhesive (Alfa Aesar), and rinsed with ultrapure water prior to the assembly of electrochemical cells.

4.2.3 Physicochemical characterization

4.2.3.1 Scanning electron microscopy and energy-dispersive X-ray spectroscopy

Surface morphology and elemental analysis were obtained using a field emission gun scanning electron microscope (FEI Quanta 650, Thermo Scientific) with an EDX detector accessory (XFLASH 6130, Bruker). All images and EDX spectra were obtained using an accelerating voltage of 20 kV and a working distance of 10 mm. Elemental analysis of EDX spectra was performed using microanalysis software (ESPIRIT, Bruker, ver. 2.1.2).

4.2.3.2 X-ray fluorescence spectroscopy

The atomic concentration of dopant (M) relative to Ti, $M/(M+Ti)$, was determined in pristine and doped H_2 -reduced TiO_2 from X-ray fluorescence (XRF) spectra obtained using an energy dispersive X-ray fluorimeter (Fischerscope XDV-SDD, Fischer Technology) equipped with a Rh X-ray source and a Si drift detector. In a typical measurement, a powder sample was illuminated for 10 s with radiation from the X-ray source excited at 10 kV passing through a 1,000 μm Al filter. $M/(M+Ti)$ was computed from the relative weight concentrations reported by the instrument software (WinFTM XDV SDD, ver. 6.35-5-PDM, Fischer Technology).

4.2.3.3 X-ray photoelectron spectroscopy

Surface analyses including elemental composition and chemical state were performed by XPS with an X-ray photoelectron spectrometer (Axis Ultra DLD, Kratos Analytical) using a monochromatic Al X-ray source and a hemispherical analyzer. Prior to acquisition, the samples were etched with a monatomic Ar^+ ion source (Minibeam 4, Kratos Analytical) having a beam energy of 3 keV for 5 minutes. Step size, dwell time, and sweeps were 1 eV, 0.8 s, and 2 for survey spectra; 0.1 eV, 0.5 s, and 2 for high resolution spectra of Ti 2p and O 1s, and 0.1 eV, 1.0 s, and 5 for high resolution spectra of V 2p and Fe 2p, respectively. XPSPEAK (Raymund W. M. Kwok, Chinese University of Hong Kong, ver. 4.1) was used to process constituent peaks within high-resolution data using Shirley backgrounds. Peak assignments were made by comparison with published data compiled in the NIST X-ray Photoelectron Spectroscopy Database (ver. 4.1) [108].

4.2.3.4 Powder X-ray diffractometry

Phase identification and structure refinement was conducted with PXRD data obtained using a Bragg-Brentano theta–theta geometry X-ray diffractometer (Phaser D2, Bruker) with a Cu X-ray source (1.5406 Å) and a Si strip detector (LYNXEYE, Bruker). Prior to acquisition, disks were manually ground with an agate mortar and pestle forming a powder. In a typical measurement, a powder sample was illuminated with radiation from the X-ray source excited at 30 kV with 10 mA passing through a 1.0 mm primary slit module, 2.5° stoller module, and a 0.5 mm Ni filter using a step size of 0.02° and an integration time of 1 s. Phase identification was carried out using the instrument software (DIFFRAC.EVA, Bruker) with reference to the Crystallography Open Database (COD) [109], later generating patterns using VESTA crystallography software (ver. 3.4.7) [110] and relevant Crystallographic Information Files (CIFs).

4.2.3.5 4-point probe method

Electrical conductivity (σ) was evaluated from resistance data generated using the 4-point probe method with manual four-point probe resistivity probing equipment (S-302-4, Signatone) and a standard head (SP4-40045TRY, Signatone). In a typical measurement, the head was brought into contact with a stationary RDE and a 1 kHz AC test current with an amplitude of 100 mA was generated using a multichannel electrochemical workstation (VMP3, BioLogic). The real component of the measured impedance (V/I) was used to evaluate the electrical conductivity using the reciprocal of the 4-point probe equation for evaluating resistivity (Eq. 4.3) where s is the tip spacing (0.10 cm) and F is the correction factor (Eq. 4.4) [148]. F_1 , the correction factor for sample thickness, is estimated to be approximately unity as the sample thickness is sufficiently greater

than the tip spacing. F_2 and F_3 , the correction factors for lateral sample dimensions and the probe placement relative to the edge are estimated to be 0.75 and 0.95, respectively.

$$\sigma = [2\pi s(V/I)F]^{-1} \quad (4.3)$$

$$F = F_1 F_2 F_3 \quad (4.4)$$

4.2.4 Electrochemical measurements

A multichannel electrochemical workstation (VMP3, BioLogic) and a standard 150 ml cell (AKCELL2, Pine Research Instrumentation) using an undivided conventional 3-electrode setup were used for all electrochemical measurements. A saturated mercury mercurous sulfate reference electrode (XR200, Radiometer Analytical) with saturated aqueous K_2SO_4 as its secondary solution and a platinum foil counter electrode (M241Pt, Radiometer Analytical) were used for all measurements. The potential of the reference electrode was measured at open circuit with a normal hydrogen electrode (NHE) constructed using platinum foil in 0.5 M H_2SO_4 saturated with H_2 (pH 0.4, 22 °C). The disk electrodes were rotated at 2,000 RPM using an electrode rotator (AFMSRCE, Pine Research Instrumentation) to assist in the removal of evolved gasses from the electrode surface. Tafel plot data were obtained by averaging the final 5 s of 10 s galvanostatic measurements. EIS conducted intermittently during ALT was done galvanostatically with a $100 \text{ mA cm}_{\text{geo}}^{-2}$ current at an amplitude of $1 \text{ mA cm}_{\text{geo}}^{-2}$. All potentials were corrected using the uncompensated resistance determined by EIS at 100 kHz at open circuit with a 20 mV amplitude.

4.3 Results & Discussion

4.3.1 Physical characteristics highly-doped Ti_4O_7

The color of the powders prior to compression into a disk suggests that the dopant is incorporated into the TiO_2 , consistent with previous preparations [65]. After compression, sintering, and H_2 reduction, the disks are dark blue in color (Figure 4.1 a), consistent with the preparation of $\text{Ti}_n\text{O}_{2n-1}$. The estimated bulk densities (ρ_{bulk}) of these disks are similar given the masses and dimensions of the samples (parenthetical values indicate uncertainties of final digit): 2.6(2), 3.1(3), 2.7(3), and 2.8(2) g cm^{-3} for pristine, V-, Cr-, and Fe-doped samples, respectively. Considering the true density (ρ) of Ti_4O_7 (4.32 g cm^{-3}) [67], the average porosity (ε , Eq. 4.5) of the samples prior to sealing with molten wax is evaluated to be $35 \pm 4\%$, which is consistent with random close packing [149, 150]. Scanning electron micrographs (Figure 4.1 b–e) illustrate the morphology of the disks typical of monolithic $\text{Ti}_n\text{O}_{2n-1}$ [70]. The disks are composed of micrometer-sized particles, which are fused to one another, as well as many voids and holes, consistent with the predicted porosity. The particles in the doped samples appear to be marginally larger than those in the pristine material. This minor size discrepancy has also been observed in powder preparations [65], where it is speculated that the metal halide in the sol act may act as a peptizing agent.

$$\varepsilon = 1 - \rho_{\text{bulk}}/\rho \quad (4.5)$$

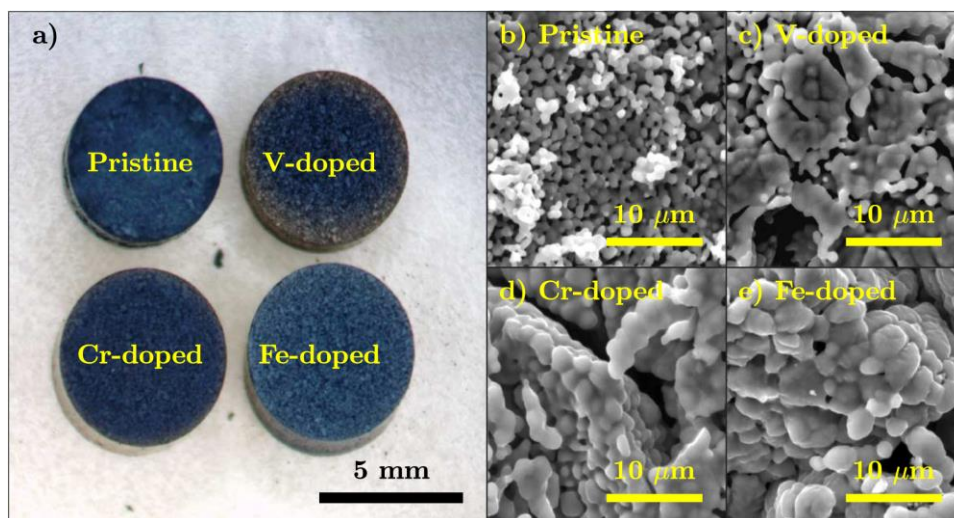


Figure 4.1 (a) Optical image and (b)–(e) scanning electron micrographs (20 kV) of H₂-reduced pristine and nominally 2 at% doped TiO₂ disks. Image reproduced from [66], which permits unrestricted reuse of the work via the Creative Commons Attribution 4.0 License (CC BY, <http://creativecommons.org/licenses/by/4.0/>).

Statistical analysis of the data obtained by EDX spectroscopy and XRF analysis of the H₂-reduced pristine and nominally 2 at% doped TiO₂ disks (Table 4.1) suggests that the dopants are present at approximately 2 at%. EDX spectroscopy results are equivalent or marginally lower than expected values whereas XRF results are equivalent to the expected values. This disparity is attributed to systematic errors in the preparation and storage of the transition metal halide solutions, the quality of the TTIP reagent, and its volatilization during the aging step of the sol-gel process. Attempts to conduct elemental mapping SEM images with EDX spectroscopy were unsuccessful. It is suspected that the accelerating voltage was too high to provide sufficient spatial resolution. Analysis of survey spectra obtained by XPS of the disks (Figure 4.2 a) identifies dopants V and Fe in their respective samples; the presence of Cr dopant could not be unambiguously identified due to the overlap of its 2p peak with the Ti 2s peak. Deconvolution of high resolution spectra of V 2p_{3/2} and Fe 2p_{3/2} peaks (Figure 4.2 b & c) suggests that the oxidation states are V^{III}/V^{IV} and

Fe^{II}/Fe^{III}. And while earlier-reported analysis of structural refinement of PXRD data suggested the presence of a metallic iron phase in Fe-doped Ti₄O₇ [65], deconvolution of the Fe 2p_{3/2} peak does not provide support of this postulation. Deconvolution of the Ti 2p and O 1s peaks (Figure A.3.1, Table A.3.1, Table A.3.2, Table A.3.3, Table A.3.4, & Table A.3.5) suggests that Ar ion etched surface is reduced relative to unetched materials. It is unclear, however, whether this is representative of the underlying material or the result of Ar ion damage to the surface. Nobel gas ion bombardment is reported to reduce surfaces of TiO₂ due to a preferential etching of oxygen [151, 152]. Valence band spectra of Ar ion etched samples (Figure A.3.2) reveal the presence of surface states above the valence band, consistent with the reduction of TiO₂ by Ar ion etching.

Dopant	Concentration (at%)	
	EDX	XRF
Vanadium	1.6 ± 0.1	2.0 ± 0.4
Chromium	1.5 ± 0.1	2.1 ± 0.3
Iron	2.4 ± 0.4	2.0 ± 0.4

Table 4.1 Summary of statistical analysis (5 observations, 5% significance level) of energy-dispersive X-ray (EDX) spectroscopy and X-ray fluorescence (XRF) of dopant in H₂-reduced pristine and nominally 2 at% doped TiO₂ disks.

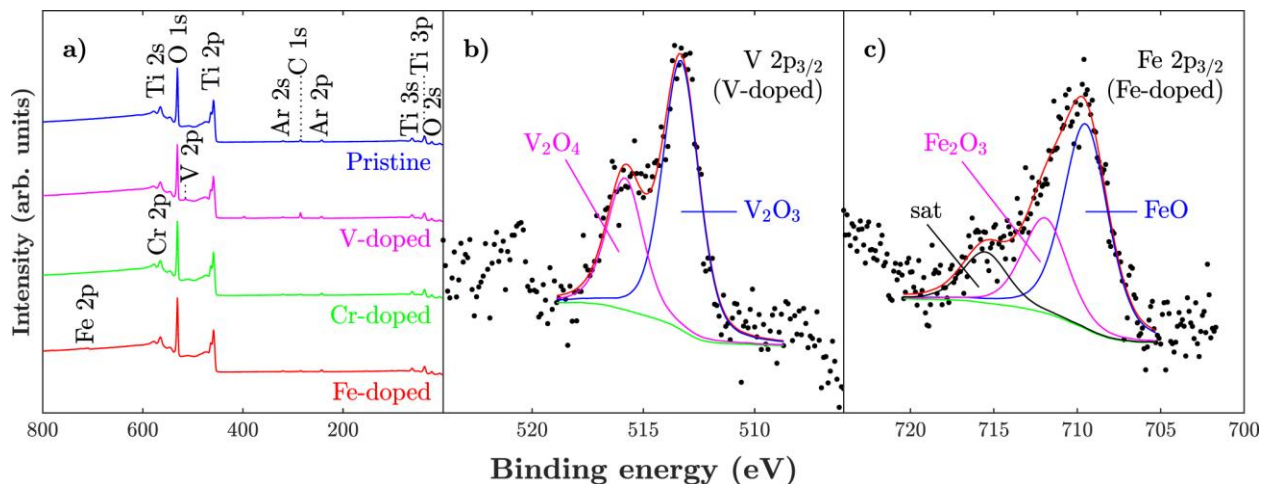


Figure 4.2 X-ray photoelectron spectra of Ar-ion etched (4 keV) H₂-reduced pristine and nominally 2 at% doped TiO₂ disks: (a) survey spectra and high resolution spectra of (b) V 2p and (c) Fe 2p peaks. Image reproduced from [66], which permits unrestricted reuse of the work via the Creative Commons Attribution 4.0 License (CC BY, <http://creativecommons.org/licenses/by/4.0/>).

Phase identification analysis of the patterns obtained by PXRD (Figure 4.3) provides evidence to suggest that the H₂-reduced pristine and doped TiO₂ disks are monophasic Ti₄O₇. Specifically, a pattern typical of Ti₄O₇ can be seen with intense peaks at 20.8° and 31.8° 2 theta. The presence of a subtle broad peak in the baseline can be attributed to the specimen holder given the small amount of sample used (~200 mg). The absence of peaks at 23.8° and 22.0° 2 theta indicative of Ti₃O₅ and Ti₅O₇, respectively [44, 65], is also noted, suggesting the absence of adventitious Magnéli phases other than Ti₄O₇ in the pristine and Fe-doped samples. There appears to be a minor adventitious phase present in the V- and Cr-doped samples as indicated by peak assigned to Ti₃O₅ (COD 4 512 563, Table A.3.6) [153]. The patterns were poorly indexed with an earlier reported structure of Ti₄O₇ [67], which was later revised by the authors [115] and nearly identical to the

structure of 0.25% V-doped Ti_4O_7 (COD 1 008 048, Table A.3.7) [116], which was used for comparison. The absence of additional crystalline phases in the nominally 2 at% doped materials suggests that the dopant must therefore be uniformly distributed within the Ti_4O_7 phase, consistent with earlier preparations [65]. This work also conducted a structural refinement study concluding that the crystal structure is not modified significantly by doping.

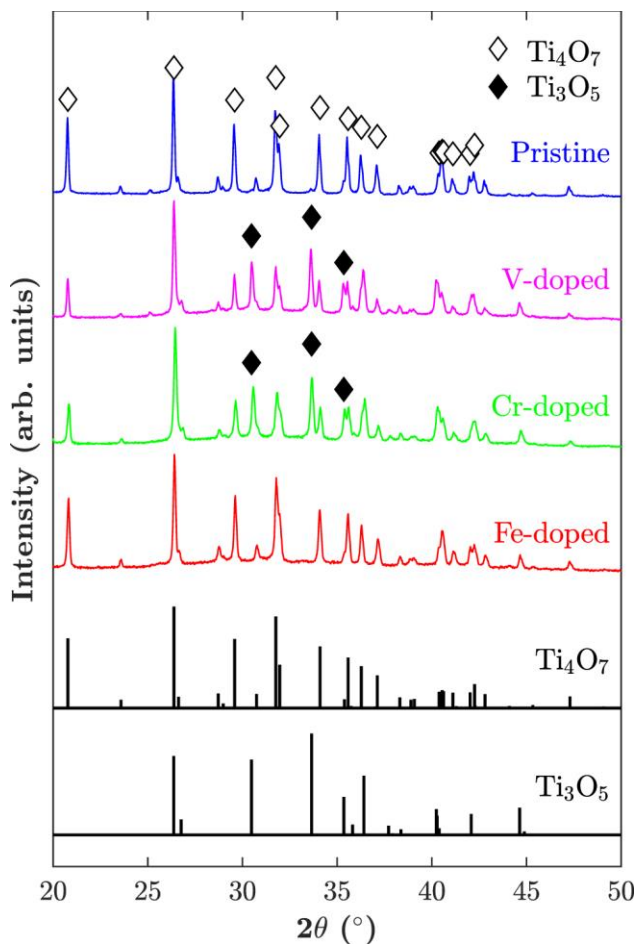


Figure 4.3 Powder X-ray diffraction patterns (1.5406 Å) of ground H_2 -reduced pristine and nominally 2 at% doped TiO_2 disks, which are well-indexed with Ti_4O_7 (empty diamonds, COD 1008048) along with a minor adventitious phase attributed to Ti_3O_5 (filled diamonds, COD 4512563) in the V- and Cr-doped samples. Image reproduced from [66], which permits unrestricted reuse of the work via the Creative Commons Attribution 4.0 License (CC BY, <http://creativecommons.org/licenses/by/4.0/>).

4.3.2 V- and Fe-doping improve electrical conductivity

V- and Fe-doped Ti_4O_7 samples exhibit significantly greater electrical conductivities (σ , Table 4.2) than pristine samples as determined from resistances measured by the 4-point probe method [148]. The electrical conductivities of pristine samples are approximately an order of magnitude lower than single-crystal measurements ($1,300\text{--}1,900 \text{ S cm}^{-1}$) [30]. The relatively lower electrical conductivity is attributed to the preponderance of grain boundaries in the samples as well as porosity (*vide supra*). However, these electrodes have conductivities comparable to nonpermeable grade Ebonex® electrodes ($100\text{--}1,000 \text{ S cm}^{-1}$) [13], the trade name for $\text{Ti}_n\text{O}_{2n-1}$ -based electrodes, and are approximately an order of magnitude greater than monolithic Ti_4O_7 reactive electrochemical membranes (REMs, $11.32\text{--}13.49 \text{ S cm}^{-1}$) [154, 155]. As the pristine and doped samples are morphologically similar, the superior electrical conductivities demonstrated by V- and Fe-doped samples are attributed to the presence of their respective dopants. Schlenker *et al.* observe a variation in the electrical resistivity of V-doped Ti_4O_7 , with the highest doped (1.64 at%) sample investigated being the least resistive [134]. The authors suggest that vanadium contributes little to the scattering of charge carriers due to the already large concentration of scattering centers in the pristine material. As the carrier mobility is likely unaffected, it is postulated that the superior electrical conductivity of these materials must therefore be due to an increase in the carrier concentration. While Gusev *et al.* observe a relatively diminished electrical conductivity in V- (1.5 wt% V_2O_5) and Fe-doped (1.36 wt% Fe) $\text{Ti}_n\text{O}_{2n-1}$ [51], these samples contain multiple phases, whose electrical conductivities also vary considerably [30].

Dopant	$\log_{10}(\sigma/S \text{ cm}^{-1})$
None	2.08 ± 0.19
Vanadium	2.58 ± 0.10
Chromium	2.30 ± 0.12
Iron	2.51 ± 0.07

Table 4.2 Summary of statistical analysis (5 observations, 5% significance level) of electrical conductivities (σ) of pristine and doped Ti_4O_7 disks.

4.3.3 Electrocatalytic behavior for water splitting reactions unaffected by doping

Cyclic voltammograms of pristine and doped Ti_4O_7 disk electrodes in 0.5 M H_2SO_4 is typical of $\text{Ti}_n\text{O}_{2n-1}$ -based electrodes (Figure 4.4). Pristine and doped Ti_4O_7 disk electrodes show a wide potential window of >3 V as measured by the onset potential for anodic and cathodic currents unambiguously attributable to the OER and the hydrogen evolution reaction (HER), respectively. For this qualitative metric, potentials at current densities of $\pm 10 \text{ mA cm}_{\text{geo}}^{-2}$ were chosen; however, this methodology is highly varied in literature, including the use of different linear potential scan rates, current densities, supporting electrolyte, and supporting electrolyte concentration. The wide potential window of $\text{Ti}_n\text{O}_{2n-1}$ -based electrodes is due to their poor electrocatalytic properties for the OER and HER [11], requiring large overpotentials—most markedly for the OER. The potential window for the Fe-doped sample is the largest, suggesting that dopant incorporation is inhibiting its electrocatalytic behavior toward the water splitting reactions with greater overpotentials required for both. Cathodic and anodic peaks found at negative potentials in the CVs are attributed to reduction and oxidation of the Ti_4O_7 film, consistent with the behavior of Ebonex® electrodes

[70]. At potentials greater than these peaks, there is an absence of prominent redox features with the exception of the Fe-doped sample, whose CV shows a small plateau around 2 V (vs NHE). It is speculated that this feature may be due to the oxidation of the electrode surface. This oxidation may also contribute to the passivation of the Fe-doped electrode explaining the relatively large overpotential for the OER due to a reduced electrochemically-active surface area (ECSA). The ECSA can be estimated based on the charging current in a region of the voltammogram devoid of prominent redox features. The ECSA is determined by Eq. 4.6, where I_a and I_c are the anodic and cathodic currents, respectively, at some fixed potential; A_{geo} is the geometric area of the electrode, 0.196 cm^2 ; ν is the linear potential scan rate, 50 mV s^{-1} ; and C_A is the areal capacitance of Ti_4O_7 , $60 \mu\text{F cm}^{-2}_{\text{ECSA}}$ [155, 156]. Based on the charging current between potentials 1 and 2 V (vs NHE), the ECSA of pristine, V-, Cr-, and Fe-doped disks does not significantly differ having estimated values of 17 ± 4 , 10 ± 3 , 14 ± 3 , and $12 \pm 3 \text{ cm}^2_{\text{ECSA}}$ (5 observations, 5% confidence level), respectively. Based on these ECSAs, the electrodes have a roughness factor of 68 ± 24 , which is an order of magnitude lower than similarly-prepared porous Ti_4O_7 electrodes [157], suggesting that the molten wax has filled most of the inner porous structure.

$$\text{ECSA} = \frac{(I_a - I_c)A_{\text{geo}}}{2\nu C_A} \quad (4.6)$$

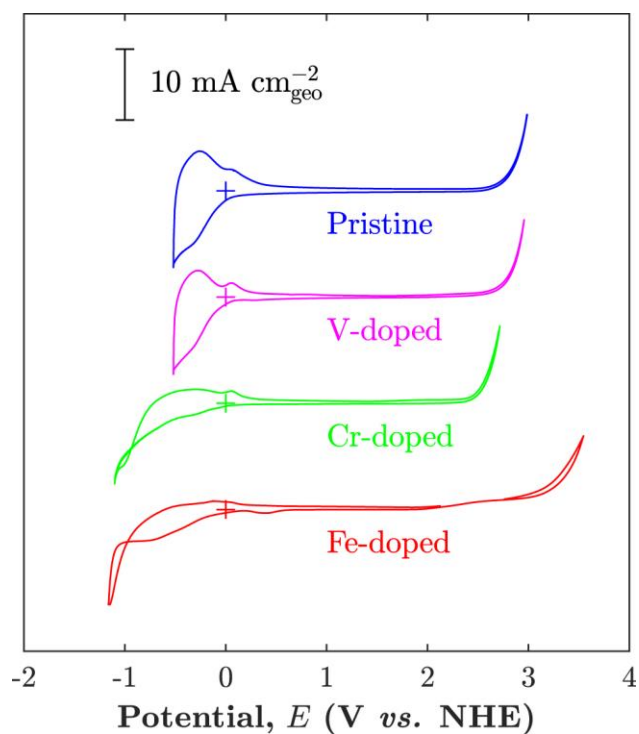


Figure 4.4 Cyclic voltammograms (50 mV s^{-1} , 5th cycle) of pristine and doped Ti_4O_7 disk electrodes (2,000 RPM) in $0.5 \text{ M H}_2\text{SO}_4$ (pH 0.4, $22 \text{ }^\circ\text{C}$). Plus signs (+) indicate origins for their respective plots. Image reproduced from [66], which permits unrestricted reuse of the work via the Creative Commons Attribution 4.0 License (CC BY, <http://creativecommons.org/licenses/by/4.0/>).

Linear regression analysis (Table 4.3) of Tafel plots (Figure 4.5) of pristine and doped Ti_4O_7 disk electrodes in $0.5 \text{ M H}_2\text{SO}_4$ suggests that V- and Cr-doping have a minimal influence on the Tafel behavior of Ti_4O_7 . Assuming that the OER is the exclusive electrochemical reaction at the electrode in $0.5 \text{ M H}_2\text{SO}_4$, Ti_4O_7 is a poor electrocatalyst for the reaction, exhibiting sluggish kinetics as described by a large Tafel slope (b) of $400 \pm 10 \text{ mV dec}^{-1}$ and a small exchange current density (j_0) of $10^{-3.5 \pm 0.4} \text{ mA cm}_{\text{geo}}^{-2}$ or $10^{-4.7 \pm 0.5} \text{ mA cm}_{\text{ECSA}}^{-2}$. This exchange current density is comparable with an estimated value for porous Ti_4O_7 electrodes of $10^{-5.1} \text{ mA cm}_{\text{ECSA}}^{-2}$ based on a reported exchange current density of $3.95 \times 10^{-3} \text{ mA cm}_{\text{geo}}^{-2}$ and a surface roughness of 500

($-\log_{10}(j_0/\text{mA cm}_{\text{ECSA}}^{-2}) = 5.1$) in 0.5 M Na₂SO₄ (25 °C) [157]. This Tafel behavior is observed by pristine Ti₄O₇ up to as high a current density of 100 mA cm_{geo}⁻², after which the Tafel slope increases abruptly. This abrupt change in the Tafel slope at high current density is attributed to the loss of ECSA due to blockage of the electrode surface by considerable evolution of gas. Similar Tafel behavior is also exhibited by V- and Cr-doped Ti₄O₇ with small differences in the Tafel slope and the exchange current density for Cr- and V-doped samples, respectively. Fe-doped Ti₄O₇, however, shows considerably different behavior with significantly different Tafel parameters. Furthermore, the Tafel slope of Fe-doped samples increases abruptly at current densities as low as 20 mA cm_{geo}⁻², rendering it unsuitable for ALT at high current densities (*vide infra*) given the impractically-large overpotentials required.

	b (mV dec ⁻¹)	$-\log_{10}(j_0/\text{mA cm}_{\text{geo}}^{-2})$	$-\log_{10}(j_0/\text{mA cm}_{\text{ECSA}}^{-2})$
Pristine	400 ± 10	3.5 ± 0.4	4.7 ± 0.5
V-doped	460 ± 50	2.5 ± 0.5	3.5 ± 0.6
Cr-doped	350 ± 20	3.4 ± 0.3	4.5 ± 0.4
Fe-doped	860 ± 330	1.0 ± 0.5	2.1 ± 0.6

Table 4.3 Summary of statistical analysis (3 observations, 5% significance level) of fitted Tafel parameters of pristine and doped Ti₄O₇ disk electrodes (2,000 RPM) in 0.5 M H₂SO₄ (0.4 pH, 22 °C). Tafel slope, b , and exchange current density, j_0 , the latter normalized for both geometric and electrochemically-active surface areas (subscripts "geo" and "ECSA", respectively).

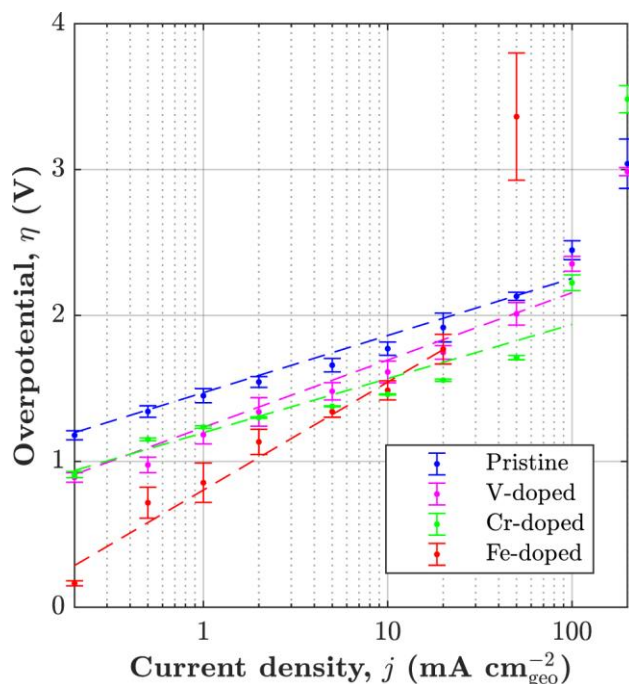


Figure 4.5 Selected Tafel plots of pristine and doped Ti_4O_7 disk electrodes (2,000 RPM) in 0.5 M H_2SO_4 (pH 0.4, 22 °C) for the oxygen evolution reaction. Image reproduced from [66], which permits unrestricted reuse of the work via the Creative Commons Attribution 4.0 License (CC BY, <http://creativecommons.org/licenses/by/4.0/>).

4.3.4 V-doping improves anodic stability

V-doped Ti_4O_7 disk electrodes are more anodically stable as demonstrated by ALT. Selected chronopotentiograms (CPs) of pristine and doped Ti_4O_7 disk electrodes in 0.5 M H_2SO_4 (Figure 4.6) illustrate typical behaviors. Generally, after a short period of conditioning, the electrode potential is $\sim 3\text{--}4$ V (vs NHE), consistent with the overpotential predicted by parameters obtained by fitting Tafel plots (*vide supra*) given the equilibrium potential of 1.2 V (vs NHE). This electrode potential is relatively stable for a period of time, after which the electrode potential increases, suggesting an increase in the resistance of the electrode, which is supported by EIS (*vide infra*). A

mechanism for passivation of Ti_4O_7 is its electrochemical oxidation forming TiO_2 (Eq. 4.7) [71, 91, 72], which is electrically insulating.

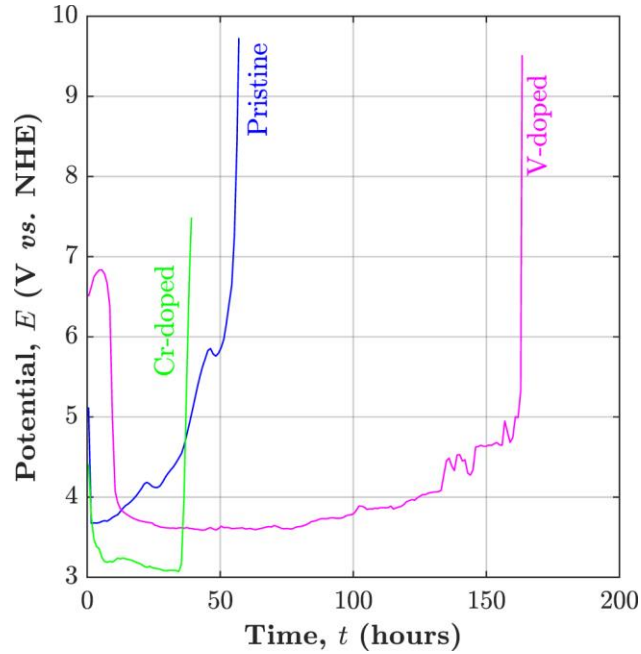
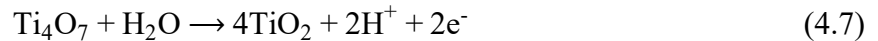


Figure 4.6 Selected chronopotentiograms ($100 \text{ mA cm}_{\text{geo}}^{-2}$) of pristine and doped Ti_4O_7 disk electrodes (2,000 RPM) in $0.5 \text{ M H}_2\text{SO}_4$ (pH 0.4, $22 \text{ }^\circ\text{C}$). Image reproduced from [66], which permits unrestricted reuse of the work via the Creative Commons Attribution 4.0 License (CC BY, <http://creativecommons.org/licenses/by/4.0/>).



The electrode potential continues to increase at an increasing rate until the electrode "fails", indicated by an asymptotic increase to large potential values. From statistical analysis of CPs generated by ALT (Table IV), it can be seen that the TTF for V-doped Ti_4O_7 is 2.57 times that of pristine Ti_4O_7 disk electrodes, which have a TTF of $10^{1.78 \pm 0.06}$ h. Similar to the improved anodic

stability of Ce-doped Ti₄O₇ sintered disk electrodes [61], which provides a 20% improvement in the TTF, it is speculated that V-doping may stabilize oxygen vacancies. Cr-doping, however, is shown to have a 40% reduction in its TTF relative to the pristine material. The influence of Fe-doping on anodic stability was not investigated due to its high overpotential at 100 mA cm_{geo}⁻² and is therefore unclear. However, were these tests conducted at a lower current density such as 20 mA cm_{geo}⁻², one would predict a TTF for V-doped Ti₄O₇ disk electrodes in excess of 3 months (Eq. 4.2, $t = 1.7$), illustrating the challenge in evaluating the stability of Fe-doped Ti₄O₇ disk electrodes using ALT with lower current densities.

	log ₁₀ (TTF/hours)
Pristine	1.78 ± 0.06
V-doped	2.19 ± 0.07
Cr-doped	1.56 ± 0.09

Table 4.4 Summary of statistical analysis (3 observations, 5% significance level) of time-to-failures (TTFs, 100 mA cm_{geo}⁻²) of pristine and doped Ti₄O₇ disk electrodes in 0.5 M H₂SO₄ (pH 0.4, 22 °C).

Nyquist (Figure 4.7) and Bode plot analysis (Figure A.3.3) of impedance data obtained by EIS of pristine, V-, and Cr-doped Ti₄O₇ disk electrodes at the beginning and end of life (BOL and EOL, respectively) reveal insights into the mechanism of passivation. At the BOL, there appears to be 2 time constants in all impedance data as indicated by the two semicircles in the Nyquist plot and the phase (ϕ) being non-zero at frequencies on the order of 10–100 and 10,000 Hz in the Bode plots. As XPS analysis suggests that there is a thin film of TiO₂ on the surface, an equivalent

electrical circuit (EEC) for this system could be a Voigt-type electrical circuit (Figure A.3.4), consisting of a resistor then two Voigt elements in series, a Voigt element being a parallel resistor and capacitor unit. In such an EEC, the resistor expresses the solution resistance, one Voigt element describes the contribution of the thin film of TiO_2 to the circuit, and the other accounts for the charge-transfer resistance and double-layer capacitance. Near the EOL, the pristine Ti_4O_7 disk electrode still appears to have two time constants, though the magnitude of the impedance increases, suggesting an increase in the thin film and charge-transfer resistances. This could be explained by the growth in thickness of the thin film of TiO_2 and loss of ECSA as the electrode passivates. Ebonex® [71] and Ti_4O_7 [158] electrodes are shown to oxidize upon extended anodic treatment as evidenced by X-ray diffractometry, forming Ti_6O_{11} —a Magnéli phase titanium oxide whose electrical conductivity is ~ 500 times lower than that of Ti_4O_7 [30]. The doped Ti_4O_7 disk electrodes at the EOL also have increased impedance, but only one time constant, suggesting that the EEC has converged into a simple parallel resistor and capacitor followed by a resistor in series circuit. As a result, the charge-transfer resistance increases, suggesting that the conditions of the ALT have sufficiently inhibited the electrocatalytic activity of these electrodes for the OER. It is unclear, however, whether this is due to an increase in the resistance of the thin film of TiO_2 , the loss of ECSA, or a combination of the two.

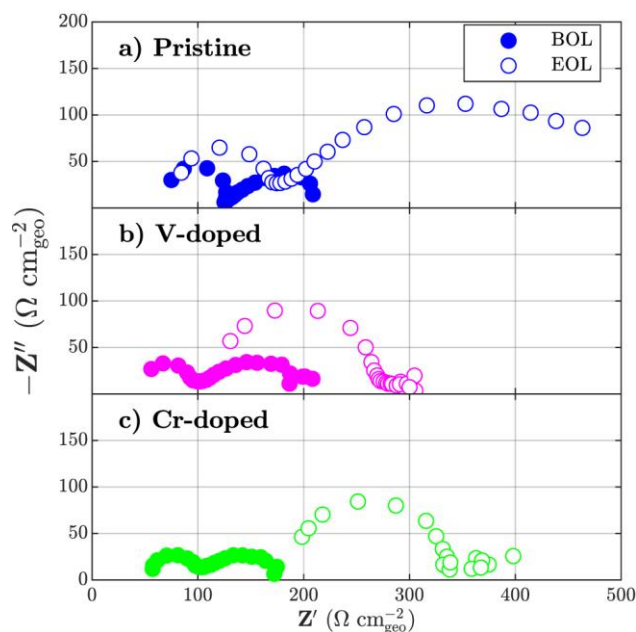


Figure 4.7 Nyquist plots ($100 \pm 1 \text{ mA cm}_{\text{geo}}^{-2}$) of pristine and doped Ti_4O_7 disk electrodes (2,000 RPM) in 0.5 M H_2SO_4 (pH 0.4, 22 °C) at the beginning (BOL, full circles, •) and near the end of life (EOL, open circles, ○) during accelerated life testing. Image reproduced from [66], which permits unrestricted reuse of the work via the Creative Commons Attribution 4.0 License (CC BY, <http://creativecommons.org/licenses/by/4.0/>).

Using the relationship between TTFs for varying current densities (Eq. 4.2), the TTF of pristine, V-, and Cr-doped Ti_4O_7 in 0.5 M H_2SO_4 operating with relatively modest current densities normalized by ECSA can be estimated. Predicted TTFs have the following trend: V-doped > Cr-doped \approx pristine. This trend in the influence of doping on anodic stability is consistent with that reported for thermal stability [65]: V-doped \approx Fe-doped > Cr-doped \approx pristine. If thermal stability is a robust predictor of trends in anodic stability, one would expect that Fe-doped Ti_4O_7 disk electrodes would therefore have anodic stabilities similar to those of V-doped materials. A similar trend is observed in the electrical conductivities, V-doped \approx Fe-doped > Cr-doped \approx pristine, sug-

gesting that it may also contribute to stability. Electrocatalytic behavior for the OER are not considered to be a factor as Tafel parameters describing this behavior do not vary significantly between pristine and vanadium doped materials. For a given current density normalized by ECSA, V-doped Ti_4O_7 shows an improvement of 533% in the TTF relative to pristine Ti_4O_7 , whereas the TTFs of pristine and Cr-doped materials do not vary significantly.

4.4 Summary

$\text{Ti}_n\text{O}_{2n-1}$ -based materials are of growing importance to aqueous electrochemical technologies and developing strategies to tailor their relevant physicochemical properties are needed to address any material shortcomings. As this work demonstrates, V-doping significantly improves the anodic stability of Ti_4O_7 , greatly increasing its time-to-failure as suggested by electrochemical accelerated life testing. Vanadium-doped materials also exhibit improved electrical conductivity, which is conducive to the development of effective high-surface area electrodes such as reactive electrochemical membranes. The use of high-surface area electrodes would allow for high geometric current densities while maintaining relatively modest current densities normalized for ECSA, increasing the time-to-failure. Finally, the use of V-doped $\text{Ti}_n\text{O}_{2n-1}$ -based materials looks promising for use in aqueous electrochemical technologies such as fuel cells, batteries, and devices for the electrochemical treatment of water.

Chapter 5: Vanadium-Doped Ti₄O₇ Porous Transport Layers for Efficient Electrochemical Oxidation of Industrial Wastewater Contaminants

5.1 Introduction

Based on the work described in Chapters 4 & 5, vanadium-doped Ti₄O₇ was chosen to assess its performance as an electrode material for the electrochemical treatment of wastewater. Electrochemical oxidation (EO) is a promising method for the treatment of water and wastewater [159, 4, 12, 160, 161, 162]. Oxidants are generated in situ from matrix constituents, obviating the need for delivery, handling, and storage of hazardous chemicals. Electrochemical cells are modular and therefore easily scaled for use in both centralized and distributed water management systems. Finally, electrochemical devices use electricity, which can be obtained cleanly from renewable and increasingly inexpensive sources of energy such as wind and solar [163]. Still, effective and inexpensive electrode materials and electrochemical cell designs are needed to improve the viability of this approach.

To date, boron-doped diamond (BDD) electrodes have enabled considerable progress in the advancement of EO technologies for the treatment of water and wastewater [33, 34, 35, 36]. BDD exhibits poor electrocatalytic behavior for the electrochemical water splitting reactions, permitting the production of hydroxyl radicals [37], which promote the complete mineralization of organic pollutants [38, 39]. However, due to painstaking nature of chemical vapor deposition methods, thin-film BDD electrodes can be cost prohibitive, exceeding 5,000 USD m⁻² [6] and providing a motivation for the development of inexpensive alternatives.

BDD belongs to a class of electrode materials called high oxidation power (HOP) materials [7], exhibiting overpotentials of ≥ 0.5 V for the oxygen evolution reaction (OER). Other prominent HOP materials are lead(IV) oxide (PbO_2), antimony-doped tin(IV) oxide (ATO), and Magnéli phase titanium oxides (MPTOs, especially Ti_4O_7), the latter also known by the trade name Ebonex® [13, 60, 14]. While issues of lead and antimony toxicity have limited the use of PbO_2 and ATO, the latter also exhibiting poor stability [40], MPTOs are emerging as a viable alternative to BDD. MPTOs are nontoxic [41], excellent electrical conductors whose single-crystal conductivity exceeds $1,000 \text{ S cm}^{-1}$ [30], dimensionally stable in aggressive media such as nitric and hydrofluoric acid [42], and inexpensive at $< 0.5 \text{ USD m}^{-2}$ [6].

Preliminary studies of the EO of wastewater impacted by synthetic organic dyes with MPTO electrodes demonstrate their effectiveness for decolorization and chemical oxygen demand (COD) removal. In particular, azo dyes are important synthetic organic chemicals used primarily in the textile industry. They comprise 50% of the 0.9 million metric tonnes of synthetic dye produced globally per annum [164], 15% of which is estimated to be released into the environment [165]. In addition to aesthetic concerns, azo dyes are suspected human carcinogens [166, 167, 168] and are recalcitrant to natural degradation and conventional treatment methods [169, 170]. Porous Ti_4O_7 electrodes operating at 10 mA cm^{-2} for 2 hours reduced the COD of industrial dyeing and finishing wastewater ($183 \text{ mg}_{\text{COD}} \text{ L}^{-1}$; $1,042 \text{ mg}_{\text{Cl}} \text{ L}^{-1}$) by 68.8% with a current efficiency of 12.8% and an energy consumption of 32 kWh m^{-3} [157]. Monolithic Ti_4O_7 electrodes prepared by spark plasma sintering operating at 10 mA cm^{-2} for 5–6 hours achieved >99% decolorization and 91.7–98.1% COD decay of synthetic wastewater (10–100 mM NaCl) containing the azo dye methyl

orange (MO) (100 mg L^{-1}) [171, 85]. The degradation of MO is attributed to mediated EO via both hydroxyl radicals ($\cdot\text{OH}$) and active chlorine species (*e.g.*, Cl_2 , HClO , and ClO^-). While satisfactory color removal and COD decay are reported, several broadly relevant considerations remain for the design and operation of such electrochemical technologies for wastewater remediation.

Relatively large cell voltages are routinely used and likely due to ohmic losses due to a large inter-electrode gap in conventional cells and high ohmic resistance of the electrolyte. Inter-electrode distances can be reduced by employing a compact cell design [172, 173]. Additionally, activation losses due to electrode passivation leads to the deterioration of performance with time. Ti_4O_7 is shown to oxidize in condition relevant to the EO of wastewater contaminants [72], though periodic cathodic reversal can restore electrode function [64]. Alternatively, doping with cerium [61] and vanadium [65, 66] is shown to improve resilience to passivation of Ti_4O_7 attributed to improved thermodynamic and structural stability [174].

Herein, we report upon our investigation using a compact wastewater electrolyzer for the EO of MO in synthetic wastewater, comparing pristine and vanadium-doped Ti_4O_7 porous transport layers (PTLs). An analytical model describing decolorization and COD removal behavior as well as performance is developed. Relevant design and operational parameters such as the volumetric flow rate, current density, and PTL composition on performance are explored and current efficiency and energy consumption are reported along with removal rates.

5.2 Experimental

5.2.1 Materials

All materials were used as received unless stated otherwise. Rutile titanium(IV) oxide powder (TiO_2 , 99–100.5%, puriss., Sigma Aldrich) was mixed with varying amounts of vanadium(III) oxide (V_2O_3) using a ball mill (8000M Mixer/Mill, SPEX SamplePrep) and zirconia ceramic grinding vial set (8005, SPEX SamplePrep). V_2O_3 was prepared by the reduction of vanadium(V) oxide (V_2O_5 , $\geq 98\%$, Sigma-Aldrich) at $900\text{ }^\circ\text{C}$ for 2 hours in flowing hydrogen (H_2 , HY 5.0UH, 99.999%, Linde) following the method of Piao *et al.* [175]. TiO_2 and $\text{TiO}_2\text{--V}_2\text{O}_3$ mixtures were then mixed with mineral oil (heavy, USP/FCC, Fisher), at 15 wt%. 5 g of these mixtures were then pressed into plates using a 2.54 cm by 2.54 cm square pellet pressing die (EQ-Die-25S, MTI Corporation) and a pressing force of 22 tonnes (430 MPa). The green bodies were then heated at 1,100 for 24 hours in stagnant air. The sintered plates were then reduced at 1,200 for 4 hours in flowing H_2 , which was passed through an oxygen and moisture trap (Supelpure-O, Supelco), forming plates whose thickness were 0.241 ± 0.08 cm (5% significance, 4 observations). A schematic overview is provided in Figure 1a. Electrolyte was prepared by diluting 50 mg of MO ($\text{C}_{14}\text{H}_{14}\text{N}_3\text{NaO}_3\text{S}$, $\geq 95\%$, ACS, Fisher) and 750 mg of sodium chloride (NaCl , 99%, ACS, Fisher) in 500 mL of ultra pure water (UPW, 18.2 $\text{M}\Omega\text{ cm}$), the latter obtained on-demand using a laboratory water system (Milli-Q Integral 5, Millipore).

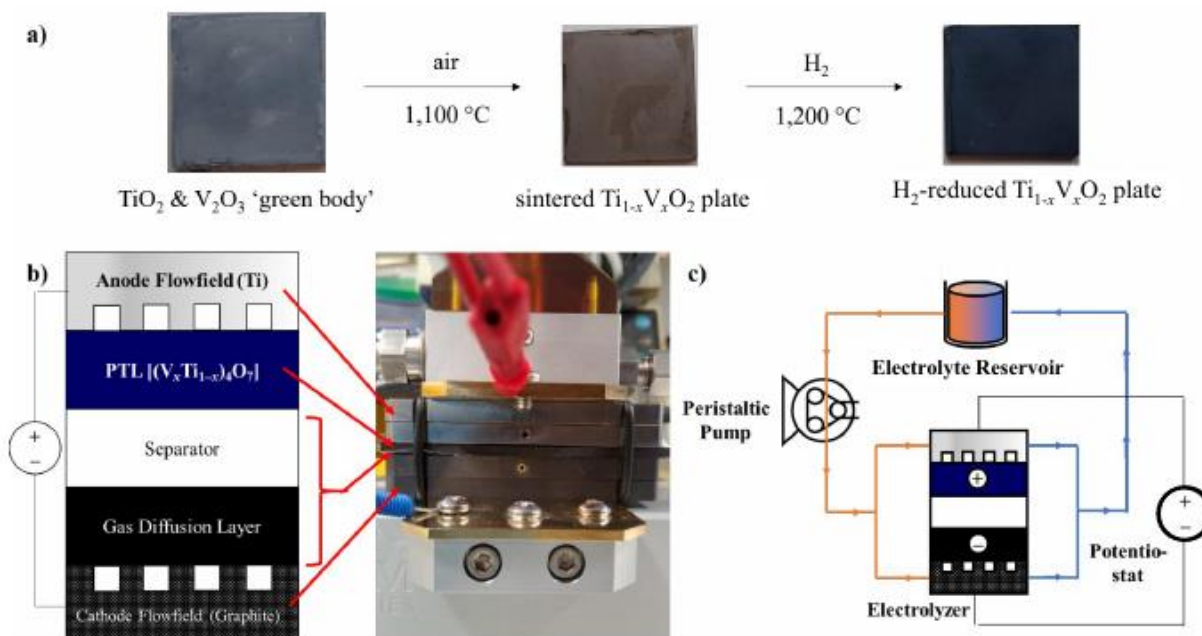


Figure 5.1 (a) Schematic of preparation of a) porous transport layers (PTLs), b) composition and assembly of compact wastewater electrolyzer, and c) its process flow diagram operating in a recirculating batch mode.

5.2.2 Electrode characterization

X-ray diffractograms were obtained using a bench top X-ray diffractometer (Phaser D2, Bruker) with a copper X-ray source (1.5406 \AA) and a silicon strip detector (LYNXEYE, Bruker). In a typical measurement, an electrode was illuminated with radiation from the X-ray source excited at 30 kV with 10 mA passing through a 1.0 mm primary slit module, 2.5° stoller module, and a 0.5 mm nickel filter using as step size of 0.02° and an integration time of 1 s. Phase identification was assisted using the instrument software (DFFRAC.EVA, Bruker) with reference to the Crystallography Open Database (COD) [109]. Reference diffractograms were generated using VESTA crystallography software (ver. 3.4.7) [110] and relevant Crystallographic Information Files (CIFs).

Surface morphology and elemental analysis were obtained using a field emission gun scanning electron microscope (FEI Quanta 650, Thermo Scientific) with an energy dispersive X-ray (EDX) detector accessory (XFLASH 6130, Bruker). All images and EDX spectra were obtained using an accelerating voltage of 20 kV and a working distance of 10 mm. Elemental analysis of EDX spectra was performed using microanalysis software (ESPIRIT, Bruker, ver. 2.1.2). The atomic concentration of vanadium relative to titanium was determined from X-ray fluorescence (XRF) spectra obtained using an energy dispersive X-ray fluorimeter (Fischerscope XDV-SDD, Fischer Technology) equipped with a rhodium X-ray source and a silicon drift detector. In a typical measurement, an electrode was illuminated for 10 s with radiation from the X-ray source excited at 10 kV passing through a 1,000 μm aluminum filter.

Electrical conductivity (σ) was evaluated from resistance data generated using the 4-point probe method with manual 4-point probe resistivity probing equipment (S-302-4, Signatone) and a standard head (SP4-40045TRY, Signatone). In a typical measurement, the head was brought into contact with an electrode and a 1 kHz AC test current with an amplitude of 100 mA was generated using a multi-channel electrochemical workstation (VMP3, BioLogic). The real or in-phase component of the measured impedance (Z') was used to evaluate the electrical conductivity using the reciprocal of the 4-point probe equation for evaluating resistivity (Eq. 5.1) [148] where s is the tip spacing (0.10 cm).

$$\sigma = (2\pi s Z')^{-1} \quad (5.1)$$

5.2.3 Electrochemical measurements

A multi-channel electrochemical workstation (VMP3, BioLogic) was used for all electrochemical measurements. All current densities (j) are reported with respect to geometric area. Electrode potentials were compensated for ohmic drop using the impedance measured at 100 kHz and an amplitude of 20 mV. Electrochemical characterization of the electrode materials was conducted using a conventional 3-electrode cell with a conductive graphite rod (6.35 mm diameter, $0.55 \text{ m}\Omega \text{ sq}^{-1}$, 9121K71, McMaster-Carr) and a saturated calomel electrode (Hg/Hg₂Cl₂/KCl (sat'd), 0.241 V vs. standard hydrogen electrode or SHE, XR110, Radiometer Analytical) as the counter and reference electrodes, respectively. Working electrodes of (Ti_{1-x}V_x)₄O₇ PTLs were constructed by using expanded titanium foil (3Ti4-031, Dexmet) as ohmic connections, sealing all submerged surfaces excluding a circular 2 cm² working area with Kapton film (Dupont). Carbon paper with a micro-porous layer (Sigracet 29 BC, SGL CARBON), which was used as a cathode-side gas diffusion layer (GDL), was characterized by adapting a modified rotating disk electrode technique [176, 177, 178] in a conventional 3-electrode cell.

Wastewater electrolysis was conducted using a commercial 5 cm² research fuel cell (TP5Ev2, Tandem Technologies, New Westminster). Identical titanium anode manifold and flow-field plates were fabricated and used instead of the graphite ones provided. (Ti_{1-x}V_x)₄O₇ PTLs were fashioned into appropriate dimensions and used as PTLs placed within rubber gaskets (neoprene rubber, 1/8 inch or 3.2 mm thick, durometer: 30A, WARCO BILTRITE). Glass fiber filter without binder resin (APFD, 450 m thick, Millipore) was used as a separator. The GDL and separator were bound together using Kapton film. The GDL, separator, and (Ti_{1-x}V_x)₄O₇ PTL were held together between the manifolds and flow-fields under compression at 100 psig or 690 kPa (Figure 5.1 b).

The volumetric flow rate of electrolyte from a reservoir and through the compact wastewater electrolyzer and back to the reservoir in batch re-circulation was controlled using a peristaltic pump (Masterflex L/S 7523-60, Cole-Parmer) with a multi-channel cartridge pump head (Masterflex L/S 7519-10, Cole-Parmer) and cartridges (Masterflex L/S 07519-10, Cole-Parmer) (Figure 5.1 c).

5.2.4 Evaluation of cell performance

5 mL aliquots were removed from a starting volume of 70 mL electrolyte periodically for the purpose of evaluating the performance of the cell. The absorbance of samples at 465 nm (A_{465} , Figure A.4.1 for initial UV-Vis spectrum) diluted with supporting electrolyte to some dilution factor (f) were measured using a UV-Vis spectrophotometer (GENESYS 10S, Thermo Scientific). Decolorization (X_D , Eq. 5.2) was evaluated using the ratio of the product of the absorbance at 465 nm and the dilution factor at some time t and initially (subscripts t and 0, respectively):

$$X_D = 1 - f_t A_{465,t} / (f_0 A_{465,0}) \quad (5.2)$$

Chemical oxygen demand (COD) was determined with COD test vials (0–150 ppm, K-7355, CHEMetrics), using a US EPA-certified dichromate method (410.4, rev. 2) [179]. In short, the absorbance at 445 nm of the vials after 2 hour digestion using a COD reactor (45600-00, Hach) was measured and the concentration of COD (c_{COD}) was determined with reference to standards containing known amounts of potassium hydrogen phthalate (KHP, 100%, ACS, Fisher). The electrolyte was undiluted as its concentration of 1,500 mg_{NaCl} L⁻¹ has a chloride concentration of 910 ppm, which is below 1,000 ppm—the level at which chloride can interfere with the results of

COD test. The extent of COD removal (X_{COD} , Eq. 5.3) was calculated using the ratio of the c_{COD} at some time t and initially (subscripts t and 0, respectively):

$$X_{\text{COD}} = 1 - c_{\text{COD},t}/c_{\text{COD},0} \quad (5.3)$$

Performance metrics of general current efficiency (ϕ , Eq. 5.4), specific energy consumption (E_{SP} , Eq. 5.5), and volumetric energy consumption (or electrical energy per order, E_{EO} , Eq. 5.6) are determined typically [4, 7, 19, 9]:

$$\phi = c_{\text{COD},0}X_{\text{COD}}F/(MQ_V) \quad (5.4)$$

$$E_{\text{SP},i} = -U_{\text{cell}}Q_V(c_{i,0}X_i) \quad (5.5)$$

$$E_{\text{EO},i} = U_{\text{cell}}Q_V[\log_{10}(1 - X_i)] \quad (5.6)$$

Modifications have been made to their usual expressions to accommodate for volumetric charge (Q_V) where F is Faraday's constant ($26.8 \text{ Ah mol}_e^{-1}$), M is a conversion factor arising from stoichiometry ($8 \text{ g}_{\text{COD}} \text{ mol}_e^{-1}$), U_{cell} is the operating voltage of the compact wastewater electrolyzer, i indicates the basis of the energy consumption being one of either decolorization (D) or COD, and $c_{i,0}$ is the initial concentration of the parameter forming the basis of the calculation: one of either $100 \text{ ppm}_{\text{MO}}$ or $145 \text{ mg}_{\text{COD}} \text{ L}^{-1}$.

5.3 Results & Discussion

5.3.1 Porous transport layers are monophasic and highly doped, exhibiting electrochemical behavior typical of Ti_4O_7

Phase identification using diffractograms obtained by XRD (Figure 5.2) suggests that both pristine and vanadium-containing H_2 -reduced TiO_2 sintered plates are predominantly Ti_4O_7 (CIF 1008048) [116]. Peaks attributable to precursors TiO_2 (rutile, CIF 9009083) [117] and V_2O_3 (karelianite, CIF 1011066) [180] are absent from the spectra, suggesting their complete conversion into pristine and vanadium-doped MPTOs. A small feature at 22° can be assigned to the (102) plane of Ti_5O_9 (CIF 539580) [181], suggesting that it may be present as a minor phase, which is typical of Ebonex® electrodes [13, 60].

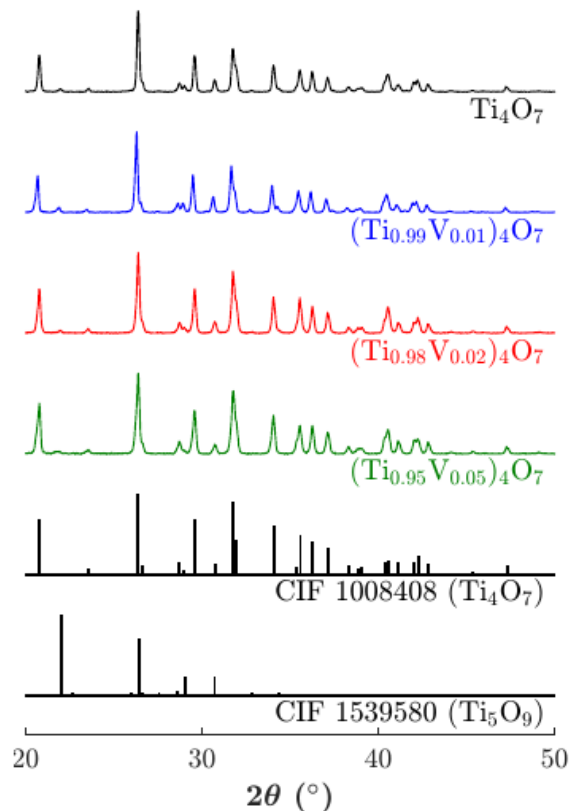


Figure 5.2 X-ray (1.5406 Å) diffraction patterns of H_2 -reduced pristine and nominally 1, 2, and 5 at% doped TiO_2 sintered plates along with idealized patterns for Ti_4O_7 (COD 1008048) and Ti_5O_9 (COD 1539580).

Electron microscopy of $(\text{Ti}_{1-x}\text{V}_x)_4\text{O}_7$ sintered plates ($0 \leq x \leq 0.05$, Figure 5.3 a–d) illustrate their porosity. Their micro-structure consists of 2–3 μm particles fused together forming a distributed network with interstitial voids. Based on geometric and gravimetric analyses and assuming a skeletal density of 4.32 g cm^{-3} [67], the voidage of these sintered plates was $26.6 \pm 1.6\%$ (4 observations, 5% significance level). This is significantly lower than 36% predicted for random close packing [149, 150], suggesting that sintering in the fashion described densifies the material. Elemental mapping of the porous $(\text{Ti}_{1-x}\text{V}_x)_4\text{O}_7$ sintered plates (Figure 5.3 e–g) shows that vanadium is uniformly distributed within titanium, suggesting the absence of discrete vanadium and titanium

oxides, which is consistent with XRD results (*vide supra*). EDX spectroscopy shows that the composition of the porous $(\text{Ti}_{1-x}\text{V}_x)_4\text{O}_7$ sintered plates is consistent with the nominal composition as well as that determined by XRF (Figure 5.3 h).

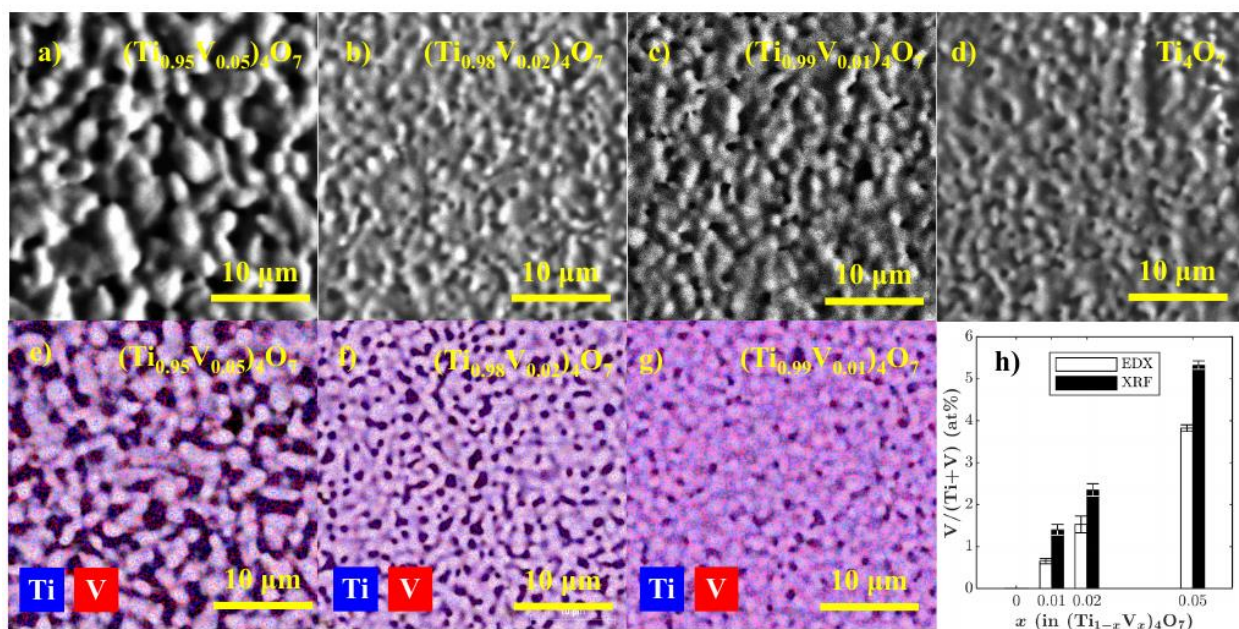


Figure 5.3 a–d) Electron micrographs (20 kV), **e–g)** elemental mapping of titanium (blue) and vanadium (red), and **h)** $\text{V}/(\text{Ti}+\text{V})$ determined by energy dispersive X-ray spectroscopy and X-ray fluorescence (EDX and XRF, respectively) of $(\text{Ti}_{1-x}\text{V}_x)_4\text{O}_7$ ($0 \leq x \leq 0.05$) porous transport layers. Error bars indicate 95% confidence intervals (5 observations).

The $(\text{Ti}_{1-x}\text{V}_x)_4\text{O}_7$ ($0 \leq x \leq 0.05$) PTLs show good electrical conductivity. Samples containing vanadium are significantly more electrically conductive than pristine materials, being 173.3 ± 0.2 , 273.1 ± 0.6 , 511.7 ± 1.4 , and $412.1 \pm 2.4 \text{ S cm}^{-1}$ (5 observations, 5% significance level) for $x = 0, 0.01, 0.02$, and 0.05 , respectively (in $(\text{Ti}_{1-x}\text{V}_x)_4\text{O}_7$). These conductivities would yield voltage drops of less than 0.1 mV for the current densities employed by this study. This trend is consistent

with an earlier reported preparation using doped precursors obtained by a sol-gel method [66]. The superiority of the electrical conductivity of $(\text{Ti}_{1-x}\text{V}_x)_4\text{O}_7$ for $x > 0$ is attributed to the presence of vanadium, whose increasing concentration in Ti_4O_7 is observed to reduce its electrical resistivity [134]. Compared with our previous report [66], a further improvement in the electrical conductivity of the materials used currently is attributed to a longer time and higher temperature of sintering, which is expected to improve fusion between grains and therefore decrease the electrical resistance between particles. Values of electrical conductivity are still less than those observed for single-crystal measurements of Ti_4O_7 : 1,000–2,000 S cm^{-1} [30]. This may be attributed to the presence of voids, whose greater preponderance is concomitant with increasing resistivity as predicted by percolation theory [182]. The Ti_5O_9 phase, which is approximately half as electrically conductive as Ti_4O_7 [30], may also slightly lower the electrical conductivity as described by the general effective medium equation [183].

The electrochemical behavior of $(\text{Ti}_{1-x}\text{V}_x)_4\text{O}_7$ ($0 \leq x \leq 0.05$) PTLs (Figure 5.4) is typical of Ti_4O_7 . The electrodes show a marked increase in the current at high potentials, which is consistent with the high overpotential for the OER of Ebonex® electrodes [11]. A large overpotential for the hydrogen evolution reaction is also observed at low potentials. Nearby redox features if present can be attributed to either the reduction and oxidation of the surface [70] or the insertion and deinsertion of protons into interior channels [184]. Relative to pristine Ti_4O_7 PTLs, vanadium-doped Ti_4O_7 PTLs exhibit markedly larger capacitive currents, masking these redox features and suggesting a greater electrochemically-active surface area (ECSA). It is suspected that the pristine Ti_4O_7 has a greater proportion of electrically-insulated and therefore electrochemically-inactive material as suggested by the observed trend in electrical conductivity (*vide supra*). It is unlikely that surface

wettability is an important factor as electrolyte is observed to be rapidly absorbed by all PTLs when dry.

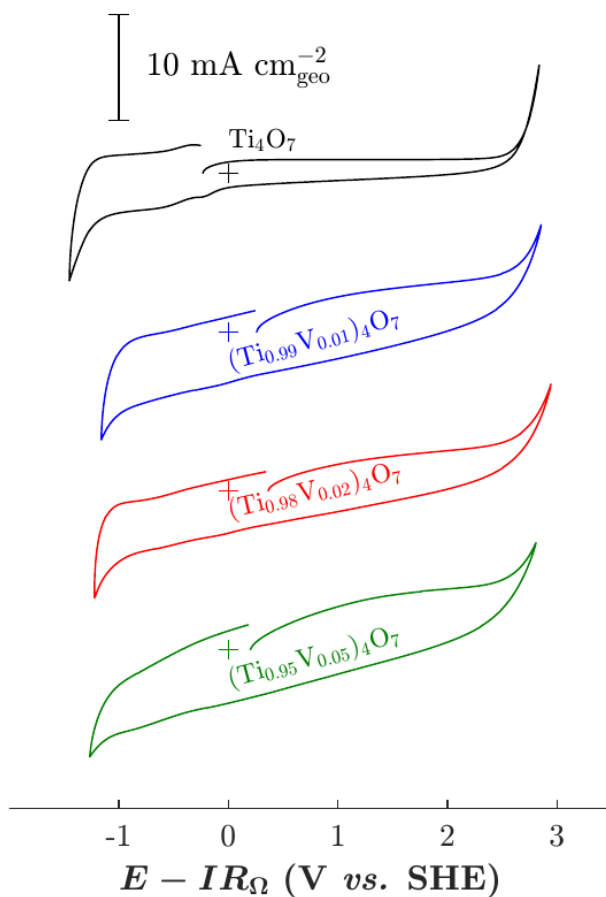


Figure 5.4 Cyclic voltammograms (100 mV s^{-1} , tenth cycle) of $(\text{Ti}_{1-x}\text{V}_x)_4\text{O}_7$ ($0 \leq x \leq 0.05$) porous transport layers in $1,500 \text{ mg}_{\text{NaCl}} \text{ L}^{-1}$ (22, pH 5.3). Plus signs (+) indicate origins of their respective plots.

5.3.2 Compact wastewater electrolyzer exhibits mass-transport controlled behavior

The current-voltage characteristics of the compact water electrolyzer are poor relative to water electrolyzers for hydrogen production (Figure 5.5). Over a range of $0.1\text{--}10 \text{ mA cm}^{-2}$, the cell volt-

age in supporting electrolyte increases from that near the equilibrium cell potential for the electrolysis of water, 1.23 V, to that approaching 5 V. As discussed earlier, Ti_4O_7 as well as $(\text{Ti}_{0.98}\text{V}_{0.02})_4\text{O}_7$ are poor electrocatalysts for the water splitting reactions including the OER [66, 11]. Additionally, the cathode compartment is composed of a carbon-based GDL, which exhibited modest catalytic behavior towards the complementary water splitting reaction (Figure A.4.2). As a result, a considerable overpotential is required for a current to pass at both electrodes as the current-voltage characteristics over this range of current densities are likely determined by these activation losses.

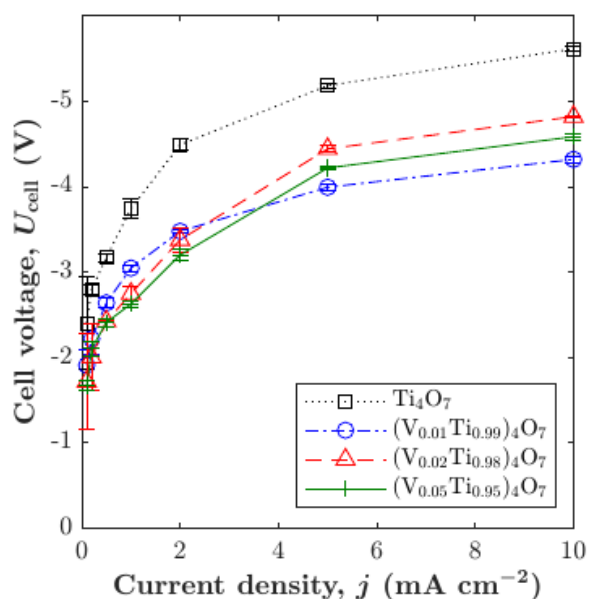
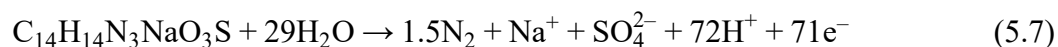


Figure 5.5 Current-voltage behavior of the compact wastewater electrolyzer with $(\text{Ti}_{1-x}\text{V}_x)_4\text{O}_7$ ($0 \leq x \leq 0.05$) porous transport layers in $1,500 \text{ mg}_{\text{NaCl}} \text{ L}^{-1}$ ($22 \text{ }^\circ\text{C}$, $\text{pH } 5.3$). Error bars indicate 95% confidence intervals (5 observations).

As a baseline case, $(\text{Ti}_{0.98}\text{V}_{0.02})_4\text{O}_7$ is observed to be an effective anode for the EO of MO, rapidly de-colorizing and removing COD (Figure 5.6 a). Using a current density of 10 mA cm^{-2} and an electrolyte flow rate of 200 mL min^{-1} , $>99\%$ decolorization is achieved between $0.5\text{--}1.0 \text{ Ah L}^{-1}$ and $>98\%$ COD removal at $1.5\text{--}2.0 \text{ Ah L}^{-1}$. Wang *et al.* have proposed that MO in similar conditions is oxidized by the mix of hydroxyl radicals and active chlorine species (ACS) such as molecular chlorine (Cl_2), hypochlorous acid (HClO), and hypochlorite (ClO^-) [85]. These chemical oxidants first attack the chromophore at or near its azo bond ($-\text{N}=\text{N}-$), leading to decolorization followed by subsequent oxidation of intermediates as expressed by further COD removal (Eq. 5.7).



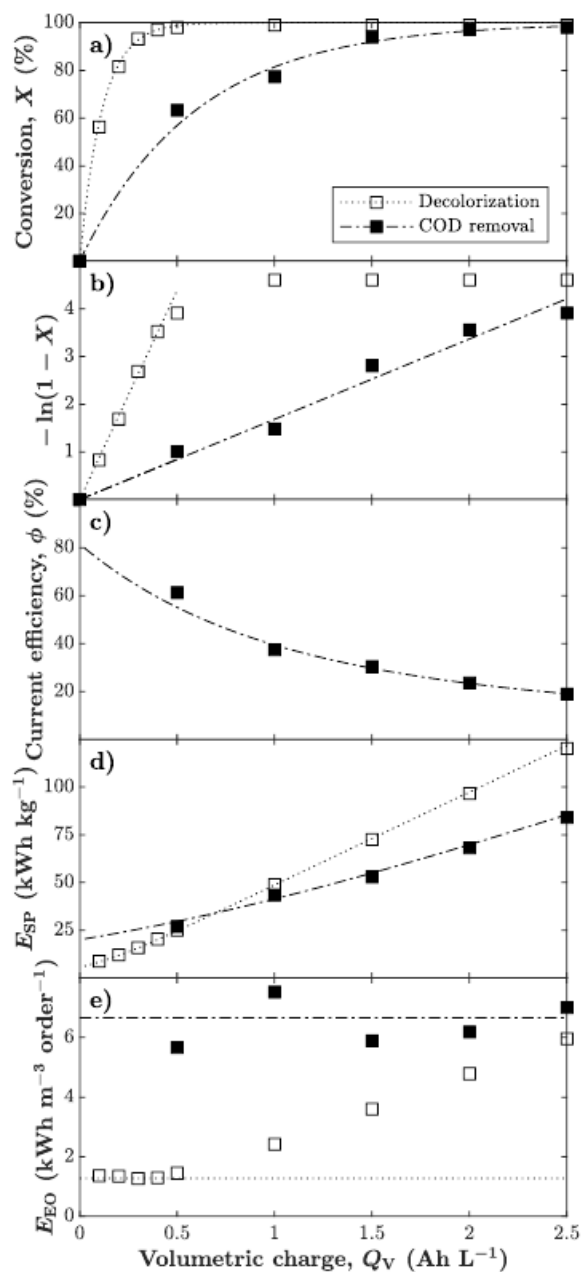


Figure 5.6 a) Conversion (X), b) linearized conversion data ($-\ln(1 - X)$), c) current efficiency (ϕ), d) specific and e) volumetric energy consumption (E_{SP} & E_{EO} , respectively) for the decolorization and chemical oxygen demand (COD) removal (empty and filled symbols, respectively) of 100 ppm_{MO} in 1,500 g_{NaCl} (200 mL min⁻¹, 21 °C, pH 4.0) with a (Ti_{0.98}V_{0.02})₄O₇ porous transport layer in a compact electrolyzer operated galvanostatically (10 mA cm⁻², 200 mL min⁻¹). Dotted and dash-dotted lines indicate either lines of best fit (a & b) or model predictions (c–e, Eqs. 5.10,) for decolorization and COD removal, respectively.

Between 0–0.5 and 0–2.5 Ah L⁻¹, decolorization and COD removal, respectively, appear to behave as if under mass transport control. Such systems can be described with an analytical model (Eq. 5.8)

$$X_i = 1 - \exp(-k_{m,i}Q_V/j) \quad (5.8)$$

where $k_{m,i}$ is the apparent mass transfer coefficient for species i : one of either decolorization or COD removal. This analytical model can be linearized (Eq. 5.9), facilitating the regression analysis of linearized data.

$$-\ln(1 - X_i) = (k_{m,i}/j)Q_V \quad (5.9)$$

A strong linear correlation between the volumetric charge and the linearized conversion data is observed (Figure 5.6 b) as expressed by its coefficient of determination or R^2 value of 0.9974 and 0.9730 for decolorization and COD removal, respectively. An apparent mass transfer coefficient of 244 ± 8 and $46.8 \pm 5.1 \mu\text{m s}^{-1}$ (5% significance) again for decolorization and COD removal, respectively, is obtained from the fitting. At values greater than 0.5 Ah L⁻¹, the linearized decolorization data deviates from the fitted model. The data trends asymptotically towards the limit of detection of the instrumental assays, which are values of 99 and 98% for decolorization and COD removal, respectively. Current efficiency decreases at a decreasing rate with increasing volumetric charge (Figure 5.6 c), which can be predicted by combining Eqs. 5.4 & 5.8 (Eq. 5.10):

$$\phi = \left(\frac{c_{\text{COD},0}F}{MQ_V} \right) [1 - \exp(-k_{\text{m,COD}}Q_V/j)] \quad (5.10)$$

Likewise, specific and volumetric energy consumption can be predicted by the combination of Eqs. 5.5 & 5.8 (Eq. 5.11) and Eqs. 5.6 & 5.8 (Eq. 5.12), respectively (Figure 5.6 d & e):

$$E_{\text{SP},i} = \frac{-\bar{U}_{\text{cell}}Q_V}{c_{i,0}[1 - \exp(-k_{\text{m},i}Q_V/j)]} \quad (5.11)$$

$$E_{\text{EO},i} = -\ln(10) \bar{U}_{\text{cell}}j/k_{\text{m},i} \quad (5.12)$$

where \bar{U}_{cell} is the mean operating cell voltage (-4.87 V). An interesting result of this analysis is that volumetric energy consumption is independent of volumetric charge and remains constant during electrolysis. Volumetric energy consumption is observed to be 1.35 ± 0.09 and 6.45 ± 0.97 kWh m⁻³ order⁻¹ for decolorization and COD removal, respectively. The latter value is approximately an order of magnitude lower than for the treatment of industrial dye and finishing wastewater which is estimated to be 63 kWh m⁻³ order⁻¹ based on provided data [157]. Using the model (Eq. 5.12), predicted values are 1.28 and 6.66 kWh m⁻³ order⁻¹ for decolorization and COD removal, respectively, which is in agreement with the observed values. The model provides a good fit of the data with current density and energy consumption for galvanostatic operation being adequately described for a system under mass transport control.

5.3.3 Flow rate, current density, and PTL composition have varying influence on performance

It can be seen that volumetric flow rate, current density, and PTL composition have a varying influence on the mass transfer coefficients governing decolorization and COD removal (Figure 5.7 a–c & Figure A.4.3–Figure A.4.12). Generally, over the range of 150–250 mL min⁻¹ increasing the flow rate may increase the mass transfer coefficient (Fig. 7a). The values at 250 mL min⁻¹ are significantly larger than those at 150 mL min⁻¹. Linear regression of the data, however, is less definitive in establishing a correlation between volumetric flow rate and mass transfer coefficient at a significance level of 5% as p-value for the slope and intercept are greater than 0.05. Lower flow rates were considered, however the cell voltage became less stable, which is attributed to poorer detachment of bubbles generated from the electrochemical water splitting reactions. 250 mL min⁻¹ was the upper limit due to the capacity of the pump. Nonetheless, it is expected that increasing the volumetric flow rate would increase the mass transfer coefficient given the dimensionless group correlations for electrochemical flow cells (Eq. 5.13) [19]:

$$\text{Sh} = a\text{Re}^b\text{Sc}^c \quad (5.13)$$

where Sh, Re, and Sc are the Sherwood, Reynolds, and Schmidt dimensionless numbers, respectively, and a , b , and c are coefficients derived from data fitting. Using the definitions of the Sherwood number, $k_m\ell/D$, where ℓ is some characteristic length and D is the diffusion coefficient and Reynolds number, $\dot{V}\ell/(A_c\nu)$, where \dot{V} is the volumetric flow rate, A_c is the cross-sectional area and ν is the kinematic viscosity of the fluid, a partial derivative of the dimensionless group correlation

(Eq. 5.14) with respect to volumetric flow rate can be taken. It is then seen that the rate of change in the mass transfer coefficient with increasing volumetric flow rate is positive (Eq. 5.14, $b > 0$):

$$\frac{\partial k_m}{\partial \dot{V}} \propto \dot{V}^{b-1} \quad (5.14)$$

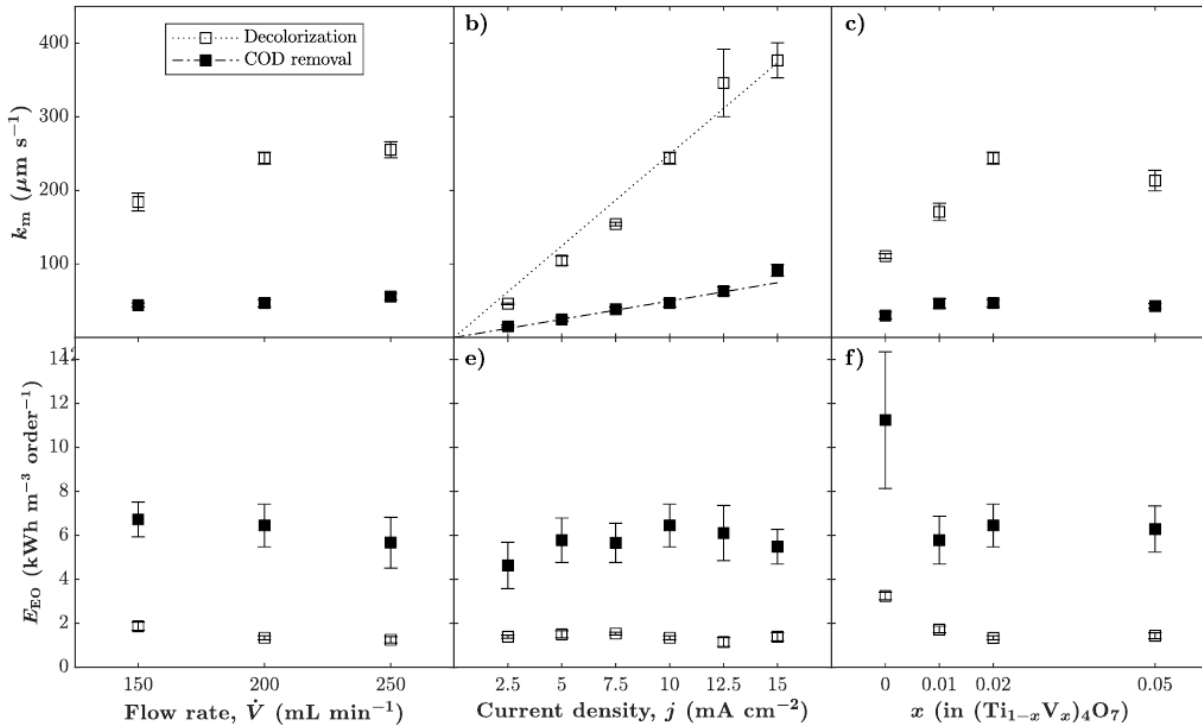


Figure 5.7 a)–c) Mass transfer coefficients (k_m) and d)–f) volumetric energy consumption (E_{EO}) for decolorization and COD removal (empty and filled markers, respectively) of 100 ppm_{MO} in 1,500 mg_{NaCl}. Unless otherwise stated, the flow rate, current density, and x (in $(\text{Ti}_{1-x}\text{V}_x)_4\text{O}_7$) are 200 mL min⁻¹, 10 mA cm⁻², and 0.02, respectively. Error bars indicate 95% confidence intervals derived from parameter fitting of linear-regressed data to analytical models.

There is a much clearer linear correlation between current density and mass transfer coefficient (Figure 5.7 b), reaching values as high as 377 ± 24 and $91.3 \pm 8.2 \text{ m s}^{-1}$ at 15 mA cm^{-2} for decolorization and COD reduction, respectively. Linear regression analysis gives a coefficient of variance of 0.9470 and 0.9802 for decolorization and COD removal, respectively. This relationship can be explained by observing that increasing current density increases the rate of gas evolution, which enhances the local mixing at the surface of the electrode and therefore mass transfer to it. As the mass transfer coefficient and current density show a strong linear correlation, the current efficiency (Eq. 5.10) is not expected to change appreciable as k_m/j is effectively constant. Specific and volumetric energy consumption (Eqs. 5.11 & 5.12), however, are expected to increase as the cell voltage increases (*cf.* Figure 5.5). Furthermore, as current densities approach 15 mA cm^{-2} , the cell potential began to exceed 5 V with voltages also became less stable likely due to oxidation of the PTL and other components of the cell. Higher current densities were therefore not investigated.

Finally, vanadium-doped Ti_4O_7 PTLs generally exhibit higher mass transfer coefficients than the pristine materials with a maximum value observed at concentrations of ≥ 2 at% (Figure 5.7 c). This may be explained by the improved ECSA of vanadium-doped Ti_4O_7 , which in turn makes available a greater ECSA at which species can be oxidized.

Volumetric energy consumption is observed to be significantly influenced only by PTL composition (Figure 5.7 d–f & Figure A.4.3–Figure A.4.12), specifically comparing pristine and vanadium-doped Ti_4O_7 . Increasing volumetric flow rate was expected to decrease the energy consumption due to enhanced mass transport, but was not observed to be the case (Figure 5.7 d) due to the confidence interval being greater than the anticipated change. Increasing current density was

expected to increase energy consumption due to a greater cell voltage caused by greater activation losses, but was also not observed again due to larger confidence intervals (Figure 5.7 e). With pristine Ti_4O_7 PTLs, it is seen that its volumetric energy consumption of 3.25 ± 0.17 and $11.2 \pm 3.1 \text{ kWh m}^{-3} \text{ order}^{-1}$ for decolorization and COD removal is significantly greater than the other conditions investigated (Figure 5.7f). This is attributed to its significantly lower mass transfer coefficient, which in turn is attributed to lower ECSA. Current efficiency is not observed to be considerably influenced by volumetric flow rate, current density, and PTL composition. This is also observed to be the case with specific energy consumption with the exception of pristine Ti_4O_7 PTLs whose values are 25–33% greater than vanadium-doped Ti_4O_7 PTLs. A sampling error in the pristine Ti_4O_7 PTLs likely explains the appearance of a linear trend in the volumetric energy consumption data not explained by theory (*viz.* Eq. 5.12).

5.4 Conclusions

A compact wastewater electrolyzer using pristine and vanadium-doped Ti_4O_7 porous transport layers has been characterized and evaluated for the treatment of synthetic wastewater containing an organic dye. Complete decolorization and chemical oxygen demand removal are observed, the latter at nearly an order of magnitude lower volumetric energy consumption than comparable reports. An analytical model was developed showing excellent agreement with the experimental data and extended to predict relevant figures of merit. Increasing flow rate and current density increase the apparent mass transfer coefficients. Vanadium-doped Ti_4O_7 porous transport layers generally performed better than pristine as attributed to their relatively greater electrochemically-active surface area and improved anodic stability.

Minimal gap electrolyzers can electrolyze wastewater effectively while being energy efficient, incorporating inexpensive vanadium-doped Ti_4O_7 porous transport layers—a difficult architecture for thin film boron-doped diamond electrodes. Performance is increased by enhancing mass transport with the use of high surface-area electrodes as well as reducing cell potentials by decreasing inter-electrode distances. Current efficiency and cell potential could further be improved by utilizing ion-exchange membranes, which can reduce inefficiencies caused by the undesired reduction of oxidized species such as radicals and active chlorine species and assist the electrochemical oxidation of industrial wastewater contaminants.

Chapter 6: Conclusions & Recommendations

6.1 Conclusions

This study investigated the rational selection of dopants for Magnéli phase titanium oxides, their influence on properties relevant to their application as high oxidation potential electrodes, and their performance in an application-specific electrochemical cell design for the treatment of industrial wastewater. The rational selection of dopants was carried out using the Hume-Rothery rules for solid substitutional solutions. The relevant properties—electrical conductivity, stability, and electrochemical behaviour—were investigated using 4-point probe measurements, thermogravimetric analysis and electrochemical accelerated life testing, and analysis of wastewater electrolysis, respectively. These studies demonstrate:

- Vanadium, chromium, and iron are good candidates for highly-soluble dopants in Ti_4O_7 . X-ray diffraction study of doped materials up to 2 at% for chromium and iron and up to 5 at% vanadium suggest that phase separation is absent from these materials. Elemental mapping of these materials also suggest that the dopant materials are uniformly distributed in the host lattice. Therefore, these transition metals, and likely many others as the growing literature suggests, provide a rich library of additives that can be used to modify these materials.
- Electrical conductivity is improved 2–3 fold fold upon doping up to a maximum ~2 at% with vanadium as evidenced by 4-point probe measurement. It has been advanced in the

literature that the presence of dopants stabilizes oxygen vacancies in Magnéli phase materials such as with Ce in Ti_4O_7 [61]. Oxygen vacancies are a charge carrier in semiconductor materials such as TiO_2 . Another possible explanation from this study is that doped materials are oxidatively more stable minimizing passivation.

- Thermal stability is improved by doping with vanadium and iron as evidenced by thermal gravimetric analysis. Specifically, the onset temperature for oxidation of 2 at% vanadium and iron doped Ti_4O_7 is increased by nearly 200 °C relative to pristine materials. Kinetic analysis of thermogravimetric data suggests that oxidation follows a 3-dimensional diffusion model. The improved stability of doped materials may again be due to the stabilization of oxygen vacancies [61]. Another explanation provided in the literature is the improved thermodynamic stability of Ti_4O_7 upon doping [174]. Interestingly, chromium doping reduces thermal stability. Correspondingly, chromium cations are predicted to destabilize the Ti_4O_7 lattice [174].
- Anodic stability is improved by vanadium doping as suggested by electrochemical accelerated life testing. Specifically, the time-to-failure of 2 at% vanadium doped anodes are nearly 2.5 times greater than that of pristine materials at 100 mA cm^{-2} . In accord with thermal stability, vanadium doped materials are significantly more stable than pristine materials with chromium doped materials being less stable. The anodic stability of iron-doped electrodes could not be explored due to their electrochemical behaviour (specifically, the electrode potential required to pass the required current density for the ALT was near 10 V), rendering them incompatible for electrochemical accelerated life testing.

- With the exception of anodic stability, the electrochemical behaviour of doped Ti_4O_7 is largely unaffected by doping with the exception of iron doped materials. Iron doped Ti_4O_7 exhibits a large potential window due to the large overpotentials for the water splitting reactions.
- Vanadium-doped Ti_4O_7 porous transport layers are shown to be exceptional electrodes for the electrolysis of industrial wastewater. Saline solutions containing an organic dye were rapidly decolorized and their organic content was reduced quickly. >99% decolorization occurs at 0.5 Ah L^{-1} and >98% removal of chemical oxygen demand occurs at 2 Ah L^{-1} with 10 mA cm^{-2} . The efficiency of the decolorization and removal of chemical oxygen demand in a compact, zero-gap wastewater electrolyzer is excellent with respect to energy consumption at ~ 2 and $\sim 6 \text{ kWh m}^{-3} \text{ order}^{-1}$, respectively, indicating it is in the top quartile for similar technologies.

6.2 Recommendations

With these insights obtained from this study, the following lines of inquiry are recommended for future research:

- The influence of the dopant type, doping level, and co-doping on oxidation stability as well as other relevant properties for electrodes such as electrical conductivity, capacitance, and electrocatalytic characteristics. Furthermore, shortcomings in describing these materials, such as the oxidation states of the dopant atoms and presence of oxygen vacancies, should

also be addressed so as to understand their potential contribution to the stability of these materials. Finally, controlling particle size when preparing these materials would facilitate any thermogravimetric study into the contributions of oxygen diffusion towards the mechanism for thermal oxidation.

- The viability of iron as a dopant for electrodes based on Magnéli phase titanium oxides should be further explored. While electrochemical accelerated life testing could not be carried out using these materials, it is possible that under the right conditions and control, iron doped Ti_4O_7 may be an effective anode for industrial wastewater electrolysis. It is possible that the dopant concentration may have not been optimal for the study and that a better behaving electrode could have been constructed by exploring other compositions.
- The viability of other dopants for Magnéli phase titanium oxides should be explored. A more comprehensive study has been recently completed into the thermodynamic stability of transition metals cations in Ti_4O_7 [174]. While the study uses a relatively high concentration of dopant atoms (~10 at%), their experimental study is limited to a single dopant: cerium. There is perhaps an opportunity to build upon this contribution to explore its applicability to electrochemical systems.
- The potentiostatic control of a wastewater electrolyzer and its influence on efficiency needs to be further explored. In this study, galvanostatic control was used given the design of the electrochemical cell and its inability to accommodate a reference electrode. If a reference electrode could be accommodated, the potentiostatic control of the electrolyzer is possible.

In such a case, potentiostatic control only requires that a specified electrode potential is maintained as opposed to a specified current. This should improve current efficiency under conditions when mass transport of pollutants to the electrode is greatly limited and thus a considerable portion of the current goes towards parasitic process.

- Technoeconomic considerations relevant to wastewater electrolyzer design should also be explored. For example, the inclusion of membranes may reduce inefficiencies due to cyclic redox reactions such as the reduction of in situ formed chemical oxidants such as active chlorine species. However, membranes would also increase the cost not only to acquire and install them but also for their upkeep and eventual replacement.
- Real industrial wastewaters and pollutants of emerging interest such as perfluorinated alkyl substances (PFASs), endocrine-disrupting chemicals (EDCs), and pharmaceuticals and personal care products (PPCPs) should also be investigated. While azo dyes are of industrial relevance, they are relatively simple to monitor and general conducive to electrochemical treatment. PFASs, EDCs, and PPCPs are generally more difficult to monitor and in some cases more recalcitrant to treatment, though there have been some successful studies using MPTO REMs [81, 88, 75].

Bibliography

- [1] Statistics Canada, "Water discharge in manufacturing industries, by type of final treatment and industry (x 1,000,000)," 2022. [Online]. Available:
<https://www150.statcan.gc.ca/t1/tb11/en/tv.action?pid=3810006001>.
- [2] Statistics Canada, "Total water costs in manufacturing industries, by water cost component and industry (x 1,000)," 2022. [Online]. Available:
<https://www150.statcan.gc.ca/t1/tb11/en/tv.action?pid=3810006401>.
- [3] J. Radjenovic and D. L. Sedlak, "Challenges and Opportunities for Electrochemical Processes as Next-Generation Technologies for the Treatment of Contaminated Water," *Environmental Science & Technology*, vol. 49, no. 19, p. 11292–11302, 2015.
- [4] M. Panizza and G. Cerisola, "Direct And Mediated Anodic Oxidation of Organic Pollutants," *Chemical Reviews*, vol. 109, no. 12, p. 6541–6569, 2009.
- [5] C. A. Martínez-Huitle, M. A. Rodrigo, I. Sirés and O. Scialdone, "Single and Coupled Electrochemical Processes and Reactors for the Abatement of Organic Water Pollutants: A Critical Review," *Chemical Reviews*, vol. 115, no. 24, p. 13362–13407, 2015.
- [6] B. P. Chaplin, "The Prospect of Electrochemical Technologies Advancing Worldwide Water Treatment," *Accounts of Chemical Research*, vol. 52, no. 3, p. 596–604, 2019.
- [7] C. Comninellis and G. Chen, *Electrochemistry for the Environment*, New York, NY: Springer, 2010.

- [8] S. O. Ganiyu, C. A. Martínez-Huitle and M. A. Rodrigo, "Renewable Energies Driven Electrochemical Wastewater/Soil Decontamination Technologies: A Critical Review of Fundamental Concepts and Applications," *Applied Catalysis B: Environmental*, vol. 270, p. 118857, 2020.
- [9] D. B. Miklos, C. Remy, M. L. K. G. Jekel, J. E. Drewes and U. Hübner, "Evaluation of advanced oxidation processes for water and wastewater treatment – A critical review," *Water Research*, vol. 129, p. 118–131, 2018.
- [10] Natural Resources Canada, "Industrial Energy Prices and Background Indicators," 2022. [Online]. Available: <https://oee.rncan.gc.ca/corporate/statistics/neud/dpa/showTable.cfm?type=HB§or=agg&juris=00&rn=7&page=0>.
- [11] R. J. Pollock, J. F. Houlihan, A. N. Bain and B. S. Coryea, "Electrochemical properties of a new electrode material, Ti₄O₇," *Materials Research Bulletin*, vol. 19, no. 1, p. 17–24, 1984.
- [12] B. P. Chaplin, "Critical Review of Electrochemical Advanced Oxidation Processes for Water Treatment Applications," *Environmental Science: Process & Impacts*, vol. 16, no. 6, p. 1182–1203, 2014.
- [13] J. R. Smith, F. C. Walsh and R. L. Clarke, "Electrodes Based on Magnéli Phase Titanium Oxides: the Properties and Applications of Ebonex® Materials," *Journal of Applied Electrochemistry*, vol. 28, p. 1021–1033, 1998.

- [14] F. C. Walsh and R. G. A. Wills, "The Continuing Development of Magnéli Phase Titanium Sub-oxides and Ebonex® Electrodes," *Electrochimica Acta*, vol. 55, no. 22, p. 6342–6351, 2010.
- [15] B. Xu, H. Y. Sohn, Y. Mohassab and Y. Lan, "Structures, Preparation and Applications of Titanium Suboxides," *RSC Advances*, vol. 6, no. 83, p. 79706–79722, 2016.
- [16] G. Chen, E. A. Betterton and R. G. Arnold, "Electrolytic Oxidation of Trichloroethylene Using a Ceramic Anode," *Journal of Applied Electrochemistry*, vol. 29, pp. 961-970, 1999.
- [17] J. Tafel, "Über die Polarisation bei kathodischer Wasserstoffentwicklung," *Zeitschrift für Physikalische Chemie*, vol. 50, pp. 641-712, 1905.
- [18] T. Erdey-Grúz and M. Volmer, "Zur Theorie der Wasserstoff Überspannung," *Zeitschrift für Physikalische Chemie*, vol. 150A, no. 1, pp. 203-213, 1930.
- [19] F. C. Walsh, "A First Course in Electrochemical Engineering," The Electrochemical Consultancy, Romsey, 1993.
- [20] P. Debye and E. Hückel, "Zur Theorie der Elektrolyte. I. Gefrierpunktserniedrigung und verwandte Erscheinungen," *Physikalische Zeitschrift*, vol. 24, no. 9, pp. 185-206, 1923.
- [21] L. Onsager and R. M. Fuoss, "Irreversible Processes in Electrolytes. Diffusion, Conductance and Viscous Flow in Arbitrary Mixtures of Strong Electrolytes," *Journal of Physical Chemistry*, vol. 36, no. 11, pp. 2689-2778, 1932.
- [22] R. M. Fuoss and L. Onsager, "Conductance of Unassociated Electrolytes," *Journal of Physical Chemistry*, vol. 61, no. 5, pp. 668-682, 1957.

- [23] R. Dillon, S. Srinivasan, A. S. Aricò and V. Antonucci, "International activities in DMFC R&D: status of technologies and potential applications," *Journal of Power Sources*, Vols. 1-2, no. 127, pp. 112-126, 2004.
- [24] X. Yu and P. G. Pickup, "Recent advances in direct formic acid fuel cells (DFAFC)," *Journal of Power Sources*, vol. 182, no. 1, pp. 124-132, 2008.
- [25] S. Trasatti, "Electrocatalysis by Oxides — Attempt at a Unifying Approach," *Journal of Electroanalytical Chemistry and Interfacial Electrochemistry*, vol. 111, no. 1, pp. 125-131, 1980.
- [26] S. Trasatti, "Electrocatalysis in the Anodic Evolution of Oxygen and Chlorine," *Electrochimica Acta*, vol. 29, no. 11, pp. 1503-1512, 1984.
- [27] W. Mindt, "Electrical Properties of Electrodeposited PbO₂ Films," *Journal of The Electrochemical Society*, vol. 116, no. 8, pp. 1076-1080, 1969.
- [28] Z. M. Jarzebski and J. P. Marton, "Physical Properties of SnO₂ Materials: II. Electrical Properties," *Journal of The Electrochemical Society*, vol. 123, no. 9, pp. 299C-310C, 1976.
- [29] J. -P. Lagrange, A. Deneuve and E. Gheeraert, "Activation Energy in Low Compensated Homoepitaxial Boron-Doped Diamond Films," *Diamond and Related Materials*, vol. 7, no. 9, pp. 1390-1393, 1998.
- [30] R. F. Bartholomew and D. R. Frankl, "Electrical Properties of Some Titanium Oxides," *Physical Review*, vol. 187, no. 3, pp. 828-833, 1969.
- [31] Y. Einaga, J. S. Foord and G. M. Swain, "Diamond Electrodes: Diversity and Maturity," *MRS Bulletin*, vol. 39, no. 6, p. 525–532, 2014.

- [32] N. Yang, J. S. Foord and X. Jiang, "Diamond Electrochemistry at the Nanoscale: A Review," *Carbon*, vol. 99, p. 90–110, 2016.
- [33] N. Yang, S. Yu, J. V. Macpherson, Y. Einaga, H. Zhao, G. M. Swain and X. Jiang, "Conductive Diamond: Synthesis, Properties, and Electrochemical Applications," *Chemical Society Reviews*, vol. 48, no. 1, p. 157–204, 2019.
- [34] P. V. Nidheesh, G. Divyapriya, N. Oturan, C. Trelu and M. A. Oturan, "Environmental Applications of Boron-Doped Diamond Electrodes: 1. Applications in Water and Wastewater Treatment," *ChemElectroChem*, vol. 6, no. 8, pp. 2124-2142, 2019.
- [35] Y. He, H. Lin, Z. Guo, W. Zhang, H. Li and W. Huang, "Recent Developments and Advances in Boron-Doped Diamond Electrodes for Electrochemical Oxidation of Organic Pollutants," *Separation and Purification Technology*, vol. 212, pp. 802-821, 2019.
- [36] S. T. McBeath, D. P. Wilkinson and N. J. D. Graham, "Application of Boron-Doped Diamond Electrodes for the Anodic Oxidation of Pesticide Micropollutants in a Water Treatment Process: a Critical Review," *Environmental Science: Water Research & Technology*, vol. 5, no. 12, pp. 2090-2107, 2019.
- [37] B. Marselli, J. Garcia-Gomez, P. -A. Michaud, M. A. Rodrigo and C. Comninellis, "Electrogeneration of Hydroxyl Radicals on Boron-Doped Diamond Electrodes," *Journal of the Electrochemical Society*, vol. 150, no. 3, pp. D79-D83, 2003.
- [38] G. Fóti, D. Gandini, C. Comninellis, A. Perret and W. Haenni, "Oxidation of Organics by Intermediates of Water Discharge on IrO₂ and Synthetic Diamond Anodes," *Electrochemical and Solid-State Letters*, vol. 2, no. 5, pp. 228-230, 1999.

- [39] M. A. Rodrigo, P. A. Michaud, M. Panizza, G. Cerisola and C. Comninellis, "Oxidation of 4-Chlorophenol at Boron-Doped Diamond Electrode for Wastewater Treatment," *Journal of The Electrochemical Society*, vol. 148, no. 5, pp. D60-D64, 2001.
- [40] B. Correa-Lozano, C. Comninellis and A. De Battisti, "Service life of Ti/SnO₂-Sb₂O₅ anodes," *Journal of Applied Electrochemistry*, vol. 27, pp. 970-974, 1997.
- [41] A. J. Kokalj, S. Novak, I. Talaber, V. Kononenko, L. B. Mali, M. Vodovnik, B. Žegura, T. Eleršek, G. Kalčíkova, A. Ž. Gotvajn, S. Kralj, D. Makovec, H. Caloudova and D. Droben, "The First Comprehensive Safety Study of Magnéli Phase Titanium Suboxides Reveals No Acute Environmental Hazard," *Environmental Science: Nano*, vol. 6, no. 4, pp. 1131-1139, 2019.
- [42] P. C. S. Hayfield and R. L. Clarke, "The Electrochemical Characteristics and Uses of Magnéli Phase Titanium Oxide Ceramic Electrodes," in *175th Meeting of The Electrochemical Society*, Los Angeles, 1989.
- [43] A. Kumar, N. H. Barbhuiya and S. P. Singh, "Magnéli phase titanium sub-oxides synthesis, fabrication and its application for environmental remediation: Current status and prospect," *Chemosphere*, vol. 307, no. 2, p. 135878, 2022.
- [44] S. Andersson, B. Collén, G. Kruuse, U. Kuylenstierna and A. Magnéli, "Phase Analysis Studies on the Titanium-Oxygen System," *Acta Chemica Scandinavica*, vol. 11, no. 10, pp. 1641-1652, 1957.
- [45] Y. Zhang, S. Yao, R. Zhuang, K. Luan, X. Qian, J. Xiang, X. Shen, T. Li, K. Xiao and S. Qin, "Shape-controlled synthesis of Ti₄O₇ nanostructures under solvothermal-assisted heat

- treatment and its application in lithium-sulfur batteries," *Journal of Alloys and Compounds*, vol. 729, pp. 1136-1144, 2017.
- [46] C. Langlade, B. Vannes, T. Sarnet and M. Autric, "Characterization of titanium oxide films with Magnéli structure elaborated by a sol–gel route," *Applied Surface Science*, vol. 186, no. 1-4, pp. 145-149, 2002.
- [47] S.-S. Huang, Y.-H. Lin, W. Chuang, P.-S. Shao, C.-H. Chuang, J.-F. Lee, M.-L. Lu, Weng, Yu-Ting and N.-L. Wu, "Synthesis of High-Performance Titanium Sub-Oxides for Electrochemical Applications Using Combination of Sol–Gel and Vacuum-Carbothermic Processes," *ACS Sustainable Chemistry & Engineering*, vol. 6, no. 3, pp. 3162-3168, 2018.
- [48] D. Portehault, V. Maneeratana, C. Candolfi, N. Oeschler, I. Veremchuk, Y. Grin, C. Sanchez and M. Antonietti, "Facile General Route toward Tunable Magnéli Nanostructures and Their Use As Thermoelectric Metal Oxide/Carbon Nanocomposites," *ACS Nano*, vol. 5, no. 11, pp. 9052-9061, 2011.
- [49] D. Calestani, F. Licci, E. Kopnin, G. Calestani, A. Gauzzi, F. Bolzoni, T. Besagni, V. Boffa and M. Marezio, "Preparation and characterization of powders and crystals of $V_n-xTi_xO_{2n-1}$ Magneli oxides," *Crystal Research & Technology*, vol. 40, no. 10-11, pp. 1067-1071, 2005.
- [50] M. N. Gardos, "Magnéli phases of anion-deficient rutile as lubricious oxides. Part II. Tribological behavior of Cu-doped polycrystalline rutile (Ti_nO_{2n-1})," *Tribology Letters*, vol. 8, pp. 79-96, 2000.

- [51] A. A. Gusev, E. G. Avvakumov, A. Z. Medvedev and A. I. Maxliy, "Ceramic electrodes based on Magneli phases of titanium oxides," *Science of Sintering*, vol. 39, no. 1, pp. 51-57, 2007.
- [52] G. Hasegawa, T. Sato, K. Kanamori, K. Nakano, T. Yajima, Y. Kobayashi, H. Kageyama, T. Abe and K. Nakanishi, "Hierarchically Porous Monoliths Based on N-Doped Reduced Titanium Oxides and Their Electric and Electrochemical Properties," *Chemistry of Materials*, vol. 25, no. 17, pp. 3504-5312, 2013.
- [53] S. R. Ovshinsky, B. Aladjov, S. Venkatesan, B. Tekkanat, M. Vijan, H. Wang, Dhar and S. K., "Performance enhancing additive material for the nickel hydroxide positive electrode in rechargeable alkaline cells". US Patent 7201857 B2, 2007.
- [54] J. Maragatha, Jothivenkatachalam, K and S. Karuppuchamy, "Synthesis and characterization of visible light-responsive carbon doped Ti₄O₇ photocatalyst," *Journal of Materials Science: Materials in Electronics*, vol. 27, pp. 9233-9239, 2016.
- [55] J. Maragatha, C. Rani, S. Ragendran and S. Karuppuchamy, "Microwave synthesis of nitrogen doped Ti₄O₇ for photocatalytic applications," *Physica E: Low-dimensional Systems and Nanostructures*, vol. 93, pp. 78-82, 2017.
- [56] T. Teramoto, Y. Takai, H. Hashiguchi, E. Okunishi and K. Tanaka, "Distribution of Alloying Quadrivalent Zirconium in TiO_{2-x} Magnèli Phase," *Materials Transactions*, vol. 60, no. 10, pp. 2199-2203, 2019.
- [57] Z. Yuan, J. Gong, S. Xu, Z. Li and G. Tang, "Investigation of the thermoelectric properties of reduced Nb-doped TiO_{2-δ} ceramics," *Journal of Alloys and Compounds*, vol. 710, pp. 778-783, 2017.

- [58] Z. Yuan, Z. Li, S. Xu, W. Ma, J. Xu and G. Tang, "Thermoelectric properties of Nb-doped TiO₂- δ ceramics reduced at elevated temperature," *Ceramics International*, vol. 43, no. 17, pp. 15454-15458, 2017.
- [59] X. Yang, J. Guo, Z. Zhu, H. Zhang and T. Qi, "Doping effects on the electro-degradation of phenol on doped titanium suboxide anodes," *Chinese Journal of Chemical Engineering*, vol. 26, no. 4, pp. 830-837, 2018.
- [60] P. C. S. Hayfield, *Development of a New Material: Monolithic Ti₄O₇ Ebonex® Ceramic*, Cambridge: Royal Society of Chemistry, 2001.
- [61] H. Lin, R. Xian, R. Xie, L. Yang, C. Tang, R. Wang, J. Chen, S. Lv and Q. Huang, "Defect Engineering on a Ti₄O₇ Electrode by Ce³⁺ Doping for the Efficient Electrooxidation of Perfluorooctanesulfonate," *Environmental Science & Technology*, vol. 55, no. 4, p. 2597–2607, 2021.
- [62] P. C. S. Hayfield, "Electrode material, electrode and electrochemical cell". United States of America Patent 4,422,917, 27 December 1983.
- [63] D. Pletcher and F. C. Walsh, *Industrial Electrochemistry*, London: Blackie Academic & Professional, 1993.
- [64] S. El-Sherif, D. Bejan and N. J. Bunce, "Electrochemical oxidation of sulfide ion in synthetic sour brines using periodic polarity reversal at Ebonex® electrodes," *Canadian Journal of Chemistry*, vol. 88, no. 9, pp. 928-936, 2010.

- [65] J. T. English and D. P. Wilkinson, "The Thermal-Oxidation Behavior of Pristine and Doped Magnéli Phase Titanium Oxides," *ECS Journal of Solid State Science and Technology*, vol. 10, p. 034004, 2021.
- [66] J. T. English and D. P. Wilkinson, "The Superior Electrical Conductivity and Anodic Stability of Vanadium-Doped Ti₄O₇," *Journal of The Electrochemical Society*, vol. 168, no. 10, p. 103509, 2021.
- [67] M. Marezio and P. D. Dernier, "The crystal structure of Ti₄O₇, a member of the homologous series Ti_nO_{2n-1}," *Journal of Solid State Chemistry*, vol. 3, no. 3, pp. 340-348, 1971.
- [68] J. L. Murray and H. A. Wriedt, "The O-Ti (Oxygen-Titanium) system," *Journal of Phase Equilibria*, vol. 8, pp. 148-165, 1987.
- [69] S. Harada, K. Tanaka and H. Inui, "Thermoelectric properties and crystallographic shear structures in titanium oxides of the Magnéli phases," *Journal of Applied Physics*, vol. 108, p. 083703, 2010.
- [70] J. E. Graves, D. Pletcher, R. L. Clarke and F. C. Walsh, "The Electrochemistry of Magnéli Phase Titanium Oxide Ceramic Electrodes Part I. The Deposition and Properties of Metal Coatings," *Journal of Applied Electrochemistry*, vol. 21, p. 848-857, 1991.
- [71] W.-H. Kao, P. Patel and S. L. Haberichter, "Formation Enhancement of a Lead/Acid Battery Positive Plate by Barium Metaplumbate and Ebonex®," *Journal of The Electrochemical Society*, vol. 144, no. 6, p. 1907-1911, 1997.

- [72] D. Bejan, J. D. Malcolm, L. Morrison and N. J. Bunce, "Mechanistic Investigation of the Conductive Ceramic Ebonex® as an Anode Material," *Electrochimica Acta*, vol. 54, no. 23, p. 5548–5556, 2009.
- [73] O. Scialdone, A. Galia and G. Filardo, "Electrochemical incineration of 1,2-dichloroethane: Effect of the electrode material," *Electrochimica Acta*, vol. 53, no. 24, pp. 7220-7225, 2008.
- [74] P. Geng, J. Su, C. Miles, C. Comninellis and G. Chen, "Highly-Ordered Magnéli Ti₄O₇ Nanotube Arrays as Effective Anodic Material for Electro-oxidation," *Electrochimica Acta*, vol. 153, pp. 316-324, 2015.
- [75] A. M. Zaky and B. P. Chaplin, "Porous Substoichiometric TiO₂ Anodes as Reactive Electrochemical Membranes for Water Treatment," *Environmental Science & Technology*, vol. 47, no. 12, pp. 6554-6563, 2013.
- [76] L. Guo, Y. Jing and B. P. Chaplin, "Development and Characterization of Ultrafiltration TiO₂ Magnéli Phase Reactive Electrochemical Membranes," *Environmental Science & Technology*, vol. 50, no. 3, pp. 1428-1436, 2016.
- [77] M. C. Santos, Y. A. Elabd, Y. Jing, B. P. Chaplin and L. Fang, "Highly porous Ti₄O₇ reactive electrochemical water filtration membranes fabricated via electrospinning/electrospraying," *AIChE Journal*, vol. 62, no. 2, pp. 508-524, 0215.
- [78] S. Liang, H. Lin, X. Yan and Q. Huang, "Electro-oxidation of tetracycline by a Magnéli phase Ti₄O₇ porous anode: Kinetics, products, and toxicity," *Chemical Engineering Journal*, vol. 332, pp. 628-636, 2018.

- [79] H. Lin, J. Niu, S. Liang, C. Wang, Y. Wang, F. Jin, Q. Luo and Q. Huang, "Development of macroporous Magnéli phase Ti₄O₇ ceramic materials: As an efficient anode for mineralization of poly- and perfluoroalkyl substances," *Chemical Engineering Journal*, vol. 354, pp. 1058-1067, 2018.
- [80] C. Trelu, C. Coetsier, J.-C. Rouch, R. Esmilaire, M. Rivallin, M. Cretin and C. Causserand, "Mineralization of organic pollutants by anodic oxidation using reactive electrochemical membrane synthesized from carbothermal reduction of TiO₂," *Water Research*, vol. 131, pp. 310-319, 2018.
- [81] T. X. H. Le, H. Haflich, A. D. Shah and B. P. Chaplin, "Energy-Efficient Electrochemical Oxidation of Perfluoroalkyl Substances Using a Ti₄O₇ Reactive Electrochemical Membrane Anode," *Environmental Science & Technology Letters*, vol. 6, no. 8, pp. 504-510, 2019.
- [82] S. You, B. Liu, Y. Gao, Y. Wang, C. T. Tang, Y. Huang and N. Ren, "Monolithic Porous Magnéli-phase Ti₄O₇ for Electro-oxidation Treatment of Industrial Wastewater," *Electrochimica Acta*, vol. 214, pp. 326-335, 2016.
- [83] G. Liu, H. Zhou, J. Teng and S. You, "Electrochemical degradation of perfluorooctanoic acid by macro-porous titanium suboxide anode in the presence of sulfate," *Chemical Engineering Journal*, vol. 371, pp. 7-14, 2019.
- [84] L. Wang, J. Lu, L. Li, Y. Wang and Q. Huang, "Effects of chloride on electrochemical degradation of perfluorooctanesulfonate by Magnéli phase Ti₄O₇ and boron doped diamond anodes," *Water Research*, vol. 170, p. 115254, 2020.

- [85] G. Wang, Y. Liu, J. Ye, Z. Lin and X. Yang, "Electrochemical oxidation of methyl orange by a Magnéli phase Ti₄O₇ anode," *Chemosphere*, vol. 241, p. 125084, 2020.
- [86] J. Wang, D. Zhi, H. Zhou, X. He and D. Zhang, "Evaluating tetracycline degradation pathway and intermediate toxicity during the electrochemical oxidation over a Ti/Ti₄O₇ anode," *Water Research*, vol. 137, pp. 324-334, 2018.
- [87] O. Ganzenko, S. Sistat, Philippe, C. Trelu, V. Bonniol, M. Rivaliin and M. Cretin, "Reactive electrochemical membrane for the elimination of carbamazepine in secondary effluent from wastewater treatment plant," *Chemical Engineering Journal*, vol. 419, p. 129467, 2021.
- [88] S. N. Misal, M.-H. Lin, S. Mehraeen and B. P. Chaplin, "Modeling electrochemical oxidation and reduction of sulfamethoxazole using electrocatalytic reactive electrochemical membranes," *Journal of Hazardous Materials*, vol. 384, p. 121420, 2020.
- [89] H. Shi, Y. Wang, C. Li, R. Pierce, S. Gao and Q. Huang, "Degradation of Perfluorooctanesulfonate by Reactive Electrochemical Membrane Composed of Magnéli Phase Titanium Suboxide," *Environmental Science & Technology*, vol. 53, no. 24, pp. 14528-14537, 2019.
- [90] S. Wang, S. Pei, J. Zhang, J. Huang and S. You, "Flow-through electrochemical removal of benzotriazole by electroactive ceramic membrane," *Water Research*, vol. 218, p. 118454, 2022.
- [91] G. W. C. C. Chen, H. Cho, D. D. Macdonald and T. E. Mallouka, "EIS Studies of Porous Oxygen Electrodes with Discrete Particles: I. Impedance of Oxide Catalyst Supports," *Journal of The Electrochemical Society*, vol. 150, no. 9, p. E423–E428, 2003.

- [92] L. L. Hench and J. K. West, "The sol-gel process," *Chemical Reviews*, vol. 90, no. 1, pp. 33-72, 1990.
- [93] W. Bragg, "The Diffraction of Short Electromagnetic Waves by a Crystal," *Proceedings of the Cambridge Philosophical Society*, vol. 17, pp. 43-57, 1913.
- [94] R. M. Rietveld, "A profile refinement method for nuclear and magnetic structures," *Journal of Applied Crystallography*, vol. 2, no. 2, pp. 65-71, 1960.
- [95] A. Einstein, "Zur Elektrodynamik bewegter Körper," *Annalen der Physik*, vol. 322, no. 10, pp. 891-921, 1905.
- [96] M. W. Bilton, "Nanoparticulate hydroxyapatite and calcium-based CO₂ sorbents," in *PhD Thesis*, Leeds, University of Leeds, 2012.
- [97] N. Elgrishi, K. J. Rountree, B. D. McCarthy, E. S. Rountree, T. T. Eisenhart and J. L. Dempsey, "A Practical Beginner's Guide to Cyclic Voltammetry," *Journal of Chemical Education*, vol. 95, no. 2, pp. 197-206, 2018.
- [98] S. Andersson and A. Magnéli, "Diskrete Titanoxydphasen im Zusammensetzungsbereich TiO_{1,75}-TiO_{1,90}," *Naturwissenschaften*, vol. 43, pp. 495-496, 1956.
- [99] D. B. Strukov, G. S. Snider, D. R. Stewart and R. S. Williams, "The missing memristor found," *Nature*, vol. 453, pp. 80-83, 2008.
- [10] D.-H. Kwon, K. M. Kim, J. H. J. M. Jang, M. H. Lee, G. H. L. X.-S. Kim, G.-S. Park, B. 0] Lee, S. Han, M. Kim and C. S. Hwang, "Atomic structure of conducting nanofilaments in TiO₂ resistive switching memory," *Nature Nanotechnology*, vol. 5, pp. 148-153, 2010.

- [10 J. P. Strachan, M. D. Pickett, J. J. Yang, S. Aloni, A. L. D. Kilcoyne, G. Medeiros-Ribeiro
1] and R. S. Williams, "Direct Identification of the Conducting Channels in a Functioning Memristive Device," *Advanced Materials*, vol. 22, no. 32, pp. 3573-3577, 2010.
- [10 G. H. Kim, J. H. Lee, J. Y. S. S. J. Seok, J. H. Yoon, K. J. Yoon, K. M. Kim, H. D. Lee, S.
2] W. Ryu, T. J. Park and C. S. Hwang, "Improved endurance of resistive switching TiO₂ thin film by hourglass shaped Magnéli filaments," *Applied Physics Letters*, vol. 98, no. 26, p. 262901, 2011.
- [10 D. Gokcen, O. Şentürk, E. Karaca, N. Ö. Pekmez and K. Pekmez, "Memristive behavior of
3] TiO_x obtained via Pb(II)-assisted anodic oxidation process," *Journal of Materials Science: Materials in Electronics*, vol. 30, pp. 5733-5743, 2019.
- [10 E. Gul and D. Gokcen, "Active Memristive Layer Deposition via Mn(II)-Assisted Anodic
4] Oxidation of Titanium," *ECS Journal of Solid State Science and Technology*, vol. 9, no. 5, p. 054004, 2020.
- [10 W. Hume-Rothery, G. W. Mabbott and K. M. C. Evans, "The freezing points, melting
5] points, and solid solubility limits of the alloys of silver and copper with the elements of the b sub-groups," *Philosophical Transactions of the Royal Society, A: Mathematical, Physical & Engineering Sciences*, vol. 233, pp. 721-730, 1934.
- [10 L. S. Darken, R. W. Gurry and M. B. Bever, Physical chemistry of metals, New York:
6] McGraw-Hill, 1953.
- [10 S. Brunauer, P. H. Emmett and E. Teller, "Adsorption of Gases in Multimolecular Layers,"
7] *Journal of the American Chemical Society*, vol. 60, no. 2, pp. 309-319, 1938.

- [10] A. V. Naumkin, A. Kraut-Vass, S. W. Gaarenstroom and C. J. Powell, "NIST X-ray
8] Photoelectron Spectroscopy Database," 2000. [Online]. Available:
<https://srdata.nist.gov/xps/>.
- [10] S. Gražulis, D. Chateigner, R. T. Downs, A. F. T. Yokochi, M. Quirós, L. Lutterotti, E.
9] Manakova, J. Butkus, P. Moeck and A. Le Bail, "Crystallography Open Database – an
open-access collection of crystal structures," *Journal of Applied Crystallography*, vol. 42,
pp. 726-729, 2009.
- [11] K. Momma and F. Izumi, "VESTA 3 for three-dimensional visualization of crystal,
0] volumetric and morphology data," *Journal of Applied Crystallography*, vol. 44, pp. 1272-
1276, 2011.
- [11] B. H. Toby and R. B. Von Dreele, "GSAS-II: the genesis of a modern open-source all
1] purpose crystallography software package," *Journal of Applied Crystallography*, vol. 46,
pp. 544-549, 2013.
- [11] R. D. Shannon, "Revised effective ionic radii and systematic studies of interatomic
2] distances in halides and chalcogenides," *Acta Crystallographica, Section A: Crystal
Physics, Diffraction, Theoretical and General Crystallography*, vol. A32, pp. 751-767,
1976.
- [11] J. Rumble, CRC Handbook of Chemistry and Physics, Boca Raton, FL: CRC Press 2020,
3] 2020.
- [11] J. T. English and D. P. Wilkinson, "The Thermal-Oxidation Behavior of Pristine and
4] Doped Magnéli Phase Titanium Oxides," *ECS Transactions*, vol. 98, no. 1, pp. 11-22,
2020.

- [11 M. Marezio, D. B. McWhan, P. D. Dernier and J. P. Remeika, "Structural aspects of the
5] metal-insulator transitions in Ti_4O_7 ," *Journal of Solid State Chemistry*, vol. 6, no. 2, pp.
213-221, 1973.
- [11 J. L. Hodeau and M. Marezio, "Structural aspects of the metal-insulator transitions in
6] $(Ti_{0.9975}V_{0.0025})_4O_7$," *Journal of Solid State Chemistry*, vol. 29, no. 1, 1979.
- [11 R. W. G. Wyckoff, *Structure of Crystals*, New York: The Chemical Catalog Company,
7] 1963.
- [11 M. W. Chase, C. A. Davies, J. R. Downey, D. J. Frurip, R. A. McDonald and A. N.
8] Syverud, "NIST-JANAF Thermochemical Tables," 1998. [Online]. Available:
<https://janaf.nist.gov>.
- [11 S. Vyazovkin, A. K. Burnham, J. M. Criado, L. A. Pérez-Maqueda, C. Popescu and N.
9] Sbirrazzuoli, "ICTAC Kinetics Committee recommendations for performing kinetic
computations on thermal analysis data," *Thermochimica Acta*, vol. 520, no. 1-2, pp. 1-19,
2011.
- [12 H. E. Kissinger, "Reaction Kinetics in Differential Thermal Analysis," *Analytical*
0] *Chemistry*, vol. 29, no. 11, pp. 1702-1706, 1957.
- [12 T. Akahira and T. Sunose, *Chiba Kogyo Daigaku Kenkyu Hokoku, Riko-hen*, vol. 16, pp.
1] 22-31, 1971.
- [12 G. I. Senum and R. T. Yang, "Rational approximations of the integral of the Arrhenius
2] function," *Journal of Thermal Analysis*, vol. 11, pp. 445-447, 1977.

- [12 W. Jander, "Reaktionen im festen Zustande bei höheren Temperaturen.
3] Reaktionsgeschwindigkeiten endotherm verlaufender Umsetzungen," *Zeitschrift für anorganische und allgemeine Chemie*, vol. 163, no. 1, pp. 1-30, 1927.
- [12 A. M. Ginstling and B. I. Brounshtein, *Zhurnal Prikladnoi Khimii (Sankt-Peterburg, Russian Federation)*, vol. 23, pp. 1327-1338, 1950.
- [12 A. Khawam and D. R. Flanagan, "Solid-State Kinetic Models: Basics and Mathematical
5] Fundamentals," *Journal of Physical Chemistry B*, vol. 110, no. 35, pp. 17315-17328, 2006.
- [12 S. Andersson, B. Collén, G. Kruuse, U. Kuylenstierna, A. Magnéli, H. Pestmalis and S.
6] Åsbrink, "Identification of Titanium Oxides by X-Ray Powder Patterns," *Acta Chemica Scandinavica*, vol. 11, no. 10, pp. 1653-1657, 1957.
- [12 T. Ioroi, Z. Siroma, N. Fujiwara, S.-i. Yamazaki and K. Yasuda, "Sub-stoichiometric
7] titanium oxide-supported platinum electrocatalyst for polymer electrolyte fuel cells," *Electrochemistry Communications*, vol. 7, no. 2, pp. 183-188, 2005.
- [12 T. Ioroi, H. Senoh, S.-i. Yamazaki, Z. Siroma, N. Fujiwara and Y. Kazuaki, "Stability of
8] Corrosion-Resistant Magnéli-Phase Ti₄O₇-Supported PEMFC Catalysts at High Potentials," *Journal of the Electrochemical Society*, vol. 155, no. 4, pp. B321-B326, 2008.
- [12 P. Krishnan, S. G. Advani and A. K. Prasad, "Magneli phase Ti_nO_{2n-1} as corrosion-
9] resistant PEM fuel cell catalyst support," *Journal of Solid State Electrochemistry*, vol. 16, pp. 2515-2521, 2012.
- [13 T. Ioroi, Z. Siroma, S.-i. Yamazaki and K. Yasuda, "Electrocatalysts for PEM Fuel Cells,"
0] *Advanced Energy Materials*, vol. 9, no. 23, p. 10.1002/aenm.201801284, 2018.

- [13 T. Ioroi and K. Yasuda, "Highly reversal-tolerant anodes using Ti₄O₇-supported platinum
1] with a very small amount of water-splitting catalyst," *Journal of Power Sources*, vol. 450,
p. 227656, 2020.
- [13 S. Siracusano, V. Baglio, C. D'Urso, V. Antonucci and A. S. Aricò, "Preparation and
2] characterization of titanium suboxides as conductive supports of IrO₂ electrocatalysts for
application in SPE electrolyzers," *Electrochimica Acta*, vol. 54, no. 26, pp. 6292-6299,
2009.
- [13 T. Lagarteira, F. Han, T. Morawietz, R. Hiesgen, D. G. Sanchez, A. Mendes, A. Gago and
3] R. Costa, "Highly active screen-printed Ir single bond Ti₄O₇ anodes for proton exchange
membrane electrolyzers," *International Journal of Hydrogen Energy*, vol. 43, no. 55, pp.
16824-16833, 2018.
- [13 C. Schlenker, S. Ahmed, R. Buder and M. Gourmala, "Metal-insulator transitions and
4] phase diagram of (Ti_{1-x}V_x)₄O₇: electrical, calorimetric, magnetic and EPR studies,"
Journal of Physics C: Solid State Physics, vol. 12, no. 17, pp. 3503-3521, 1979.
- [13 H. Usui, Y. Domi, K. Takama, Y. Tanaka and H. Sakaguchi, "Tantalum-Doped Titanium
5] Oxide with Rutile Structure as a Novel Anode Material for Sodium-Ion Battery," *ACS
Applied Energy Materials*, vol. 2, no. 5, pp. 3056-3060, 2019.
- [13 H. Usui, Y. Domi, S. Ohnishi and H. Sakaguchi, "Single-Crystalline Nb-Doped Rutile
6] TiO₂ Nanoparticles as Anode Materials for Na-Ion Batteries," *ACS Applied Nano
Materials*, vol. 2, no. 9, pp. 5360-5364, 2019.

- [13 H. Usui, Y. Domi, T. H. Nguyen, Y. Tanaka and H. Sakaguchi, "Indium-Doped Rutile
7] Titanium Oxide with Reduced Particle Length and Its Sodium Storage Properties," *ACS Omega*, vol. 5, no. 25, pp. 15495-15501, 2020.
- [13 R. A. M. Esfahani, L. M. R. Gavidia, G. García, E. Pastor and S. Specchia, "Highly active
8] platinum supported on Mo-doped titanium nanotubes suboxide (Pt/TNTS-Mo)
electrocatalyst for oxygen reduction reaction in PEMFC," *Renewable Energy*, vol. 120, pp. 209-219, 2018.
- [13 R. A. M. Esfahani, I. I. Ebralidze, S. Specchia and E. B. Easton, "A fuel cell catalyst
9] support based on doped titanium suboxides with enhanced conductivity, durability and fuel
cell performance," *Journal of Materials Chemistry A*, vol. 6, no. 30, pp. 14805-14815,
2018.
- [14 R. A. M. Esfahani, H. M. Fruehwald, N. O. Laschuk, M. T. Sullivan, J. G. Egan, I. I.
0] Ebralidze, O. V. Zenkina and E. B. Easton, "A highly durable N-enriched titanium
nanotube suboxide fuel cell catalyst support," *Applied Catalysis B: Environmental*, vol.
263, p. 118272, 2020.
- [14 F. Hine, M. Yasuda, T. Noda, T. Yoshida and J. Okuda, "Electrochemical Behavior of the
1] Oxide-Coated Metal Anodes," *Journal of The Electrochemical Society*, vol. 126, no. 9, pp.
1439-1445, 1979.
- [14 I. Malkin, "DSA® - Anodes for Electroplating," in *Precious Metals 1982: Proceedings of
2] the Sixth International Precious Metals Institute Conference*, Newport Beach, CA, 1982.
- [14 R. Hutchings, K. Müller, R. Kötz and S. Stucki, "A structural investigation of stabilized
3] oxygen evolution catalysts," *Journal of Materials Science*, vol. 19, pp. 3987-3994, 1984.

- [14 J. Rolewicz, C. Comninellis, E. Plattner and J. Hinden, "Caractérisation des électrodes de
4] type DSA pour le dégagement de O₂—I. L'électrode Ti/IrO₂-Ta₂O₅," *Electrochimica Acta*, vol. 33, no. 4, pp. 573-580, 1988.
- [14 C. Comninellis and G. P. Vercesi, "Characterization of DSA®-type oxygen evolving
5] electrodes: Choice of a coating," *Journal of Applied Electrochemistry*, vol. 21, pp. 335-345, 1991.
- [14 G. P. Vercesi, J. Rolewicz, C. Comninellis and J. Hinder, "Characterization of dsa-type
6] oxygen evolving electrodes. Choice of base metal," *Thermochimica Acta*, vol. 176, pp. 31-47, 1991.
- [14 X. Chen, G. Chen and P. L. Yue, "Stable Ti/IrO_x-Sb₂O₅-SnO₂ Anode for O₂ Evolution
7] with Low Ir Content," *Journal of Physical Chemistry B*, vol. 105, no. 20, pp. 4623-4628, 2001.
- [14 D. K. Schroder, *Semiconductor Material and Device Characterization*, Hoboken, NJ:
8] Wiley, 2013.
- [14 G. D. Scott, "Packing of Spheres: Packing of Equal Spheres," *Nature*, vol. 188, pp. 908-
9] 909, 1960.
- [15 G. D. Scott, "Radial Distribution of the Random Close Packing of Equal Spheres," *Nature*,
0] vol. 194, pp. 956-957, 1962.
- [15 V. E. Henrich, G. Dresselhaus and H. J. Zeiger, "Observation of Two-Dimensional Phases
1] Associated with Defect States on the Surface of TiO₂," *Physical Review Letters*, vol. 36, no. 22, pp. 1335-1339, 1976.

- [15 Y. W. Chung, W. J. Lo and G. A. Somorjai, "Low energy electron diffraction and electron spectroscopy studies of the clean (110) and (100) titanium dioxide (rutile) crystal surfaces," *Surface Science*, vol. 64, no. 2, pp. 588-602, 1977.
- [15 K. Tanaka, T. Nasu, Y. Miyamoto, N. Ozaki, S. Tanaka, T. Nagata, F. Hakoe, M. Yoshikiyo, K. Nakagawa, Y. Umeta, K. Imoto, H. Tokoro, A. Namai and S.-i. Ohkoshi, "Structural Phase Transition between γ -Ti₃O₅ and δ -Ti₃O₅ by Breaking of a One-Dimensionally Conducting Pathway," *Crystal Growth & Design*, vol. 15, no. 2, pp. 653-657, 2014.
- [15 L. Guo, Y. Jing and B. P. Chaplin, "Development and Characterization of Ultrafiltration TiO₂ Magnéli Phase Reactive Electrochemical Membranes," *Environmental Science & Technology*, vol. 50, no. 3, pp. 1428-1436, 2016.
- [15 S. Nayak and B. P. Chaplin, "Fabrication and characterization of porous, conductive, monolithic Ti₄O₇ electrodes," *Electrochimica Acta*, vol. 263, pp. 299-310, 2018.
- [15 S. Levine and A. L. Smith, "Theory of the differential capacity of the oxide/aqueous electrolyte interface," *Discussions of the Faraday Society*, vol. 52, pp. 290-301, 1971.
- [15 S. You, B. Liu, Y. Gao, Y. Wang, C. Y. Tang, Y. Huang and N. Ren, "Monolithic Porous Magnéli-phase Ti₄O₇ for Electro-oxidation Treatment of Industrial Wastewater," *Electrochimica Acta*, vol. 214, pp. 326-335, 2016.
- [15 Y. Jing, S. Almassi, S. Mehraeen, R. J. LeSuer and B. P. Chaplin, "The roles of oxygen vacancies, electrolyte composition, lattice structure, and doping density on the electrochemical reactivity of Magnéli phase TiO₂ anodes," *Journal of Materials Chemistry A*, vol. 6, no. 46, pp. 23826-23839, 2018.

- [15 C. A. Martínez-Huitle and S. Ferro, "Electrochemical oxidation of organic pollutants for
9] the wastewater treatment: direct and indirect processes," *Chemical Society Reviews*, vol.
35, no. 12, pp. 1324-1340, 2006.
- [16 F. C. Moreira, R. A. R. Boaventura, E. Brillas and V. J. P. Vilar, "Electrochemical
0] advanced oxidation processes: A review on their application to synthetic and real
wastewaters," *Applied Catalysis B: Environmental*, vol. 202, pp. 217-261, 2017.
- [16 C. A. Martínez-Huitle and M. Panizza, "Electrochemical oxidation of organic pollutants for
1] wastewater treatment," *Current Opinion in Electrochemistry*, vol. 11, pp. 62-71, 2018.
- [16 Y. Jiang, H. Zhao, J. Liang, L. Yue, T. Li, Y. Luo, Q. Liu, S. Lu, A. M. Asiri, Z. Gong and
2] X. Sun, "Anodic oxidation for the degradation of organic pollutants: Anode materials,
operating conditions and mechanisms. A mini review," *Electrochemistry Communications*,
vol. 123, p. 106912, 2021.
- [16 S. O. Ganiyu, C. A. Martínez-Huitle and M. A. Rodrigo, "Renewable energies driven
3] electrochemical wastewater/soil decontamination technologies: A critical review of
fundamental concepts and applications," *Applied Catalysis B: Environmental*, vol. 270, p.
118857, 270.
- [16 Zolinger, *Color Chemistry: Synthesis, Properties and Applications of Organic Dyes and
4] Pigments*, 3rd ed., Cambridge: Wiley-VCH, 2003.
- [16 R. Anliker, "Color chemistry and the environment," *Ecotoxicology and Environmental
5] Safety*, vol. 1, no. 2, pp. 211-237, 1977.

- [16 M. A. Brown and S. C. De Vito, "Predicting azo dye toxicity," *Critical Reviews in Environmental Science and Technology*, vol. 23, no. 3, pp. 249-324, 1993.
- [16 K. Golka, S. Kopps and Z. W. Myslak, "Carcinogenicity of azo colorants: influence of solubility and bioavailability," *Toxicology Letters*, vol. 151, no. 1, pp. 203-210, 2004.
- [16 K.-T. Chung, "Azo dyes and human health: A review," *Journal of Environmental Science and Health, Part C: Environmental Carcinogenesis and Ecotoxicology Reviews*, vol. 34, no. 4, pp. 233-261, 2016.
- [16 C. A. Martínez-Huitle and E. Brillas, "Decontamination of wastewaters containing synthetic organic dyes by electrochemical methods: A general review," *Applied Catalysis B: Environmental*, vol. 87, no. 3-4, pp. 105-145, 2009.
- [17 E. Brillas and C. A. Martínez-Huitle, "Decontamination of wastewaters containing synthetic organic dyes by electrochemical methods. An updated review," *Applied Catalysis B: Environmental*, Vols. 166-167, pp. 603-643, 2015.
- [17 W. He, Y. Liu and J. Ye, "Electrochemical degradation of azo dye methyl orange by anodic oxidation on Ti4O7 electrodes," *Journal of Materials Science: Materials in Electronics*, vol. 29, pp. 14065-14072, 2018.
- [17 F. C. Walsh and C. Ponce de León, "Progress in electrochemical flow reactors for laboratory and pilot scale processing," *Electrochimica Acta*, vol. 280, pp. 121-148, 2018.
- [17 S. C. Perry, C. Ponce de León and F. C. Walsh, "Review—The Design, Performance and Continuing Development of Electrochemical Reactors for Clean Electrosynthesis," *Journal of The Electrochemical Society*, vol. 167, no. 15, p. 155525, 2020.

- [17 T. Yuan, N. Jin, W. Cheng, Y. Yun, X. Tian, L. Wang and Y. Jinwen, "Insight into the
4] stability in cation substitution of Magnéli phase Ti_4O_7 ," *Applied Physics Letters*, vol. 121,
no. 21, p. 214101, 2022.
- [17 J. Piao, S. Takahashi and S. Kohiki, "Preparation and Characterization of V_2O_3 Powder
5] and Film," *Japanese Journal of Applied Physics*, vol. 37, no. 12R, pp. 6519-6523, 1998.
- [17 J. T. H. Kwan, A. Bonakdarour, G. Afonso and D. P. Wilkinson, "Bridging Fundamental
6] Electrochemistry with Applied Fuel Cell Testing: A Novel and Economical Rotating Disk
Electrode Tip for Electrochemical Assessment of Catalyst-Coated Membranes,"
Electrochimica Acta, vol. 258, pp. 208-219, 2017.
- [17 M. B. A. Kroschel, J. T. H. Kwan, P. Strasser and D. P. Wilkinson, "Analysis of oxygen
7] evolving catalyst coated membranes with different current collectors using a new modified
rotating disk electrode technique," *Electrochimica Acta*, vol. 317, pp. 722-736, 2019.
- [17 P. J. Petzoldt, J. T. H. Kwan, A. Bonakdarpour and D. P. Wilkinson, "Deconvoluting
8] Reversible and Irreversible Degradation Phenomena in OER Catalyst Coated Membranes
Using a Modified RDE Technique," *Journal of The Electrochemical Society*, vol. 168, no.
2, p. 026507, 2021.
- [17 J. W. O'Dell, "Method 410.4, Revision 2.0: The Determination of Chemical Oxygen
9] Demand by Semi-Automated Colorimetry," US EPA, Cincinnati, 1993.
- [18 W. H. Zachariasen, "Untersuchungen ueber die Kristallstruktur von Sesquioxyden und
0] Verbindungen ABO_3 ," *Skrifter utgitt av det Norske Videnskaps-Akademi i Oslo I:
Matematisk- Naturvidenskapelig Klasse*, pp. 1-165, 1928.

- [18 S. Andersson, "The Crystal Structure of Ti_5O_9 ," *Acta Chemica Scandinavica*, vol. 14, no. 1] 5, pp. 1161-1172, 1960.
- [18 D. Stauffer and A. Aharony, *Introduction to Percolation Theory*, London: Taylor & Francis, 1992.
- [18 D. S. McLachlan, M. Blaszkiewicz and R. E. Newnham, "Electrical Resistivity of Composites," *Journal of the American Ceramic Society*, vol. 73, no. 8, pp. 2187-2203, 1990.
- [18 J. Przyłuski and K. Kolbrecka, "Voltametric behaviour of Ti_nO_{2n-1} ceramic electrodes close to the hydrogen evolution reaction," *Journal of Applied Electrochemistry*, vol. 23, pp. 1063-1068, 1993.
- [18 A. A. Voskanyan and A. Navrotsky, "Shear Pleasure: The Structure, Formation, and Thermodynamics of Crystallographic Shear Phases," *Annual Review of Materials Research*, vol. 51, pp. 521-540, 2021.
- [18 J. van Landuyt, "Shear Structures and Crystallographic Shear Propagation," *Le Journal de Physique, Colloque*, vol. 35, no. C7, pp. 53-63, 1974.
- [18 J. van Landuyt and S. Amelinckx, "On the Generation Mechanism for Shear Planes in Shear Structures," *Journal of Solid State Chemistry*, vol. 6, no. 2, pp. 222-229, 1973.
- [18 J. van Landuyt, R. Gevers and S. Amelinckx, "Electron Microscopic Study of Twins, Anti-Phase Boundaries, and Dislocations in Thin Films of Rutile," *Physica Status Solidi*, vol. 7, no. 1, pp. 307-329, 1964.

- [18 R. J. D. Tilley, "Correlation Between Dielectric Constant and Defect Structure of Non-stoichiometric Solids," *Nature*, vol. 269, pp. 229-231, 1977.
- [19 A. M. Stoneham and P. J. Durham, "The Ordering of Crystallographic Shear Planes: Theory of Regular Arrays," *Journal of Physics and Chemistry of Solids*, vol. 34, no. 12, pp. 2127-2135, 1973.
- [19 Y. Shimizu and E. Iguchi, "Theory of the Elastic Strain Energy Due to Crystallographic Shear Plane Arrays in Reduced Rutile (TiO₂)," *Physical Review B: Solid State*, vol. 17, no. 6, pp. 2505-2517, 1978.
- [19 R. Riffat and T. Husnain, *Fundamentals of Wastewater Treatment and Engineering*, 2nd ed., Boca Raton, FL: CRC Press, 2022.
- [19 L. N. Mulay and W. J. Danley, "Cooperative Magnetic Transitions in the Titanium-Oxygen System: A New Approach," *Journal of Applied Physics*, vol. 41, no. 3, pp. 877-879, 1970.
- [19 R. R. Merritt, B. G. Hyde, L. A. Bursill and D. K. Philp, "The Thermodynamics of the Titanium + Oxygen System: An Isothermal Gravimetric Study of the Composition Range Ti₃O₅ to TiO₂ at 1304 K," *Philosophical Transactions of the Royal Society of London. Series A, Mathematical and Physical Sciences*, vol. 274, no. 1245, pp. 627-661, 1973.
- [19 A. Magnéli, "Structures of the ReO₃-Type with Recurrent Dislocations of Atoms: 'Homologous Series' of Molybdenum and Tungsten Oxides," *Acta Crystallographica*, vol. 6, pp. 495-500, 1953.

- [19 L. Liborio and N. Harrison, "Thermodynamics of Oxygen Defective Magnéli Phases in
6] Rutile: A First-Principles Study," *Physical Review B: Condensed Matter and Materials
Physics*, vol. 77, no. 10, p. 104104, 2008.
- [19 P. Kofstad, "Note on the Defect Structure of Rutile (TiO₂)," *Journal of the Less Common
7] Metals*, vol. 13, no. 6, pp. 635-638, 1967.
- [19 L. K. Keys and L. N. Mulay, "Magnetic Susceptibility Measurements of Rutile and the
8] Magnéli Phases of the Ti-O System," *Physical Reviews*, vol. 154, no. 2, pp. 453-456, 1967.
- [19 R. James and C. R. A. Catlow, "The Energetics of Shear Plane Formation in Reduced
9] TiO₂," *Journal de Physique Colloques*, vol. 38, no. C7, pp. 32-35, 1977.
- [20 E. Iguchi and R. J. D. Tilley, "The Elastic Strain Energy of Crystallographic Shear Planes
0] in Reduced Tungsten Trioxide," *Philosophical Transactions of the Royal Society of
London. Series A, Mathematical and Physical Sciences*, vol. 286, no. 1332, pp. 55-85,
1977.
- [20 P. Gadó, B. Holmberg and A. Magnéli, "Wolfram Tantalum and Wolfram Niobium Oxides
1] of the MnO_{3n-2}(ReO₃) Series," *Acta Chemica Scandinavica*, vol. 19, no. 8, pp. 2010-
2011, 1965.
- [20 C. R. A. Catlow and R. James, "Non-Stoichiometry and Dielectric Properties," *Nature*, vol.
2] 272, pp. 603-605, 1978.
- [20 C. R. A. Catlow and R. James, "Disorder in TiO_{2-x}," *Proceedings of the Royal Society of
3] London. Series A, Mathematical and Physical Sciences*, vol. 384, no. 1786, pp. 157-173,
1982.

- [20 L. A. Bursill, B. G. Hyde, O. Terasaki and D. Watanabe, "On a New Family of Titanium
4] Oxides and the Nature of Slightly-Reduced Rutile," *The Philosophical Magazine: A
Journal of Theoretical Experimental and Applied Physics*, vol. 20, pp. 347-359, 1969.
- [20 L. A. Bursill, B. G. Hyde and D. K. Philp, "New Crystallographic Shear Families Derived
5] From the Rutile Structure, and the Possibility of Continuous Ordered Solid Solution," *The
Philosophical Magazine: A Journal of Theoretical Experimental and Applied Physics*, vol.
23, no. 186, pp. 1501-1513, 1971.
- [20 L. A. Bursill and B. G. Hyde, "Crystallographic Shear in the Higher Titanium Oxides:
6] Structure, Texture, Mechanisms and Thermodynamics," *Progress in Solid State Chemistry*,
vol. 7, pp. 177-253, 1972.
- [20 L. A. Bursill and B. G. Hyde, "Crystal Structures in the {132} CS family of higher titanium
7] oxides Ti_nO_{2n-1} ," *Acta Crystallographica Section B: Structural Crystallography and
Crystal Chemistry*, vol. B27, pp. 210-215, 1971.
- [20 S. Andersson and A. D. Wadsley, "Crystallographic Shear and Diffusion Paths in Certain
8] Higher Oxides of Niobium, Tungsten, Molybdenum and Titanium," *Nature*, vol. 211, no.
5048, pp. 581-583, 1966.
- [20 S. Andersson, A. Sundholm and A. Magnéli, "A Homologous Series of Mixed Titanium
9] Chromium Oxides $Ti_{(n-2)}Cr_2O_{(2n-1)}$ Isomorphous with the Series $Ti_{(n)}O_{(2n-1)}$ and
 $V_{(n)}O_{(2n-1)}$," *Acta Chemica Scandinavica*, vol. 13, no. 5, pp. 989-997, 1959.
- [21 S. Andersson and L. Jahnberg, "Crystal structure studies on the homologous series TiO_{2n-}
0] $1, VnO_{2n-1}$ and $Ti_{n-2}Cr_2O_{2n-1}$," *Arkiv Kemi*, vol. 21, pp. 413-426, 1963.

- [21 G. Andersson, "Studies on Vanadium Oxides. I. Phase Analysis," *Acta Chemica Scandinavica*, vol. 8, no. 9, pp. 1599-1606, 1954.
- [21 J. S. Anderson and B. G. Hyde, "On the Possible Role of Dislocations in Generating Ordered and Disordered Shear Structures," *Journal of Physics and Chemistry of Solids*, vol. 28, no. 8, pp. 1393-1408, 1967.
- [21 J. S. Anderson and B. G. Hyde, "A dislocation mechanism for the production of Magnéli shear structures," *Bulletin de la Société Chimique de France*, vol. 4, pp. 1215-1216, 1965.
- [21 D. Bejan, E. Guinea and N. J. Bunce, "On the nature of the hydroxyl radicals produced at boron-doped diamond and Ebonex (R) anodes," *Electrochimica Acta*, vol. 69, no. 275-281, pp. 275-281, 2012.
- [21 C. Comninellis, "Electrocatalysis in the Electrochemical Conversion/Combustion of Organic Pollutants for Waste-Water Treatment," *Electrochimica Acta*, vol. 39, no. 11-12, pp. 1857-1862, 1994.
- [21 P. A. Michaud, M. Panizza, L. Ouattara, T. Diaco, G. Foti and C. Comninellis, "Electrochemical oxidation of water on synthetic boron-doped diamond thin film anodes," *Journal of Applied Electrochemistry*, vol. 33, pp. 1515-154, 2003.

Appendices

Appendix A Supplementary Data

A.1 Supplementary Data for Chapter 1: Introduction

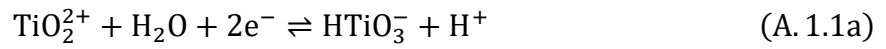
Potential-equilibria (Pourbaix) diagram of titanium in water

Chemical species considered

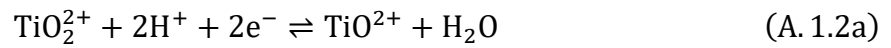
Ti oxidation state	Species	$\Delta_f G^0$ (kJ mol ⁻¹)	Reference
0	Ti	0.	
2+	Ti ²⁺	-314.	78
2+	TiO	-495.0	59
3+	Ti ³⁺	-350.	78
3+	Ti ₂ O ₃	-1,434.2	59
3.33+	Ti ₃ O ₅	-2,317.4	59
3.5+	Ti ₄ O ₇	-3,213.	79
4+	HTiO ₃ ⁻	-955.9	78
4+	TiO ²⁺	-577.4	78
4+	TiO ₂	-888.8	59
6+	TiO ₂ ²⁺	-467.2	78
	H ⁺	0.00	
	H ₂	0.00	
	H ₂ O	-237.1	59
	O ₂	0.00	
	·OH	7.74	78

Reactions involving two dissolved chemical species

Involving species with OS 6+ and 4+:



$$E_{\text{eq}} = 1.304 + 0.0296\text{pH} - 0.0296 \log\left(\frac{a_{\text{HTiO}_3^-}}{a_{\text{TiO}_2^{2+}}}\right) \quad (\text{A. 1.1b})$$



$$E_{\text{eq}} = 1.800 - 0.00591\text{pH} - 0.0296 \log\left(\frac{a_{\text{TiO}^{2+}}}{a_{\text{TiO}_2^{2+}}}\right) \quad (\text{A. 1.2b})$$

Involving species with OS 4+:



Involving species with OS 4+ and 3+:

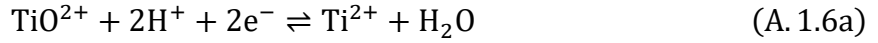


$$E_{\text{eq}} = 0.101 - 0.1182\text{pH} - 0.0591 \log\left(\frac{a_{\text{Ti}^{3+}}}{a_{\text{HTiO}_3^-}}\right) \quad (\text{A. 1.4b})$$

Involving species with OS 4+ and 2+:



$$E_{\text{eq}} = 0.359 - 0.1479\text{pH} - 0.0296 \log\left(\frac{a_{\text{Ti}^{2+}}}{a_{\text{HTiO}_3^-}}\right) \quad (\text{A. 1.5b})$$



$$E_{\text{eq}} = -0.136 - 0.0591\text{pH} - 0.0296 \log\left(\frac{a_{\text{Ti}^{2+}}}{a_{\text{TiO}^{2+}}}\right) \quad (\text{A. 1.6b})$$

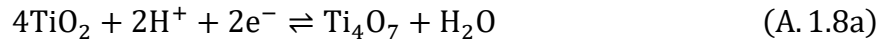
Involving species with OS 3+ and 2+:



$$E_{\text{eq}} = -0.373 - 0.0591 \log\left(\frac{a_{\text{Ti}^{2+}}}{a_{\text{Ti}^{3+}}}\right) \quad (\text{A. 1.7b})$$

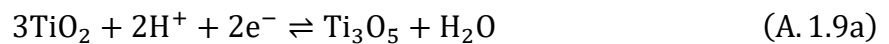
Reactions involving two solid chemical species

Involving species with OS 4+ and 3.5+:



$$E_{\text{eq}} = -0.545 - 0.0591\text{pH} \quad (\text{A. 1.8b})$$

Involving species with OS 4+ and 3.33+:



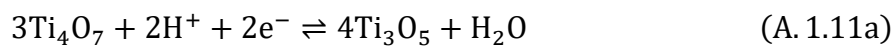
$$E_{\text{eq}} = -0.580 - 0.0591\text{pH} \quad (\text{A. 1.9b})$$

Involving species with OS 4+ and 3+:



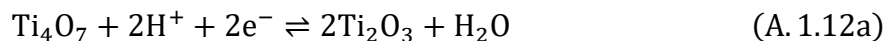
$$E_{\text{eq}} = -0.551 - 0.0591\text{pH} \quad (\text{A. 1.10b})$$

Involving species with OS 3.5+ and 3.33+:



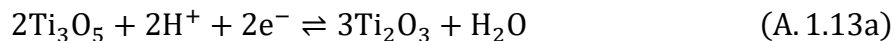
$$E_{\text{eq}} = -0.686 - 0.0591\text{pH} \quad (\text{A. 1.11b})$$

Involving species with OS 3.5+ and 3+:



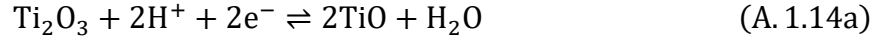
$$E_{\text{eq}} = -0.557 - 0.0591\text{pH} \quad (\text{A. 1.12b})$$

Involving species with OS 3.33+ and 3+:



$$E_{\text{eq}} = -0.493 - 0.0591\text{pH} \quad (\text{A. 1.13b})$$

Involving species with OS 3+ and 2+:



$$E_{\text{eq}} = -1.073 - 0.0591\text{pH} \quad (\text{A. 1.14b})$$

Involving species with OS 2+ and 0:



$$E_{\text{eq}} = -1.073 - 0.0591\text{pH} \quad (\text{A. 1.15b})$$

Reactions involving one dissolved and one solid chemical species

Involving species with OS 6+ and 4+:

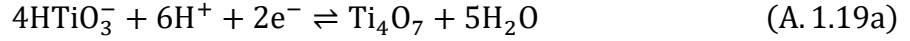


$$E_{\text{eq}} = 2.185 + 0.0296 \log(a_{\text{TiO}_2^{2+}}) \quad (\text{A. 1.16b})$$

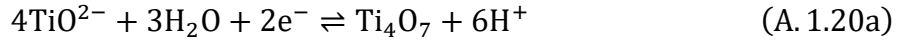
Involving species with OS 4+:



Involving species with OS 4+ and 3.5+:

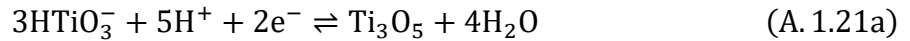


$$E_{\text{eq}} = 2.979 - 0.1775\text{pH} + 0.1183 \log(a_{\text{HTiO}_3^-}) \quad (\text{A. 1.19b})$$

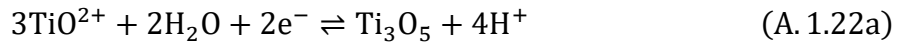


$$E_{\text{eq}} = 2.979 + 0.1775\text{pH} + 0.1183 \log(a_{\text{TiO}^{2-}}) \quad (\text{A. 1.20b})$$

Involving species with OS 4+ and 3.33+:

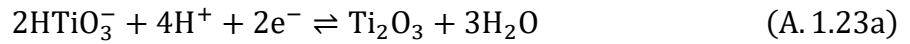


$$E_{\text{eq}} = 2.063 - 0.1479\text{pH} + 0.0887 \log(a_{\text{HTiO}_3^-}) \quad (\text{A. 1.21b})$$

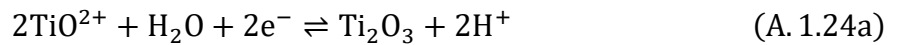


$$E_{\text{eq}} = 0.575 + 0.1183\text{pH} + 0.0887 \log(a_{\text{TiO}^{2-}}) \quad (\text{A. 1.22b})$$

Involving species with OS 4+ and 3+:



$$E_{\text{eq}} = 1.211 - 0.1183\text{pH} + 0.0592 \log(a_{\text{HTiO}_3^-}) \quad (\text{A. 1.23b})$$



$$E_{\text{eq}} = 0.219 + 0.0592\text{pH} + 0.0592 \log(a_{\text{TiO}^{2-}}) \quad (\text{A. 1.24b})$$



$$E_{\text{eq}} = -0.670 - 0.2366\text{pH} - 0.0296 \log(a_{\text{Ti}^{3+}}) \quad (\text{A. 1.25b})$$

A.2 Supplementary Data for Chapter 3: The Thermal-Oxidation Behaviour of Pristine and Doped Magnéli Phase Titanium Oxides

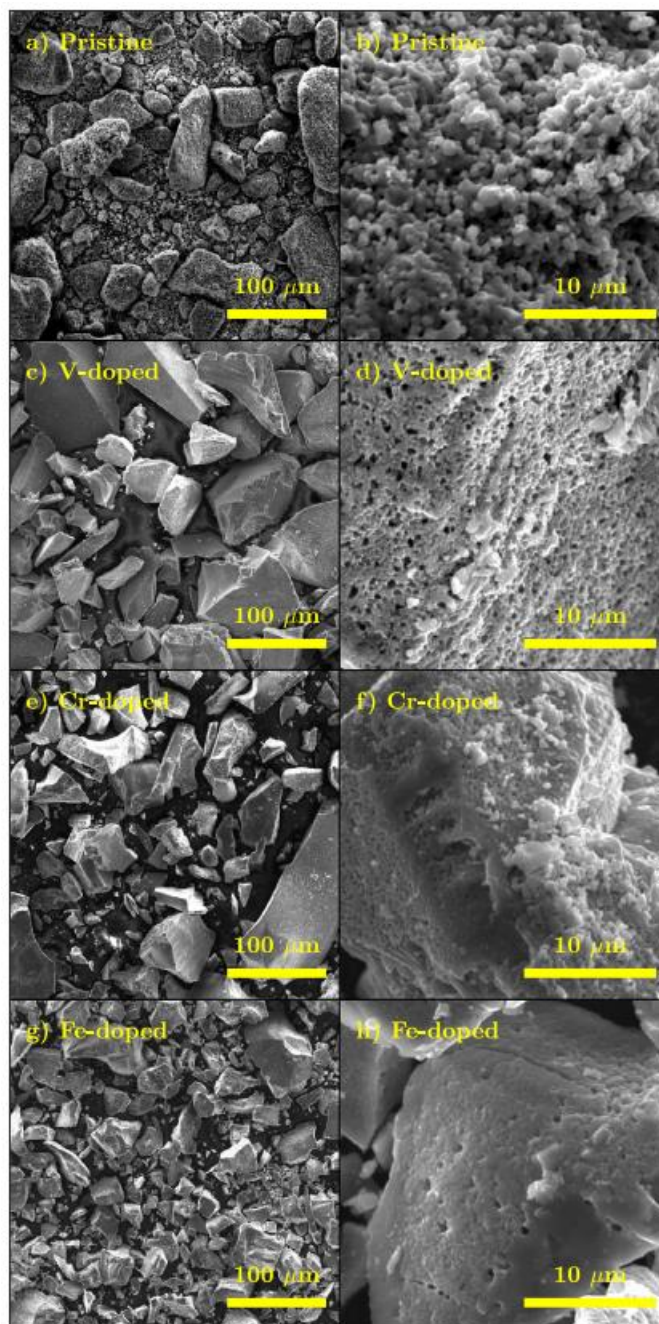


Figure A.2.1 Scanning electron micrographs (20 kV) of pristine and dopant-containing H₂-reduced TiO₂ at 200 (a, c, e, & g) and 3,200 (b, d, f, & h) magnification. Image reproduced from [65], which permits unrestricted reuse of the work via the Creative Commons Attribution 4.0 License (CC BY, <http://creativecommons.org/licenses/by/4.0/>).

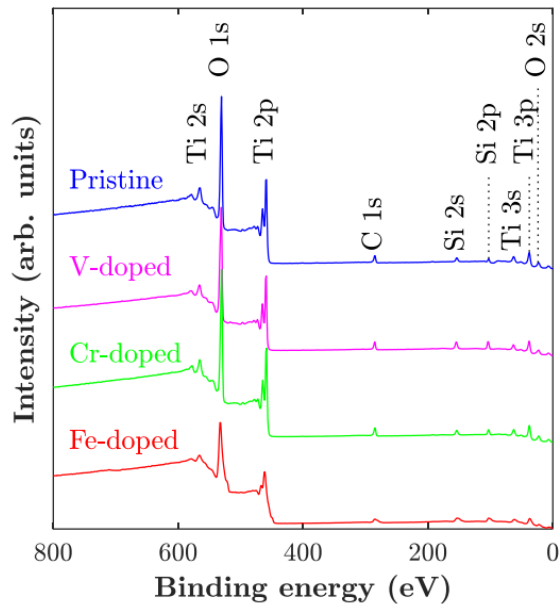


Figure A.2.2 Survey X-ray photoelectron spectra of pristine (blue line) and V-, Cr-, and Fe-doped (magenta, green, & red lines, respectively) H₂-reduced TiO₂. Image reproduced from [65], which permits unrestricted reuse of the work via the Creative Commons Attribution 4.0 License (CC BY, <http://creativecommons.org/licenses/by/4.0/>).

	O (at%)	Ti (at%)	C (at%)	Si (at%)
Pristine	64.4	21.1	11.2	3.2
V-doped	63.5	17.5	10.3	8.7
Cr-doped	63.1	20.4	11.3	5.2
Fe-doped	63.0	14.7	11.3	11.0

Table A.2.1 Summary of elemental analysis of survey spectra from X-ray photoelectron spectroscopy of pristine and dopant-containing H₂-reduced TiO₂.

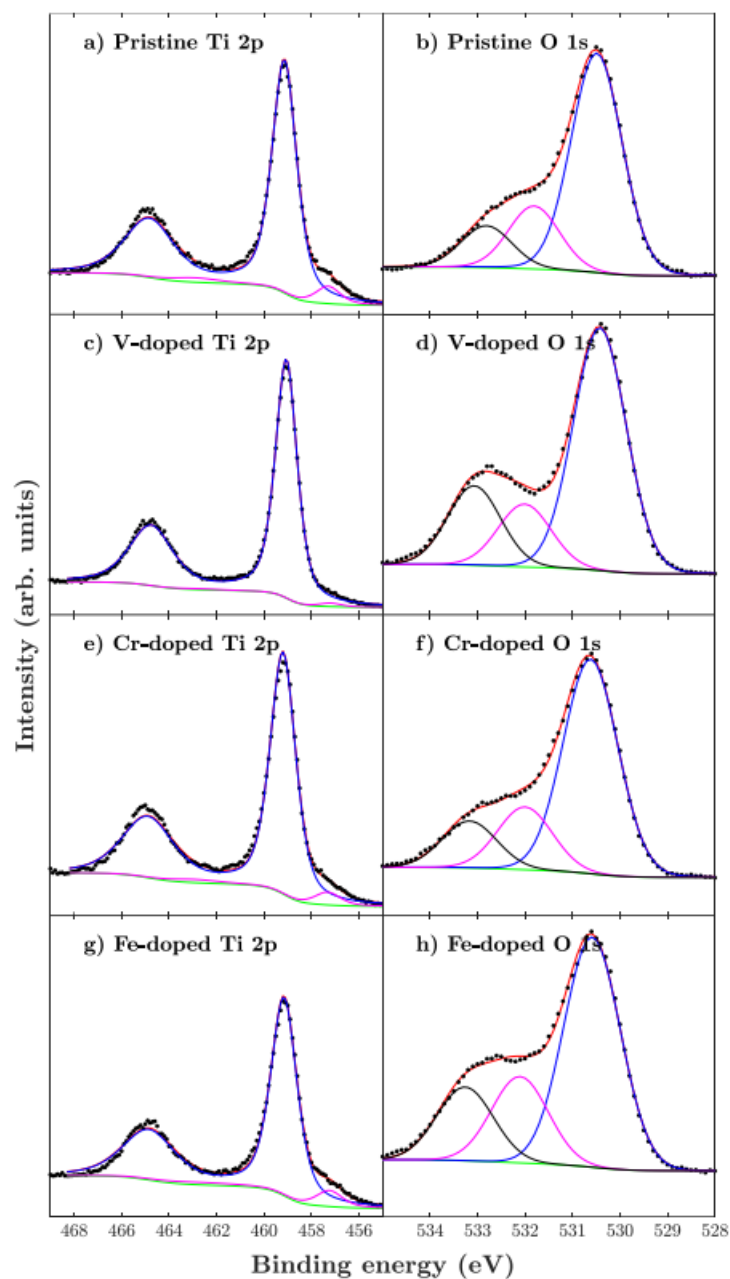


Figure A.2.3 High resolution X-ray photoelectron spectra (black dots) of (a, c, e, & g) Ti 2p and (b, d, f, & h) O 1s of (a & b) pristine and (c–h) dopant-containing H₂-reduced TiO₂ along with a Taylor baseline (green line), constituent peaks (blue, magenta, & black lines), and sum of baseline and constituent peaks (red line) Image reproduced from [65], which permits unrestricted reuse of the work via the Creative Commons Attribution 4.0 License (CC BY, <http://creativecommons.org/licenses/by/4.0/>).

	Peak	Species	BE (eV)	FWHM (eV)	Area ^a (%)	L-G (%)	χ^2		
Pristine	O 1s	TiO ₂	530.5	1.26	67.7	6	2.63		
		M(OH) _x	531.8		19.4				
		SiO ₂	532.8		12.1				
	Ti 2p _{3/2}	TiO ₂	459.1	1.24	62.0	53	7.93		
		Ti ₂ O ₃	457.3		4.6				
		Ti 2p _{1/2}	TiO ₂	465.0	2.47	31.0			
		Ti ₂ O ₃	462.9		2.3				
		V-doped	O 1s	TiO ₂	530.4	1.31	63.0	4	3.15
				M(OH) _x	532.0		16.3		
		SiO ₂	533.1		20.6				
	Ti 2p _{3/2}	TiO ₂	459.1	1.29	65.7	54	3.79		
		Ti ₂ O ₃	457.2		1.0				
		Ti 2p _{1/2}	TiO ₂	464.8	2.57	32.8			
		Ti ₂ O ₃	462.8		0.5				

^a Areas of Ti 2p_{3/2} and 2p_{1/2} peaks combined sum to 100%.

Table A.2.2 Summary of peak fitting of high-resolution X-ray photoelectron spectra including their binding energy (BE), full width half maximum (FWHM), Lorentzian-Gaussian (L-G), and results of chi-squared (χ^2) testing of pristine and V-containing H₂-reduced TiO₂.

	Peak	Species	BE (eV)	FWHM (eV)	Area ^a (%)	L-G (%)	χ^2
Cr-doped	O 1s	TiO ₂	530.6	1.36	66.1	4	2.59
		M(OH) _x	532.0		19.4		
		SiO ₂	533.2		14.5		
	Ti 2p _{3/2}	TiO ₂	459.2	1.29	63.3	48	9.77
		Ti ₂ O ₃	457.3		3.4		
	Ti 2p _{1/2}	TiO ₂	464.9	2.57	31.7		
		Ti ₂ O ₃	462.9		1.7		
Fe-doped	O 1s	TiO ₂	530.6	1.40	59.0	1	2.66
		M(OH) _x	532.1		22.1		
		SiO ₂	533.3		18.9		
	Ti 2p _{3/2}	TiO ₂	459.2	1.31	61.7	51	8.07
		Ti ₂ O ₃	457.2		5.0		
	Ti 2p _{1/2}	TiO ₂	464.8	2.62	30.8		
		Ti ₂ O ₃	462.8		2.5		

^a Areas of Ti 2p_{3/2} and 2p_{1/2} peaks combined sum to 100%.

Table A.2.3 Summary of peak fitting of high-resolution X-ray photoelectron spectra including their binding energy (BE), full width half maximum (FWHM), Lorentzian-Gaussian (L-G), and results of chi-squared (χ^2) testing of Cr- and Fe-containing H₂-reduced TiO₂.

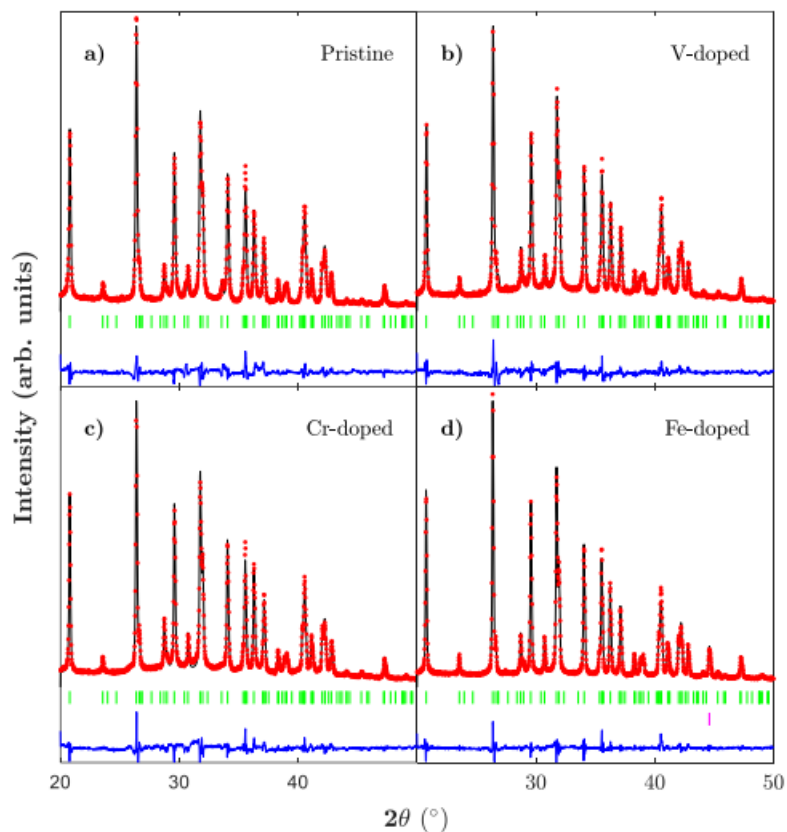


Figure A.2.4 Structure refinement data (Y_{calc} , black line) of powder X-ray diffraction data (Y_{obs} , red dots), their difference ($Y_{\text{obs}} - Y_{\text{calc}}$, blue line), and the Bragg positions of Ti_4O_7 (green vertical lines) and alpha iron ($\alpha\text{-Fe}$, magenta vertical lines) for (a) pristine and (b–d) dopant-containing H_2 -reduced TiO_2 . Image reproduced from [65], which permits unrestricted reuse of the work via the Creative Commons Attribution 4.0 License (CC BY, <http://creativecommons.org/licenses/by/4.0/>).

	Pristine	V-doped	Cr-doped	Fe-doped
Crystal system	Triclinic			
Space group	$\bar{1}$			
Z-value	4			
a (Å)	5.60(01)	5.60(01)	5.58(01)	5.59(01)
b (Å)	7.12(02)	7.12(02)	7.10(02)	7.10(01)
c (Å)	12.46(04)	12.46(04)	12.43(03)	12.44(02)
α (°)	95.04(11)	95.02(10)	95.02(09)	95.01(06)
β (°)	95.16(01)	95.14(01)	95.15(010)	95.16(01)
γ (°)	108.79(01)	108.76(01)	108.77(01)	108.76(01)
V (Å ³)	464(2)	464(2)	461(1)	462(1)
τ (nm)	86(05)	122(10)	128(09)	173(11)
ε (%)	0.03(4)	0.15(4)	0.09(3)	0.23(1)
R_{wp} (%)	8.06	7.03	7.11	5.61

Table A.2.4 Summary of the fitted lattice parameters and volume (V) of the unit cell, crystallite size (τ), and strain (ε) of the Ti_4O_7 phase as well as the weighted profile R-factor (R_{wp}) obtained by structure refinement of powder X-ray diffraction data of H_2 -reduced pristine and doped TiO_2 .

	Pristine	V-doped	Cr-doped	Fe-doped
Ti(1) <i>x</i>	0.227(03)	0.207(03)	0.208(03)	0.215(03)
<i>y</i>	0.158(03)	0.150(02)	0.154(03)	0.158(02)
<i>z</i>	0.067(01)	0.060(02)	0.061(02)	0.061(01)
Ti(2) <i>x</i>	0.212(02)	0.230(03)	0.235(03)	0.223(04)
<i>y</i>	0.665(03)	0.667(05)	0.671(04)	0.661(03)
<i>z</i>	0.067(02)	0.076(02)	0.073(02)	0.072(01)
Ti(3) <i>x</i>	0.690(04)	0.674(04)	0.681(02)	0.679(02)
<i>y</i>	0.438(03)	0.435(03)	0.442(02)	0.442(02)
<i>z</i>	0.196(01)	0.195(02)	0.197(02)	0.199(01)
Ti(4) <i>x</i>	0.677(02)	0.682(05)	0.676(04)	0.687(05)
<i>y</i>	0.931(04)	0.931(04)	0.932(04)	0.934(04)
<i>z</i>	0.204(01)	0.204(01)	0.205(02)	0.207(01)
O(1) <i>x</i>	0.127(09)	0.131(11)	0.108(01)	0.146(08)
<i>y</i>	0.853(08)	0.836(09)	0.848(10)	0.864(09)
<i>z</i>	0.022(03)	0.026(03)	0.029(04)	0.025(03)
O(2) <i>x</i>	0.607(07)	0.584(08)	0.603(09)	0.564(10)
<i>y</i>	0.809(04)	0.795(06)	0.810(06)	0.791(06)
<i>z</i>	0.056(03)	0.054(03)	0.053(03)	0.066(03)

Table A.2.5 Summary of the positional parameters of the unit cell of the Ti₄O₇ phase obtained by structure refinement of powder X-ray diffraction data of H₂-reduced pristine and doped TiO₂.

	Pristine	V-doped	Cr-doped	Fe-doped
O(3) <i>x</i>	0.908(08)	0.879(05)	0.857(07)	0.849(09)
<i>y</i>	0.489(07)	0.466(05)	0.478(08)	0.471(06)
<i>z</i>	0.067(02)	0.062(02)	0.056(04)	0.063(04)
O(4) <i>x</i>	0.367(06)	0.347(07)	0.345(07)	0.358(05)
<i>y</i>	0.499(06)	0.487(09)	0.475(10)	0.463(05)
<i>z</i>	0.143(03)	0.151(03)	0.150(04)	0.150(03)
O(5) <i>x</i>	0.604(08)	0.575(12)	0.527(08)	0.540(06)
<i>y</i>	0.137(12)	0.124(14)	0.118(11)	0.128(07)
<i>z</i>	0.168(04)	0.153(05)	0.146(03)	0.162(03)
O(6) <i>x</i>	-0.003(10)	-0.038(09)	-0.034(07)	-0.013(13)
<i>y</i>	0.037(04)	0.042(05)	0.031(04)	0.053(06)
<i>z</i>	0.196(02)	0.199(02)	0.196(02)	0.196(02)
O(7) <i>x</i>	0.289(05)	0.291(07)	0.287(06)	0.310(05)
<i>y</i>	0.769(05)	0.770(05)	0.770(04)	0.775(03)
<i>z</i>	0.208(02)	0.214(03)	0.219(03)	0.219(02)

Table A.2.6 (Continued from Table A.2.5) Summary of the positional parameters of the unit cell of the Ti₄O₇ phase obtained by structure refinement of powder X-ray diffraction data of H₂-reduced pristine and doped TiO₂.

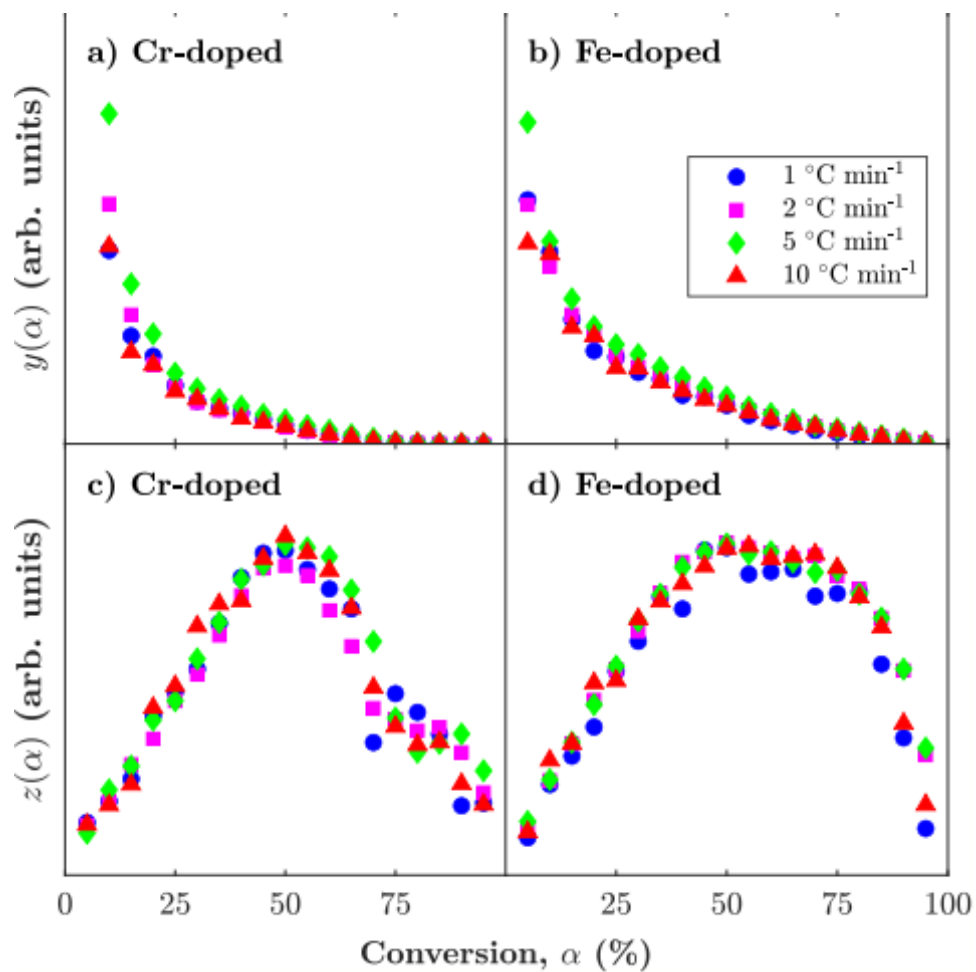


Figure A.2.5 (a & b) $y(\alpha)$ and (c & d) $z(\alpha)$ master plots for the thermal oxidation of (a & c) Cr- and (b & d) Fe-doped Ti_4O_7 in air. Image reproduced from [65], which permits unrestricted reuse of the work via the Creative Commons Attribution 4.0 License (CC BY, <http://creativecommons.org/licenses/by/4.0/>).

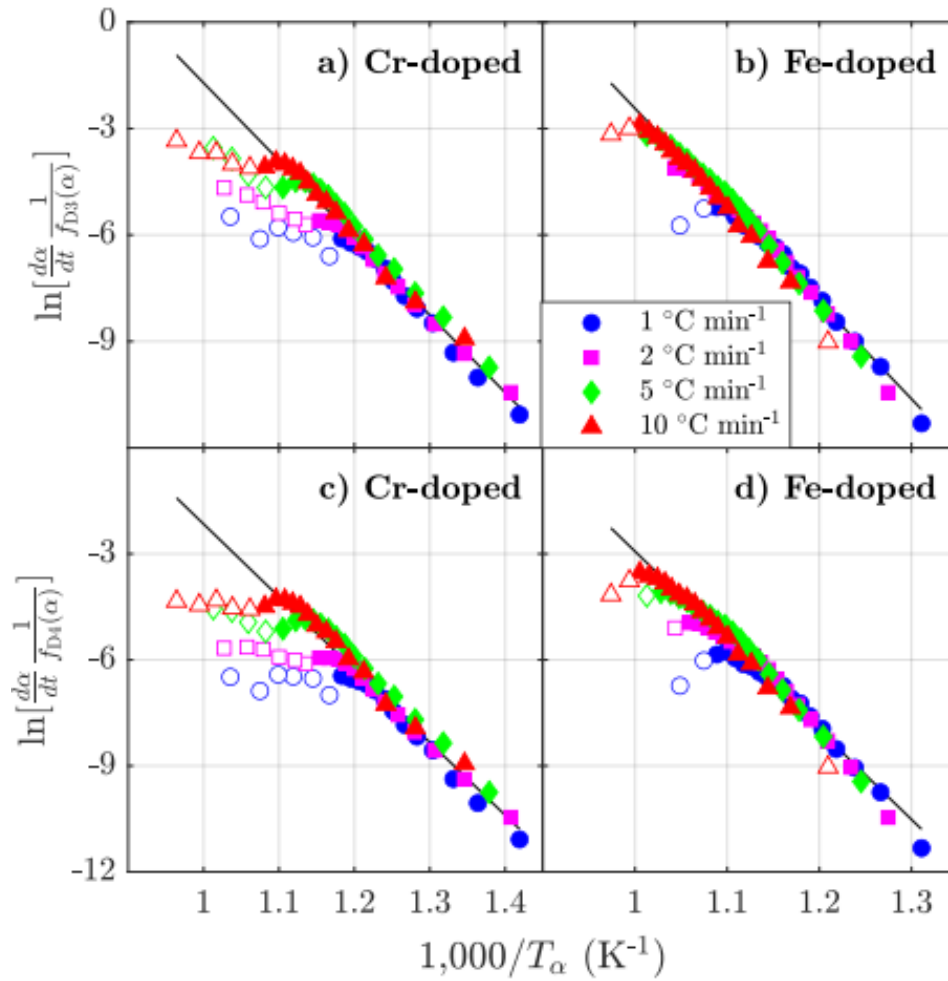


Figure A.2.6 Linearized differential data ($\ln\{f(d\alpha/dt)[1/f(\alpha)]\}$) for three-dimensional diffusion reaction models (a & b) Jander (D3, $f(\alpha) = f_{D3}(\alpha)$) and (c & d) Ginstling-Brounshtein (D4, $f(\alpha) = f_{D4}(\alpha)$) versus $1,000/T$ for the thermal oxidation of (a & c) Cr- and (b & d) Fe-doped Ti_4O_7 in air with linear fit (straight line, empty markers indicating outliers). Image reproduced from [65], which permits unrestricted reuse of the work via the Creative Commons Attribution 4.0 License (CC BY, <http://creativecommons.org/licenses/by/4.0/>).

A.3 Supplementary Data for Chapter 4: The Superior Electrical Conductivity and Anodic Stability of Vanadium-Doped Ti_4O_7

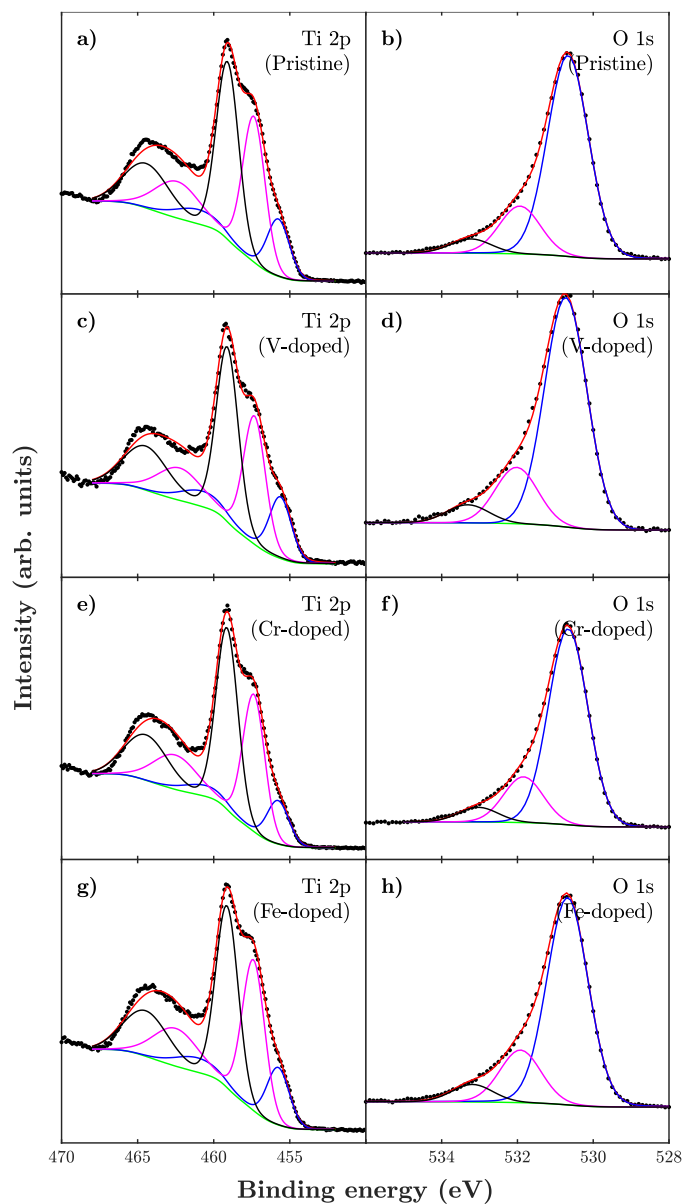


Figure A.3.1 High-resolution X-ray photoelectron spectra (20 kV) of (a, c, e, & g) Ti 2p and O 1s (b, d, f, & h) peaks of Ar-ion etched (4 keV) H₂-reduced (a & b) pristine and (c–h) dopant-containing sintered TiO₂ disks and their deconvolution including Taylor baseline (green lines), constituent peaks (blue, magenta, and black lines) and sum of baseline and constituent peaks (red lines). Image reproduced from [66], which permits unrestricted reuse of the work via the Creative Commons Attribution 4.0 License (CC BY, <http://creativecommons.org/licenses/by/4.0/>).

BE (eV)	Peak	Species	FWHM (eV)	Area ^a (%)	L-G (%)	χ^2
455.8	Ti 2p _{3/2}	TiO	15.1	1.73	4	5.13
457.4		Ti ₂ O ₃	38.3			
459.1		TiO ₂	46.7			
461.0	Ti 2p _{1/2}	TiO	15.1	3.45		
462.4		Ti ₂ O ₃	38.3			
464.4		TiO ₂	46.7			
530.7	O 1s	TiO ₂	76.3	1.27	4	2.87
531.9		M(OH) _x	18.2			
533.2		H ₂ O	5.4			

Table A.3.1 Summary of peak fitting of high-resolution X-ray photoelectron spectra including their binding energy (BE), full width half maximum (FWHM), Lorentzian-Gaussian (L-G), and results of chi-squared (χ^2) testing of H₂-reduced pristine sintered TiO₂ disks.

BE (eV)	Peak	Species	FWHM (eV)	Area ^a (%)	L-G (%)	χ^2
455.6	Ti 2p _{3/2}	TiO	17.0	1.70	11	3.45
457.3		Ti ₂ O ₃	35.1			
459.1		TiO ₂	48.0			
460.7	Ti 2p _{1/2}	TiO	17.0	3.40		
462.3		Ti ₂ O ₃	35.1			
464.5		TiO ₂	48.0			
513.3	V 2p _{3/2}	V ₂ O ₃	67.1	1.93	35	0.13
515.8		V ₂ O ₄	32.9			
530.7	O 1s	TiO ₂	75.5	1.31	0	2.01

Table A.3.2 Summary of peak fitting of high-resolution X-ray photoelectron spectra including their binding energy (BE), full width half maximum (FWHM), Lorentzian-Gaussian (L-G), and results of chi-squared (χ^2) testing of H₂-reduced vanadium-containing sintered TiO₂ disks.

BE (eV)	Peak	Species	FWHM (eV)	Area ^a (%)	L-G (%)	χ^2
455.8	Ti 2p _{3/2}	TiO	12.0	1.68	3	4.38
457.4		Ti ₂ O ₃	37.9			
459.1		TiO ₂	50.1			
460.5	Ti 2p _{1/2}	TiO	12.0	3.37		
462.5		Ti ₂ O ₃	37.9			
464.5		TiO ₂	50.1			
530.7	O 1s	TiO ₂	76.4	1.22	2	2.35
531.8		M(OH) _x	17.9			
533.3		H ₂ O	5.7			

Table A.3.3 Summary of peak fitting of high-resolution X-ray photoelectron spectra including their binding energy (BE), full width half maximum (FWHM), Lorentzian-Gaussian (L-G), and results of chi-squared (χ^2) testing of H₂-reduced chromium-containing sintered TiO₂ disks.

BE (eV)	Peak	Species	FWHM (eV)	Area ^a (%)	L-G (%)	χ^2
455.8	Ti 2p _{3/2}	TiO	14.7	1.73	3	2.40
457.4		Ti ₂ O ₃	38.7			
459.1		TiO ₂	46.6			
461.0	Ti 2p _{1/2}	TiO	14.7	3.47		
462.5		Ti ₂ O ₃	38.7			
464.5		TiO ₂	46.6			
530.7	O 1s	TiO ₂	74.7	1.28	6	2.37
531.9		M(OH) _x	18.9			
533.2		H ₂ O	6.3			

Table A.3.4 Summary of peak fitting of high-resolution X-ray photoelectron spectra including their binding energy (BE), full width half maximum (FWHM), Lorentzian-Gaussian (L-G), and results of chi-squared (χ^2) testing of H₂-reduced iron-containing sintered TiO₂ disks.

Element	Peak	Species	BE (eV)	SBE (eV)	<i>n</i>
Ti	2p3/2	Ti	453.9	0.2	12
		TiO	455.2	0.7	3
		Ti ₂ O ₃	457.0	1.1	6
		TiO ₂	458.6	0.2	42
	2p1/2	Ti	460.0	0.1	2
		TiO	460.2		1
		Ti ₂ O ₃	462.0		1
		TiO ₂	464.5	0.2	10
V	2p3/2	V	512.4	0.2	11
		V ₂ O ₃	515.7	1.6	5
		V ₂ O ₄	516.2	0.4	3
		V ₂ O ₅	517.3	0.3	25
Fe	2p3/2	Fe	706.9	0.2	26
		FeO	709.8	0.5	7
		Fe ₂ O ₃	711.0	0.4	20

Table A.3.5 Summary of statistical analysis of reported values of compounds used in the deconvolution of high-resolution X-ray photoelectron spectra including the binding energy (BE), its sample standard deviation (SBE), and number of observations (*n*).

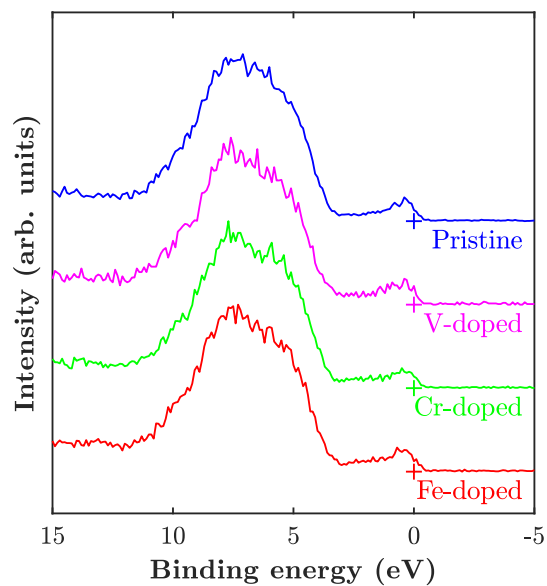


Figure A.3.2 Valence band spectra of H₂-reduced pristine and dopant-containing sintered TiO₂ disks obtained by X-ray photoelectron spectroscopy (20 kV). Plus signs (+) indicate the origin for their respective spectra. Image reproduced from [66], which permits unrestricted reuse of the work via the Creative Commons Attribution 4.0 License (CC BY, <http://creativecommons.org/licenses/by/4.0/>).

2θ	Intensity (%)	h	k	l
26.4	77.7	1	0	-2
26.8	15.2	1	-2	0
30.5	74.2	1	-2	2
33.7	100.0	1	0	-4
35.4	37.4	0	2	2
36.4	58.4	2	0	0
40.2	25.5	1	0	4
40.3	19.0	1	2	0
42.1	20.6	0	2	-4
44.6	26.8	2	1	-1

Table A.3.6 Summary of prominent peaks (>15% intensity) of powder X-ray diffractograms of Ti_3O_5 , their (relative) intensity, and assigned Miller indices (h , k , and l) between 2θ and $50^\circ 2\theta$.

2θ	Intensity (%)	h	k	l
20.8	68.8	1	0	-2
26.4	100.0	1	-2	0
29.6	68.2	1	-2	2
31.8	90.4	1	0	-4
32.0	42.7	0	2	2
34.1	60.7	2	0	0
35.6	49.9	1	0	4
36.3	41.3	1	2	0
37.1	32.3	0	2	-4
40.4	16.0	2	1	-1
40.5	17.7	0	1	5
40.6	16.8	2	-1	3
41.1	15.1	1	1	-5
42.0	15.4	0	3	1
42.3	23.7	0	2	4

Table A.3.7 Summary of prominent peaks (>15% intensity) of powder X-ray diffractograms of Ti₄O₇, their (relative) intensity, and assigned Miller indices (h, k, and l) between 20 and 50° 2 θ .

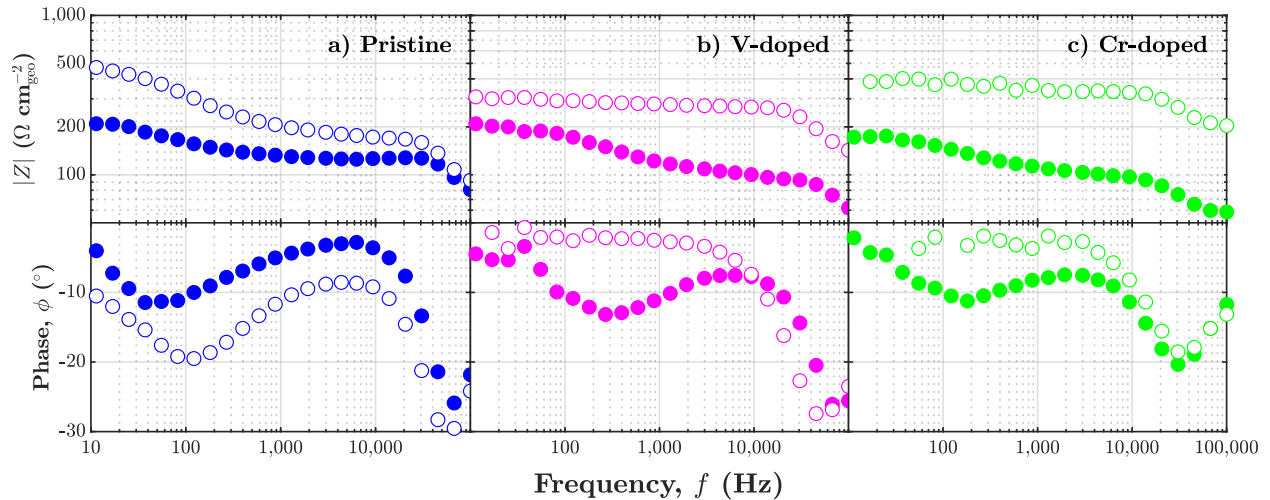


Figure A.3.3 Bode plots ($100 \pm 1 \text{ mA cm}^{-2}_{\text{geo}}$) of (a) pristine and (b & c) doped Ti_4O_7 disk electrodes (2,000 RPM) in $0.5 \text{ M H}_2\text{SO}_4$ (pH 0.4, $22 \text{ }^\circ\text{C}$) at the beginning (BOL, full circles) and near the end of life (EOL, open circles) during accelerated life testing. Image reproduced from [66], which permits unrestricted reuse of the work via the Creative Commons Attribution 4.0 License (CC BY, <http://creativecommons.org/licenses/by/4.0/>).

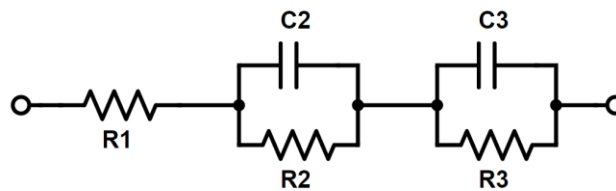


Figure A.3.4 Voigt-type electrical circuit as possible equivalent electrochemical circuit. Elements labelled with C and R refer to capacitors and resistors, respectively. R_1 refers to the solution resistance, C_2 & R_2 and C_3 & R_3 refer to individual Voigt elements, accounting for double layer and film capacitances and charge transfer and film resistances. Image reproduced from [66], which permits unrestricted reuse of the work via the Creative Commons Attribution 4.0 License (CC BY, <http://creativecommons.org/licenses/by/4.0/>).

A.4 Supplementary Data for Chapter 5: Vanadium-Doped TiO₂ Porous Transport Layers for Efficient Electrochemical Oxidation of Industrial Wastewater Contaminants

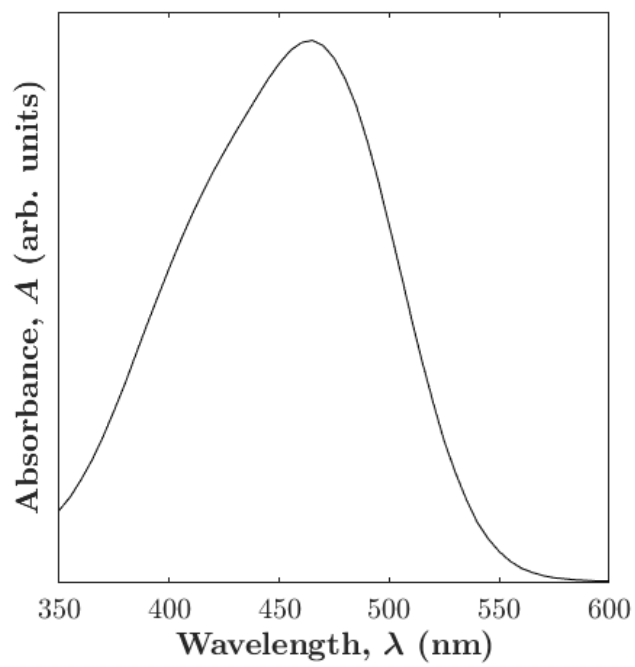


Figure A.4.1 UV-Visible absorbance spectra of methyl orange (100 ppm in 1,500 mg_{NaCl} L⁻¹).

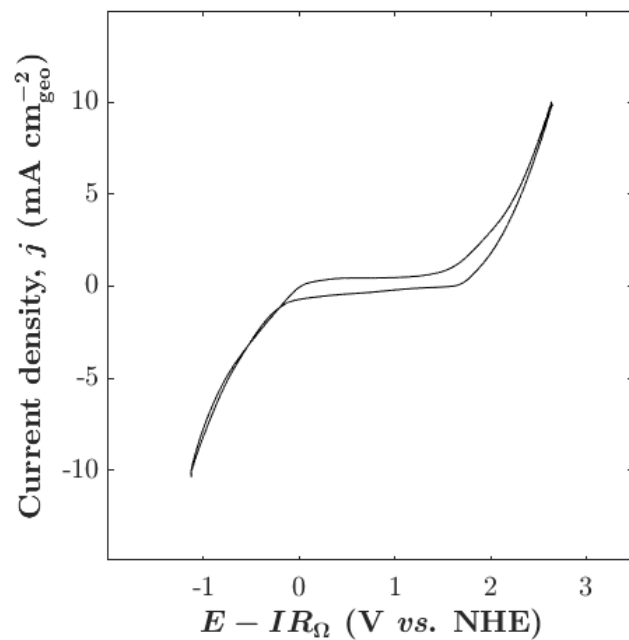


Figure A.4.2 Cyclic voltammograms (100 mV s^{-1} , tenth cycle) of Sigracet 29 BC gas diffusion layer in $1,500 \text{ mg}_{\text{NaCl}} \text{ L}^{-1}$ ($22 \text{ }^{\circ}\text{C}$, pH 5.3).

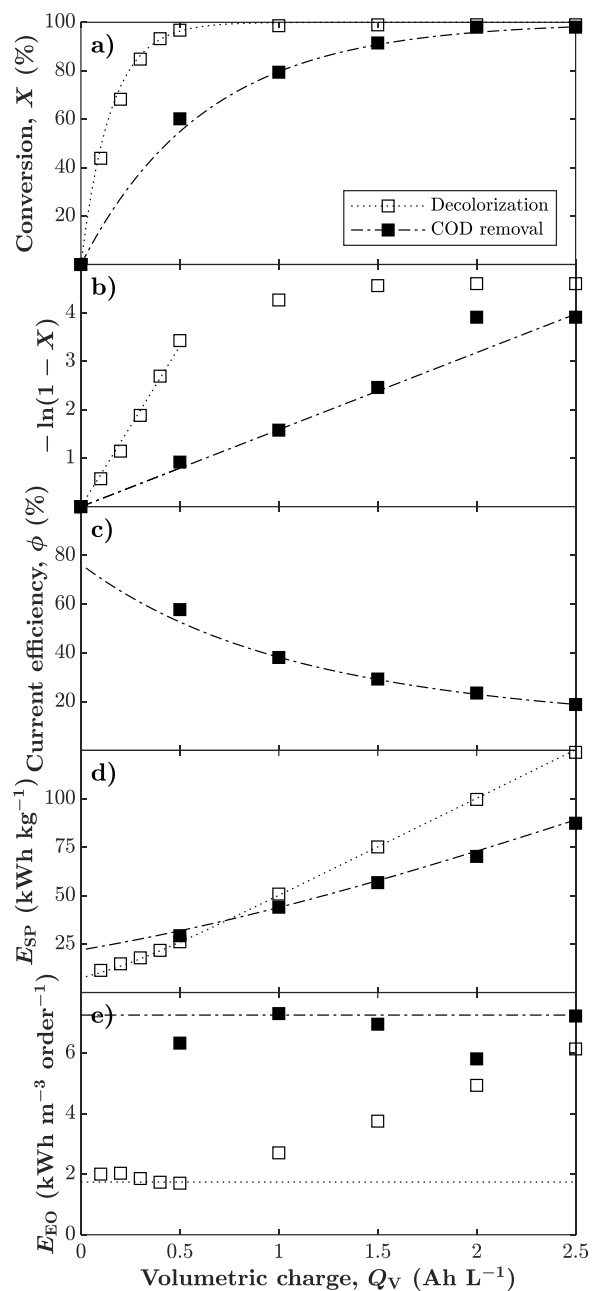


Figure A.4.3 Conversion (X , a), linearized conversion data ($-\ln(1 - X)$, b), current efficiency (ϕ , c), specific and volumetric energy consumption (E_{SP} & E_{EO} , respectively, d & e) for the decolorization and chemical oxygen demand (COD) removal (empty and filled symbols, respectively) of 100 ppm_{MO} in 1,500 g_{NaCl} (150 mL min⁻¹, 21 °C, 4.0 pH) with a (Ti_{0.98}V_{0.02})₄O₇ porous transport layer in a compact electrolyzer operated galvanostatically (10 mA cm⁻²). Dotted and dash-dotted lines indicate either lines of best fit (a & b) or model predictions (c–e, Eqs. 5.10, 5.11, & 5.6) for decolorization and COD removal, respectively.

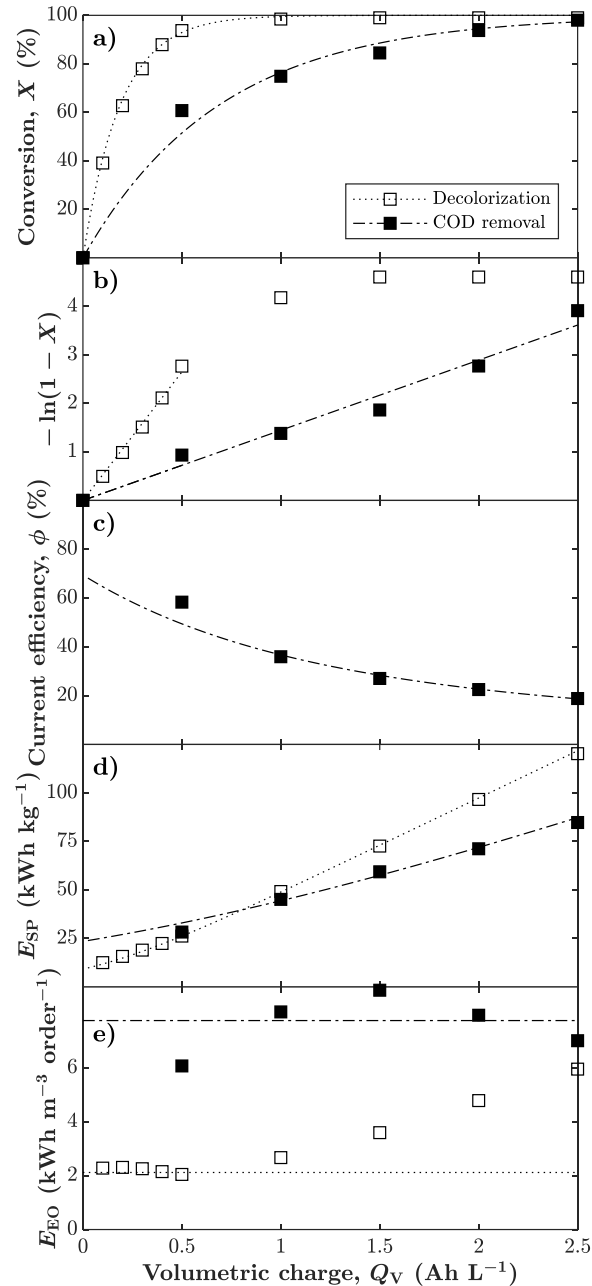


Figure A.4.4 Conversion (X , a), linearized conversion data ($-\ln(1 - X)$, b), current efficiency (ϕ , c), specific and volumetric energy consumption (E_{SP} & E_{EO} , respectively, d & e) for the decolorization and chemical oxygen demand (COD) removal (empty and filled symbols, respectively) of 100 ppm_{MO} in 1,500 g_{NaCl} (250 mL min⁻¹, 21 °C, 4.0 pH) with a (Ti_{0.98}V_{0.02})₄O₇ porous transport layer in a compact electrolyzer operated galvanostatically (10 mA cm⁻²). Dotted and dash-dotted lines indicate either lines of best fit (a & b) or model predictions (c–e, Eqs. 5.10, 5.11, & 5.6) for decolorization and COD removal, respectively.

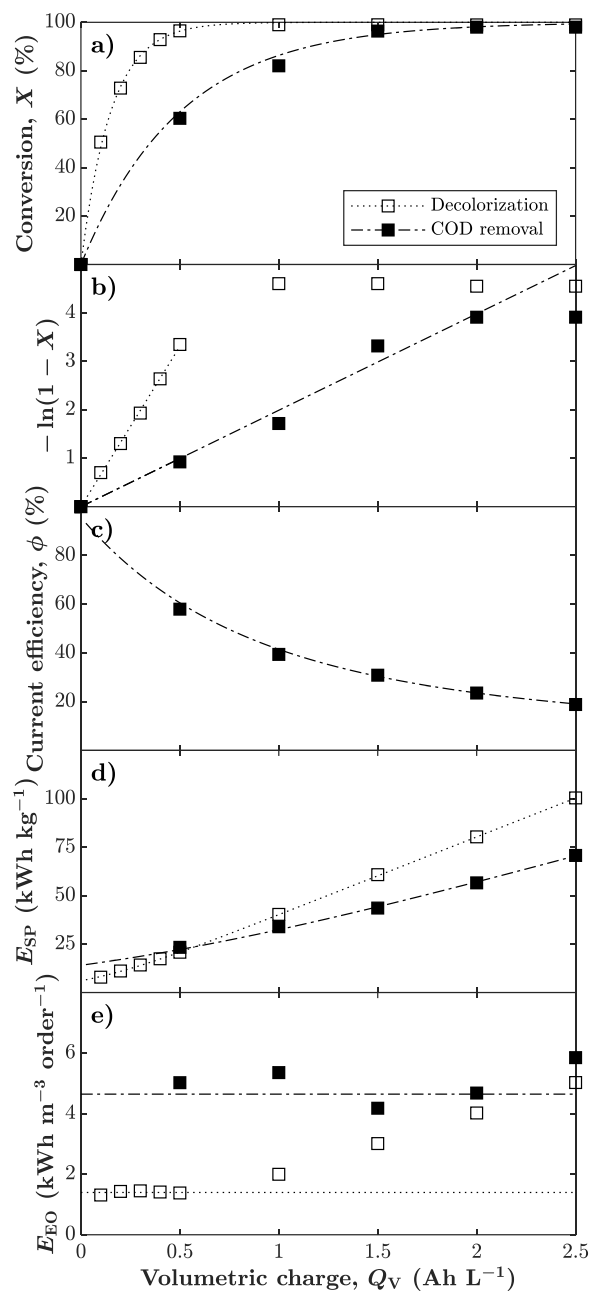


Figure A.4.5 Conversion (X , a), linearized conversion data ($-\ln(1 - X)$, b), current efficiency (ϕ , c), specific and volumetric energy consumption (E_{SP} & E_{EO} , respectively, d & e) for the decolorization and chemical oxygen demand (COD) removal (empty and filled symbols, respectively) of 100 ppm_{MO} in 1,500 g_{NaCl} (200 mL min⁻¹, 21 °C, 4.0 pH) with a (Ti_{0.98}V_{0.02})₄O₇ porous transport layer in a compact electrolyzer operated galvanostatically (2.5 mA cm⁻²). Dotted and dash-dotted lines indicate either lines of best fit (a & b) or model predictions (c–e, Eqs. 5.10, 5.11, & 5.6) for decolorization and COD removal, respectively.

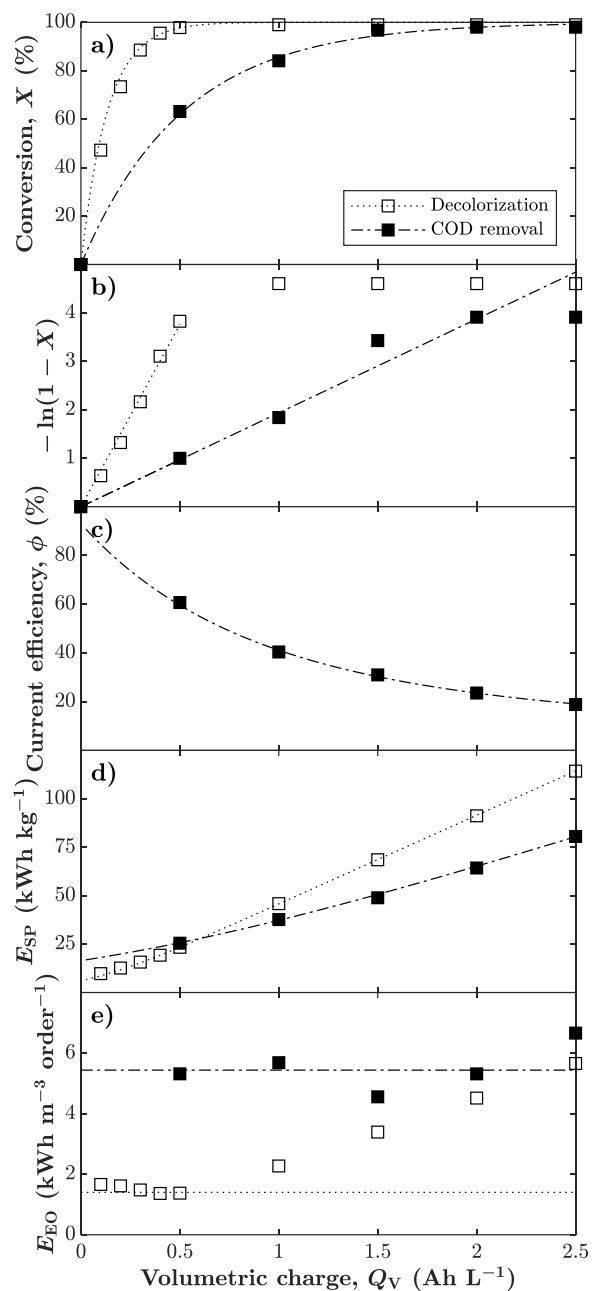


Figure A.4.6 Conversion (X , a), linearized conversion data ($-\ln(1 - X)$, b), current efficiency (ϕ , c), specific and volumetric energy consumption (E_{SP} & E_{EO} , respectively, d & e) for the decolorization and chemical oxygen demand (COD) removal (empty and filled symbols, respectively) of 100 ppm_{MO} in 1,500 g_{NaCl} (200 mL min⁻¹, 21 °C, 4.0 pH) with a (Ti_{0.98}V_{0.02})₄O₇ porous transport layer in a compact electrolyzer operated galvanostatically (5 mA cm⁻²). Dotted and dash-dotted lines indicate either lines of best fit (a & b) or model predictions (c–e, Eqs. 5.10, 5.11, & 5.6) for decolorization and COD removal, respectively.

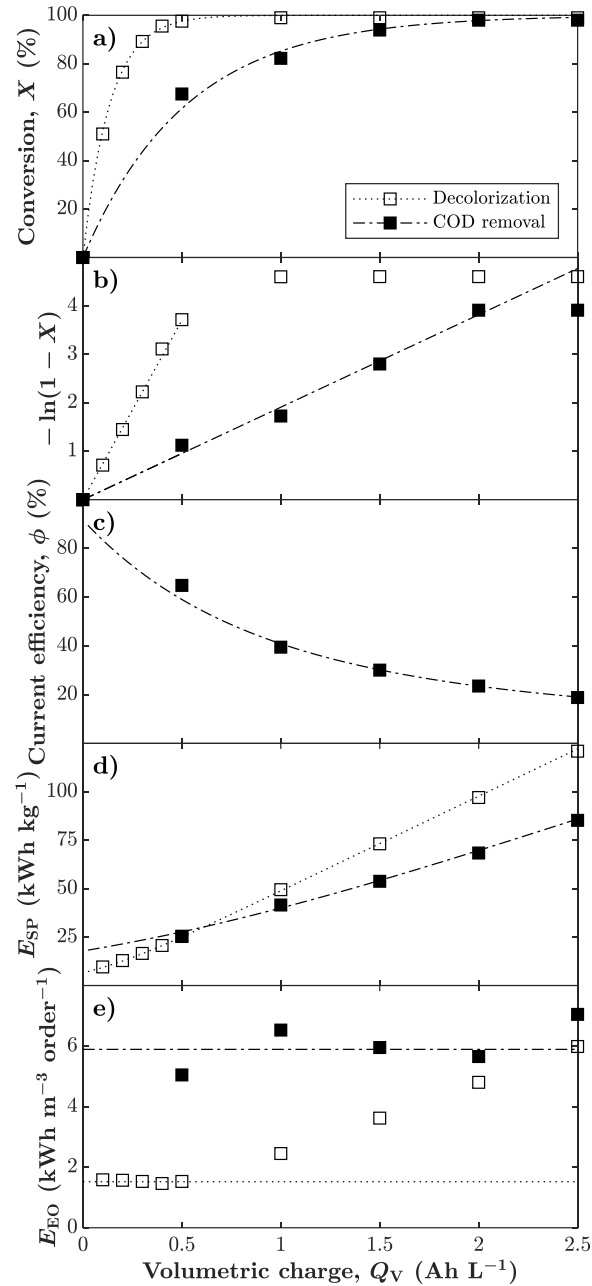


Figure A.4.7 Conversion (X , a), linearized conversion data ($-\ln(1 - X)$, b), current efficiency (ϕ , c), specific and volumetric energy consumption (E_{SP} & E_{EO} , respectively, d & e) for the decolorization and chemical oxygen demand (COD) removal (empty and filled symbols, respectively) of 100 ppm_{MO} in 1,500 g_{NaCl} (200 mL min⁻¹, 21 °C, 4.0 pH) with a (Ti_{0.98}V_{0.02})₄O₇ porous transport layer in a compact electrolyzer operated galvanostatically (7.5 mA cm⁻²). Dotted and dash-dotted lines indicate either lines of best fit (a & b) or model predictions (c–e, Eqs. 5.10, 5.11, & 5.6) for decolorization and COD removal, respectively.

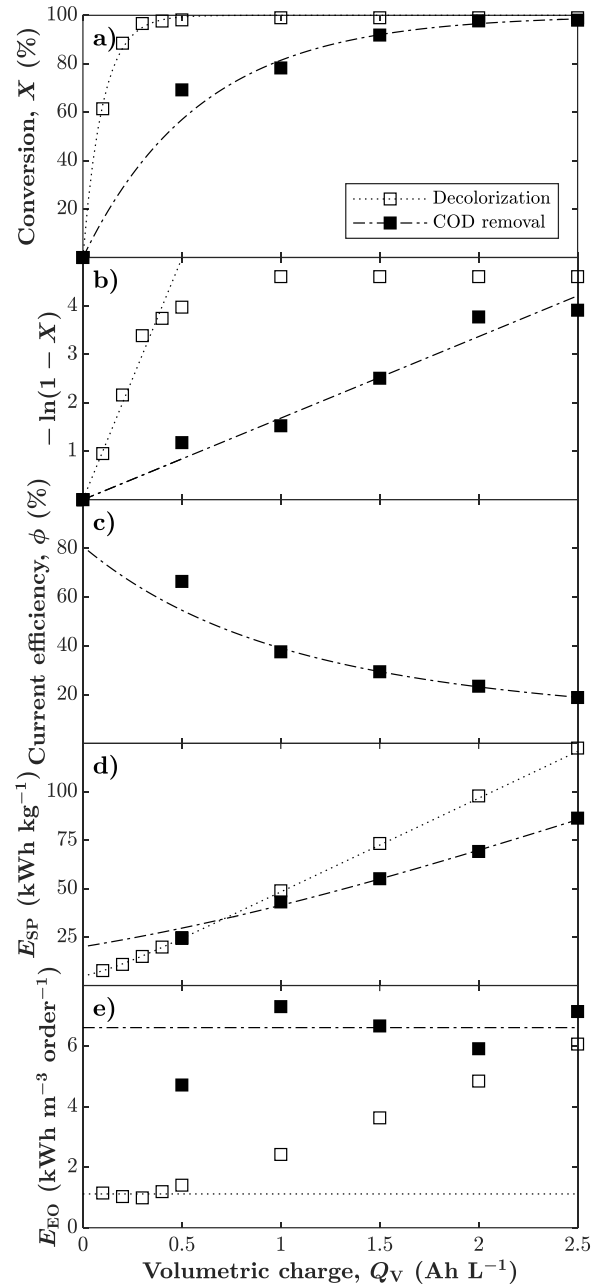


Figure A.4.8 Conversion (X , a), linearized conversion data ($-\ln(1 - X)$, b), current efficiency (ϕ , c), specific and volumetric energy consumption (E_{SP} & E_{EO} , respectively, d & e) for the decolorization and chemical oxygen demand (COD) removal (empty and filled symbols, respectively) of 100 ppm_{MO} in 1,500 g_{NaCl} (200 mL min⁻¹, 21 °C, 4.0 pH) with a (Ti_{0.98}V_{0.02})₄O₇ porous transport layer in a compact electrolyzer operated galvanostatically (12.5 mA cm⁻²). Dotted and dash-dotted lines indicate either lines of best fit (a & b) or model predictions (c–e, Eqs. 5.10, 5.11, & 5.6) for decolorization and COD removal, respectively.

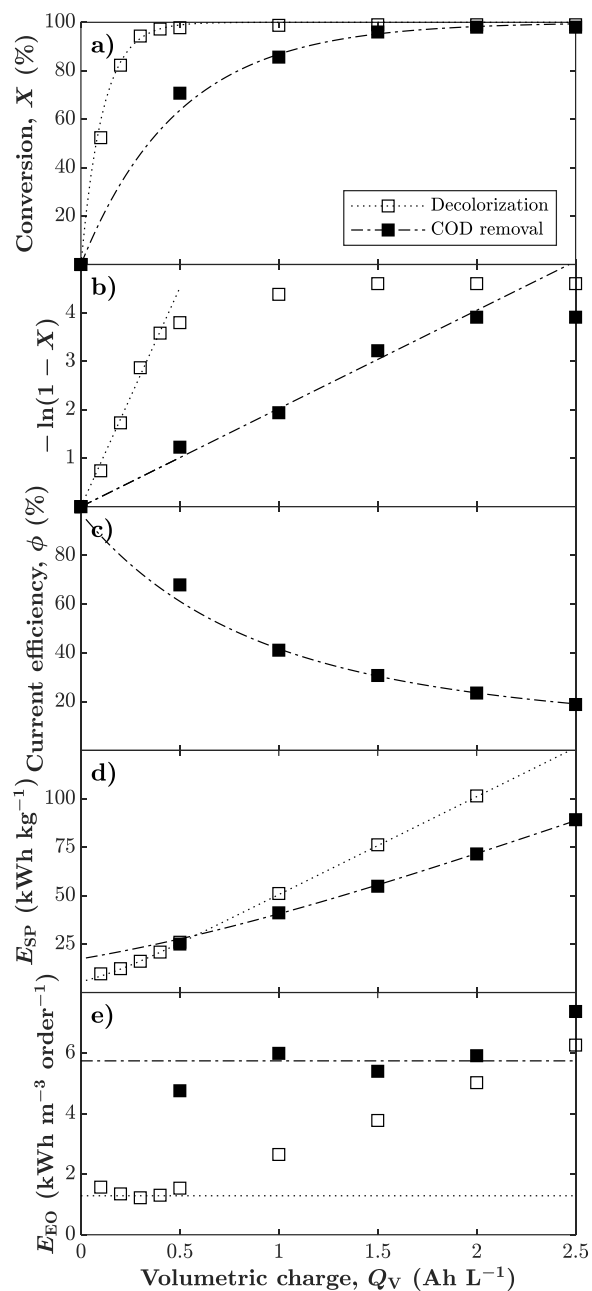


Figure A.4.9 Conversion (X , a), linearized conversion data ($-\ln(1 - X)$, b), current efficiency (ϕ , c), specific and volumetric energy consumption (E_{SP} & E_{EO} , respectively, d & e) for the decolorization and chemical oxygen demand (COD) removal (empty and filled symbols, respectively) of 100 ppm_{MO} in 1,500 g_{NaCl} (200 mL min^{-1} , $21 \text{ }^\circ\text{C}$, 4.0 pH) with a $(\text{Ti}_{0.98}\text{V}_{0.02})_4\text{O}_7$ porous transport layer in a compact electrolyzer operated galvanostatically (15 mA cm^{-2}). Dotted and dash-dotted lines indicate either lines of best fit (a & b) or model predictions (c–e, Eqs. 5.10, 5.11, & 5.6) for decolorization and COD removal, respectively.

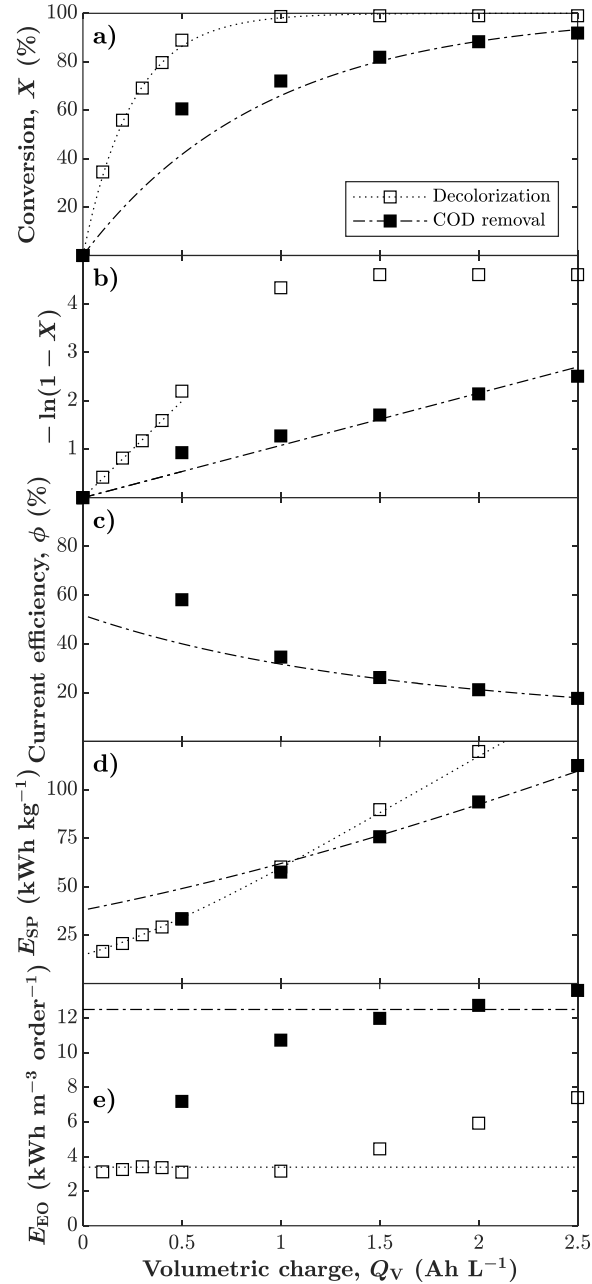


Figure A.4.10 Conversion (X , a), linearized conversion data ($-\ln(1 - X)$, b), current efficiency (ϕ , c), specific and volumetric energy consumption (E_{SP} & E_{EO} , respectively, d & e) for the decolorization and chemical oxygen demand (COD) removal (empty and filled symbols, respectively) of 100 ppm_{MO} in 1,500 g_{NaCl} (200 mL min⁻¹, 21 °C, 4.0 pH) with a Ti₄O₇ porous transport layer in a compact electrolyzer operated galvanostatically (10 mA cm⁻²). Dotted and dash-dotted lines indicate either lines of best fit (a & b) or model predictions (c–e, Eqs. 5.10, 5.11, & 5.6) for decolorization and COD removal, respectively.

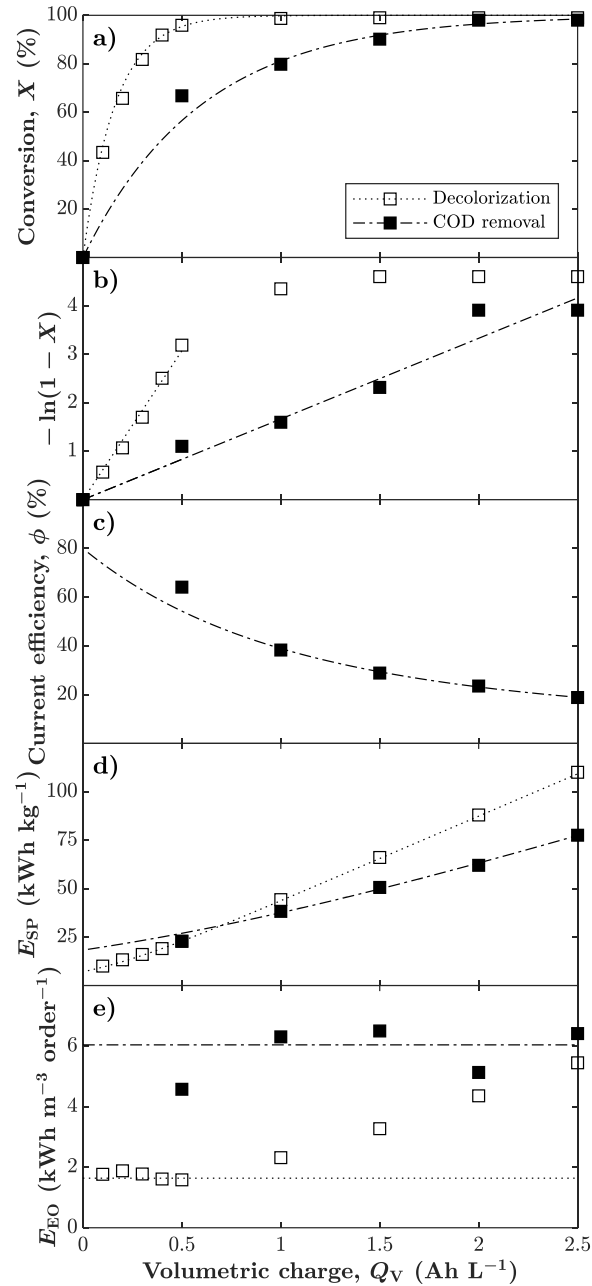


Figure A.4.11 Conversion (X , a), linearized conversion data ($-\ln(1 - X)$, b), current efficiency (ϕ , c), specific and volumetric energy consumption (E_{SP} & E_{EO} , respectively, d & e) for the decolorization and chemical oxygen demand (COD) removal (empty and filled symbols, respectively) of 100 ppm_{MO} in 1,500 g_{NaCl} (200 mL min⁻¹, 21 °C, 4.0 pH) with a (Ti_{0.99}V_{0.01})₄O₇ porous transport layer in a compact electrolyzer operated galvanostatically (10 mA cm⁻²). Dotted and dash-dotted lines indicate either lines of best fit (a & b) or model predictions (c–e, Eqs. 5.10, 5.11, & 5.6) for decolorization and COD removal, respectively.

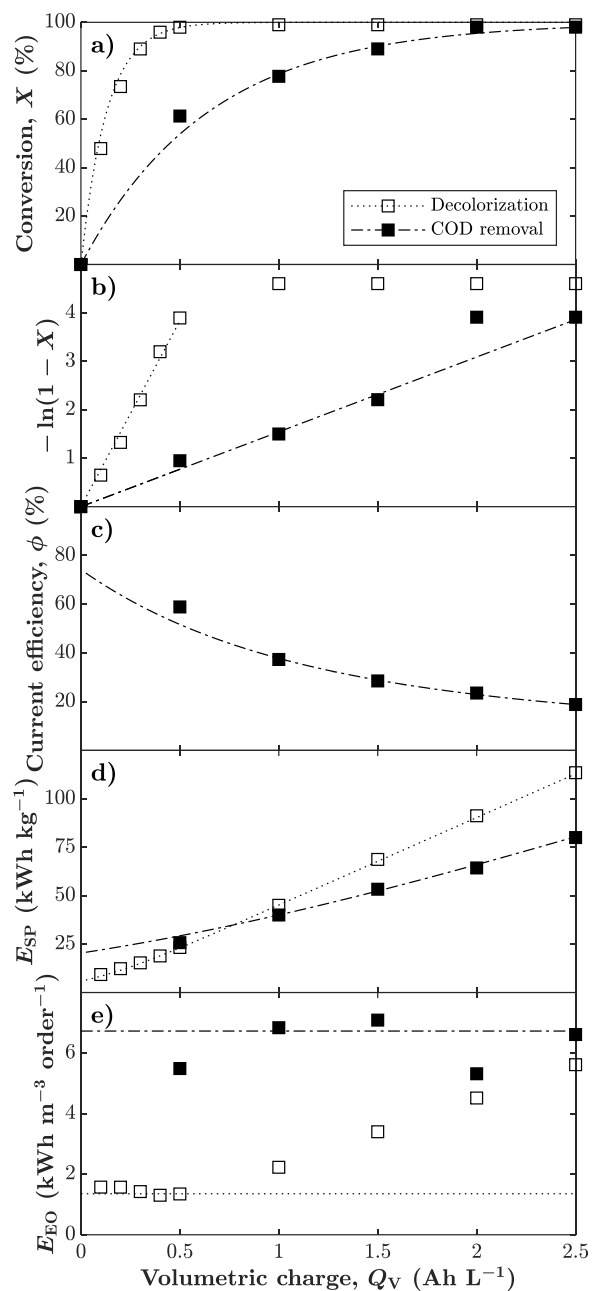


Figure A.4.12 Conversion (X , a), linearized conversion data ($-\ln(1 - X)$, b), current efficiency (ϕ , c), specific and volumetric energy consumption (E_{SP} & E_{EO} , respectively, d & e) for the decolorization and chemical oxygen demand (COD) removal (empty and filled symbols, respectively) of 100 ppm_{MO} in 1,500 g_{NaCl} (200 mL min⁻¹, 21 °C, 4.0 pH) with a (Ti_{0.95}V_{0.05})₄O₇ porous transport layer in a compact electrolyzer operated galvanostatically (10 mA cm⁻²). Dotted and dash-dotted lines indicate either lines of best fit (a & b) or model predictions (c–e, Eqs. 5.10, 5.11, & 5.6) for decolorization and COD removal, respectively.

Appendix B Publications and Presentations

B.1 Publications

1. J. T. English and D. P. Wilkinson, “Vanadium-doped Ti_4O_7 porous transport layers for efficient electrochemical oxidation of industrial wastewater contaminants”, *Journal of the Electrochemical Society*, in press.
2. J. T. English and D. P. Wilkinson, “The Superior Electrical Conductivity and Anodic Stability of Vanadium-Doped Ti_4O_7 ”, *Journal of the Electrochemical Society*, 168(10), 103509, 2021.
3. S. T. McBeath, J. T. English, D. P. Wilkinson, and N. J. D. Graham, “Circumneutral Electrosynthesis of Ferrate Oxidant: An Emerging Technology for Small, Remote and Decentralised Water Treatment Applications”, *Current Opinion in Electrochemistry*, 27, 100680, 2021.
4. J. T. English and D. P. Wilkinson, “The Thermal Oxidation Behavior of Pristine and Doped Magnéli Phase Titanium Oxides.” *ECS Journal of Solid State Science and Technology*, 10(3), 034004, 2021.
5. M. A. Cataldo–Hernández, A. Bonakdarpour, A.; J. T. English, M. Mohseni, D. P. Wilkinson, “A membrane-based electrochemical flow reactor for generation of ferrates at near neutral pH conditions” *Reaction Chemistry & Engineering*, 4(6), 1116–1125, 2019.

B.2 Presentations

1. J. T. English and D. P. Wilkinson “V-doped Ti_4O_7 : A passivation-resilient high oxidation power material,” accepted for oral presentation at the CSC 2023, Vancouver, June 4–8, 2023.
2. J. T. English and D. P. Wilkinson “A Compact Electrolyzer with Vanadium-Doped Ti_4O_7 Porous Transport Layers for Effective Industrial Wastewater Treatment, presented (oral) at the CCEC 2022, Vancouver, Oct. 23–26, 2022.
3. J. T. English and D. P. Wilkinson “Electrochemistry on the Edge: Advancing High Oxidation Power Materials for Applications at Strongly Oxidizing Potentials,” presented (oral) at the ECS 241 Meeting, Vancouver, May 29–June 2, 2022.
4. J. T. English and D. P. Wilkinson “The Superior Electrical Conductivity and Anodic Stability of Vanadium-Doped Ti_4O_7 ,” presented (oral) at the ECS 240th Meeting, Virtual, Oct. 10–14, 2021.
5. J. T. English and D. P. Wilkinson “The Thermal Oxidation Behavior of Pristine and Doped Magnéli Phase Titanium Oxides,” presented (oral) at the PRiME 2020, Virtual, Oct. 4–9, 2020.
9. J. T. English, M. A. Cataldo-Hernández, A. Bonakdarpour, M. Mohseni, M.; D. P. Wilkinson “Electrochemical Ferrates for Water Treatment,” presented (poster) at the 8th Annual Canadian Water Summit, Vancouver, Canada, Jun 20–22, 2018.